



Transient Optical and Electrical Effects in Polymeric Semiconductors

Dissertation

in partial fulfilment of the
requirements of the degree of
doctor rerum naturalium (Dr. rer. nat)
in Physics

Submitted to the
Faculty of Mathematics and Natural Sciences
of the University of Potsdam

by
SEBASTIAN BANGE

Potsdam, May 28, 2009

This work is licensed under a Creative Commons License:
Attribution - Noncommercial - Share Alike 3.0 Germany
To view a copy of this license visit
<http://creativecommons.org/licenses/by-nc-sa/3.0/de/deed.en>

Published online at the
Institutional Repository of the University of Potsdam:
URL <http://opus.kobv.de/ubp/volltexte/2009/3631/>
URN <urn:nbn:de:kobv:517-opus-36314>
[<http://nbn-resolving.org/urn:nbn:de:kobv:517-opus-36314>]



Transiente Optische und Elektrische Effekte in Polymeren Halbleitern

Doktorarbeit

zur Erlangung des akademischen Grades

doctor rerum naturalium

(Dr. rer. nat)

in der Wissenschaftsdisziplin „Physik“

eingereicht an der
Mathematisch-Naturwissenschaftlichen Fakultät
der Universität Potsdam

von
SEBASTIAN BANGE

Potsdam, den 28. Mai 2009

Abstract

Classical semiconductor physics has been continuously improving electronic components such as diodes, light-emitting diodes, solar cells and transistors based on highly purified inorganic crystals over the past decades. Organic semiconductors, notably polymeric, are a comparatively young field of research, the first light-emitting diode based on conjugated polymers having been demonstrated in 1990. Polymeric semiconductors are of tremendous interest for high-volume, low-cost manufacturing (“printed electronics”). Due to their rather simple device structure mostly comprising only one or two functional layers, polymeric diodes are much more difficult to optimize compared to small-molecular organic devices. Usually, functions such as charge injection and transport are handled by the same material which thus needs to be highly optimized. The present work contributes to expanding the knowledge on the physical mechanisms determining device performance by analyzing the role of charge injection and transport on device efficiency for blue and white-emitting devices, based on commercially relevant spiro-linked polyfluorene derivatives. It is shown that such polymers can act as very efficient electron conductors and that interface effects such as charge trapping play the key role in determining the overall device efficiency. This work contributes to the knowledge of how charges drift through the polymer layer to finally find neutral emissive trap states and thus allows a quantitative prediction of the emission color of multichromophoric systems, compatible with the observed color shifts upon driving voltage and temperature variation as well as with electrical conditioning effects. In a more methodically oriented part, it is demonstrated that the transient device emission observed upon terminating the driving voltage can be used to monitor the decay of geminately-bound species as well as to determine trapped charge densities. This enables direct comparisons with numerical simulations based on the known properties of charge injection, transport and recombination. The method of *charge extraction under linear increasing voltages* (CELIV) is investigated in some detail, correcting for errors in the published approach and highlighting the role of non-idealized conditions typically present in experiments. An improved method is suggested to determine the field dependence of charge mobility in a more accurate way. Finally, it is shown that the neglect of charge recombination has led to a misunderstanding of experimental results in terms of a time-dependent mobility relaxation.

Zusammenfassung

Klassische Halbleiterphysik beschäftigt sich bereits seit mehreren Jahrzehnten erfolgreich mit der Weiterentwicklung elektronischer Bauteile wie Dioden, Leuchtdioden, Solarzellen und Transistoren auf der Basis von hochreinen anorganischen Kristallstrukturen. Im Gegensatz hierzu ist das Forschungsgebiet der organischen, insbesondere der polymeren Halbleiter noch recht jung: Die erste Leuchtdiode auf der Basis von „leitfähigem Plastik“ wurde erst 1990 demonstriert. Polymere Halbleiter sind hierbei von besonderem Interesse für hochvolumige Anwendungen im Beleuchtungsbereich, da sie sich kostengünstig herstellen und verarbeiten lassen („gedruckte Elektronik“). Die vereinfachte Herstellung bedingt dabei eine vergleichsweise geringe Komplexität der Bauteilstruktur und verringert die Optimierungsmöglichkeiten. Die vorliegende Arbeit leistet einen Beitrag zum Verständnis der Vorgänge an Grenzflächen und im Volumen von polymeren Leuchtdioden und ermöglicht damit ein besseres Verständnis der Bauteilfunktion. Im Fokus steht hierbei mit einem spiroverknüpften Polyfluorenderivat ein kommerziell relevanter Polymertyp, der amorphe und hochgradig temperaturstabile Halbleiterschichten bildet. Ausgehend von einer Charakterisierung der Ladungstransporteigenschaften wird im Zusammenspiel mit numerischen Simulationen der Bauteilemission gezeigt, welche Rolle die polymeren und metallenen Kontaktelektroden für die Bauteilfunktion und -effizienz spielen. Des Weiteren wird ein weißemittierendes Polymer untersucht, bei dem die Mischung von blauen, grünen und roten Farbstoffen die Emissionsfarbe bestimmt. Hierbei wird das komplexe Wechselspiel aus Energieübertrag zwischen den Farbstoffen und direktem Ladungseinfang aufgeklärt. Es wird ein quantitatives Modell entwickelt, das die beobachtete Verschiebung der Emissionsfarbe unter wechselnden elektrischen Betriebsparametern erklärt und zusätzlich die Vorhersage von Temperatur- und elektrischen Konditionierungseffekten ermöglicht. Ausgehend von leicht messbaren Parametern wie Stromstärken und Emissionsspektren ermöglicht es Rückschlüsse auf mikroskopische Vorgänge wie die Diffusion von Ladungen hin zu Farbstoffen. Es wird gezeigt, dass im Gegensatz zu bisherigen Erkenntnissen der Ladungseinfang durch Drift im elektrischen Feld gegenüber der Diffusion überwiegt. In einem eher methodisch orientierten Teil zeigt die Arbeit, wie die beim Abschalten von Leuchtdioden beobachtbare Emission dazu verwendet werden kann, Erkenntnisse zu Ladungsdichten während der Betriebsphase zu gewinnen. Es wird abschließend nachgewiesen, dass eine gängige Methode zur Bestimmung von Ladungsbeweglichkeiten unter typischen Messbedingungen fehlerbehaftet ist. Ergebnisse, die bisher als eine zeitliche Relaxation der Beweglichkeit in ungeordneten Halbleitern interpretiert wurden, können damit auf die Rekombination von Ladungen während der Messung zurückgeführt werden. Es wird außerdem gezeigt, dass eine Modifikation der bei der Auswertung verwendeten Analytik die genauere Vermessung der Feldstärkeabhängigkeit der Beweglichkeit ermöglicht.

Contents

Introduction	1
Polymeric Semiconductors	1
Outline of the Thesis	2
1 Fundamentals	5
1.1 Charge Transport	5
1.2 Charge Injection	7
1.3 Charge Recombination and Electroluminescence	10
1.4 White Emission from Organic Semiconductors	11
2 Charge Transport in a Blue-emitting Copolymer	15
2.1 Introduction	15
2.2 Time-of-flight Photocurrent Measurements	16
2.3 Transient Electroluminescence	22
2.4 Conclusion	31
3 Charge Injection and Electrical Conditioning Effects	33
3.1 Introduction	33
3.2 Charge Injection	35
3.3 Numerical Simulation of Device Behavior	45
3.4 The Role of Electron Blocking and Device Conditioning	51
3.5 Conclusion	54
4 Emission Color and Charge Trapping	55
4.1 Introduction	55
4.2 Energy Transfer and its Impact on Emission Color	55
4.3 Charge Transport and Deep Trapping	64
4.4 Color Balance in Electroluminescence	70
4.5 Charge Density Effects on the Emission Color	76
4.6 Temperature Effects on the Emission Color	83
4.7 Anode Interface Conditioning Effects	85
4.8 Conclusion	87
5 Electroluminescence Decay Transients: the Role of Charge Traps	89
5.1 Introduction	89
5.2 Experimental	90
5.3 Review of Delayed EL Mechanisms	93
5.4 Results and Discussion	96

5.5	Conclusion	106
6	Applications and Limits of the CELIV Technique	107
6.1	Introduction	107
6.2	Analytic Description of CELIV Transients	108
6.3	Numerical Analysis of CELIV Transients	111
6.4	CELIV Transients under Non-Ideal Conditions	115
	Summary	121
A	Numerical Simulation of Drift-Diffusion Equations	125
A.1	Summary of the Simulation Algorithm	128
A.2	Methods and Algorithms	130
B	Organic Materials	133
C	Sample Preparation	137
D	Measurement Techniques	141
E	List of Abbreviations	143
F	List of Symbols	145
	Bibliography	148
	Publications	163
	Acknowledgment	165
	Curriculum Vitae	167

Introduction

Polymeric Semiconductors

For a long time, research of organic polymers was focused on *saturated* organic compounds that did not readily provide intrinsic electronic functionalities. Here, saturated refers to the participation of all four carbon atom's valence electrons in covalent σ -bonds. A huge variety of organic compounds instead falls into the class of *unsaturated* systems, with a typical example being the ideal $(-\text{CH})_n$ polyene (or polyacetylene) chain of carbon atoms bonded by alternating double and single bonds. Such compounds are also known as *conjugated polymers*. The carbon atoms are sp_2 hybridized, leaving one electron per carbon atom in an unpaired p_z state that contributes to a molecular π -orbital. For an ideal infinite chain, these orbitals merge into a continuous band of localized states, which is half-filled by electrons. Therefore, polyacetylene is expected to behave as a one-dimensional metal. In the 1950s it became theoretically evident that a dimerization of the chain lowers the overall energy by breaking the symmetry ('Peierls instability'), which leads to an alternation of the bond lengths between adjacent carbon atoms. In fact, the lowest energy state of polyacetylene is $(-\text{CH}=\text{CH})_n$, with two carbon atoms per repeat unit. As a result, two (instead of one) bands are formed, one fully occupied and one empty, separated by an energy gap E_g . Correspondingly, polyacetylene films were found to exhibit semiconductive properties [1] and a wide range of conductivity could be realized by introducing additional charge carriers into the polymer backbone via chemical doping [2], a development finally leading to the award of the Nobel prize in chemistry to A. Heeger, A. MacDiarmid and H. Shirakawa in 2000. Even in the undoped state, polymeric semiconductors became highly interesting materials that can be used for optoelectronic devices. In 1990, Burroughes et al. [3] demonstrated the feasibility of light-emitting devices fabricated from the conjugated polymer poly-*para*-phenylenevinylene (*PPV*), just shortly after the first realization of efficient electroluminescence from a small-molecular organic semiconductor by Tang and VanSlyke [4] in 1987. Since the bandgap energy E_g can be tuned by chemical modifications in many ways,[5] the emission wavelength and thus the color of such light-emitting diodes can be varied over the whole visible range. Light-emitting diodes fabricated from polymeric and small-molecular organic semiconductors, together with new applications such as organic solar cells and organic field-effect transistors, have since become one of the driving motors for research, the focus being placed on easy processibility, high luminescent efficiency, environmental stability and operational lifetime.

Outline of the Thesis

Recently, research in the field of organic light-emitting diodes has become focused on achieving low-cost, highly efficient lighting solutions capable to be competitive with and finally replace more common technologies such as incandescent or fluorescent lighting within the next decade. Polymeric semiconductors are especially attractive when targeting mass-market applications such as large area lighting and signage applications, mainly due to their low-cost processability including screen-printing, inkjetting and high volume roll-to-roll manufacturing. One unique feature of semiconducting polymers is that different functional units can be combined in a single polymer. Ideally, this copolymer approach allows one to independently tune the injection and transport properties for holes and electrons of a single polymer layer, without the need to form multilayer devices. Recently, white-emitting single polymers comprising two or more fluorescent or phosphorescent units with different emission colors have been synthesized and applied in light-emitting diodes. However, very little is known about the processes determining efficiency and color of these multifunctional polymers.

The present thesis aims at improving the understanding of the fundamental processes that determine the operation of light-emitting diodes based on 'single polymer, single layer' semiconductor structures. It is focused on two types of commercially available blue and white electrofluorescent polymeric semiconductors falling into the general class of spiro-linked polyfluorene derivatives. Such polymers are of considerable interest due to their amorphous, temperature stable morphology and their good hole and electron transport properties.

Using a combination of complementary transient and steady-state analysis methods, the properties of charge transport and charge injection are analyzed in chapters 2 and 3, respectively. The aim of both chapters is to provide insight into the equilibrium and transient response of bipolar devices by a 'bottom-up' approach. The chapters gather enough data to provide a solid basis for numerical simulations of the device behavior that are essentially free of unknown parameters. The comparison of simulated device characteristics and experimental observations provides insight into the role of the interface between the conductive electrode material PEDOT:PSS and the polymer. It is shown that both charge trapping as well as an energetic barrier that hinders electron extraction impact the device behavior.

Chapter 4 studies the principles governing the operation of white light emitting diodes based on polyspirofluorene wide-bandgap backbone structures that were copolymerized with green and red chromophores. The interplay of interchromophoric energy transfer and the direct trapping of electrons on deep trap states represented by the red chromophores is shown to determine the emission color of these devices. Exercising control of the emission spectrum over a large range of operating conditions is important for the application of such devices as replacements of incandescent lighting technologies, since these usually require a relatively precise control of the emission color. It is shown that rate equations provide reasonable insight into the device behavior under varying driving field, current and temperature conditions. More specifically, the employed analysis is used to determine the rate of charge trapping attributed to drift and of charge trapping attributed to charge diffusion, which is discussed in terms of continuum diffusion and random walk models. The results show that it is possible to gain detailed insight into microscopic processes purely by measurement of macroscopic parameters such as charge transport, injection and emission spectra.

Chapter 5 concludes the studies of white light-emitting diodes by analyzing the physical

processes that govern the transient electroluminescence observed upon termination of the device's driving voltage. The density of electrons is shown to dominate this operation regime, where decay of geminately bound charges, the extraction and trapping of free electrons are responsible for the decay on short time scales and the slow decay of trapped electrons with free holes for longer times. The amount of trapped charges can be extracted from this decay using a relatively simple analysis, an approach that is verified by comparison to numerical simulations.

The thesis is concluded by a study of the method of current extraction under linear increasing voltage (CELIV) in chapter 6. This chapter is focused on the method instead of experimental investigations. It rederives the fundamental equations, closing a gap in the published literature on the method and pointing out minor errors in the original derivations. This derivation is used as a starting point to analyze the method under the aspect of more realistic measurement conditions such as bimolecular charge recombination and field-dependent charge mobilities, aspects that have not been treated so far. It is shown how the method can be improved analytically and that the usual interpretation of measurement results in terms of a time-dependent mobility relaxation actually derives from shortcomings of the analytic evaluation procedure.

Chapter 1

Fundamentals

This chapter gives a brief introduction into the basic concepts of charge injection, transport and recombination in organic semiconductors. Because of the very large variety of known organic semiconductors, only the most common and general concepts are presented. A more detailed description of specific processes relevant for the understanding of a certain polymer or model is contained in the respective chapter.

1.1 Charge Transport

It is generally accepted that the delocalized π -orbitals, characteristic for conjugated polymers, do not extend along the full polymer backbone, their length being limited by chemical defects as well as changes of the chain conformation such as kinks and torsions.[6] The optoelectronic properties are thus determined by conjugated segments much shorter than the average chain length. These conjugated segments act as individual *sites* in terms of the properties of the excited state and those of the singly-charged (oxidized or reduced) states acting as charge carriers. Here, the term ‘site’ usually does not represent an entity that is fixed in time but rather depends on the molecular motions of the underlying polymer chain. Charge transport in solids is typically classified into being either of band type or hopping type. Band type transport occurs when the mean scattering time τ is much larger than $h/\Delta\varepsilon$, where h is the Planck constant and $\Delta\varepsilon$ is the energetic width of the transport band. In this case, the mean free path λ is much larger than the lattice constant a and electrons move coherently as plane waves. When $\lambda \sim a$ charges move between localized states by phonon-assisted *hopping*, i.e. by a quantum mechanical state transition not involving intermediates. In any case, the charge mobility $\mu = v/E$ is defined by their average drift velocity v in the electric field E . For band-type transport, $\mu = e\tau/m^*$ where m^* is the effective mass and the mobility typically drops as $\mu \propto T^{-n}$ ($n > 1$) with temperature T , see Pope and Swenberg [7, p. 337]. In contrast to this, hopping transport is assisted by phonons and thus typically features a temperature-activated behavior. Generally, the physical framework used for the description of charge transport in an organic semiconductor depends on the amount of order present at the molecular level. Large mean free paths are usually obtained for highly purified molecular single crystals such as anthracene and pentacene, with the transport mechanism showing characteristics of both band-type and hopping-type conduction.[7] On the contrary, the optoelectronic properties of *disordered* organic semiconductors are inhomogeneously broadened to a significant amount. The distribution is usually assumed to be of gaussian nature due to the action of a large number of internal coordinates on the lattice polarization energies.[8, 9] Charge carriers in these disordered systems are considered to be polarons or bipolarons that

move between localized states by hopping. The framework used for describing the charge transport depends on the coupling of the charges to the vibrational modes: for strong coupling, the *small polaron model* discussed by Holstein [10] is usually used. When the coupling to vibrational modes is weak and the spatial disorder of site energies large, charge carriers hop between localized states depending on the energy difference between those sites. This is usually described in terms of a gaussian disorder model (*GDM*), neglecting polaronic effects. It has been argued that for molecularly doped and conjugated polymers the disorder model provides a more reasonable starting point.[9]

The gaussian disorder model of charge transport assumes that the energy of charge transporting states provided by the transport sites is distributed according to the density of states (*DOS*)

$$g(\varepsilon) = \frac{N}{\sigma\sqrt{2\pi}} \exp\left(\frac{-\varepsilon^2}{2\sigma^2}\right), \quad (1.1.1)$$

where σ is the energetic (*diagonal*) disorder assuming the energy ε is measured from the center of the distribution and N is the total number of states.[9] The jump rate for charge carriers between sites i and j is assumed to be of the form

$$v_{ij} = v_0 \exp\left(-\frac{2r_{ij}}{\alpha}\right) \exp\left(-\frac{\varepsilon_j - \varepsilon_i + |\varepsilon_j - \varepsilon_i|}{2k_B T}\right), \quad (1.1.2)$$

where α is the localization length of charges and v_0 is a prefactor that depends on the electron-electron interaction mechanism. Transitions upwards in energy $\varepsilon_j > \varepsilon_i$ are mediated by phonons, such that an Arrhenius-activated behavior is expected. At low densities, charge carriers starting at $t = 0$ anywhere in the density of states relax towards the equilibration energy $\varepsilon_\infty = \lim_{t \rightarrow \infty} \varepsilon(t) = -\sigma^2/k_B T$ resulting from the assumption that equilibrium charge carrier energies are distributed according to a Boltzmann distribution at reasonably low charge densities. At this equilibrium energy, only few sites are available for isoenergetic jumps of the charge carrier. For charge transport, temperature activation to states higher in the DOS is needed and it was shown by Bässler and coworkers [9] by numerical and analytic techniques that the activation behavior is described by a temperature-dependent mobility $\mu = \mu_0 \exp(-(2\sigma/3k_B T)^2)$ corresponding to an average *transport level* at $\varepsilon_{\text{transp.}} = -5\sigma^2/9k_B T$. The Marburg group conducted Monte-Carlo simulations of disordered systems, additionally accounting for variations of the site energies due to electric fields and for *positional* disorder in the wavefunction overlap α of neighboring sites.[9, 11] The resulting field- and temperature dependence of mobility is

$$\mu(E, T) = \mu_0 \exp\left\{-\left(\frac{2\sigma}{3k_B T}\right)^2 + C_0 \left[\left(\frac{\sigma}{k_B T}\right)^2 - \Sigma^2\right] \sqrt{E}\right\}. \quad (1.1.3)$$

at sufficiently high fields. While $C_0 = 2.9 \times 10^{-4} \text{ (cm/V)}^{1/2}$ is an empirical constant of their simulations which varies with intersite distance,[8] the model parameters σ and Σ represent the energetic and positional disorder, respectively. This model correctly predicts the $\log(\mu) \propto \sqrt{E}$ behavior usually observed at high electric fields. This is referred to as a *Poole-Frenkel* type behavior, although the underlying mechanism strongly differs from Frenkel's assumptions that charge carrier mobility is limited by the field-assisted escape

from *charged* coulomb traps.[12, 13] Gartstein and Conwell suggested an improvement of the GDM by taking into account additional energetic disorder due to charge-induced spatial correlations.[14] Their model extends the Poole-Frenkel field dependence towards lower electric fields. The GDM predicts a non-Arrhenius temperature activation $\log(\mu) \propto 1/T^2$ of charge mobility, consistent with experimental results on both amorphous small-molecular materials and conjugated polymers.[11, 15] Contrary to these findings, measurements of the field-effect mobility in organic transistor structures have also been explained in terms of multiple trapping and release models that yield an Arrhenius-type temperature activation inconsistent with the results of the GDM model.[16] This deficiency is discussed, among others, by Coehoorn et al. [17] and Baranovski et al. [8] and attributed to the neglect of electron-electron interactions in the original GDM model. When the charge density $n > n_c$ exceeds some critical charge density estimated as $n_c = N \exp(-\sigma^2/2(k_B T)^2)$, electrons have a significant probability to find already occupied states during their hopping motion. At high charge densities, this leads to $\log(\mu) \propto 1/T$ instead of $1/T^2$. Generally, the impact of charge density on charge mobility cannot be neglected and unified models have been proposed.[17] In contrast to completely amorphous systems, charge transport in partially crystalline samples is much more difficult to treat theoretically in a consistent way due to the presence of both coherent and incoherent transport modes.[16]

1.2 Charge Injection

Organic semiconductors are characterized by a wide bandgap in the visible region and low relative permittivity $\epsilon \sim 3$. As a rough estimate, the electron-hole binding energy can be calculated based on the lowest energy state of the Bohr model as $\epsilon = e^4 m_e / 8 \epsilon^2 \epsilon_0^2 h^2 \sim 1.5$ eV, corresponding to a mean electron-hole distance of $\epsilon \epsilon_0 h^2 / e^2 m_e \sim 1.6$ nm. The *optical bandgap* of typical conjugated polymers ranges between 2 eV and 3.5 eV, corresponding to the energetic difference of HOMO and LUMO. Indeed, the *transport bandgap* is even higher since polarization of the molecular environment tends to stabilize the neutral states. Excited states are thus considered to be Frenkel-type intramolecular or intermolecular charge transfer type states instead of the Mott-Wannier excitons usually found for crystalline inorganic semiconductors. The direct thermal excitation of electrons into conductive states is highly unlikely and the *intrinsic* charge carrier density thus neglectible. The amount of doping introduced by chemical defects is usually low but can be raised by deliberate introduction of charge transfer atoms, molecules or salts. Since dopants tend to quench the intrinsic excited states of the materials, this route is usually not followed for the materials used in the central functional layers of optoelectronic devices such as photovoltaic cells or light-emitting diodes.[18] The most simple configuration to achieve reasonable charge densities in organic semiconductors is thus the typical metal-semiconductor-metal (*MSM*) structure, where the organic layer is contacted by two metallic electrodes. Charge injection into low-mobility semiconductors is limited by space charge effects since the current density j is determined by the charge mobility μ and the electric field E as $j = e \mu n E$. When the metal/semiconductor contact is free of barriers (*Ohmic contact*), the injected current is limited only by this ability to transport charges. The local charge density then diverges at the electrode interface and the space charge reduces the local electric field to near zero. The resulting space-charge limited

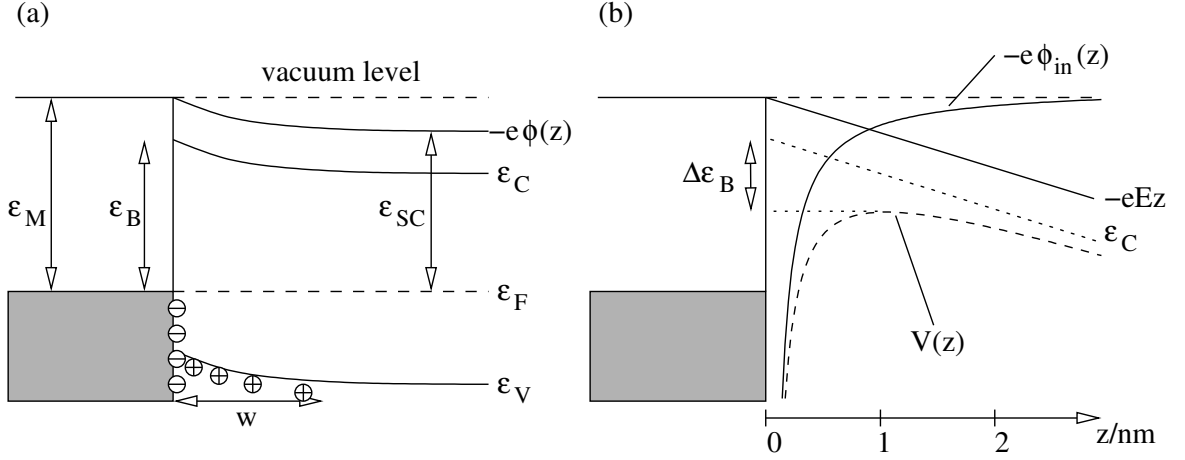


Figure 1.1: (a) Schottky contact with electron depletion layer of width w due to equilibration of the Fermi levels ϵ_M and ϵ_{SC} of metal and semiconductor, respectively. The space charge layer causes an electric potential $\phi(z)$. (b) The Schottky effect of the image charge potential ϕ_{in} is the bending of the valence band effective energy $V(z)$ and a lowering of the injection barrier ϵ_B by $\Delta\epsilon_B = (e^3 E / 4\pi\epsilon\epsilon_0)^{1/2}$ under an applied electric field E .

current (SCLC) density is

$$j_{SCLC} = \frac{9}{8} \epsilon\epsilon_0 \mu U^2 / d^3, \quad (1.2.1)$$

where d is the layer thickness and U is the applied voltage. It represents the maximum possible injection current assuming the simplified concepts of semiconductor transport in terms of field-independent mobility are (approximately) valid. Figure 1.1 shows the energetic situation of a classical metal-semiconductor Schottky contact. In thermodynamic equilibrium, the Fermi levels of metal and semiconductors must align and thus charges may be transferred between both materials. The figure shows the situation of electron transfer from the semiconductor to the metal due to a lower work function ϵ_{SC} compared to ϵ_M of the metal. An electron depletion (hole accumulation) layer of width

$$w = \sqrt{\frac{2\epsilon\epsilon_0}{e^2 n} (\epsilon_M - \epsilon_{SC} - eU_{ext} - k_B T)} \quad (1.2.2)$$

is formed, where n is the free charge density and U_{ext} is the externally applied voltage. The impact of such accumulation zones on the device physics of organic semiconductors varies, where it is generally assumed that under conditions of trap-free transport the width of the depletion layer is larger than the layer thickness, which would render the treatment of sandwiched structures in terms of a metal-insulator-metal (MIM) description more appropriate.[18] Figure 1.1 (b) shows that the effective injection barrier is also determined by the applied electric field through the Schottky barrier lowering effect: electric charges in front of the conducting metal electrode feel an image charge potential $\phi_{in}(z) = -e^2 / 16\pi\epsilon\epsilon_0 z$, resulting in a lowering of the effective injection barrier by $\Delta\epsilon_B = \sqrt{e^3 E / 4\pi\epsilon\epsilon_0}$. The resulting energetic barrier for carrier injection (here: electron injection) can be overcome by two basic principles: thermal excitation and quantum tunneling. At high electric fields, electrons

can directly tunnel through the energetic barrier once the barrier thickness is on the order of extent of their quantum mechanical wavefunctions. The resulting field effect depends on the shape of the barrier potential, where usually a triangular shape is assumed. The resulting tunneling current density

$$j_{\text{FN}}(E) = \alpha_1 \frac{E^2}{\epsilon_{\text{B}}} \exp\left(\alpha_2 \frac{\epsilon_{\text{B}}^{3/2}}{E}\right) \quad (1.2.3)$$

has been treated by Fowler and Nordheim [19] and is extensively discussed in textbooks on semiconductor physics such as [20]. Several authors used a tunneling mechanism to study the injection currents of organic semiconductors, see [21, 22]. At finite temperature, a fraction of the electrons in the metal can gain enough energy from phonons to overcome the injection barrier. This was investigated by Richardson, who concluded that the current density is

$$j_{\text{R}} = AT^2 \exp\left(-\frac{\epsilon_{\text{B}}}{k_{\text{B}}T}\right), \quad (1.2.4)$$

where $A = 4\pi m_e k_{\text{B}}^2 e / h^3$. [23, 24] At non-zero electric fields, ϵ_{B} is replaced by $\epsilon_{\text{B}} - \Delta\epsilon_{\text{B}}$, resulting in the Richardson-Schottky field-enhanced thermionic emission model. [13, 25] These idealized models do not provide a faithful description of the physics of charge injection into low mobility solids such as organic semiconductors. Improvements have been suggested e.g. by Simmons [25], Davids et al. [26] and Scott et al. [27, 28] by accounting for the interface recombination current due to charges flowing from the semiconductor back to the electrode. The Scott model will be discussed in more detail in appendix A in terms of its application to numerical device simulations. The theoretical models for charge injection discussed so far fall into the general class of ‘semi-classical’ descriptions and assume that the charge transport is fairly well described by a single transport level and field-independent mobility. An alternative approach considers the injection of electrons from the metal Fermi level into a disordered hopping system of localized states, as is also the basis of gaussian disorder models of charge transport. [29–31] Arkhipov et al. [32, 33] considered an analytic model taking into account the temperature and field dependence of both a primary charge injection event and a subsequent diffusive escape from the interface-near potential well provided by the Schottky effect via $V(z)$, compare figure 1.1. The injection current follows from

$$j = ev_0 \int_a^\infty dz e^{-2\gamma z} p_{\text{esc.}}(z) \left(\int_{-\infty}^0 dE + \int_0^\infty dE e^{-\frac{E}{k_{\text{B}}T}} \right) g(V(z) - E), \quad (1.2.5)$$

where v_0 is a normalizing ‘attempt-to-jump’ frequency, γ is the inverse localization radius as used in the GDM model and a is the distance between the interface and the first hopping site. $p_{\text{esc.}}$ is the probability of diffusive escape from position z to the bulk of the semiconductor and is similar to the Onsager escape formalism of bound electron-hole pairs. [34, 35] This model was shown to be in accordance with Monte-Carlo simulations [36] and was used by T. van Woudenberg to consistently model the temperature and field dependence of charge injection from Al and Ag into the polymeric semiconductor poly(2-methoxy-5-(3',7'-dimethyloctyloxy)-p-phenylene vinylene) (OC₁C₁₀-PPV). Fong et al. [37] report that this model does not correctly reproduce the observed flat temperature dependence of hole injection from indium-tin oxide (ITO) and Au anodes into poly[(9,9'-dioctylfluorenyl-2,7-diyl)-co-(4,4'-(N-(4-sec-butyl)diphenylamine))] (TFB). A complete theory unifying all of the

observed characteristics of charge injection into organic semiconductors thus still needs to be developed. Apart from the mechanisms discussed so far, charge injection into organic semiconductors depends on several other physical mechanisms such as the interfacial electronic structure modified by dipoles and charge transfer, chemical alterations at the interface, deep trapping states and tunneling barriers.

1.3 Charge Recombination and Electroluminescence

Electrically excited light emission from organic semiconductors due to the bimolecular recombination of injected charge carriers was first reported by Pope and coworkers in 1963 for the molecular crystal anthracene.[38, 39] These experiments were limited to fairly high driving voltages due to the macroscopic dimensions of the crystals used in the experiments. Most of the work in the following two decades was focused on the development of photoconductors based on molecularly doped polymers due to their relevance for industrial applications.[40] The scientific interest in organic electroluminescence was much stimulated by the report of electroluminescence in small-molecular thin film devices fabricated via thermal evaporation of 8-hydroxyquinoline aluminum (Alq_3) by Tang and VanSlyke in 1987, where light emission was achieved at more practicable voltage levels of less than 10 V.[4] Electroluminescence from conjugated polymer semiconductors was first reported by Burroughes et al. in 1990 for devices made with *in-situ* polymerized poly(*p*-phenylenevinylene) (PPV) films of 100 nm thickness.[3]

Bimolecular recombination of positive and negative charge carrying species requires that the charges pass each other within some distance set by the mutual Coulomb attraction. This situation is usually described in terms of the Langevin mechanism [41] when the probability of redissociation is sufficiently small. Without loss of generality, assume that only one charge carrier moves at a mobility μ and that charges are separated sufficiently far from each other such that trimolecular processes can be neglected. The flux of charges through a sphere of radius r towards a single countercharge is $\mu en/\epsilon\epsilon_0$ and the total recombination rate of the electron density n_e and hole density n_h thus becomes

$$\frac{dn_{h,e}}{dt} = \frac{\mu e}{\epsilon\epsilon_0} n_e n_h. \quad (1.3.1)$$

As pointed out by Ries and Bäessler [42], this result is equivalent to the recombination of *neutral* particles diffusing with a diffusion constant D , assuming validity of the Einstein equation $D/\mu = k_B T/e$ and using the trapping rate $\gamma = 4\pi r_c D$ predicted from the Smoluchovski diffusion equation,[43] when their recombination radius $r = r_c$ is assumed to equal the *Coulomb radius*

$$r_c = \frac{e^2}{4\pi\epsilon\epsilon_0 k_B T}. \quad (1.3.2)$$

This result is not surprising since r_c is the distance where the mutual Coulomb binding energy equals the thermal energy $k_B T$. It should be noted that Langevin neglected the direct recombination of charges induced by drift motion in *external* electric fields, assuming that the ballistic reaction cross section set by the wavefunction extents of the charged species is much smaller than r_c . This is justified in organic semiconductors due to the relatively

low dielectric constant $\epsilon \sim 3$ of these materials. As discussed in chapter 4.3, the situation is different for the capture of charge carriers by *neutral* trapping sites where both diffusion and drift contribute to the total trapping ratio.

Upon recombination, both singlet and triplet excited states can be formed which are usually confined to the conjugated segment of a polymer chain but may also correspond to intermolecular excited states.[44] These states can be described well by the molecular excited states formed via direct photoexcitation, as evidenced by the usually very similar fluorescence spectra. Since the charges are injected at the electrodes in an uncorrelated manner, the two spin-1/2 charge carriers recombine to a singlet exciton or one out of three possible triplet excitons at a ratio of $\eta_{ST} = 1/3$. Deviations from this singlet-triplet splitting ratio can arise from spin-dependent charge recombination and have been discussed recently, with one possible mechanism being a difference in recombination cross sections since singlet exciton states tend to be more delocalized compared to triplet states.[45–47] Increased cross sections for singlet formation have been reported for regioregular poly(3-hexylthiophene) layers for which high amounts of local ordering and thus longer conjugation lengths are expected.[46]

The overall quantum efficiency of organic light-emitting diodes based on singlet-emitting materials can generally be expressed as $\eta_{ext} = \eta_r \eta_{ST} \eta_F \eta_{extr}$, where η_r is a charge balance factor, i.e. the probability that injected electrons and holes recombine, η_{ST} is the ratio of emissive singlet states to non-emissive triplet states formed by the recombination and η_F is the fluorescence quantum efficiency of the singlet excited states. The photon extraction efficiency η_{extr} is usually less than one due to losses into waveguiding modes and reduced transparency of the substrates. η_r is the most complex parameter from a physical point of view. In order to guarantee the recombination of injected charges before they are extracted at the counterelectrode, internal energetic barriers, e.g. introduced by organic/organic heterojunctions, are normally used. These barriers hinder charge movement towards the extracting electrode, locally enhance the charge density and thus enforce bimolecular recombination. Polymeric light-emitting diodes are designed employing only one or two active layer since mutual intermixing during film preparation cannot be easily prevented with organic solvent based deposition methods. For these devices, the general paradigm for achieving high η_r is the balancing of hole and electron mobilities. Chapter 3 will discuss this in more detail, demonstrating that relatively high η_r can be achieved by interface effects between the charge injecting electrode and the semiconducting polymer even under conditions of $\mu_e \gg \mu_h$.

1.4 White Emission from Organic Semiconductors

Daylight vision of the human eye is provided by three types of cone cells (S, M, L) in the retina. While S-type cones are most responsive at the blue end of the visible light spectrum, L-type cones provide the ability for vision at the longest wavelengths. Separating total luminance from color, the perception of light stimulus by the human brain (i.e. the color) can be described by a two-dimensional vector space of which several variants exist, the ubiquitous Commission Internationale de l'Éclairage (CIE) 1931 XYZ space being one of the earliest. White light perception is already achieved by mixing two or more light sources of suitable color coordinates, even in case each emits monochromatic light. However, the color per-

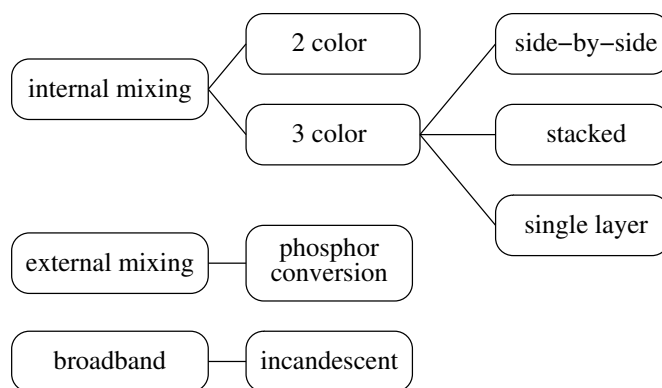


Figure 1.2: Concepts for white-light emission from organic light-emitting diodes.

ceived when looking directly into the light source is not sufficient to describe the usefulness of light sources for illumination purposes. Since we perceive objects by the light reflected from their surface, knowledge of the color coordinates of an illuminant is insufficient. The reflected light's spectral distribution, i.e. its color, will strongly depend on the specific interaction of the corresponding wavelengths with the object. Usually, the *natural* color of objects is defined by illumination with light of broad spectral distribution similar to that provided by sunlight. Illuminants such as incandescent lamps, fluorescence lamps, inorganic and organic light-emitting diodes strongly differ in their ability to reproduce the natural color of objects, which is quantified by the color rendering index (CRI). In terms of CRI, organic white-light emitters are usually superior to either inorganic LED as well as fluorescent lamps due to the typically broad spectrum of the chromophores employed. The combination of emission from several chromophore types proceeds either internally to the (electrically active) layers, or externally, see figure 1.2. External mixing concepts are usually employed for inorganic light-emitting diodes: Ce^{3+} :YAG phosphors are often used to reabsorb light emitted from deep-blue LEDs. They emit a broadly distributed yellow spectrum which, when mixed with the blue emission, yields white light. Light-emitting diodes based on organic molecules instead can be easily tailored to emit any color of the visible spectrum by chemical band-gap engineering of the constituent molecules. This enables the direct generation of white emission by mixing the emission of at least two different chromophore types. In OLEDs based on small organic molecules, which can be made with more complicated structures, the chromophores are usually contained in separate layers either stacked on top of each other or in the lateral direction. This allows to tune the electrical properties of each subunit separately. Polymeric LEDs normally employ much simpler single-layer fabrication techniques. The chromophores share a common environment and are combined by doping or blending. Another approach involves the polymerization of all functional units into a single polymer. This would include charge transport and the blue, green and red emission functionalities, the emission color being determined during synthesis by choosing the relative amount of each chromophore. The copolymer approach has the advantage that the layer morphology cannot be influenced by aggregation of chromophores nor by phase segregation usually observed for polymer blends.

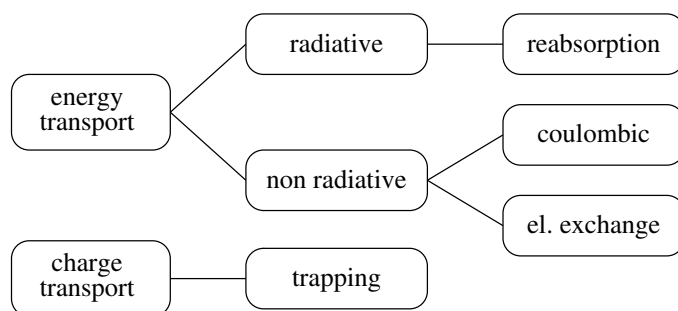


Figure 1.3: Mechanisms for the distribution of excitations in-between several chromophores can be coarsely divided into transportation of charges and distribution of energy, where no free charge carriers are involved.

Excitation energy is funneled to the chromophores either by direct sequential trapping of positive and negative charge carriers on a single chromophore or by migration of energy in-between chromophores, see figure 1.3. The direct trapping of charge carriers strongly depends on the energetic position of the chromophore's HOMO and LUMO relative to those of the charge transporting sites. For singlet-emitting chromophores, strong trapping is to be expected especially for red chromophores, since they have the smallest bandgap. Charge trapping effects are expected to be smaller for phosphorescent molecules emitting at the same wavelength since they usually have a larger optical bandgap due to the exchange interaction.[48] Reabsorption as used by phosphor conversion techniques involves the emission and absorption of photons and is thus classified as radiative energy transfer, while non-radiative energy migration or resonant energy transfer (*RET*) is effective by direct coulombic (for fluorescent molecules) or electron-exchange interaction (for phosphorescent molecules) of the transition dipoles.

Chapter 2

Charge Transport in a Blue-emitting Copolymer with High Electron Mobility

2.1 Introduction

The knowledge of charge transport properties is one of the most fundamental issues in understanding the operation principle of organic light-emitting diodes. Together with the injection efficiency of the electrodes, the difference in charge mobility of electrons and holes mainly determines the quantum efficiency of such devices as outlined in the introduction. Measures to influence charge injection in polymeric light-emitting diodes are fairly limited since these devices are usually restricted to only few organic layers without specialized charge-blocking or recombination layers that could counteract these asymmetries. While hole transport in polymers is relatively well understood and an abundance of reports on hole mobility measurements has been published, electron transport is seldom investigated explicitly. This can be attributed to the observation that electron transport is more often affected by inadvertent impurities and trapping sites, especially oxygen and residual water molecules are known for causing problems. This chapter studies the charge transport properties, notably those of electrons, of the blue-emitting copolymer **PB** (see figure 2.1 for structure) provided by Merck KGaA, Germany. This polymer is based on a spirobifluorene backbone and comprises an additional 11% (monomer feed ratio) of a blue-emitting chromophore and 10% of a hole-conducting triarylamine derivative. The synthesis of this copolymer was carried out by Merck KGaA and is described in detail in references [49, 50]. The polymer has a molecular weight* of $M_w = 3.15 \times 10^5$ g/mol ($M_n = 5.8 \times 10^4$ g/mol) and is easily processable from toluene solutions even at high concentrations of up to 6 wt%. The class of oligo- and polyfluorenes with a spiro linkage at the 9-position of the fluorene unit is of general interest for the fabrication of light-emitting diodes since they are usually highly efficient photoluminescent emitters and the bulky steric configuration increases the glass transition temperature to facilitate fabrication of amorphous and temperature-stable films. Amorphous polymer and oligomeric layers have several advantages for device fabrication, including an improved reproducibility of the optoelectronic properties, spatial homogeneous charge transport and the ability to form optically clear films due to the lack of crystalline grain boundaries. A general review of the properties of spiro compounds was given by Saragi et al. [51], and it was pointed out that they generally provide improved solubility when compared to the corresponding flat molecules without spiro linkage. The steric conformation readily suppresses the interchromophoric interaction and thus excimer emission which would lead to

*As determined by Merck KGaA via gel permeation chromatography.

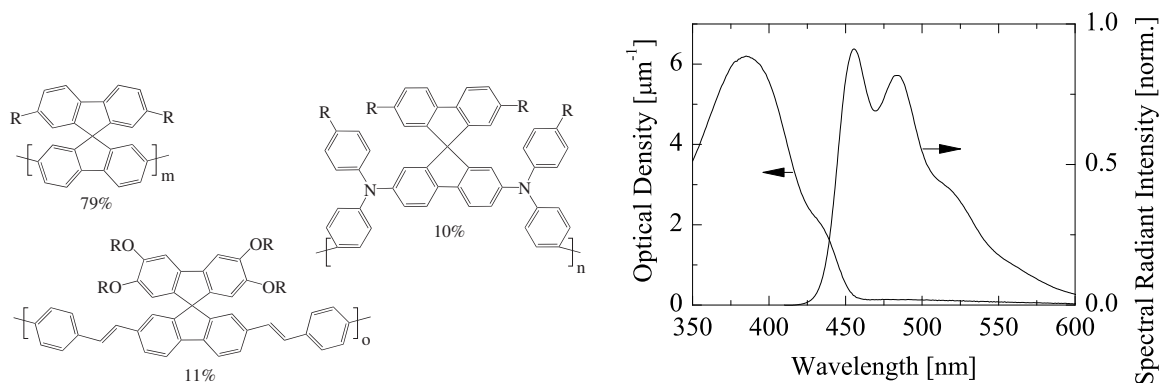


Figure 2.1: Left: Chemical structure of the blue-emitting polyspirobifluorene **PB** comprising 79% backbone, 10% hole transporter and 11% blue-emitting repeat units. Right: Absorbance and photoluminescence spectrum (385 nm excitation) of **PB**.

a reduction of the photoluminescence efficiency. A recent review of the properties of spiro-linked fluorenes was given by Wallace and Chen [52]. (Oligo)spirofluorenes were found to exhibit high charge mobilities both for electrons and holes and thus support bipolar charge transport. They have been used to fabricate blue-emitting organic light-emitting diodes but can be tuned through green to red emission by variation of the molecular structure. Light-emitting polymers based on similar polyspirofluorene backbones have been investigated by Merck KGaA for several years and determination of charge transport properties on these was reported before by Laquai and coworkers [15, 53–55], the results of which will be discussed in more detail further below.

In the first part of this chapter, the charge transport properties of **PB** will be studied for polymer layers of more than 1 μm thickness using the time-of-flight photocurrent method. The applicability of these results to thin film devices comprising spincoated layers of typically less than 100 nm thickness will be discussed in section 2.3.

2.2 Time-of-flight Photocurrent Measurements

The most popular experimental method to determine the mobility of charge carriers is the time-of-flight (TOF) photocurrent method.[56] A thin semiconductor film of thickness d is studied in a capacitor geometry having at least one semitransparent electrode, see figure 2.2. A pulsed light source of sufficiently short pulse length, typically a Q-switched pulsed laser, illuminates the sample at a wavelength of strong absorption by the semiconductor. A thin sheet of charge carriers of thickness dz , where $dz \ll d$, is thus induced by photogeneration. One type of charge carrier drifts in the applied electric field $E = U/d$ towards the counterelectrode, while the other type is forced to the front electrode and rapidly leaves the conductor or remains sufficiently immobile at the interface. As long as charges are moving across the conductor, the current $I = ne\mu E/d$ flows in the external circuit to keep the voltage across the sample, dropping to zero when the charges reach the electrode. The mobility can be determined from the transit time t_{tr} via $\mu = d/t_{\text{tr}}E$ when space charge effects can be ignored. During the transit time, the sheet of charges additionally spreads due to diffusion, causing a

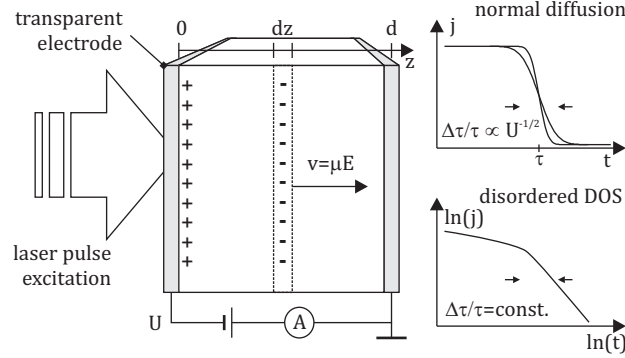


Figure 2.2: Time-of-flight photocurrent measurements. A thin sheet of charge carriers is generated by laser pulse excitation and transported over the film of thickness d in an applied electric field of $E = U/d$.

width of $\Delta t_{\text{tr}}/t_{\text{tr}} = \sqrt{2k_{\text{B}}T/eU}$ of the falling edge of the current transient if validity of the Einstein relation $D/\mu = k_{\text{B}}T/e$ is assumed (*Gaussian transport*). These considerations are strictly valid only for band-type transport. Disordered semiconductors, due to the hopping transport of charge carriers, tend to show a spread $\Delta t_{\text{tr}}/t_{\text{tr}}$ of arrival times which is independent of the applied voltage and thus cannot be understood from standard diffusion considerations. Several models have been proposed to explain this behavior, centering on the disordered nature of the charge conduction process. Scher and Montroll [57] have shown that assuming a continuous-time random walk with a distribution $\psi(t) \sim t^{-(1+\alpha)}$ ($0 < \alpha < 1$) of nearest-neighbor hopping times, the TOF current is $I \propto t^{-(1-\alpha)}$ ($I \propto t^{-(1+\alpha)}$) for $t < t_{\text{tr}}$ ($t > t_{\text{tr}}$). The sum of the slopes in double-logarithmic diagrams such as that of figure 2.2 of plateau and decay region should thus be 2. Rudenko and Arkhipov [58–60] analyzed a multiple trapping model and arrived at the conclusion that the distribution function $\psi(t)$, assumed by Scher and Montroll based on general considerations, is exact for an exponential distribution of trap state energies while for other distributions deviations are expected. Deviations from Scher/Montroll behavior were also found experimentally, e.g. by Mozer et al. [61] for hole mobility in regioregular poly(3-hexylthiophene), although these deviations were small. The theoretical models of charge transport in disordered media identified that $\Delta t_{\text{tr}}/t_{\text{tr}}$ being independent of the average applied field U/d is a typical feature of the hopping-type transport in these systems. The apparent diffusivity manifesting in $\Delta t_{\text{tr}}/t_{\text{tr}}$ is found to be much larger than that predicted from the Einstein relation. Tseng et al. [62] analyzed TOF transients of hole transport in MEH-PPV by fitting a general analytic equation derived by Hirao et al. [63]. They found the apparent diffusivity to exceed the value predicted from the apparent mobility by up to three orders of magnitude, depending on the film morphology due to different solvents used. In terms of the Gaussian disorder model put forward by the Marburg group (see chapter 1.1), this is consistent with transport involving a Gaussian-distributed density of states of widths in excess of $3.5k_{\text{B}}T$, when the transit time is much smaller than the time needed for the relaxation of charges within the DOS.[64, 65] The general result is that mobility is not a well-defined parameter in systems with distributed density of states and possibly deep trap states. It depends on the relaxation of the charge carriers and thus on time and sample thickness. Consequently, the approach by Hirao received criticism for its

interpretation of TOF transients in terms of equilibrium charge transport.[66]

Charge transport in **PB** was studied using the TOF technique on polymer layers with a nominal thickness of $d = 1.25 \mu\text{m}$. Substrates covered by conductive indium tin oxide (*ITO*) were etched to provide 2 mm wide conductive electrodes (see appendix C for details on sample preparation) and thoroughly cleaned by wet processing and O_2 plasma treatment. The polymer was dissolved in toluene at concentrations of 50 mg/ml, stirred for at least 24 h and spincoated onto the ITO substrates, yielding optically clear polymer films with relatively smooth surfaces. The film thickness was measured using a stylus-type profilometer on reference films spincoated on cleaned soda-lime glass substrates and generally varied $\sim 10\%$ across the substrate. The films were afterwards annealed below the glass transition temperature for 30 min at 180°C on a hot plate to remove the solvent. After transfer to a vacuum chamber, aluminum electrodes of 100 nm nominal thickness were thermally evaporated on top of the polymer film to define the active device area of approximately $A = 1 \text{ mm}^2$ by the overlap of metal and ITO electrodes. All sample preparation and handling was performed in dry nitrogen atmosphere in closed glove-box systems. Prior to TOF measurements, the samples were encapsulated with OLED-grade UV curable glue (Addison Clear Wave AC1438) and a glass lid. All further measurements were conducted outside of the protective glovebox atmosphere, where the encapsulation proved to be sufficient to ensure that the measurements were free of trapping effects associated with increased oxygen and water concentrations within the polymer layer.* For TOF measurements, the samples were mounted in a heatable sample holder and illuminated through the glass substrate and ITO electrode by 355 nm wavelength laser pulses of approximately 20 ns pulse length at a repetition rate of 10 Hz, while applying varying bias voltages to both electrodes using a Keithley 237 voltage source. Due to the moderately high absorption coefficient of $4.0 \mu\text{m}^{-1}$ at the laser wavelength, roughly 90% of the photons are assumed to be absorbed within the first 200 nm of the polymer layer. The laser pulse energies were carefully chosen to guarantee that the amount of photogenerated charges $Q \ll CU/20$ stays well below the capacitor charge CU at the applied voltage U , assuming a sample capacitance of $C = \epsilon_0\epsilon_r A/d$ and $\epsilon_r \approx 3$. Under this condition, space charge effects can be neglected and the electric field remains homogeneous across the polymer layer. Depending on the direction of the applied electric field, either holes or electrons are transported across the polymer layer and the resulting current transient was amplified using a FEMTO DHP-100 variable-gain high-speed transimpedance amplifier, providing enough bandwidth to amplify the short transients with less than 300 ns transit time observed for electron conduction. The amplified signal was digitized with a 400 MHz digital storage oscilloscope by averaging over several hundred laser pulses and afterwards transferred to a personal computer for further analysis.

Figure 2.3 shows representative photocurrent transients measured on $1.25 \mu\text{m}$ thick **PB** films at an applied electric field of $E = 4 \times 10^7 \text{ V/m}$ in double-logarithmic representation. The hole transport is characterized by a flat plateau region, indicating that hole mobility is a well defined parameter and roughly constant during transit through the layer. In contrast to this, the electron displacement current continuously decreases during transit through the layer. This is attributed to the relaxation of the photogenerated charges within the density of states

*The author is indebted to Andriy Kuksov (then with the University of Potsdam) for sample preparation, design of the sample holder and for conducting most of the TOF experiments reported in this section.

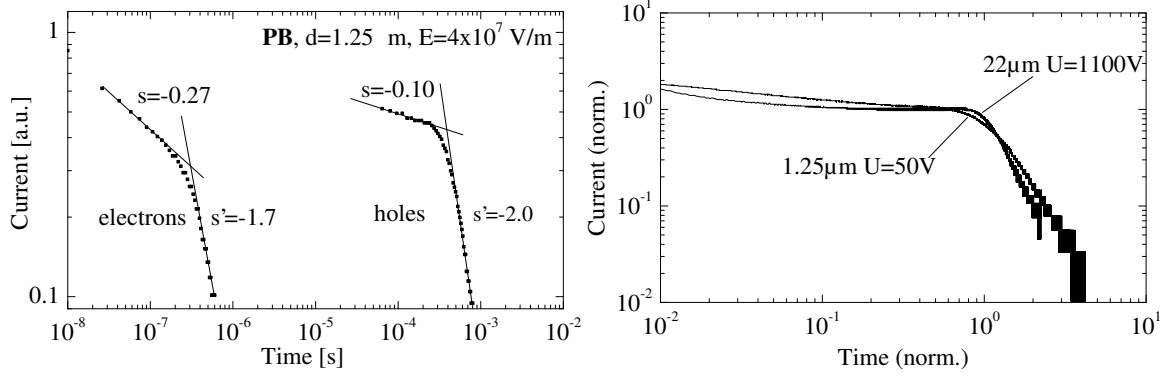


Figure 2.3: Left: Time-of-flight photocurrent transients for electron and hole transport in a 1.25 μm thick PB film contacted by ITO and aluminum electrodes at an applied electric field of 4×10^7 V/m. The approximate slope parameters s for plateau and decay regions are indicated. Right: Comparison of hole transport transients recorded for 1.25 μm and 22 μm thick samples at an applied voltage of 50 V ($E = 4 \times 10^7$ V/m) and 1100 V ($E = 5 \times 10^7$ V/m), respectively. Data is represented with time axis normalized to the transit time and current axis normalized to the plateau current.

not being terminated before the carriers reach the counterelectrode. For both electrons and holes, the observed slopes in the double-logarithmic representation are approximately consistent with $s = -(1 - \alpha)$ and $s' = -(1 + \alpha)$ predicted by Scher and Montroll, where $\alpha \approx 0.7$ ($\alpha \approx 1$) for electron (hole) transport. Generally, transients with $\alpha < 1$ are considered as being *dispersive*, although Borsenberger [67] pointed out that moderately dispersive transients with $s \sim -0.3$ still allow to reliably define the charge mobility as a bulk time-independent property: The inflection point in double-logarithmic representation is due to the fastest charge carriers which will equilibrate earlier, while the slow carriers in the lower energy states do not reach equilibrium during transit time and are mostly responsible for the decay of the current transient. Although hole transport is non-dispersive in nature, the experimental results are not consistent with the notion of Gaussian transport. When the film thickness is increased from 1.25 μm to 22 μm while keeping the electric field U/d roughly constant, an approximately fivefold decrease of $\Delta t/t$ is to be expected from $\Delta t_{\text{tr}}/t_{\text{tr}} = \sqrt{2k_{\text{B}}T/eU}$, but as shown in figure 2.3 this is clearly not observed in the experiments. The apparent diffusivities determined from the transients were generally found to exceed the Einstein value $\mu k_{\text{B}}T/e$ by a factor of 250 to 1000, similar to those reported by others as discussed above.

For the measurements discussed here, electron and hole mobilities were determined from the transit time defined by the intersection of linear fits to the plateau and decay part of the photocurrents in double-logarithmic representation. Mobility data was collected over a range of electric fields typical for OLED operation and for temperatures between 303 K and 383 K, see figure 2.4. Hole mobilities are independent of the electric field up to $\sim 6 \times 10^7$ V/m after which they increase roughly proportional to $\exp(\beta E^{1/2})$ where the slope parameter β decreases as a function of temperature. This is a typical Poole-Frenkel type behavior that has been reported before e.g. for hole mobility in triphenylamine doped polycarbonate [68, 69] and polystyrene [70], although the absolute magnitudes of mobility were rather different. Photocurrents observed under polarity chosen to transport electrons across the layer were

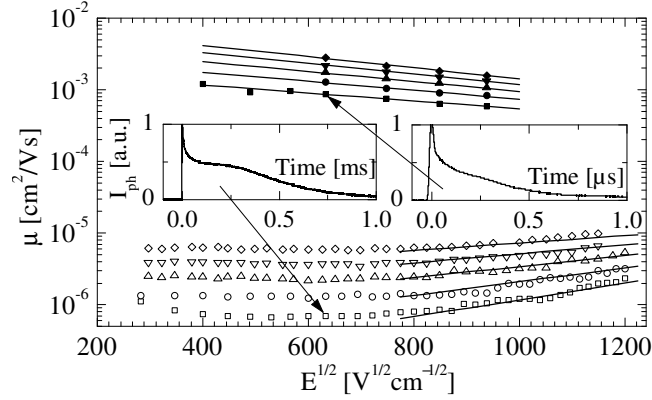


Figure 2.4: Field dependence of hole and electron mobilities determined from TOF transit times, shown as open and solid symbols, respectively. Temperatures shown are 303 K (squares) to 383 K (diamonds) in intervals of 20 K. Solid lines: mobilities recalculated from the Gaussian disorder model, for parameters see text. The inset shows representative electron and hole transport photocurrent transients in a linearly scaled representation.

generally three orders of magnitude faster, severely limiting the assessable field region due to their short timescales. In the studied field range, electron mobilities follow a Poole-Frenkel behavior with negative slope parameter β that slightly increases in absolute magnitude with rising temperature. Negative field dependence of charge mobility is somewhat surprising for hopping-type transport since one generally suspects such behavior to be temperature activated. It has also been observed for other polymers [61] and is generally attributed to strong positional disorder, i.e. a broad distribution of intersite distances for charge carrier hopping. A general explanation for such effects is provided by the Gaussian disorder model that explains charge transport as an incoherent hopping process in a distribution of localized states. It is valid in the high-field linear region of the Poole-Frenkel plot and at sufficiently low charge densities, see chapter 1.1. The general argument is that under presence of considerable amounts of spatial disorder, an applied electric field prevents charge carriers from following hopping routes that involve sites that are spatially close but could only be reached by hopping in directions opposite to the electric field. This reduces the effective mobility until the electric field is large enough to considerably facilitate forward jumps. The intermediate regime is not covered directly by the GDM mobility equation (1.1.3) since it was derived from Monte-Carlo simulations at high electric fields only. The model parameters for equation (1.1.3) were extracted from the measurement data by determination of the temperature dependence of the slope β in the Poole-Frenkel plot and a linear extrapolation of the mobility values to zero electric fields. The resulting temperature dependence of the zero-field mobilities $\mu(E=0, T)$ and of the slope parameter β is shown in figure 2.5. Note that for the case of hole transport the determined parameter $\mu(E=0, T)$ clearly differs from the measured low field mobilities and should be considered a model parameter only, the Gaussian disorder model cannot properly account for field-dependent changes of the Poole-Frenkel slope parameter. The temperature dependence of $\mu(E=0)$ and β roughly follows the predicted T^{-2} proportionality and thus C_0 , σ and Σ can be determined from linear fits to the data points. For hole (electron) transport, the obtained parameters are $C_0 = 2.0 \times 10^{-4} \text{ cm}^{1/2}\text{V}^{-1/2}$

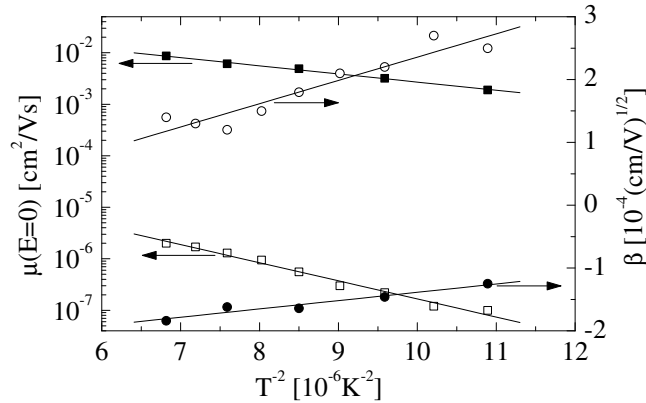


Figure 2.5: Temperature dependence of zero-field hole (open squares) and electron (filled squares) mobilities as determined from TOF data, temperature dependence of the Poole-Frenkel slope parameter β for hole mobility (open circles) and electron mobility (filled circles).

($C_0 = 1.6 \times 10^{-4} \text{ cm}^{1/2}\text{V}^{-1/2}$), $\mu_0 = 5.8 \times 10^{-4} \text{ cm}^2/\text{Vs}$ ($\mu_0 = 1.0 \times 10^{-1} \text{ cm}^2/\text{Vs}$), $\sigma = 117 \text{ meV}$ ($\sigma = 78 \text{ meV}$) and $\Sigma = 2.6$ ($\Sigma = 4.1$).

Hole transport in similar polymers comprising spirofluorene backbones incorporating arylamine-type hole transporting moieties was investigated before by Laquai et al. [53, 54]. They found that the addition of 10% of hole transport monomers leads to a decrease of hole mobility by approximately one order of magnitude while the diagonal disorder parameter increases from 86 meV to 107 meV. This was interpreted in terms of hole transport along the spirofluorene units with the hole transporting molecules acting as charge traps, effectively increasing the energetic width of the density of states. In another publication it was shown that hole transport is only improved at rather high concentrations of the hole transporter of 50%. [55] It is thus concluded that also in **PB**, the HT moieties might act as charge traps for holes moving along backbone sites, albeit no direct evidence for this could be provided. As discussed in chapter 4, the introduction of additional green and red-emitting chromophores with HOMO levels between the HT and the backbones levels does not significantly alter the hole mobility. Thus the direct hopping of holes between HT sites seems a more likely depiction of the transport mode. It should be noted that the difference between the polymer studied here and the material studied by Laquai et al. is the missing of alkoxy side chains in the **PB** backbone. Thus, the **PB** backbone monomers miss the electron donating character of the oxygen and have a higher bandgap and much larger anode/backbone injection barrier, enforcing hole transport along the more widely spaced HT moieties. The results obtained here for electron transport are in variance with the conclusions published in [55]. From a comparison of OLED efficiencies, Laquai et al. concluded that the highest efficiency observed for a hole transporter concentration of 10% should correlate with a balanced hole and electron mobility which should be correct for devices without strong injection barriers. Thus zero-field electron mobility was expected to be around $10^{-7} \text{ cm}^2/\text{Vs}$, much lower than found here. No direct investigation of electron transport by the TOF method was reported, though. The results reported here show that the electron transport is indeed quite fast and characterized by a significant amount of spatial (off-diagonal) disorder, while the energetic disorder is

rather low. To our knowledge, such high electron mobilities have never been reported before for charge transport in spirofluorene-derived polymers. It should be noted that oligofluorenes are already well-known for their extraordinarily good bipolar charge transport characteristics. Chen et al. [71] have shown that tetrafluorene oligomers without spiro-linkage support bipolar charge transport at electron and hole mobilities of 10^{-3} cm²/Vs already in the amorphous state, with additional improvements upon crystallization. Wu et al. [72] report that spirobifluorene dimers and trimers have electron and hole mobilities both on the order of 10^{-3} cm²/Vs. For polymers, the achievement of such high mobilities seemed difficult up to now, probably due to the inadvertent impurities present in the synthesized polymers. The material studied here was polymerized from highly purified monomer compounds which might help in achieving a relatively trap-free polymer. Compared to the results published for oligomers, electron transport in the polymer is still rather dispersive indicating an ample amount of disorder induced by charge trapping sites. The results shown here are important for the understanding of the working mechanisms of polymeric light-emitting diodes, since in the past electron transport properties have usually been guessed from unipolar current measurements and by assessing the efficiency of light-emission, notably in ignorance of the role of energetic barriers for charge transport at the electrode/polymer interfaces. Chapter 3 treats the role of these interfaces in more detail.

2.3 Transient Electroluminescence

Since the determined charge mobilities are of considerable importance for the modeling of light-emitting devices by charge transport simulations, further insight needs to be obtained concerning the validity of the TOF results. It is not *a priori* evident that the charge transport properties of the relatively thick layers used in TOF experiments are the same as those in thin films of less than 100 nm used for light-emitting devices. Although the solubility of **PB** is extraordinarily good, film morphology and molecular packing might differ slightly at the involved high concentrations and long drying times of the fabricated thick films. The absence of any changes in absorption or photoluminescence spectra already indicated that crystallization did not occur on larger scales, but the direct measurement of charge mobility in thin polymer films fabricated using the same protocol as used for light-emitting devices would be highly advantageous. In this section, the method of transient electroluminescence is employed to gain insight into the transit time of charge carriers across polymer films of approximately 100 nm thickness.

The transient response of light-emitting diodes has been studied since the first days of organic electroluminescence. Hosokawa et al. [73] reported the determination of electron mobility in tris (8-hydroxyquinolino) aluminum (Alq₃) by measuring the delay time between application of a rectangular voltage pulse to a bilayer light-emitting diode and observation of the first light emission. Examples of the application of such transient electroluminescence (*transient EL*) measurements to study the physics of organic light-emitting diodes are numerous in literature. They include studies of the onset behavior with conclusions about the charge mobility [74–77] as well as the decay behavior upon termination of the voltage pulse [78, 79], which will be studied in more detail in chapter 5. The Cambridge group has been especially active in explaining a multitude of effects that can be observed by this

type of experiments. Pinner et al. [80] gave an extensive analysis of transient EL measurements on different types of polymeric light-emitting diodes and pointed out that the method is mainly interesting for devices with Ohmic charge carrier injection. They presented an analysis of the rising part of the transient luminance output by comparing to a numerical drift/diffusion simulation of the experiment, enabling an exact approach to mobility measurements on barrier-free diodes. Other publications analyzed the decay behavior [81], the application of multiple electrical pulses in series [82] as well as transient EL experiments on bilayer devices [83].

The experimental setup used here for measurements of the transient response of light emitting diodes is described in appendix D. The geometric sample design optimized for experiments involving fast transient response is detailed in appendix C. The light-emitting diodes have an active area of 1 mm² defined by the orthogonal overlap of a 2 mm wide indium-tin-oxide trace and a 0.5 mm metal cathode trace. This rectangular shape of the light-emitting area was used to keep the serial resistance in the low-conductivity ITO trace as low as possible. The active area is symmetrically connected by two ITO traces where the shorter is used to apply the voltage pulse and the longer allows for Kelvin-type measurements of the voltage drop across the device. The low resistance of the cathode metal trace and additional contact resistance for contacting the cathode was below few Ohms and could be ignored for this purpose. The calculated sample capacity amounts to approximately 270 pF, assuming $\epsilon_r = 3$ and a polymer layer thickness of $d = 100$ nm. Note that the PEDOT:PSS anode layer used as part of the device layer structure is sufficiently conductive and is thus usually considered to not contribute to the sample capacitance under DC conditions.[84] The total rise time of the electric excitation was usually $\tau_{10-90} \sim 23$ ns, defined in terms of the 10%–90% voltage transition and measured using the Kelvin-type 3 point connection, i.e. without being affected by the relatively large resistance of the ITO trace and thus reflecting the rise time of the internal electric field in the organic layer.

Light-emitting diodes were prepared on structured and pre-cleaned ITO substrates by deposition of a thin layer of conductive PEDOT:PSS (obtained under the trade name Clevis AI4083 from H.C. Starck, Germany) and subsequent spincoating of **PB** from a 12 g/l toluene solution. To obtain the lowest serial resistance possible, the PEDOT:PSS film was partially metallized along the ITO anode traces outside of the active device area by vacuum evaporation of 100 nm aluminum layers. Direct metallization of the ITO traces usually led to strong oxidation of the aluminum upon spincoating of the aqueous PEDOT:PSS dispersion and inhomogeneous PEDOT:PSS layer thickness. Directly after spincoating, the **PB** layer was annealed at 180°C for 30 min, well below its glass transition temperature. The sample was then completed by transferring to a vacuum chamber and thermal evaporation of the metallic cathodes. Finished devices were encapsulated to protect against ambient moisture and oxygen, upon which all further measurements were done under ambient conditions. For further details of the sample fabrication procedure, see appendix C. In the following, two types of devices are considered: sample type I features a cathode consisting of 1 nm cesium fluoride capped by 200 nm aluminum and is considered to feature good electron injection while sample type II features a cathode consisting of 50 nm calcium capped by 200 nm aluminum and is considered to feature worse electron injection.

Figure 2.6 shows the transient response of a type I device after application of a 4.6 V rectangular voltage pulse of 70 μ s width at a repetition rate of 20 Hz, averaged over several

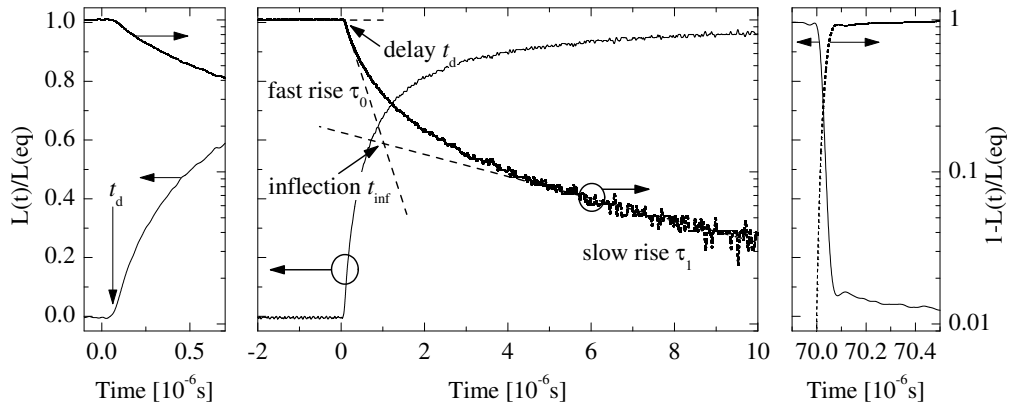


Figure 2.6: Transient response of a 100 nm thick **PB** light-emitting device after application of a rectangular voltage pulse of 4.6 V height and 70 μ s length, corresponding to an electric field of 2.3×10^7 V/m. The left axis shows the luminance $L(t)$ normalized to the equilibrium value $L(\text{eq})$, the right axis shows the saturation transient $1 - L(t)/L(\text{eq})$. Regimes of fast and slow luminance rise behavior are indicated.

shots. The luminance transient was recorded at a wavelength of 455 nm, i.e. at the maximum of the photoluminescence (and of the electroluminescence) response. Due to the difference of the electrode work functions and possibly interface dipoles, the devices feature a built-in potential of approximately 2.3 V that was determined for each device by photocurrent measurements under applied bias fields. The observed EL transients typically exhibited a short delay time t_d directly after application of the electric field until the first emission could be detected. This delay was followed by a luminance rise roughly biexponential in time (characterized by exponential rise times τ_0 and τ_1). Due to the short delay times it is of paramount importance to also take into consideration the effects of cable and electronic delays. For the experiments reported here, normalization of the time axis was done by checking that the luminance starts to fall exactly at the time of termination of the voltage pulse. See chapter 5 for a more detailed analysis of the luminance fall behavior. Pinner et al. [80] have analyzed such transients in terms of the saturation function $1 - L(t)/L(\text{eq})$, which on a logarithmic scale reveals two roughly linear regimes, indicated in figure 2.6 as fast rise and slow rise according to their rise (fall) times. From a comparison of their transient EL data with numerical drift-diffusion simulations, Pinner et al. correlated the inflection point t_{inf} of the EL saturation function with the mobility $\mu_{\text{fast}} = d/t_{\text{inf}}E$ of the fast charge carrier, where d is the polymer layer's thickness and $E = (U - U_{\text{bi}})/d$ is the effective electric field corrected by the built-in potential U_{bi} . When attempting to apply this analysis to the data collected for **PB** devices, several problems are encountered. Firstly, the transition between fast and slow rise behavior is somewhat less defined than in Pinner's work, although this varies among samples and applied voltages. The ratio of fast rise time and delay time is around 10 for the measurement shown and thus rather large. In the simulations of Pinner et al., this ratio is on the order of one and arises mainly from charge diffusion and the dynamic effects of space charge buildup. According to their work, largely increased values might indicate an intermixing of hole and electron dynamics through field-induced injection

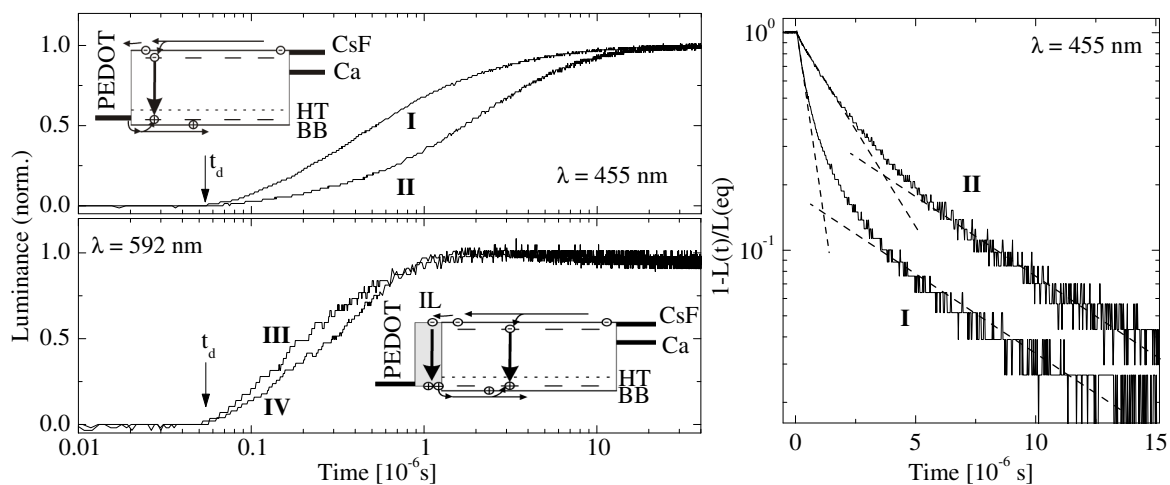


Figure 2.7: Left: Transient EL type I and II devices, recorded at a wavelength of 455 nm and of type III and IV devices, recorded at 592 nm, at an electric field strength of approximately 3.4×10^7 V/m. The luminance curves have been normalized to their respective maximum. Right: the same data for type I and II devices plotted in terms of the saturation transient $1 - L(t)/L(eq)$.

processes, i.e. charge accumulation. Secondly, the observed transient EL dynamics were largely affected by the choice of electron-injecting cathode. Figure 2.7 shows a comparison of type I and II devices operated at comparable electric fields. Devices with Ca cathodes feature a much slower turn-on behavior in the time range below $1 \mu\text{s}$, while the slow rise behavior at larger time scales is very similar to type I devices comprising a CsF cathode. Since modifications of the cathode should primarily influence the electron injection, the observed differences in fast rise time τ_0 are attributed to a reduced injection efficiency of the Ca electrodes. Pinner et al. showed that the slow rise time should correlate with the movement of the slower charge carrier (here: holes) and indeed the slow rise times τ_1 were found to be largely independent of the choice of cathode. It is concluded that neither the observed fast rise times nor the inflection points are sufficient to unambiguously define the electron mobility since they strongly depend on the electron injection efficiency.

It is shown in the following that multilayer structures can be employed to provide a less ambiguous way to assess the interconnection of t_d and electron transport. Klenkler et al. [85] recently demonstrated the feasibility of small-molecular multilayer structures prepared by vacuum evaporation to study charge transport in thin organic layers. The general idea is that the arrival of one type of charges at a particular site within the device can be monitored by introducing a chromophore layer emitting light spectrally well separated from the bulk layer emission. Such multilayer structures are inherently difficult to fabricate using solution-based techniques since subsequently spincoated layers tend to dissolve already deposited material, leading to ill-defined layering and diffuse layer interfaces. Recently, it was shown that several soluble polymers form thin insoluble layers (*interlayers*) on PEDOT:PSS upon spin coating from organic solvents and subsequent thermal annealing close to the glass transition temperature.[86, 87] These layers are only a few nanometers thick and, in many cases, allow the preparation of well-defined solution processed polymeric bilayer

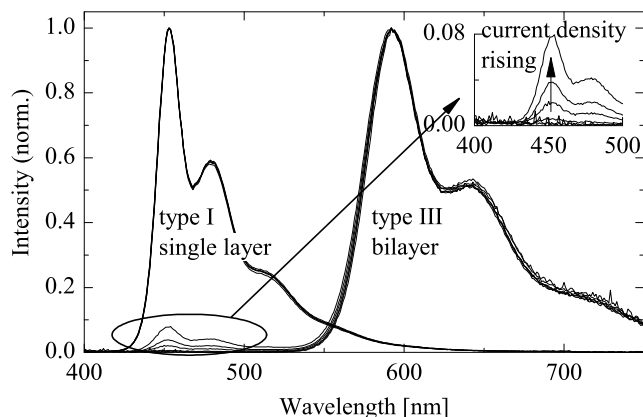


Figure 2.8: Electroluminescence emission spectra normalized to maximum (not corrected for the spectral detector response) of type I and type III devices at various current densities.

systems directly by the spincoating technique.[88] Here, an interlayer of poly [2-methoxy-5-(2-ethylhexyloxy)-1,4-phenylenevinylene] – poly [2,5-dimethoxy-1,4-phenylenevinylene-2-methoxy-5-(2-ethylhexyloxy)-1,4-phenylenevinylene] (**MEH-M3EH-PPV**, see appendix B for structure) is fabricated by spincoating from chlorobenzene solution at a concentration of 5 g/l onto PEDOT:PSS-covered substrates and subsequent annealing for 30 min at 150°C on a hot plate. The resulting polymer layer is washed several times with pure chlorobenzene solvent, leaving an insoluble interlayer of only a few nanometers thickness as determined by absorption spectroscopy and comparison with the optical density of **MEH-M3EH-PPV** films. Spectroscopically, no modification of the photoluminescent properties of the interlayer compared to the bulk properties of neat films was found. After fabrication of the interlayer, devices were completed as before by spincoating of the **PB** layer from toluene solution and thermal evaporation of CsF/Al (device type III) or Ca (device type IV) cathodes. The energy levels for this class of PPV polymers are expected to be approximately $\epsilon_{\text{HOMO}} = -5.1$ eV and $\epsilon_{\text{LUMO}} = -2.7$ eV. This can be compared with the energy levels* of $\epsilon_{\text{HOMO}} = -5.57$ eV (-5.19 eV) and $\epsilon_{\text{LUMO}} = -2.50$ eV (-2.75 eV) of the polymer backbone (and of the blue emitter), see insets of figure 2.7. The hole transporter has $\epsilon_{\text{HOMO}} = -4.9$ eV and would thus constitute a shallow trap with respect to the blue chromophore. Note that Gather et al. [48] studied the energy levels of this polymer by means of cyclic voltammetry and arrived at the conclusion that the HT has $\epsilon_{\text{HOMO}} \approx -5.3$ eV and the blue chromophore $\epsilon_{\text{HOMO}} \approx 5.5$ eV. As discussed above, it is more likely that the hole transporting moieties directly contribute to charge transport. Since the **MEH-M3EH-PPV** interlayer has a HOMO level very similar to that reported for PEDOT:PSS, it is expected that while being easily populated by electrons from the **PB** layer, it will not promote hole injection across the polymer/polymer interface (*PPI*) into **PB**. This picture is indeed supported by a comparison of the electroluminescence spectra observed for type I and type III devices, see figure 2.8. Upon introduction of the

*These energy levels for **PB** have been provided by Merck KGaA and were obtained by quantum chemical calculations on trimers, i.e. one blue-emitting monomer sandwiched between two backbone monomers. Absolute calibration was achieved by calculation of energy levels for several model monomers for which published cyclovoltammetric data exists.

interlayer, nearly pure **MEH-M3EH-PPV** emission is observed under electrical excitation of type III samples even though the interlayer is only a few nanometers thick. The small fraction of blue emission observed for this type of devices generally increased at higher current densities. It is thus expected that most of the holes are unable to overcome the energetic barrier between **MEH-M3EH-PPV** and **PB** without the assistance of a considerable electric field. Due to the low absorbance of the thin interlayer, reabsorption of **PB** emission can be safely neglected as an alternative explanation for this red emission. Contrary to this, resonant energy transfer may contribute since **PB** emission and absorption of **MEH-M3EH-PPV** overlap significantly, but this is considered to be effective only for excitons created in direct vicinity of the PPI, which will not affect the intended purpose of the measurements.

Light emission from the interlayer requires both types of charge carriers to be present and thus can be used to determine the transit time of electrons across the bulk **PB** layer after application of a voltage pulse to type III and type IV devices. Figure 2.7 compares the transient EL observed for these devices at a wavelength of 592 nm to that of type I/II devices at 455 nm. The interlayer emission features a much shorter ‘fast’ rise time followed by a roughly constant or even slightly decaying emission at longer time intervals. Since the time constant of this slow decay is comparable to τ_1 of type I devices, this is attributed to slow penetration of holes into the bulk **PB** layer and thus away from the PPI, reducing the amount of energy transfer contribution to red emission. The observed red emission delay time t_d is equal to that observed for blue emission from type I devices. Upon replacing the CsF/Al cathode by a Ca cathode with worse electron injection properties (type IV devices), hardly any effect could be observed on the transient EL response. The observed differences were well within typical sample to sample variations. This indicates that the delay and rise times observed for the red emission of interlayer devices are not governed by charge accumulation processes but mostly by the transport properties of electrons across the **PB** layer. Although type IV devices showed a reduction by a factor of 2 of the device currents and luminance, the luminance efficiency as determined at the same current densities hardly changed, see figure 2.9. This also indicates that most of the holes stay inside the interlayer and cannot penetrate deeply into the bulk.

Figure 2.10 shows the apparent electron mobilities calculated as $\mu = d/t_d E$ from the measured delay times t_d . All types of samples studied in this section (type I–IV) feature comparable delay times, although the delay is more well-defined in interlayer devices. The calculated mobilities reach well within the range of $10^{-3} \text{ cm}^2/\text{Vs}$ and are thus comparable to the TOF mobilities determined in thick layers. Since the involved delay times at the highest electric fields are already near the RC time limit $\tau_{10-90} \sim 23 \text{ ns}$ of the setup, the effect of finite electric field rise time upon application of the voltage shall be estimated. Let $E(t) = E_0(1 - \exp(-t/\tau))$ using $\tau = \tau_{10-90}/(\log(0.9) - \log(0.1))$. The electron drift speed is $v(t) = \mu(E(t)) \cdot E(t)$ where $\mu(E)$ is given by equation (1.1.3) using the parameters determined in section 2.2. Solving the integral equation

$$d = \int_0^{t_d} \mu(E(t))E(t) dt \quad (2.3.1)$$

for $t_d(d)$ allows to calculate the apparent mobility $\mu' = d/(t_d(d)E_0)$. The solution of this procedure cannot be given in analytic form but is easily calculated by numeric means. Figure 2.10 shows apparent mobilities calculated for field-independent mobilities of $10^{-2} \text{ cm}^2/\text{Vs}$,

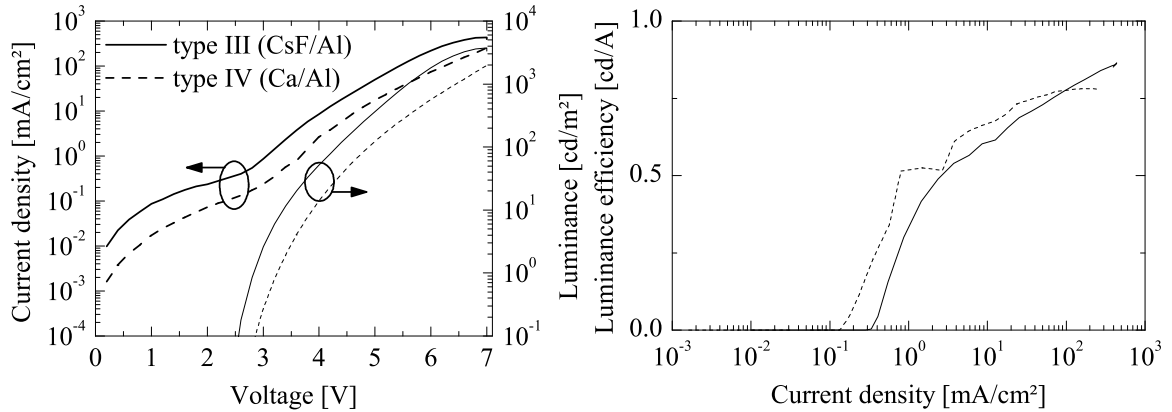


Figure 2.9: Left: Comparison of current densities and luminances (left) measured for type III (solid lines) and type IV (dashed lines) devices. Right: Luminance efficiency as a function of total device current (right) is hardly changed by replacing the CsF/Al cathode with Ca/Al.

10^{-3} cm²/Vs and 10^{-4} cm²/Vs and an electric field rise time of $\tau_{10-90} = 25$ ns. This shows that the observed delay times should be only weakly affected by the resistance-capacitance time limitations of the setup and that the observed flattening of field dependence above $E^{1/2} = 400$ V^{1/2}cm^{-1/2} ($E = 1.6 \times 10^7$ V/m) is not an artifact of resistance-capacitance limitations. Although significant sample-to-sample variations of the determined mobilities was found, the general result is that both single layer (type I and II) and double layer (type III and IV) devices feature comparable delay times of first emission, with calculated mobilities on the same order of magnitude as those determined from TOF experiments. This coincidence of delay times is a strong evidence that the first emission of single layer **PB** devices after application of the electric field is caused by the transit of electrons from the cathode to the anode side of the polymer layer. Below electric fields of approximately 2×10^7 V/m, the apparent mobility determined from transient EL sharply decreases. Similar effects were observed by Brütting et al. [89] for the multilayer system CuPc / NPB / Alq₃ and interpreted in terms of charge accumulation at the organic/organic interface. The single layer devices showed a similar behavior of mobilities calculated from the delay times, although in this case it should be attributed to other effects: these devices generally featured a transition to slow single-exponential luminance rise behavior at low electric fields. At these fields it is thus expected that the spreading of holes across the bulk layer towards their equilibrium distribution dominates the transient EL, thus the delay time will gradually shift from being dominated by the electron transit time to that of holes. In type III/IV bilayer devices, these effects are excluded since the interlayer emission was observed, not that of **PB**. It is thus expected that a residual barrier exists for electron injection from **PB** into MEH-M3EH-PPV exists, although in this case one should expect a modification of the transient behavior upon reduction of the electron injection efficiency into **PB** when using Ca cathodes instead of CsF/Al, which is not clearly observed experimentally. An alternative explanation could be the existence of a similar electron accumulation mechanism being effective at the PE-DOT:PSS / MEH-M3EH-PPV interface at low electric fields.

Finally, transient EL experiments were conducted on samples with thicker polymer layers

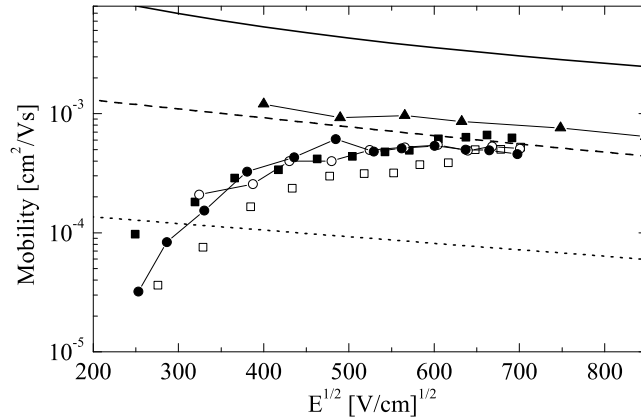


Figure 2.10: Apparent mobilities calculated from transient EL delay times for type I (solid squares) and type II (open squares) single layer devices, measured at 455 nm emission wavelength and for type III (solid circles, connected for clarity) and type IV (open circles, connected for clarity) bilayer devices at 592 nm emission wavelength. Room-temperature mobilities as obtained from TOF experiments are shown as solid triangles, connected for clarity. The lines indicate calculated apparent mobilities assuming constant charge mobilities of 10^{-2} cm^2/Vs (solid line), 10^{-3} cm^2/Vs (dashed) and 10^{-4} cm^2/Vs (dotted) and a field rise time of $\tau_{10-90} = 25$ ns.

to show that the observed delay times do not correlate with the τ_{10-90} voltage rise time but rather with an intrinsic transit time. Type III devices with thick polymer layers were prepared by spincoating **PB** from a 24 g/l toluene solution. All other sample preparation steps were the same as above. Figure 2.11 shows the transient response of device current, voltage across the sample capacitor and luminance both at the emission wavelength of the interlayer and of the bulk for a device comprising a $d = 253$ nm thick **PB** layer. The transition from zero to 10.46 V applied voltage is completed within 25 ns, while some additional charging current is found to flow until approximately 50 ns. The total excitation pulse width was 160 μs , with a transient luminance overshoot being observed at the time of termination of the driving voltage (see chapter 5 for an explanation of the origin of this phenomenon). The observed delay time of $t_d = 99$ ns for interlayer emission is unambiguously defined from the observed transients, being much larger than the voltage transition time. The applied electric field was $E = 3.23 \times 10^7$ V/m considering the built-in potential of 2.3 V determined for these samples. The calculated mobility is $\mu = d/t_d E \approx 8 \times 10^{-4}$ cm^2/Vs , in agreement with the results obtained on thinner samples. Figure 2.12 shows that the field dependence of mobility is of Poole-Frenkel type above a field of 1.6×10^7 V/m, below which again a sharp transition to lower apparent mobilities occurs. The absolute values at high electric field are very similar to those determined by time-of-flight photocurrent experiments, although both methods result in slightly different slope parameters β . It turned out that the interlayer devices with thick **PB** layer feature a much more defined slow (τ_1) rise behavior of the bulk emission when compared to those with thin **PB** layer, enabling a quantitative analysis of this feature. Figure 2.12 shows luminance transients measured at the bulk emission wavelength of 453 nm of the type III devices in logarithmic representation. Compared to transients observed for the thinner devices, the τ_1 rise behavior was observed for longer timescales and the transition

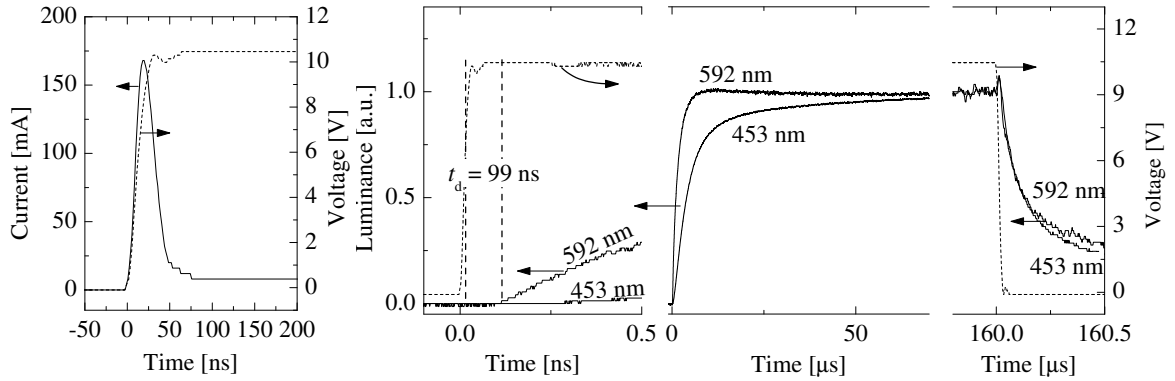


Figure 2.11: Transient EL of type III interlayer devices comprising a 253 nm thick **PB** layer. Left: Current (solid line) and voltage transients (dashed line) upon switching a 10.46 V pulse of 160 μ s length. Right: Luminance transients (solid) measured at 453 nm (bulk emission) and 592 nm (interlayer emission) as well as the measured voltage transients (dashed). The observed interlayer emission delay time is indicated.

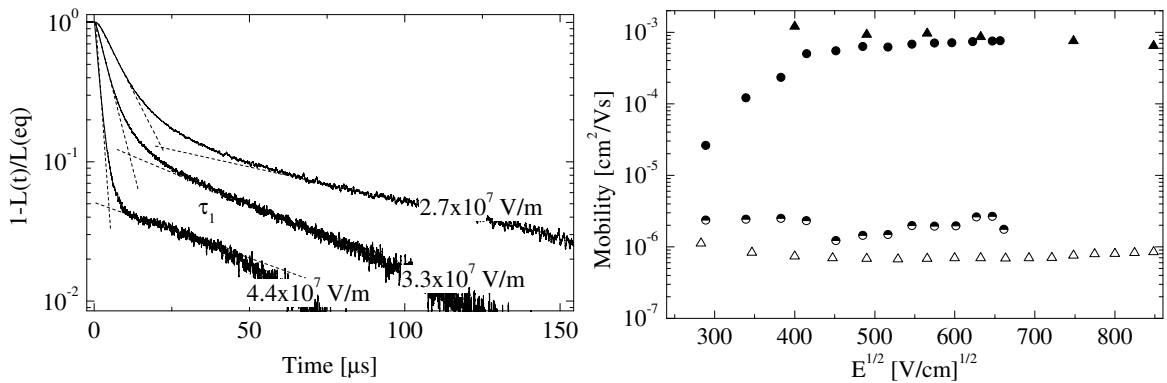


Figure 2.12: Left: Transient EL of type III devices comprising a 253 nm thick **PB** layer, measured at the bulk emission wavelength of 453 nm at three different applied electric fields. Right: Apparent mobilities calculated from transient EL data for this type of device, determined from the delay time t_d of interlayer emission observed at 592 nm (solid circles) and from the slow rise time τ_1 of bulk emission at 453 nm (half-filled circles). Room-temperature mobilities as obtained from TOF experiments are shown for electron transport (closed triangles) as well as hole transport (open triangles).

between τ_0 and τ_1 domains occurred in a less gradual way. Each transient was analyzed by a linear regression of the logarithmic data to determine the corresponding slow rise time constants τ_1 . The corresponding mobility $\mu = d/\tau_1 E$ is plotted in figure 2.12 against the charge mobilities determined by the time-of-flight technique for both electrons and holes. As already pointed out above, the slow rise of blue emission is attributed to penetration of holes into the bulk **PB** layer and it is thus not surprising that the corresponding exponential rise times τ_1 yield mobility values comparable to the hole mobilities determined by the time-of-flight technique. Again, a concomitant decrease of interlayer emission is observed which has comparable time dynamics to the slow rise of bulk emission, see figure 2.11. The evaluation of the slow charge carrier mobility from the τ_1 times is certainly more erroneous than the time-of-flight measurements. For a more quantitative result, the penetration depth of holes and their spatial density distribution should be known. Space charge effects will additionally alter the equilibration dynamics and are difficult to assess without detailed simulations of the internal charge dynamics.

2.4 Conclusion

This chapter analyzed the charge transport properties of a blue-emitting polyspirobifluorene in terms of both hole transport and electron transport. A surprisingly high value of electron mobility was found for this polymer. The relatively low dispersivity of electron transport observed in time-of-flight studies on 1.25 μm thick samples highlights the extraordinary purity of this material, containing only low amounts of electron-trapping impurities. Hole transport was much slower than electron transport and most likely a result of shallow hole trapping on the triphenylamine-type moieties or direct hopping within the HT manifold. Hole transport was nondispersive in both 1.25 μm thick films prepared by spincoating as well as in 22 μm films prepared by dropcasting. As an alternative method for the determination of charge mobilities, transient electroluminescence response measurements were employed. For the polymer studied here, the established evaluation scheme for transient EL data published by Pinner et al. [80] proved insufficient for an analysis of charge transport. This was attributed to strong energetic barriers for the injection of charges at the electrodes and to a possible accumulation of electrons at the hole injecting contact, leading to a correlation of hole injection and electron accumulation. Bilayer structures were prepared by including a polymeric interlayer of a red-emitting poly(*p*-phenylene-vinylene) derivative to separately sense the arrival times of electrons at the anode side of the device, thereby enabling the determination of transit time across the polymer layer for the fastest carriers. Results for both 100 nm as well as 253 nm thick devices show that this enables the unequivocal definition of the electron transit time. At electric fields above 2×10^7 V/m, the electron mobilities were similar to those determined by time-of-flight experiments. At lower fields the results diverge, which was attributed to a residual injection barrier for electrons crossing from **PB** into the interlayer or to similar accumulation mechanisms as observed for single layer devices at the PEDOT:PSS / interlayer interface. The conclusion that electron accumulation significantly influences transient EL measurements of charge mobility is also supported by the results presented in chapter 3. The hole transport properties could be loosely correlated with the observed rise time of bulk **PB** emission observed for the bilayer devices. The apparent mo-

bilities determined from this were similar to the hole mobilities obtained from time-of-flight studies. In summary, no major differences were observed at sufficiently high electric fields for the charge transport properties of both thick polymer films prepared by drop casting and spincoating from thick solutions and films prepared by spincoating from less concentrated solutions as used for the fabrication of light-emitting devices. This is attributed to the highly amorphous layer morphology enforced by the bulky spiro linkage present on each monomer.

Having obtained reliable data for the charge transport properties for both holes and electrons, this polymer represents an ideal model system for further studies concerning the operation principles of light-emitting diodes fabricated from it. Here, the role of charge injection across the electrode/polymer interfaces can be investigated in more detail, being able to separate the effects of charge mobility and charge injection. This will provide additional insight into the mechanism of the conjectured electron-accumulation assisted hole injection and is studied in the next chapter.

Chapter 3

Charge Injection and Electrical Conditioning Effects

3.1 Introduction

A prominent choice of hole-injecting electrodes for polymer light-emitting devices is poly(3,4-ethylenedioxythiophene):poly(styrenesulphonate) (PEDOT:PSS), a dispersion of oxidized PEDOT and polyanionic PSS in water. It is commercially available in large quantities and at a HOMO level of approximately 5.2 eV [90] it usually provides better hole injection properties than ITO substrates while still being sufficiently transparent when applied as thin film coating. Despite its tremendous success in the polymer light-emitting diode business, the interface between PEDOT:PSS and organic semiconductors is poorly understood and still in the focus of research. PEDOT:PSS itself has a complicated nanomorphology due to the formation of gel particles of sizes typically some tens of nanometers, see figure 3.1. Due to the abundance of PSS, these particles usually feature an insulating shell consisting of a PSS-rich phase while their core is a highly conductive PEDOT-rich phase. It has been shown that these particles become somewhat oblate spheroids upon spincoating but retain the core-shell structure, leading to highly anisotropic conductivity of dried PEDOT:PSS thin films attributed to the prevalence of insulating PSS-rich domains.[91] Additionally, inhomogeneous currents were observed for the perpendicular (out-of-plane) direction and attributed to the expression of either PSS-rich or PEDOT-rich phases at the film surface.[91, 92]

It was recently shown that at least for some semiconducting organics, the hole injection is impeded by an injection barrier that is largely independent of the anode work function, which was attributed to pinning of the Fermi level.[93] Additionally, the anode/organic interface is believed to interfere with the electron transport in bipolar devices, strongly depending on the polymers studied: for poly(9,9-dioctylfluorene) (PFO) [94, 95] and its derivatives such as poly(9,9-dioctylfluorene-*alt*-benzothiadiazole) (F8BT) [96], a significant amount of electron trapping at the PEDOT:PSS/polymer interface was reported. Such trapping of space charge eventually leads to improved hole injection or even to complete screening of the electric field in the polymer bulk.[97] An additionally proposed mechanism involves the accumulation of electrons at the insulating PSS-rich surface layer and subsequent injection of holes due to the locally enhanced electric field.[92]

This chapter studies the role of PEDOT:PSS as the anodic hole injecting layer in a light-emitting diode comprising the blue-emitting copolymer **PB** that was already introduced in chapter 2. It was shown that the charge transport in **PB** is strongly imbalanced in favor of electrons with charge mobilities reaching 10^{-3} cm²/Vs for electrons and 2×10^{-6} cm²/Vs for

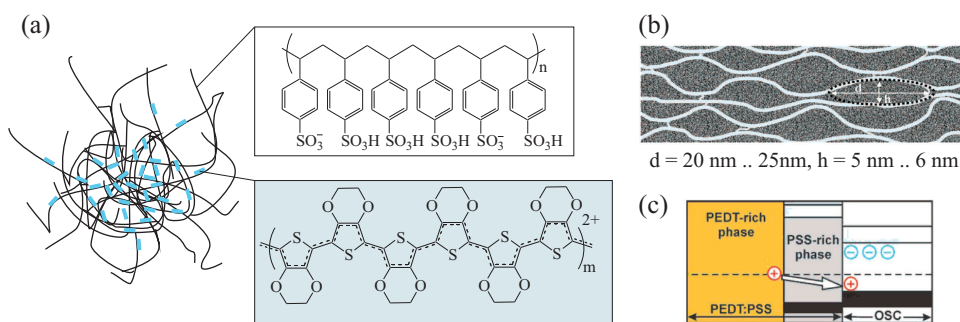


Figure 3.1: (a) Composition of PEDOT:PSS and schematic structure of the water-dispersed gel particles. (b) Schematic cross section of a PEDOT:PSS film prepared by spincoating, reproduced from [91]. The highly conductive PEDOT rich phase (dark color) is separated into individual domains by a thin sheet of a PSS-rich phase (light color). (c) Energetic barrier for electron extraction as proposed by Koch et al., reproduced from [92].

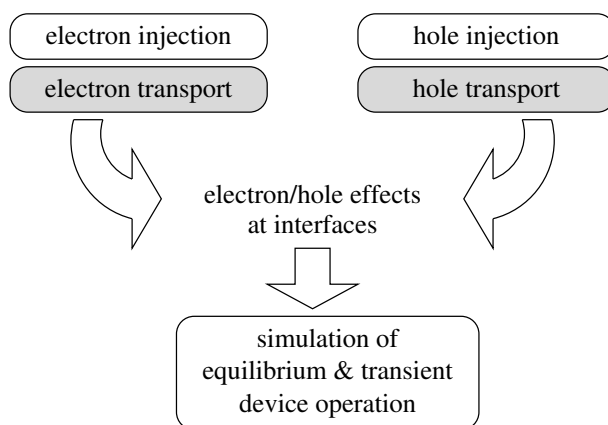


Figure 3.2: General scheme for the analysis procedure followed in this chapter. Transport properties for electrons and holes have already been discussed in chapter 2.

holes. While the high electron mobility itself is rather surprising, it leads to interesting device physics when additional electron trapping moieties are introduced. As will be discussed in chapter 4, the blue-emitting copolymer **PB** has been designed to host additional green and red chromophores, the latter of which are strong electron traps. For devices fabricated from such white-emitting copolymers, the low hole mobility is shown to control both the total device efficiency as well as the emission color by determining the density of free holes. Here, the analysis of anode interface effects for **PB** devices follows along the general scheme depicted in figure 3.2. Chapter 2 provided evidence that charge mobilities determined by the time-of-flight photocurrent technique are also valid in thin film devices of less than 100 nm thickness as typically used for OLEDs. The additional acquisition of quantitative information on the charge injection properties for both electrons and holes on unipolar device structures should thus allow for a complete understanding of bipolar device operation. This is tested by numerical simulations of both the equilibrium operation and the transient device response. It turns out that the simulations based on these parameters are not sufficiently close to

the observed device behavior. The proposed properties of PEDOT:PSS/polymer interfaces are then tested for their ability to remedy this situation, eventually leading to a deeper understanding of the interface effects governing both transient and steady state operation of these light-emitting devices.

3.2 Charge Injection

Before charge injection is studied in more detail, the properties of bipolar devices are reviewed. Light-emitting bipolar devices were fabricated according to the procedure already described in section 2.3, featuring a PEDOT:PSS hole injection layer, a light-emission layer of $d = 100$ nm **PB** and a cathode consisting of 1 nm CsF capped by 100 nm–200 nm aluminum. Figure 3.3 shows the typical performance of such devices in terms of current density and luminance as a function of applied voltage. Note that the devices used in this section have not been optimized for maximum efficiency e.g. by variation of the emission layer thickness. In assessing the performance of the light-emitting devices, it is helpful to compare to observed bipolar currents with the maximum allowed unipolar currents. These can be calculated from the charge mobilities measured by the time-of-flight technique as reported in chapter 2 under the assumption of Ohmic contacts using equation (1.2.1) for the space charge limited current density j_{SCLC} . The result is shown in figure 3.3 for both electron and hole transport, assuming that the effective potential is $U = U_{\text{ext}} - U_{\text{bi}}$ using a built-in potential of $U_{\text{bi}} = 2.3$ V mainly caused by the difference in electrode work functions that has been estimated from the onset voltage of light emission. It is immediately evident that the measured bipolar current density is more than two orders of magnitude lower than the possible space-charge limited unipolar electron current. Considering that the presence of holes should lower the effect of space charges and thus increase the allowable current densities, this can only be rationalized by assuming a significant barrier for the injection of electrons from the cathode into the polymer. Before quantifying this in more detail, the hole injection at the anodic interface is discussed. In order to test if SCL conditions are achieved under unipolar hole injection conditions, *hole-only* single carrier type devices were fabricated by suppressing electron injection from the cathode. Here, instead of the usual CsF/Al electrodes, metal electrodes fabricated by evaporating 100 nm gold or 100 nm palladium on top of the **PB** layer were employed, while leaving the remainder of the device structure unchanged. Figure 3.4 shows the measured device currents as function of the applied voltage both in forward (hole injection from PEDOT:PSS) as well as in reverse direction (hole injection from the metal electrode). The current densities measured for hole injection via the metal electrodes remained relatively low, with only minor differences between injection by Au and Pd. A pronounced sample to sample variation indicates that the injection performance of these electrodes is probably dominated by inadvertent contaminations. Compared to j_{SCLC} , these currents are two orders of magnitude lower but surprisingly feature a comparable field dependence.

As already discussed in chapter 2, it is expected that the triarylamine-type HT moieties present in **PB** do not act as charge traps for holes moving along the backbone but rather contributes to charge transport by direct hopping between HT sites. The work function of Au has been reported as 4.8 eV for the polycrystalline form [98, 99] and 5.1 eV for the Au (111) crystal face [99], while that of Pd was reported [100] as 5.0 eV. Having a HOMO

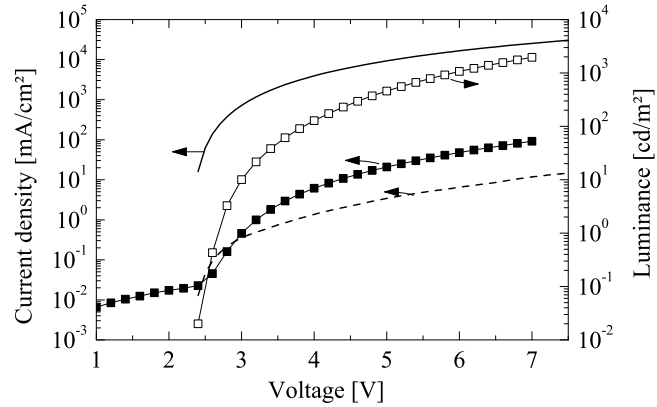


Figure 3.3: Current density (closed symbols) and luminance (open symbols) of light-emitting devices comprising a 100 nm thick PB layer and CsF/Al cathodes. The solid and dashed curves represent the maximum space charge limited unipolar currents calculated from time-of-flight mobilities for electrons and holes, respectively.

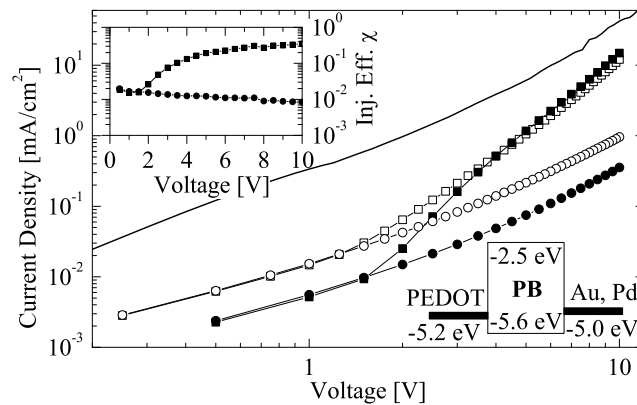


Figure 3.4: Current-voltage characteristics of hole-only devices comprising a 100 nm PB layer on top of a PEDOT:PSS electrode, capped by a 100 nm thick Au (closed symbols) or Pd (open symbols) electrode. Squares (circles) show data measured under appropriate polarity for hole injection from the PEDOT:PSS (metal) electrode, respectively. The SCL current expected for the TOF mobilities is plotted as a solid line. The injection efficiency shown in the inset was calculated from the ratio of the observed currents and the SCL current.

level of ~ 4.9 eV (5.3 eV as obtained by cyclic voltammetry, see chapter 4), the HT should thus support SCL currents, given that energy barriers below 0.3 eV can be generally considered to provide Ohmic contacts, at least at sufficiently low charge mobilities.[27, 101] Given that hole injection into charge transporting states predominantly occurs onto the backbone monomer HOMO at 5.6 eV (see chapter 2) the observed low currents are not surprising, leaving an energetic barrier of ~ 0.6 eV that severely limits the injection of holes. This reasoning is less obvious for charge injection directly onto the HT moieties, although their number density is only 1/10 that of the backbone monomers. The injection efficiency has traditionally been characterized in terms of the figure of merit $\chi = j/j_{\text{SCL}}$, the ratio of achieved current density to the SCL current.[102, 103] For injection from Au and Pd, the injection efficiency was found to be $\chi \sim 0.01$ and surprisingly independent of the applied voltage, which implies that the field dependence of current density resembles that of j_{SCL} although the absolute magnitude is much smaller. The situation is rather different for hole injection from PEDOT:PSS. Although its work function should be only ~ 0.2 eV larger, the injected currents steeply rise starting from approximately 1 V–2 V applied bias, reaching $\chi \sim 0.35$ at $U = 10$ V. Low injection efficiencies from common anode materials have also been reported by Campbell et al. [103] for poly(9,9-dioctylfluorene) where $\chi \sim 10^{-3}$ was not exceeded even using PEDOT:PSS anodes. This was attributed to the severe energetic injection barrier and possibly to inadvertent chemical changes of the polymer upon thermal evaporation of metal electrodes.[104] The observation of SCL-type field dependence of severely injection limited currents from Au and Pd electrodes might be explained by taking into account the generally grainy emission observed across such electrode surfaces upon incomplete suppression of electron injection. This indicates that emission predominantly occurs in spatially strongly confined regions, probably at defects or contaminations. If these provide sufficient charge injection, charge densities might achieve SCL conditions *locally*, leading to a similar field dependence but overall reduced currents due to the lowered fraction of active electrode area.

In order to further elucidate the energetical situation at the anode/polymer interface, ultraviolet (UPS) and x-ray (XPS) photoelectron spectroscopy experiments were performed by N. Koch and A. Vollmer at the SurICat end station of the synchrotron light source BESSY GmbH, Berlin. The system comprises interconnected preparation and analysis chambers at base pressures below 5×10^{-10} mbar. The excitation energy for UPS and XPS was 35 eV and 630 eV, respectively. Photoemission spectra were recorded employing a hemispherical electron energy analyzer at 100 meV resolution in UPS. The Fermi energy level was determined by reference to a freshly sputtered Au(111) surface and the sample work function calculated from the secondary electron cutoff measured at -10 V sample bias. PEDOT:PSS was spin coated onto cleaned ITO substrates treated by UV/ozone for 30 min and subsequently annealed at 200°C for 5 min in air before being transferred into the vacuum chamber. The work function of the PEDOT:PSS variety used here (Clevios AI4083 provided by H.C. Starck, Germany) was determined as 5.15 eV but slightly differs among the available varieties of PEDOT:PSS according to varying concentrations of PSS in the surface region.[90] In order to determine the hole injection barrier at the PEDOT:PSS/polymer interface, samples were covered with a layer of **PB** by spincoating from 2 g/l chloroform solutions. Samples with both thin (~ 1 nm on average as determined from the XPS attenuation of PEDOT:PSS S2p core levels, possibly incomplete coverage of PEDOT:PSS) and thick ($\gg 1$ nm, com-

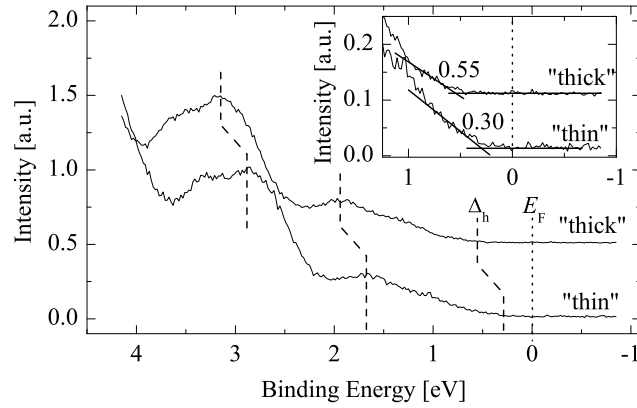


Figure 3.5: UPS valence band region spectra of thin and thick (see text) **PB** layers on top of PEDOT:PSS in terms of the binding energy relative to the Fermi level of PEDOT:PSS. The rigid energy shift is indicated by dashed lines and also corresponds to the difference in hole injection barrier Δ_h (energy difference between the valence band onset and the Fermi level E_F). The inset shows an enlarged plot of the valence band onset region. The spectra are displaced vertically for clarity.

plete attenuation of the PEDOT:PSS core level signals) coverage by **PB** were compared. Figure 3.5 shows two representative UPS valence level spectra for thin and thick **PB** coverage, the overall shape of which was independent of layer thickness. However, a rigid shift of the thick **PB** valence spectrum towards larger binding energy (BE) by ~ 0.25 eV is observed when comparing to that of thin layers. The hole injection barrier Δ_h was determined as the energy difference between the onset of photoemission at low binding energies and the Fermi level E_F . It varied between (0.30 ± 0.05) eV and (0.55 ± 0.05) eV for thin and thick films, respectively. The work function was determined for thick **PB** layers as (4.85 ± 0.05) eV. This indicates that the Schottky-Mott limit does not apply to these conducting polymer/semiconducting polymer interfaces, as the sample work function changed upon deposition of **PB**. In literature, this is often referred to as an *interface dipole* and attributed to charge exchange reactions across the interface [105] or thermodynamically driven charge transfer when the the polymer HOMO state distribution overlaps with the substrates E_F . [93, 106]. In both cases, excess interface charges accumulate in the semiconducting polymer and the resulting field limits further charge penetration into the bulk. This situation is reminiscent of *band bending* at metal/inorganic semiconductor interfaces and has also been suggested for the interface of PEDOT:PSS with either poly(9,9'-dioctylfluorene-co-bis-N,N'-(4-butylphenyl)diphenylamine) (TFB) or poly(9,9'-dioctylfluorene-co-bis-N,N'-(4-butylphenyl)-bis-N,N'-phenyl-1,4-phenylenediamine) (PFB). [107] For **PB**, it is proposed that the measured valence-band onset at a BE of (5.4 ± 0.1) eV corresponds to the HOMO level of the HT moieties. This was estimated from calculations as 4.9 eV as reported in chapter 2 but was measured by Gather et al. [48] by cyclic voltammetry as 5.3 eV, see chapter 4. As an alternative explanation of these results, consider that the work function of PEDOT:PSS has been found to strongly depend on the residual water content. Koch et al. [90] showed that the work function of PEDOT:PSS can be reversibly tuned over ~ 0.6 eV by drying under ultra high vacuum conditions. The results were interpreted in terms of

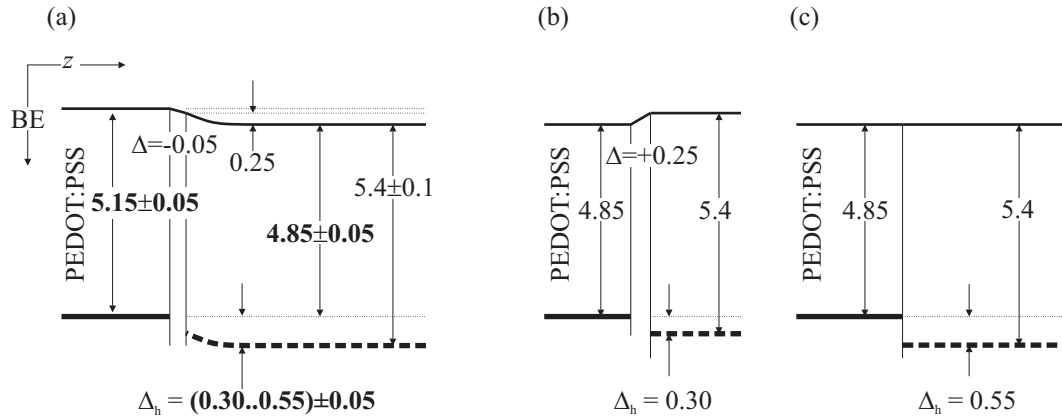


Figure 3.6: Proposed energy level schemes in terms of binding energy BE and layer stacking direction z , constructed from UPS measurements. (a) shows the situation assuming the work function of 5.15 eV for the PEDOT:PSS substrate holds also in case of an overcoating with **PB** and that band bending occurs in the polymer layer due to hole transfer from PEDOT:PSS. Bold parameters correspond to actual measurement values. The remaining interface dipole $\Delta \lesssim 0$ needed to explain the data is negligible. (b) and (c) depict the proposed situation for thin and thick **PB** layers, respectively, assuming a hypothetical bulk work function of 4.85 eV for PEDOT:PSS and in case of (b) an additional interface dipole $\Delta > 0$ due to the presence of a PSS-rich surface region. All numeric values are binding energies in eV.

swelling under water exposure, increasing the amount of PEDOT expressed at the surface of the film and thus reducing the observed work function. Since overcoating of PEDOT:PSS by a polymer layer may significantly hinder efficient water removal and lead to thickness-dependent residual water content, figure 3.6 (b) and (c) are proposed as alternative energy level schemes consistent with the UPS results. Here, an interface dipole of $\Delta = 0.25$ eV due to higher PSS surface concentration is assumed for thin **PB** samples while it is absent for thick samples. Although this might be a somewhat exaggerated picture, such effects might readily contribute to the observed vacuum level shifts and should be taken into account as a refinement of the band bending scheme proposed before. In any case, these results support the conclusion that hole injection into **PB** is severely limited by an energetic barrier of up to 0.55 eV, leading to low injection currents. When interpreted in terms of band bending, the results indicate some hole transfer from the electrode into the polymer. Such an accumulation layer would be expected to enhance charge injection which might cause the significant difference of hole injection efficiencies observed between PEDOT:PSS and metallic anodes despite very similar work functions.

The fabrication of unipolar electron-only devices generally requires the use of low work-function substrate materials to sufficiently suppress the injection of holes into the HOMO states of the polymer layer. While the fabrication and application of hole-only devices has been reported in a wealth of publications, there is a general lack of reports on electron-only devices and charge transport properties measured via this route. This is attributed not only to the relatively small amount of polymers that are known to feature fast and trap-free electron transport, but also to systematic difficulties in obtaining “good” samples. Low work-function substrate materials such as Ca evaporated on glass tend to easily oxidize and

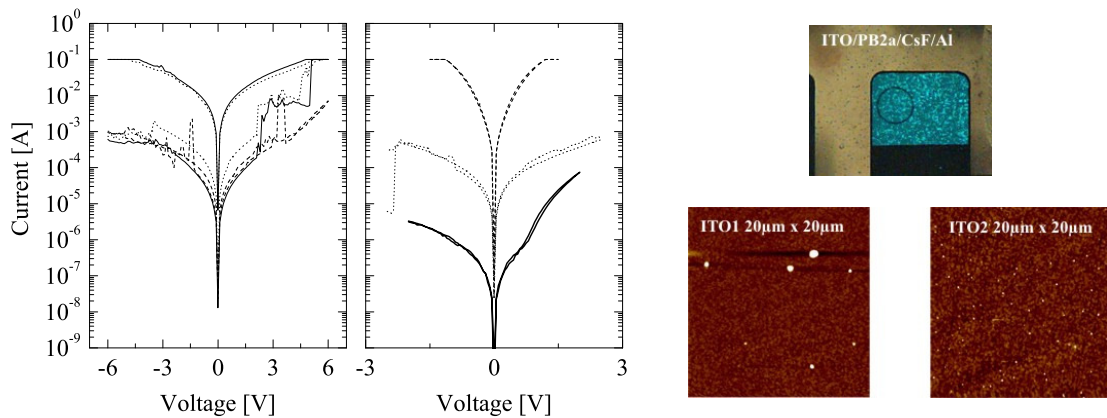


Figure 3.7: Left: Comparison of typical current-voltage characteristics for electron-only devices comprising a 70 nm thick **PB2a** layer (similar to **PB** and used here for its availability in larger quantities, for details see chapter 4.5) on top of ITO (left side) and on top of ITO substrates covered by 100 nm of aluminum (right side), using a CsF/Al electron injection cathode evaporated on top of the polymer layer. Results shown are from measurements of three different pixels on the same substrate but are representative for the general device behavior, also those comprising other types of polymer layers such as **PB**. Pixel size varies between 0.14 cm^2 and 0.18 cm^2 . Only one pixel (thick solid line) features rectifying behavior. Top right: Inhomogeneous emission pattern observed for devices with ITO anode during operation. The black circle indicates the measurement spot of the luminance meter. Bottom right: AFM topography scans of two different types of ITO substrates, vertical scales 132 nm (left) and 23 nm (right).

thus alter the electrodes conductivity in an unpredictable way. In principle, aluminum and even plain ITO surfaces should feature work functions low enough to suppress hole injection. Figure 3.7 shows typical current-voltage characteristics for unipolar devices fabricated with either plain ITO substrates or ITO substrates covered by 100 nm aluminum. At fixed voltages, the currents measured for several devices spread over up to 3 orders of magnitude while being unstable in time and lacking reproducibility upon repetitive measurements on the same pixel. This is attributed to the presence of large amounts of leakage channels that tend to be unstable at the high electric fields applied to the samples. Most devices show low amounts of luminescence at elevated driving voltages, the emission being highly inhomogeneous with bright spots occurring on length scales of $\sim 100 \mu\text{m}$. While leakage paths in samples with ITO anodes tend to be destroyed at high voltages (eventually leading to macroscopic *dark spots*), devices with aluminum anodes featured similarly inconsistent current-voltage characteristics but generally short-circuited completely during high-voltage operation. Surface topography of the ITO substrates was measured for two different ITO varieties using an atomic force microscope (Solver, NT-MDT) in tapping mode. **ITO1** was obtained from Merck KGaA, Germany while **ITO2** was obtained from Präzisions Glas & Optik, Germany. Total ITO thickness was comparable, leading to sheet resistances of $\sim 15 \Omega$ and $\sim 20 \Omega$ for **ITO1** and **ITO2**, respectively. Figure 3.7 compares large area ($40 \mu\text{m} \times 40 \mu\text{m}$) topography scans of these substrates after thorough cleaning. While the average surface roughness was relatively low at 3.4 nm (1.3 nm) for **ITO1** (**ITO2**), the peak-to-peak roughness was as high as 130 nm (23 nm) due to isolated protrusions of down to 100 nm

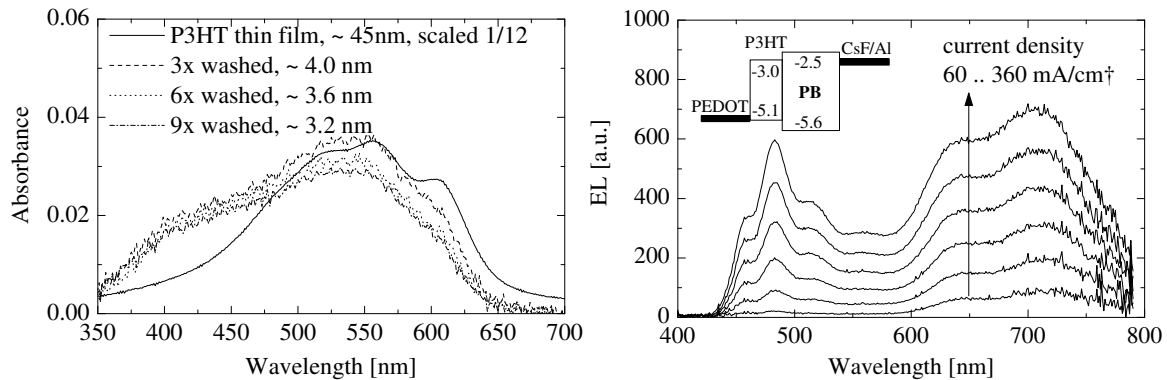


Figure 3.8: Left: Absorption spectra of a P3HT film of 45 nm thickness on glass and of P3HT interlayers on top of glass/ITO/PEDOT:PSS after several washing steps. All spectra are referenced to the corresponding substrate. Right: Electroluminescence spectra of P3HT/PB devices, parametric in the current density. Emission from PB is only observed at current densities in excess of 30 mA/cm² and its relative contribution rises with current density. The inset shows the approximate energy level structure of these bilayer devices.

lateral size. Since these defects were found on all investigated samples, they are most likely growth defects intrinsic to the ITO sputtering process. Due to their high aspect ratio, these defects may protrude partly or fully through subsequently deposited organic layers, leading to erroneous and leaky device behavior due to local shortcuts formed at elevated electric fields. Semitransparent metal electrodes deposited on glass substrates were found to exhibit similar shortcuts. An approach to make semitransparent metal electrodes of sufficiently low roughness that yield leakage-free electron-only devices is discussed in appendix C and was further analyzed by R. Steyrlleuthner [108, 109].

Here, another route is followed in order to sufficiently suppress hole injection into PB while retaining leakage-free device behavior: the single-layer device design comprising a PEDOT:PSS anode is replaced by a bilayer structure comprising a thin, insoluble layer (*interlayer*) of poly(3-hexylthiophene) (P3HT) fabricated on top of PEDOT:PSS. This interlayer was prepared by dissolving P3HT ($M_n = 1.2 \times 10^4$ g/mol, $M_w = 1.5 \times 10^4$ g/mol) in chloroform and spincoating onto PEDOT:PSS, baking the film for 30 min at 180°C and subsequent washing with neat chloroform. As observed for other polymers, a thin layer of P3HT remains on top of PEDOT:PSS which is insoluble in common organic solvents.[86, 87, 110, 111] Figure 3.8 compares absorption spectra of these interlayers after 3, 6 and 9 washing rounds, each consisting of spreading neat chloroform solvent on the substrate, waiting for 5 s and subsequently removing it by spinning the substrate. These spectra are measured in reference to a neat PEDOT:PSS covered substrate and compared to the absorption of a neat annealed P3HT film of 45 nm thickness. Already after the first washing rounds, the layer thickness is reduced to around 4 nm upon which further washing has only minor impact on the amount of P3HT observed in absorbance. Comparing the absorption of these insoluble residues with the neat film, a reduction of the 600 nm feature is observed. This feature has been attributed to the interchain interaction between planarized P3HT chains [112] and its reduction indicates that the interlayer P3HT is less ordered than the bulk films. The origin of the broad

featureless absorption at 425 nm is unknown and its absolute contribution to absorbance varied between different preparations. Note that this absorbance is similar to that reported both for P3HT solutions as well as for annealed thin films of low molecular weight P3HT.[113] A strong hypsochromic shift upon annealing was reported and has been attributed to a transition from planarized chains to a twisted coil-like conformation.[113, 114] The absorbance features of the P3HT interlayers indicate that the conformation of the P3HT residues differs significantly from the bulk film properties. This has not been investigated in more detail since the central interest here lies in the charge transport/injection behavior of these interlayers when incorporated into light-emitting devices with **PB** as active layer. Figure 3.8 shows electroluminescence spectra of bilayer light-emitting diodes featuring a thin interlayer of P3HT at the anode side and a regular **PB** layer spincoated on top. At low current densities and voltages, nearly pure P3HT interlayer emission in the far red spectral region of 600 nm to 800 nm is observed. Upon increasing the current densities up to 360 mA/cm², the **PB** emission fraction continuously rises. The approximate energy level scheme shown in the inset of figure 3.8 (right side) suggests that the P3HT interlayer should not promote hole injection into **PB** due to the HOMO energy level of 5.1 eV, which is very similar to that of PEDOT:PSS itself. Additionally, the **PB**/P3HT interface should not present an energetic barrier to electron transport while holes should be easily injected from PEDOT:PSS into P3HT on basis of the similar HOMO levels. Due to the high electron mobility in **PB**, a significant amount of electron/hole pairs is thus expected to recombine in the interlayer. No evidence for the formation of excited P3HT/**PB** interface states was found and thus the observed low amount of emission is attributed to mainly two effects. Excitons formed by electron/hole recombination directly in the interlayer will mostly decay non-radiatively due to the low luminescence quantum efficiency of P3HT of < 2%.[115] Also, those formed in the **PB** layer close to the P3HT/**PB** interface may undergo energy transfer to P3HT and thus do not contribute fully to the blue emission. Since the interlayer is very thin and has an absorbance of less than 0.03 in the blue spectral region, reabsorption of **PB** emission is negligible. Figure 3.9 shows the current-voltage and luminance-voltage characteristics of light-emitting devices of the structure ITO/PEDOT:PSS/[P3HT/]**PB**/CsF/Al with and without a P3HT interlayer. While the current density at fixed voltages does not change notably, a reduction of luminance of two to three orders of magnitude is observed for interlayer devices. The luminance efficiency correspondingly shows the same amount of reduction and is found to increase somewhat only at current densities above 20 mA/cm². This is correlated with the increase of bulk (blue) emission reported in figure 3.8. Since only holes recombining sufficiently far from the P3HT/**PB** interface lead to efficient luminescence, one should suspect that the device efficiency is larger for thicker devices when operated at the same current density and assuming strongly injection limited device behavior. This thickness dependence of current density was relatively small when the device thickness was kept below 200 nm, see figure 3.10. It is therefore suggested that the recombination of electrons and holes takes place either directly in the interlayer or within **PB** relatively near to the interlayer as long as the device thickness is sufficiently small. This implies that the amount of holes injected into the **PB** layer stays rather low and a mostly unipolar electron transport is achieved in the bulk. In what follows, such devices are designated *quasi electron-only* devices. Figure 3.10 shows field-dependent current densities of such P3HT interlayer *quasi* electron-only devices for varying film thickness of the **PB** layer. The electric fields have been approximately corrected for the built-in

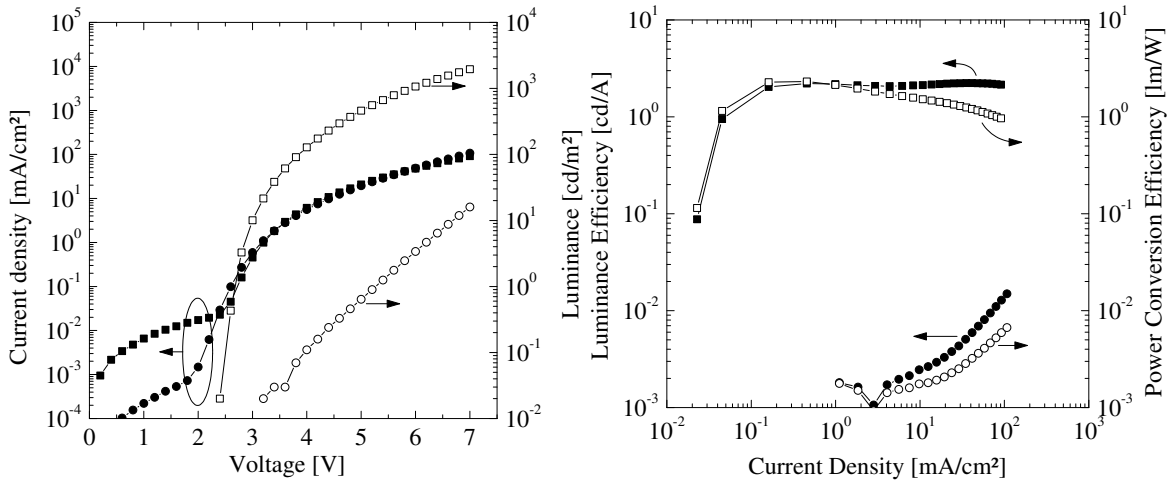


Figure 3.9: Left: Voltage dependence of current density (solid symbols) and luminance (open symbols) of a P3HT/PB device (circles) compared to a device without the P3HT interlayer (squares). Right: luminance efficiency (closed symbols) and power conversion efficiency (open symbols) of the same samples plotted against the current density. Below $10 \text{ mA}/\text{cm}^2$, nearly pure P3HT emission is observed and the luminance rapidly drops below the measurement limit of $\sim 10^{-2} \text{ cd}/\text{m}^2$.

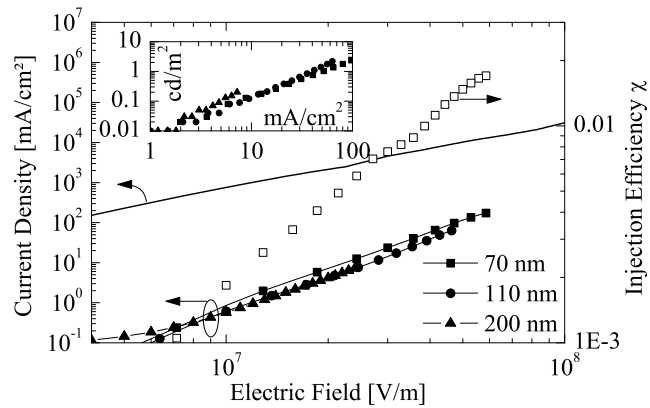


Figure 3.10: Field-dependence of current densities of *quasi* electron-only devices with P3HT interlayer and CsF/Al cathodes for various PB layer thicknesses. Data is compared to the current density expected for SCL conditions in a 70 nm thick layer using the TOF electron mobility (solid line). The calculated injection efficiency calculated for the 70 nm thick device is shown as open squares. The inset shows the luminance's dependence on current density.

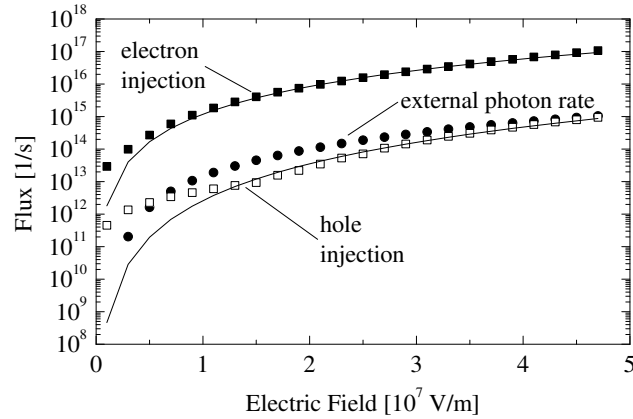


Figure 3.11: Injection rates of electrons (filled squares) and holes (open squares) for an active electrode area of 0.16 cm^2 as determined from 100 nm thick hole-only and *quasi* electron-only devices. The charge injection rates are compared to the external photon rate (filled circles) observed for bipolar devices with a PEDOT:PSS anode, 100 nm **PB** layer and a CsF/Al cathode. Electric fields shown were calculated taking into account the values of built-in potential observed for bipolar, electron-only and hole-only devices and thus represent the approximate average internal field across the **PB** layer. The solid lines were calculated from the power-law approximations shown in figure 3.12 and neglect leakage currents.

potential U_{bi} , mainly due to the work function differences of PEDOT:PSS and the CsF/Al cathode, by subtraction of the onset voltage of $U_{\text{onset}} \sim 2.0 \text{ V}$. For an electron injection that is strongly limited by energetic barriers, one would suspect thickness-independent current densities when evaluated at the same electric field. This is also found experimentally, with a tendency for slightly elevated currents at the film thickness $< 70 \text{ nm}$. This might be attributed to diffusion currents, which have been shown to play an important role for thin polymer films.[116] As for hole-only devices, the observed current densities are again compared to the SCL currents expected for barrier-free electron injection as calculated from the time-of-flight charge mobilities determined in chapter 2. The observed current is up to three orders of magnitude lower, with the injection efficiency χ rising as $\chi \propto E^{1.3}$ to approximately $\chi = 0.017$ at an electric field of $E = 5.3 \times 10^7 \text{ V/m}$, as observed for a 70 nm thick **PB** layer.

In order to obtain insight into the working mechanisms of bipolar **PB** devices and pave the way for a quantitative comparison with numerical simulation data, the presented techniques of hole-only and *quasi* electron-only device measurement were used to determine the injected charge currents for devices featuring a **PB** layer of 100 nm thickness, see figure 3.11. The data is presented in terms of the charge flux (units of s^{-1}) integrated for an active device area of 16 mm^2 . To facilitate the comparison of unipolar and bipolar device data, it is shown as a function of the average internal electric field, calculated by taking into account the different values of the built-in potential observed e.g. for electron-only and hole-only devices. The external photon flux of light-emitting devices is calculated from the measured luminous power taking into account the emission spectrum, see appendix D for details. The result is somewhat surprising, since the *internal* electron-hole recombination rate should be at least one order higher considering the singlet-triplet recombination ratio of $\eta_{\text{ST}} = 0.25$ and the

outcoupling efficiency, which can be approximated [117] by $\eta_{\text{extr.}} \approx 1/(2n^2) = 0.17$ with the polymer's index of refraction $n \approx 1.7$. The electron-hole recombination rate is thus at least one order of magnitude higher than the hole injection rate observed for unipolar hole-only devices. To explain this discrepancy, it is proposed that hole injection into **PB** significantly improves during bipolar device operation, presumably by accumulation or trapping of electrons near the anode/polymer interface.

3.3 Numerical Simulation of Device Behavior

Numerical simulations of both current-voltage (equilibrium) as well as transient device behavior were performed by implementing a one-dimensional drift-diffusion simulation model. It is based on the solution of the Poisson and continuity equations for positive and negative carriers, taking into account electron-hole recombination, transport and diffusion as well as exciton formation, diffusion and recombination. The underlying analytical model is similar to those used by Ruhstaller et al. [118] and Malliaras and Scott [101]. Even though such simulations are somewhat simplistic considering the hopping type of transport in amorphous semiconductors, there are numerous examples of successful application to the modeling of organic light-emitting devices, including their current-voltage and luminance-voltage characteristics.[119] Details of the underlying differential equations and the corresponding numerical algorithms are not central to the results here and can be found in appendix A. One crucial point for the numerical integration of differential equations is the correct choice of boundary conditions, e.g. the properties of charge injection at the electrode/polymer interfaces. Several models of varying complexity have been proposed and it is still a matter of debate which of them provides the best description.[23, 26, 28] To begin with, these ambiguities are resolved here by directly using the measured field dependencies of charge injection rates and charge mobilities as an input to the simulation.

Figure 3.12 shows the measured hole and electron injection current densities as a function of the applied electric field. At sufficiently high electric fields, these currents approximately follow power laws of the form $j = a_1 E^{a_2}$ with parameters $a_1 = 8.1 \times 10^{-7} \text{ cm}^2/\text{Vs}$ ($a_1 = 1.9 \times 10^{-3} \text{ cm}^2/\text{Vs}$) and $a_2 = -3.2 \times 10^{-4} \text{ cm}^{1/2}\text{V}^{-1/2}$ ($a_2 = -1.3 \times 10^{-3} \text{ cm}^{1/2}\text{V}^{-1/2}$) for hole injection (electron injection). At low electric fields, the current density is approximately proportional to the applied field and the absolute magnitude of currents observed in this regime varied between different samples. This current is attributed to Ohmic leakage currents. The power-law injection currents were used as boundary condition for the simulations described in the following. The electron mobilities were used as stated in chapter 2.2. The hole mobilities are also described in chapter 2.2 in terms of the Gaussian disorder model and the corresponding evaluation is based on the high-field behavior. In contrast to electron transport, a pronounced change of field dependence at electric fields of $\sim 6.4 \times 10^7 \text{ V/m}$ from negative slope to positive slope can be observed. Since the GDM model mobility equation (1.1.3) is only applicable to the high-field Poole-Frenkel region, directly using the determined model parameters would lead to wrong values for the hole mobility over a large range of electric fields. Here, the charge mobility at electric fields $< 6 \times 10^7 \text{ V/m}$ is of more interest and the room-temperature measurement data shown in figure 2.4 was fitted by a Poole-Frenkel type behavior, providing a negative field dependence at the electric

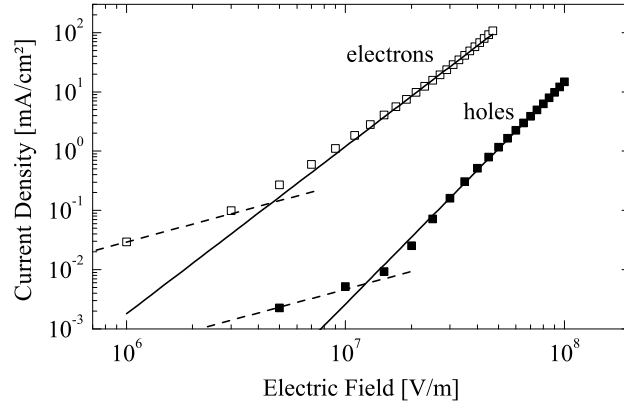


Figure 3.12: Charge injection currents measured for unipolar electron-only (open squares) and hole-only (closed squares) devices. The numerical device simulation uses field-dependent injection currents of the form $j(E) = a_1 E^{a_2}$ (solid lines) where the parameters are defined by a linear fit of the data at high electric fields in double-logarithmic scaling. The dashed lines are guides to the eye of unity slope. At low electric fields, measured currents roughly follow $j \propto E$ due to Ohmic leakage currents.

fields of interest. The corresponding fit parameters are reproduced in table 3.1 together with all remaining parameters contributing to the simulation model. The numerical simulations were performed by starting with an empty distribution of charges and excitons. Figure 3.13 shows snapshots of the simulated charge density, exciton density, drift current density and electric field distributions at various times after the application of a 6 V driving voltage. Due to the high electron mobility and low injection efficiency, the electron distribution reaches its equilibrium value already after 100 ns. Contrary to this, the hole distribution only approaches its equilibrium on timescales or more than 10 μ s. The electric field remains flat throughout the device due to the low charge densities achieved: to achieve a field drop of $\Delta E = 1 \times 10^7$ V/m within a distance of $\Delta d = 10$ nm from the anode, a much higher average hole density of $\bar{n} = \epsilon \epsilon_r \Delta E / e \Delta d \approx 2 \times 10^{23}$ m $^{-3}$ is required. The exciton density resulting from electron-hole recombination is of roughly Gaussian spatial distribution, centered in the polymer layer near to the anode. In order to extract the steady-state device characteristics, the simulated time evolution was advanced sufficiently far in time to allow for the charge and exciton distributions to reach equilibrium. The current-voltage characteristics were then extracted by stepwise variation of the applied voltage and running the simulation again while using the previous distribution as starting value. Figure 3.14 shows the calculated external photon flux in comparison with the measured photon flux already shown in figure 3.11. As discussed above, it is not surprising that the charge injection currents measured for single-carrier devices and used for the simulation are insufficient for reaching the experimentally observed external photon flux. The simulated values are nearly two orders of magnitude lower. Due to the strong imbalance in the charge transport properties of electrons and holes, the simulated device luminous efficacy was only ~ 0.01 lm/W, while the measured values reached up to 2.6 lm/W at 3.0 V although the **PB** layer thickness was not optimized for best performance in these devices. As discussed in chapter 2.3, the transient luminescence

parameter	value
layer thickness d	100 nm
number of simulation cells N	200
simulation step size Δt	0.1 ns
series resistance (current-voltage) R_s	20 Ω
series resistance (transient) R	32 Ω
area (current-voltage) A	16 mm ²
area (transient) A	1 mm ²
relative dielectric constant ϵ_r	2.9
built-in potential U_{bi}	2.4 V
hole mobility $\mu_h(E)$	$8.1 \times 10^{-7} \frac{\text{cm}^2}{\text{Vs}} \exp(-3.2 \times 10^{-4} \sqrt{\frac{\text{cm}}{\text{V}}} \sqrt{E})$
electron mobility $\mu_e(E)$	$1.9 \times 10^{-3} \frac{\text{cm}^2}{\text{Vs}} \exp(-1.3 \times 10^{-3} \sqrt{\frac{\text{cm}}{\text{V}}} \sqrt{E})$
charge diffusion constant D	$\mu k_B T / e$
hole injection current $j_h(E)$	$8.3 \times 10^4 \frac{\text{mA}}{\text{cm}^2} (10^{-9} \frac{\text{V}}{\text{m}} \cdot E)^{3.75}$
electron injection current $j_e(E)$	$5.2 \times 10^5 \frac{\text{mA}}{\text{cm}^2} (10^{-9} \frac{\text{V}}{\text{m}} \cdot E)^{2.82}$
density of states N_0	10^{27} m^{-3}
singlet-triplet branching ratio η_{ST}	1/4
outcoupling efficiency $\eta_{\text{extr.}}$	0.17
singlet exciton diffusion length L_D	10 nm
singlet exciton lifetime τ	1 ns
singlet exciton diffusion constant D_S	L_D^2 / τ
singlet exciton quantum efficiency η_F	0.5

Table 3.1: Parameters used for the numerical simulation of device behavior. These were kept fixed for all simulations except when stated otherwise in the text. Transient simulations used a device model with an emissive area of 1 mm² and an RC time constant of < 10 ns to faithfully model the experimental conditions of transient experiments. For the calculation of equilibrium properties such as luminance-voltage characteristics, the device area was adapted to allow for direct comparison with results measured on samples with 16 mm² emission area.

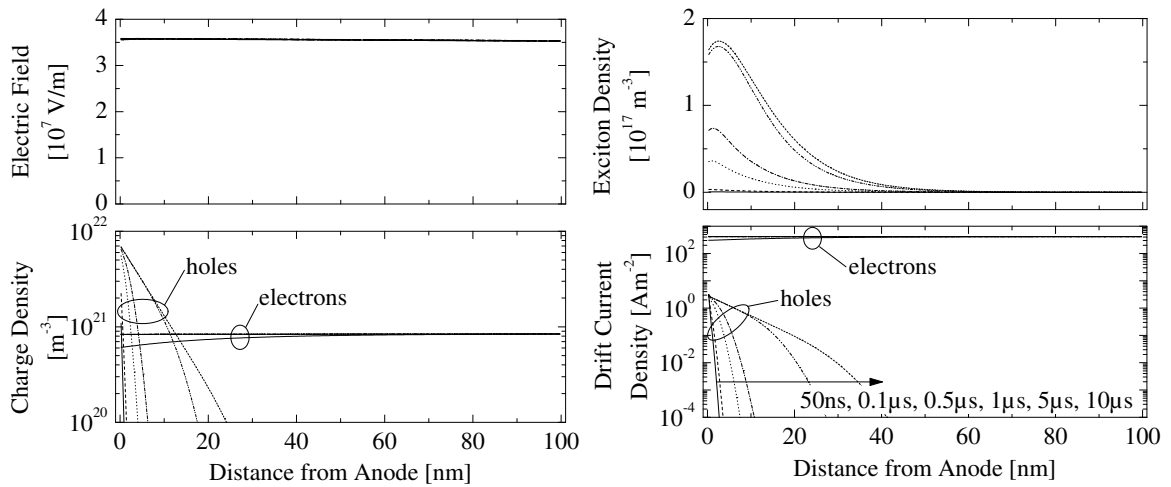


Figure 3.13: Snapshots of charge density (bottom left), electric field (top left), exciton density (top right) and drift current density (bottom right) distributions, parametric in time after the application of a 6 V driving voltage. The electron distribution is in equilibrium already at less than 100 ns after voltage turn-on, while the hole distribution still changes with time after more than 10 μ s. The exciton density is centered close to the anode due to the low penetration depth of holes into the PB layer.

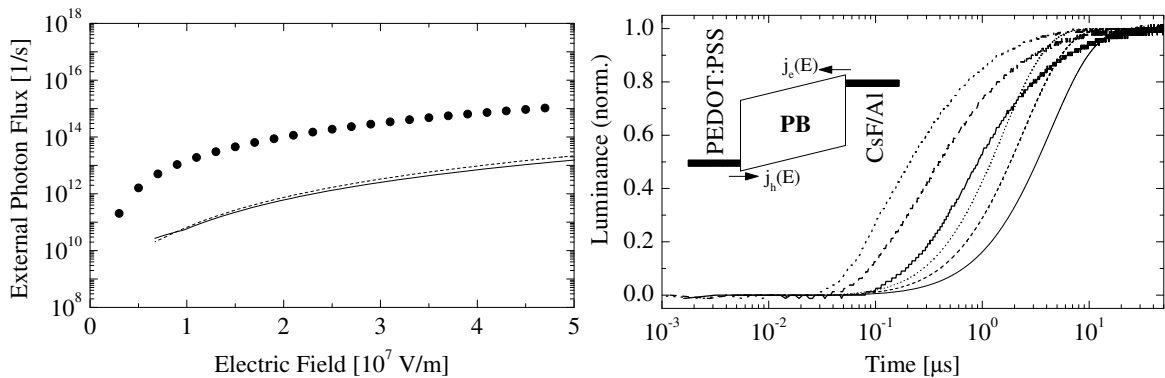


Figure 3.14: Left: Electric field-dependence of simulated external photon flux in equilibrium. The flux was calculated assuming that excitons are quenched upon diffusing into the PEDOT:PSS anode interface at $x = 0$ (solid line). Alternatively, the dashed line shows the flux in case such exciton quenching effects are neglected. The solid circles correspond to the measured data already shown in figure 3.11. Right: Measured (thick lines) and simulated (thin lines) electroluminescence transients after application of 5.0 V (solid lines), 6.1 V (dashed lines) and 7.3 V (dotted lines).

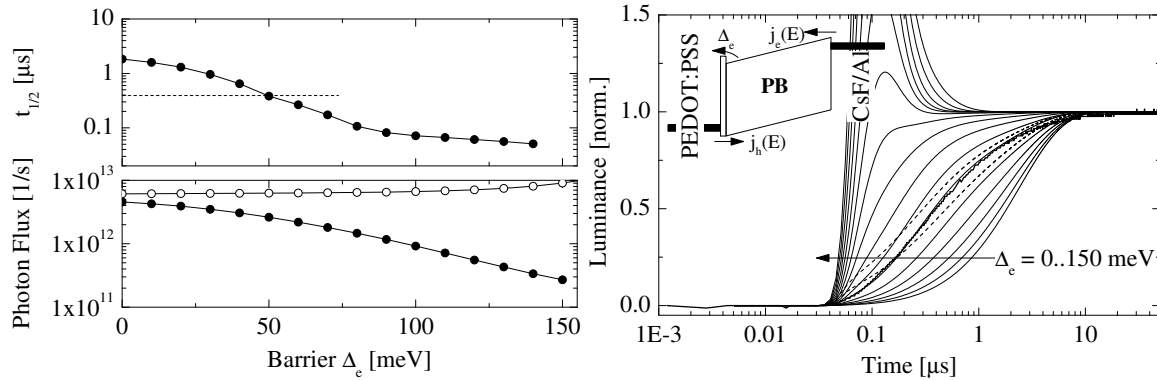


Figure 3.15: The effect of an extraction barrier Δ_e for electrons at the PEDOT:PSS/PB interface on the luminance rise time $t_{1/2}$ (top left, dashed line indicates experimental value), equilibrium photon flux (bottom left) and luminance transients (right, normalized to equilibrium) under conditions of 6 V driving voltage. Transients are calculated assuming exciton quenching at the interface. Additional transients are plotted for 30 meV and 40 meV barrier neglecting this quenching (dashed curves). The equilibrium photon flux under this condition (open circles) is found to slightly rise with the barrier height in contrast to the data calculated including the quenching (solid circles).

response is an especially sensitive parameter for both charge transport and charge injection properties. Figure 3.14 compares experimental transient EL data obtained for light-emitting diodes of structure ITO/PEDOT:PSS/PB(100 nm)/CsF/Al with the simulation results at applied voltages in the range of 5 V to 7 V. The simulation is obviously unable to reproduce the observed fast onset times of $< 0.1 \mu\text{s}$.

The discussion of the properties of the PEDOT:PSS/polymer interface in the introduction of this chapter motivates several adaptations of the simulation model. In what follows, such modifications are tested for their ability to obtain a closer correspondence between calculations and experimental results. As discussed, the PEDOT:PSS/polymer interface might interfere with electron transport due to the insulating properties of the PSS-enriched surface layer. This was investigated by introducing an energetic barrier Δ_e for electrons drifting across the interface, effectively scaling the electron drift current by the Arrhenius term $\exp(-\Delta_e/k_B T)$. Figure 3.15 shows that such a barrier significantly reduces the calculated onset times of light-emission and for strong barriers in excess of 90 meV leads to luminescence overshoot effects. Comparing the time $t_{1/2}$ for reaching half of the equilibrium luminance to the experimental value, a barrier height of $\Delta_e \sim 50 \text{ meV}$ yields the best result. Indeed, the simulated transient luminance output closely follows the experimental data over several orders of magnitude in time. Figure 3.16 shows that the introduced extraction barrier also ensures the correct scaling of transient EL with the applied voltage. Due to the barrier, the electron density accumulated at the interface increases by one order of magnitude, leading to a $\sim 30\%$ narrower recombination zone. Although these results are promising, the accumulated charge densities are too small to significantly enhance the interfacial electric field and thus the total amount of hole injection. Figure 3.15 shows that the total photon flux only changes to a minor extent. While electron extraction barriers thus provide a reasonable description of transient EL experiments (charge injection into a layer mainly devoid of charges) they fail in case of equilibrium operation of the devices where average stored charge densi-

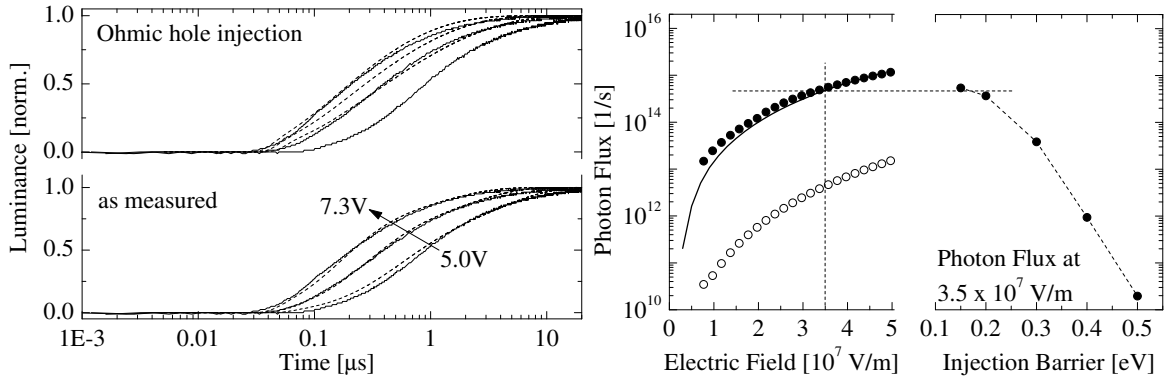


Figure 3.16: Left: Transient EL simulated for 5.0 V, 6.1 V and 7.3 V applied voltage using the measured field-dependence of hole injection and a 50 meV electron extraction barrier at the anode/polymer interface (bottom, dashed lines); transient EL simulated assuming Ohmic hole injection instead (top, dashed lines). Data is compared to experimental results (solid lines) as in figure 3.14. Right: Electric field dependence of the simulated photon flux using hole injection as measured (open circles) and Ohmic hole injection (closed circles) compared to the measured photon flux (solid line). Photon flux at an electric field of 3.5×10^7 V/m as a function of the injection barrier for holes within the Scott/Malliaras injection model. Dashed lines are guides to the eye.

ties might be much higher. While the cathode/polymer interface region stays mainly free of holes during device operation, the imbalance of hole and electron mobility leads to a continuous presence of electrons at the anode interface. This might cause long-term alterations of the hole injection due to e.g. the trapping of charges. As another modification of the simulation model, the fixed field-dependence of hole injection is replaced by the analytic model proposed by Scott and Malliaras [28], see appendix A for details. Figure 3.16 shows the equilibrium luminance parametric in the effective hole injection barrier thus introduced into the simulation. The device behavior observed for the fixed injection model is retained at a barrier of ~ 0.36 eV while for lower values the luminance increases. At less than 0.2 eV injection barrier, the contact becomes mainly *Ohmic*, i.e. the electric field drops to near zero at the anode/polymer interface. At the same time, the simulated field-dependence of total emission is found to closely reproduce the experimental values. This shows that equilibrium device operation might be accompanied by a significant reduction of the hole injection barriers. Despite this correspondence, transient EL simulations under conditions of Ohmic hole injection fail to reproduce the time shifts observed for the experimental data under variation of the driving voltage, see figure 3.16. The enhancement mechanism is thus supposed to be ineffective in devices operated under the low duty cycle conditions prevalent in transient EL experiments. One subtle additional parameter that has not been discussed up to here concerns the quenching of excitons at interfaces. It is well known that luminescent states of organic molecules are quenched in vicinity to conducting metal electrodes due to modifications of the radiative and non-radiative decay rates.[120] In the simulations performed here, excitons are quenched by the metal cathode only upon diffusing to the polymer/metal interface. This is a strong simplification but does not impact the results since exciton density is concentrated at the anode side of the polymer layer. Interference effects are a function of the emitter position within the layer but are taken into account here only by the effective

outcoupling efficiency η_{extr} . The situation is somewhat more complicated for the anode. While PEDOT:PSS is not a metal and thus contributes only weakly to the interference effects, it has been reported to quench the luminescent states of at least some polymers by increasing the rate of nonradiative decay.[121] One of the main mechanisms discussed in literature is a doping of the interfacial polymer layer by holes, stabilized by counterions on the PSS chains of PEDOT:PSS.[121, 122] Indeed, one interpretation of the UPS results discussed in section 3.2 indicated that transfer of holes into the **PB** layer occurred within the first few nanometers. Assuming a homogeneous hole density n_h due to doping within the first $d = 3$ nm of the **PB** layer and a total level shift of the electric potential of $\Delta\Phi = 0.25$ V, a rather high charge density of $n_h = 2\epsilon\epsilon_0\Delta\Phi/ed^2 = 9 \times 10^{24} \text{ m}^{-3}$ is to be expected. Since in the simulations performed here, the exciton densities in the anode region are rather high, the effect of quenching shall be discussed explicitly. So far, the results presented have been obtained assuming a complete quenching of excitons upon reaching the interface by diffusion. Figure 3.14 shows that the external photon flux only slightly increases upon neglecting this quenching. For the calculations involving an electron extraction barrier (figure 3.15, the photon flux was observed to slightly decrease upon increasing the extraction barrier for electrons mainly due to the anode quenching effect. When the quenching is not included in the simulations, the photon flux instead slightly rises with the extraction barrier but is still several orders of magnitude below the measured values for equilibrium operation. The luminance transients could be well reproduced under the assumption of quenching at the anode but are distinctly different when the quenching is ignored, see figure 3.15. The main difference arises in form of a luminescence “hump” on timescales $< 0.1 \mu\text{s}$ for simulations without quenching when electrons first reach the anode and excitons are generated closely to the interface. The absence of this feature in the experimental data suggests that quenching of excitons at the PEDOT:PSS/polymer interface should be taken into account.

3.4 The Role of Electron Blocking and Device Conditioning

The numerical device simulations discussed so far have shown that transient EL experiments can be understood from measured charge injection and transport properties by additionally assuming an extraction barrier for electrons at the interface of the polymer with PEDOT:PSS. Using this device model to simulate equilibrium emission properties leads to a strong underestimation of the luminance output. When the anodic hole injection is modeled by an Ohmic contact instead of the fixed field dependence determined from hole-only devices, the equilibrium properties and luminance-voltage characteristics are faithfully reproduced while the transient results are in variance with experiments. This contradiction indicates the presence of two distinct operating regimes, one being observed for hole-only devices and bipolar devices directly after application of a driving voltage, the other under continuous bipolar operation. In order to experimentally bridge the gap between transient EL and continuous (equilibrium) device operation, transient EL experiments were conducted for varying pulse repetition rates and pulse lengths. Figure 3.17 analyzes the luminance level measured 2 μs after application of a 7.4 V driving pulse to 89 nm thick light-emitting diodes. Pulse lengths were varied from $< 4 \mu\text{s}$ to 4 ms at a repetition rate of 200 Hz and up to 40 ms at a repetition rate of 20 Hz. Between successive voltage pulses, the applied voltage is lowered to zero.

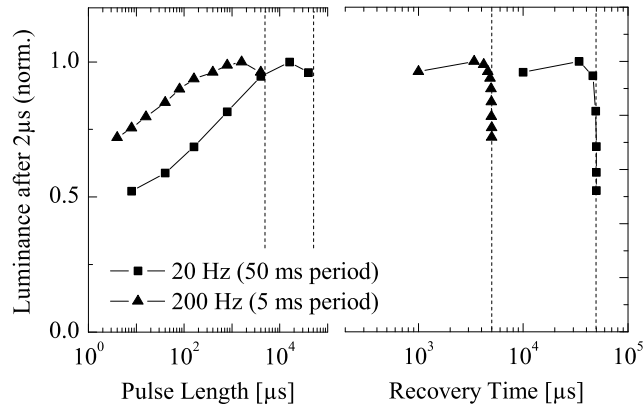


Figure 3.17: Luminance measured 2 μs after the application of a 7.4 V driving voltage to a light-emitting device with 89 nm PB layer thickness. The voltage was applied as a rectangular waveform of 20 Hz (squares) and 200 Hz (triangles) repetition frequency with a baseline voltage of 0 V and variable pulse lengths. Luminance values are found to rise with increasing pulse length. The limits on pulse length and recovery times imposed by the repetition frequency are indicated by dashed lines.

Generally, devices driven at higher pulse lengths were found to attain the equilibrium faster and thus feature a corresponding increase of the early emission level. Despite the general trend, the observed effects did not correlate well with either the pulse length or the recovery time upon variation of the pulse repetition frequency. The strongest enhancement of initial luminance was always observed for pulse lengths of $\Delta t > 0.2T$, where T is the pulse period. Figure 3.18 shows that indeed a strong correlation of early luminance emission and the duty cycle $D = \Delta t/T$ exists. Significant sample to sample variations of this effect were observed, with a general tendency for stronger luminance improvements occurring for thicker devices when compared at similar applied electric fields. The efficiency improvement reached up to two orders of magnitude, similar to the difference in total emission levels observed for the proposed simulation models for transient and equilibrium device behavior. The simulations already indicated that the difference in device behavior is due to a strong improvement of hole injection under continuous device operation (*conditioning*). It is proposed that this is actually caused by charge accumulation, since the effect correlates with the duty cycle and thus with the average amount of charges present in the polymer layer. Since these effects were only observed for bipolar devices, electron trapping near the anode/polymer interface is the most likely mechanism of hole injection improvement: the extraction barrier introduced in the simulations helps to correctly model the transient EL but is insufficient to accumulate electron densities large enough to modify the hole injection behavior. As discussed in the introduction, such extraction barriers are most likely caused by the PSS surface enrichment of PEDOT:PSS films. Pingree et al. [123] reported that charge injection is distributed inhomogeneously across the PEDOT:PSS layer, with small local hotspots attributed to the exposition of PEDOT-rich domains while the more insulating areas are attributed to a surface rich in PSS. In order to assess the effect of this surface region on the device characteristics, PEDOT:PSS substrates were treated with oxygen plasma to remove the surface and expose the bulk properties. It is well known that oxygen plasma can be used to etch

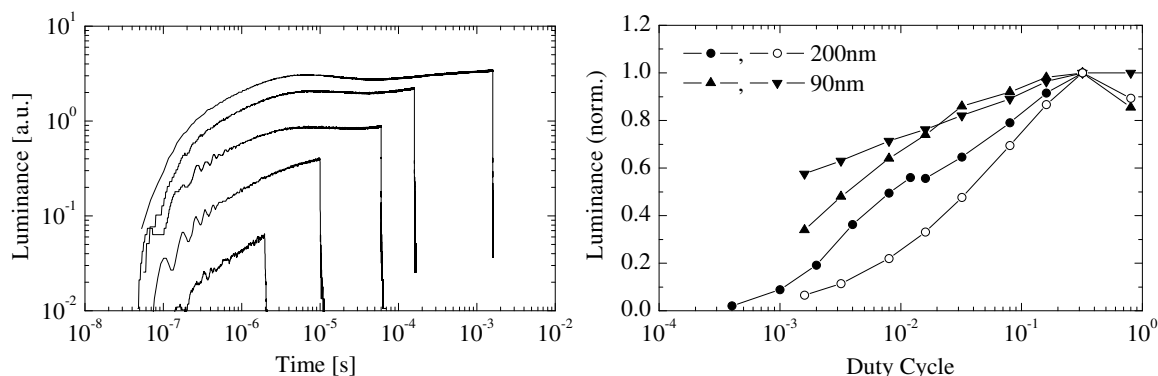


Figure 3.18: Left: Luminance transients of a 200 nm thick light-emitting device driven by 7.4 V electric pulses at a repetition frequency of 200 Hz. The pulse lengths were varied between 2 μ s and 1.6 ms, corresponding to duty cycles of 4×10^{-4} to 3.2×10^{-1} . Right: Duty-cycle effects on the observed luminance 2 μ s (8 μ s) after application of a 7.4 V (3.7 V) pulse to samples of 200 nm (90 nm) thickness. Results for a total of four samples are shown.

polymers [124, 125] and even structure PEDOT:PSS films [126]. Zhou et al. [127] reported that mild treatment of PEDOT:PSS with oxygen plasma decreases the total layer thickness while altering the surface roughness. They observed an increase of device efficiency and concluded that for their type of light-emitting devices charge injection improved due to the better exposition of the conductive PEDOT-rich phase at the etched surface. Figure 3.19 shows the results of treating neat ITO/PEDOT:PSS substrates in an O_2 plasma ashing system (TePla 200-G, excitation frequency 2.45 GHz, base pressure 0.1 mbar, O_2 pressure 1 mbar). Prior to this treatment, PEDOT:PSS films were dried as usual at 180°C for 10 min to remove residual water content. Thickness of the PEDOT:PSS film was determined by a Dektak 3ST (Veeco) stylus profilometer at freshly made scratches. A uniform etching rate of ~ 9 nm/min is observed which does not vary significantly with the plasma excitation power. The average roughness of the films was ~ 0.7 nm both before and after plasma treatment. Light-emitting devices of final structure ITO/PEDOT:PSS/PB/CsF/Al were built on top of substrates with both neat and etched PEDOT:PSS films. Figure 3.19 shows the performance of these devices in terms of current density and current efficacy. Compared to untreated PEDOT:PSS, devices with etched layers showed a 35% reduction of the total current and a $< 16\%$ reduction of current efficacy. These changes in device performance are only moderate in comparison to the conditioning effects upon going from low to high duty cycles. This again supports the conclusion of charge trapping instead of charge accumulation as the main mechanism for the conditioning effect.

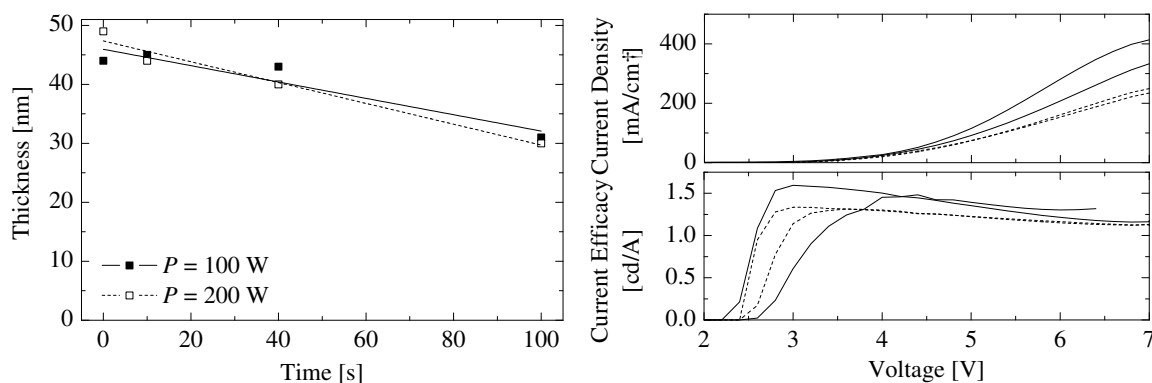


Figure 3.19: Left: Thickness reduction of a PEDOT:PSS layer treated in an oxygen plasma asher at different power levels P . Right: Current density and current efficacy measured for two PB light-emitting devices based on neat PEDOT:PSS films (solid lines) and two devices based on plasma treated (60 s at 100 W) PEDOT:PSS films (dashed lines).

3.5 Conclusion

This chapter analyzed the hole and electron injection properties of the blue-emitting copolymer **PB**. Measurements of hole-only devices were employed to assess the hole injection efficiency. The results were related to UPS/XPS studies of the electronic structure of the PEDOT:PSS/polymer interface and it was shown that severe energetic barriers hinder the injection of holes into the polymer layer. Injection efficiencies for electrons were determined by employing *quasi* electron-only devices and comparing with the charge mobilities determined in chapter 2. This type of measurement circumvented the problem of manufacturing leakage-free unipolar devices on low work function substrates by employing a thin polymeric interlayer on ITO/PEDOT:PSS substrates that sufficiently blocks hole injection. As for holes, electron injection was found to be strongly reduced when compared to the space charge limited case calculated from the charge mobilities. The determined field dependence of charge injection and mobilities was used to numerically simulate both equilibrium and transient luminescence response of the light-emitting diodes. The simulations are consistent with the bipolar operation of these devices being determined by (1) an extraction barrier of ~ 50 meV for electrons at the PEDOT:PSS/**PB** interface due to a PSS-rich surface layer and (2) the formation of an Ohmic contact for hole injection by electron trapping in an interface-near region. While process (1) determined the transient luminescence response observed for devices mainly devoid of charges, process (2) accounts for the much higher luminance values observed under continuous operation and a more than hundred-fold increase in luminance efficacy. Comparable conditioning effects of hole injection under application of high driving voltages were also reported for other polyfluorene derivatives such as poly(9,9-dioctylfluorene) (PFO) [94] but differ from the effects reported here in the observed timescales. While for PFO, the conditioning effects were of much longer lifetime and lasted tens of hours, here these effects diminish on much faster timescales and thus do not contribute to typical (low duty cycle) transient EL measurements even when the device was operated at constant voltages before.

Chapter 4

White-emitting Polymeric LED: Emission Color and the Role of Charge Trapping

4.1 Introduction

In this chapter, the properties of white-emitting copolymers provided by Merck KGaA, Germany are studied. The focus is put on the development of an analytic model that provides enhanced understanding of the physical mechanisms determining the emission color under variation of driving parameters such as temperature, voltage and current. The chemical structure of one of these polymers (**PW**) is shown in figure B.1 on page 135. It comprises a spirobifluorene backbone **BB** and 10 mol% triphenylamine-type moieties **HT** providing electron transport and hole transport, respectively. The concentration of the blue, green and red singlet emitting chromophores **B**, **G**, **R** are 11%, 0.05% and 0.04%, respectively. This polymer has also been studied by Gather et al. [48] concerning its energy levels and electroluminescent emission properties. To gain additional insight into the role of the chromophores, model polymers with reduced chromophore content were also provided. **PB** was polymerized using only the **BB**, **HT** and **B** monomers and was already investigated in terms of charge transport and charge injection properties in chapters 2 and 3. **BG** additionally contains **G** (completely lacks **R**) while **BR** contains **R** but lacks **G**. As is discussed below, OLEDs fabricated from **PW** suffer from severe bias voltage-dependent color shifts which are attributed to the charge trapping properties of the red chromophore. While Gather et al. utilize purely kinetic arguments for explaining these effects, this chapter aims at developing a rate equation approach which will provide more insight into the interplay between charge transport and charge injection in determining the emission color. It is shown that the results from the purely kinetic approach are reproduced only as a special case under adequate presumptions. Before treating the charge transport properties in more detail, the energy transfer in between the chromophores is discussed. This is essential for an understanding of the electroluminescent properties, since the excited states generated by light absorption and by sequential charge trapping are the same.

4.2 Energy Transfer and its Impact on Emission Color

Absorption and photoluminescence emission spectra were measured for **PW**, **PB**, **BG** and **BR**, see figure 4.1. The samples were thin polymer films spin coated on standard glass substrates and encapsulated along the edges by a spacer and a second glass slide using two-component

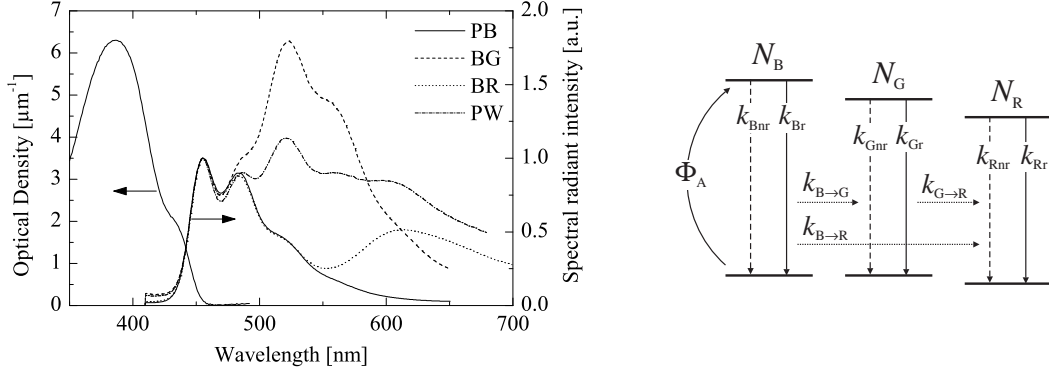


Figure 4.1: Left: Absorbance and normalized photoluminescence spectra of thin films of the copolymers PW, PB, BG and BR after excitation at 385 nm (film thickness less than 100 nm). Right: The proposed relaxation and energy transfer pathways of blue, green and red chromophores. Radiative (nonradiative) pathways are represented by solid (dashed) arrows, energy transfer pathways by dotted arrows.

epoxy resin. All sample preparation steps were done under nitrogen atmosphere. All of these polymers feature the same absorption spectrum attributed to the spirobifluorene backbone and the blue chromophore. Despite having the same absorption spectrum, significant fluorescence emission in the green to red spectral region is observed for the polymer layers that include the green and/or the red chromophores. Since the photocarrier generation efficiency is low and thus nearly no mobile carriers are present, this is attributed to resonant energy transfer from the blue chromophore to the green and red chromophores. Resonant energy transfer was first introduced by Förster [128] and describes energy transfer between adjacent chromophores by a coulombic coupling of the corresponding transition dipoles. It results in a radiationless transfer of excitation energy from one molecule (the donor) to another (the acceptor), where the corresponding first-order rate constant is

$$k_{\text{FT}} = k_0 \left(\frac{r_0}{r} \right)^6 \quad (4.2.1)$$

$$r_0 \propto \eta_{\text{D}} \int_0^{\infty} I_{\text{D}}(\lambda) \varepsilon_{\text{A}}(\lambda) \lambda^4 d\lambda, \quad (4.2.2)$$

where η_{D} is the donor's quantum efficiency, I_{D} its fluorescence spectrum and ε_{A} the extinction coefficient of the acceptor. Due to the r^{-6} dependence on donor-acceptor distance r , energy transfer of Förster type is usually effective only over short distances of less than 10 nm. It strongly depends on the spectral overlap of donor emission and acceptor absorption, although no photons are interchanged. This can be easily understood from the Fermi golden rule which predicts $k_{\text{FT}} = \frac{2\pi}{\hbar} \langle V \rangle^2 \rho$, where V is the coulombic interaction energy $V \propto r^{-3}$ of two dipoles and ρ is the energetic overlap integral of the involved quantum states. Excitation and emission spectra for **PW** are shown in figure 4.2. Using an excitation wavelength of 520 nm, direct excitation of the red chromophores is possible. The corresponding emission has a broad distribution from 550 nm to 750 nm, the peak emission being located at 620 nm. The excitation spectrum recorded for the 620 nm emission is limited in wavelengths due to the onset of the green chromophore's absorption, which also leads to emission at that

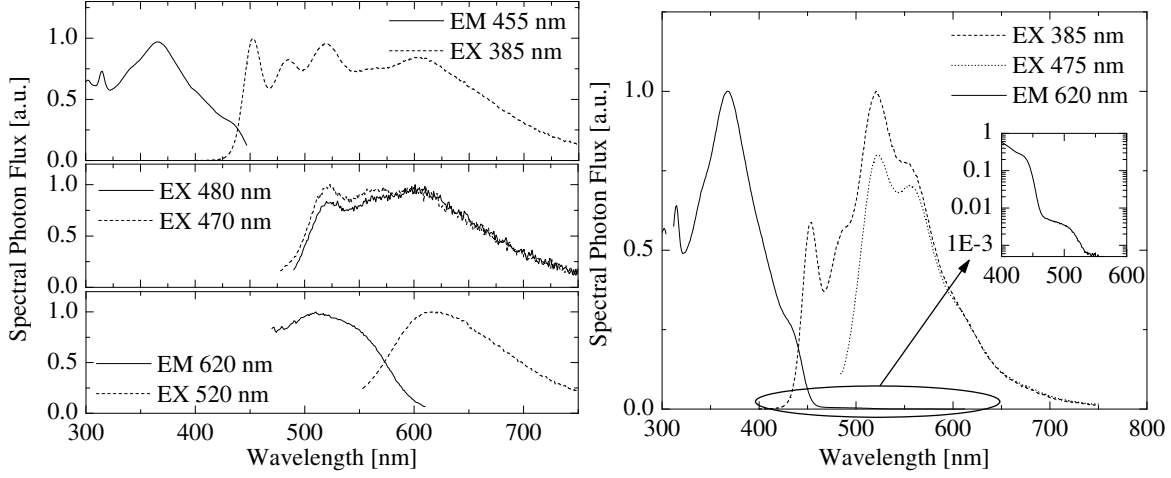


Figure 4.2: Excitation and emission spectra for **PW** (left) and **BG** (right), obtained for the indicated emission (EM) and excitation (EX) wavelengths, respectively. It was not possible to unambiguously determine the direct excitation spectrum of the green chromophore (insight in right figure), since it overlaps with that of the blue chromophore and efficient energy transfer to green occurs.

wavelength. The excitation spectrum is thus expected to extend further well into the blue spectral region. The green chromophore's emission spectrum cannot be measured directly in **PW** due to energy transfer to red chromophores and a significant overlap of the corresponding emission spectra. Thus, properties of the green emitter were determined in **BG**, which lacks red chromophores. The emission spectrum was recorded under excitation by 475 nm light, where no absorption by the blue chromophore occurs. However, measurement of the corresponding excitation spectrum is hampered by the overlap with absorption by the blue chromophore and strong energy transfer to green. From these experiments it is evident that significant emission-absorption spectral overlap is to be expected for blue/green, green/red as well as blue/red chromophore combinations.

In the following, the energy transfer is analyzed in more detail in terms of a three-component rate equation model schematically depicted in figure 4.1. Each type of chromophore $X=B,G,R$ (blue, green, red) is characterized by singlet-exciton occupation numbers N_X and first-order radiative and nonradiative recombination rate constants k_{Xr} and k_{Xnr} . The blue-green, blue-red and green-red energy transfer is characterized by the rate constants $k_{B \rightarrow G}$, $k_{B \rightarrow R}$ and $k_{G \rightarrow R}$, respectively. The rate equations for the occupation numbers are

$$\frac{dN_B}{dt} = -(k_{Br} + k_{Bnr} + k_{B \rightarrow G} + k_{B \rightarrow R})N_B + \Phi_A \quad (4.2.3)$$

$$\frac{dN_G}{dt} = k_{B \rightarrow G}N_B - (k_{Gr} + k_{Gnr} + k_{G \rightarrow R})N_G \quad (4.2.4)$$

$$\frac{dN_R}{dt} = k_{B \rightarrow R}N_B + k_{G \rightarrow R}N_G - (k_{Rr} + k_{Rnr})N_R, \quad (4.2.5)$$

where Φ_A is the rate of exciton generation on B due to the absorption of photons. The equilibrium situation is obtained by setting all time derivatives $dN_X/dt = 0$. The mixed-

system quantum efficiencies of the chromophores are defined by

$$\eta_X = \frac{k_{Xr}N_X}{\Phi_A} \quad (4.2.6)$$

relative to the photon rate absorbed onto the blue chromophores. For **BG** and **BR**, no G→R transfer occurs and the corresponding efficiencies are calculated as

$$\eta_G^{BG} = \left(1 - \frac{\eta_B^{BG}}{\eta_B^B}\right) \eta_G^G = \eta_G^G \eta_{B \rightarrow G}^{BG} \quad (4.2.7)$$

$$\eta_R^{BR} = \left(1 - \frac{\eta_B^{BR}}{\eta_B^B}\right) \eta_R^R = \eta_R^R \eta_{B \rightarrow R}^{BR}, \quad (4.2.8)$$

where $\eta_X^X := k_{Xr}/(k_{Xr} + k_{Xnr})$ is the fluorescence quantum efficiency of chromophore X in case of direct absorption of light on that chromophore, using the Förster transfer efficiencies

$$\eta_{B \rightarrow X}^{BX} = \frac{k_{B \rightarrow X}}{k_{Br} + k_{Bnr} + k_{B \rightarrow X}} = \frac{k_{B \rightarrow X} \eta_X^{BX}}{k_{Br}} = 1 - \frac{\eta_B^{BX}}{\eta_B^B}. \quad (4.2.9)$$

The ratio η_X^{BX}/η_B^B corresponds to the reduction of blue emission due to the introduction of chromophore X. It can be determined by comparing the emission spectra of **PB** with those of **BG** and **BR** under otherwise identical conditions, i.e. the same excitation intensity, wavelength and layer thickness. In order to determine estimates for these coefficients, emission spectra were recorded for the chemically closely comparable **PB**, **BG** and **BR** on polymer films of 80 nm thickness prepared by spin coating onto standard glass slides in nitrogen atmosphere. Care was exercised to obtain the same film thickness for the different polymers, but errors of up to 5% are to be expected for the layer thickness and thus for the transfer rates determined below. The samples were encapsulated under nitrogen atmosphere with a second glass slide and two-component epoxy resin before measurement to protect the films from moisture and oxygen. Figure 4.3 shows the measured spectra: Upon introduction of the green chromophore, the blue emission is reduced to $\eta_B^{BG}/\eta_B^B = 0.296$ relative to the emission observed for **PB** under identical excitation conditions, resulting in a Förster transfer efficiency of $\eta_G^{BG} = 1 - 0.296 = 0.704$. The ratio between the efficiency η_G^{BG} of the green emitter in **BG** and the fluorescence quantum efficiency is thus also given by $\eta_G^{BG}/\eta_G^G = \eta_{B \rightarrow G}^{BG} = 0.704$. Using this ratio, it is possible to reconstruct the pure green chromophore spectrum quantitatively by subtracting the blue part from the **BG** spectrum and dividing the result by η_G^{BG}/η_G^G . The same holds for **BR**, where $\eta_{B \rightarrow R}^{BR} = 0.268$. The transfer rates can be calculated from the transfer efficiencies in terms of the natural lifetime $\tau_X = k_{Xr}/(k_{Xr} + k_{Xnr})$ by $k_{B \rightarrow X} = \tau_B^{-1} \eta_{B \rightarrow X}^{BX} (1 - \eta_{B \rightarrow X}^{BX})$, resulting in $k_{B \rightarrow G} \tau_B = 2.38$ and $k_{B \rightarrow R} \tau_B = 0.37$. Figure 4.4 shows the obtained chromophore spectra. Note that these spectra still include the quantum efficiencies: Let f_X be the chromophore spectrum for one photon emission event, then the emission spectrum of **PB** is $F_B = \Phi_A f_B \eta_B^B$. For **BG** and **BR**, the fraction of the spectrum corresponding to blue emission is $\Phi_A f_B \eta_B^{BX}$ and the X=G,R fraction of the emission is $\Phi_A f_X \eta_X^{BX}$. The obtained emitter spectrum of X thus corresponds to $F_X = \Phi_A f_X \eta_X^X$. It is evident from figure 4.4 that the quantum efficiencies of the emitters vary. Integration yields the relation $\eta_B^B : \eta_G^G : \eta_R^R \sim 1 : 0.86 : 2.3$.

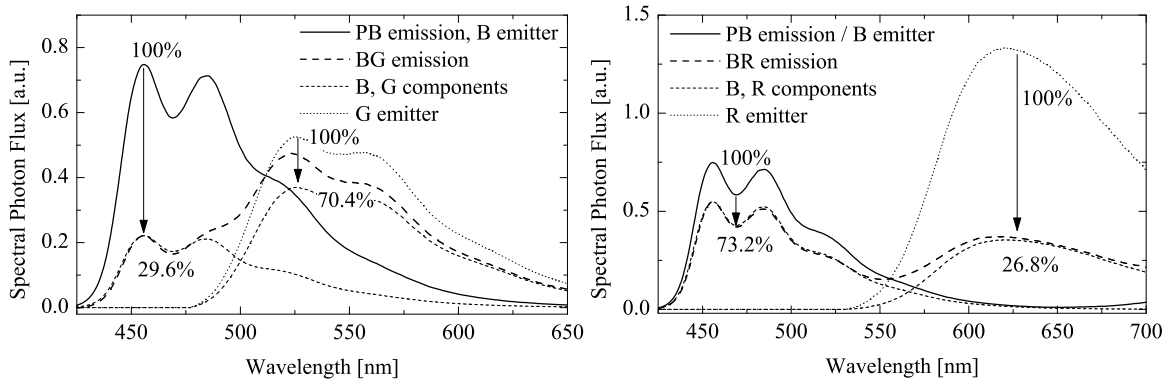


Figure 4.3: Reconstruction of the green and red chromophore emission spectra by direct comparison of emission from PB, BG and BR polymer films.

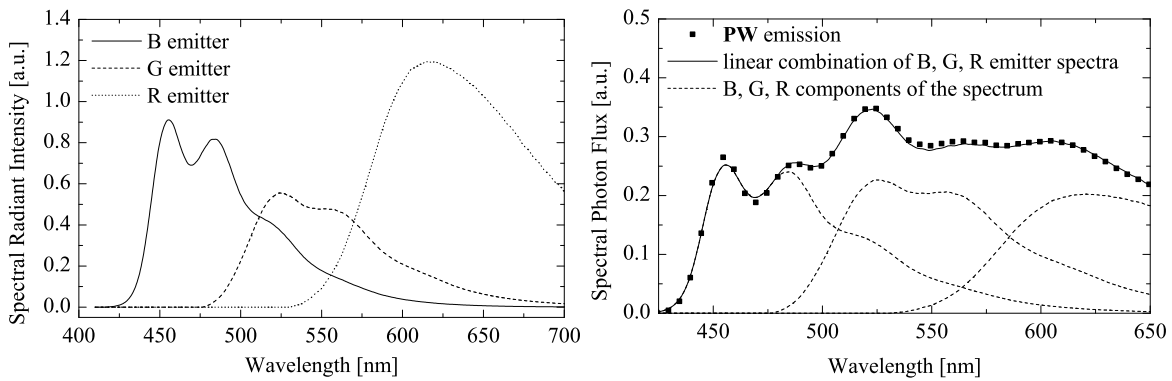


Figure 4.4: Calculated emitter spectra of blue, green and red chromophores (left). Reconstruction of the PW fluorescence spectrum using the calculated emitter spectra. Good fit to the white spectrum is obtained for 36.6% blue, 46.9% green and 16.5% red excited chromophores.

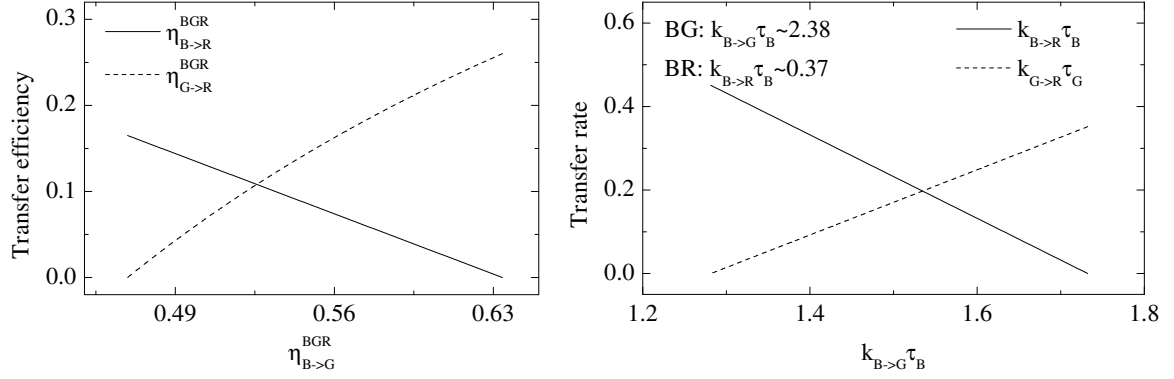


Figure 4.5: Combinations of transfer efficiencies and transfer rates compatible with the observed distribution of blue, green and red emission observed for **PW** emission.

The emission spectrum of **PW** upon excitation of the blue chromophore can be reconstructed by a linear combination $\sum_{X=B,G,R} X F_X$ of the calculated chromophore spectra as shown in figure 4.4. The analysis shows that $\frac{G}{B+G+R} \approx 47\%$ of the excitations end up on the green chromophores, while $\frac{B}{B+G+R} \approx 37\%$ stay with the blue and the remainder of $\frac{R}{B+G+R} \approx 17\%$ is transferred to the red chromophores. Using the above formalism, one can show that the transfer efficiencies

$$\eta_{B \rightarrow X}^{\text{BGR}} = \frac{k_{B \rightarrow X}}{k_{Br} + k_{Bnr} + k_{B \rightarrow G} + k_{B \rightarrow R}} \quad (X=G, R) \quad \text{and} \quad (4.2.10)$$

$$\eta_{G \rightarrow R}^{\text{BGR}} = \frac{k_{G \rightarrow R}}{k_{Gr} + k_{Gnr} + k_{G \rightarrow R}} \quad (4.2.11)$$

obey the equations

$$\eta_{B \rightarrow G}^{\text{BGR}} = \frac{G+R}{B+G+R} - \eta_{B \rightarrow R}^{\text{BGR}} \quad (4.2.12)$$

$$\eta_{G \rightarrow R}^{\text{BGR}} = \frac{\frac{R}{B+G+R} - \eta_{B \rightarrow R}^{\text{BGR}}}{\frac{G+R}{B+G+R} - \eta_{B \rightarrow R}^{\text{BGR}}} \quad (4.2.13)$$

From these, the transfer rates can be calculated as

$$k_{B \rightarrow G} = \tau_B^{-1} \eta_{B \rightarrow G}^{\text{BGR}} (1 - \eta_{B \rightarrow G}^{\text{BGR}} - \eta_{B \rightarrow R}^{\text{BGR}})^{-1} \quad (4.2.14)$$

$$k_{B \rightarrow R} = \tau_B^{-1} \eta_{B \rightarrow R}^{\text{BGR}} (1 - \eta_{B \rightarrow G}^{\text{BGR}} - \eta_{B \rightarrow R}^{\text{BGR}})^{-1} \quad (4.2.15)$$

$$k_{G \rightarrow R} = \tau_G^{-1} \eta_{G \rightarrow R}^{\text{BGR}} (1 - \eta_{G \rightarrow R}^{\text{BGR}})^{-1}. \quad (4.2.16)$$

Figure 4.5 shows the transfer rates compatible with the **PW** emission spectrum. It is clear from this figure that the transfer rates compatible with the spectral distribution of **PW** emission are in conflict with those determined for **BG** and **BR** polymers. The amount of energy transfer from green to red chromophores cannot be determined absolutely, but the figure shows that it competes with the blue→red energy transfer. Anni et al. [129] studied similar copolymers by means of time-resolved fluorescence measurements. Proper integration of

their results allows to determine average transfer rates valid for steady-state spectroscopy. This yields $k_{B \rightarrow G} \tau_B = 0.32$, $k_{B \rightarrow R} \tau_B = 0.06$ and $k_{G \rightarrow R} \tau_G = 0.22$. The B→G transfer rate is much lower than for the polymer studied here and, contrary to what is reflected in figure 4.2, direct and indirect (via energy transfer) excitation of the green chromophores has comparable efficiency.

Energy transfer in disordered systems has been intensely discussed by Förster [130], Eisenthal and Siegel [131], Powell and Kepler [132] and Powell and Soos [133]. The main result is that for energy transfer from isolated donors to spatially distributed acceptor sites, k_{FT} varies with time since short-range transfers occurs on a much faster timescale than long-range transfer. The corresponding transfer efficiency is

$$\eta_{FT} = \sqrt{\pi} x \exp(x^2) [1 - \operatorname{erf}(x)], \quad (4.2.17)$$

where $x = \frac{4}{6} \pi^{3/2} N_A R_0^3$ corresponds to the amount of acceptor molecules within a distance of R_0 from the donor. In case of efficient donor-donor homotransfer, i.e. exciton diffusion, the transfer rate to acceptors is limited by diffusion of donor excitons to acceptor sites. Using the pure donor decay rate $k_D = k_{D,r} + k_{D,nr}$ and $y = 4N_A R_A^2 \sqrt{\pi D} (k_D + 4\pi D R_A N_A)^{-1/2}$,

$$\eta_{FT} = \frac{4\pi D R_A N_A + k_D \sqrt{\pi} y \exp(y^2) [1 - \operatorname{erf}(y)]}{k_D + 4\pi D R_A N_A}, \quad (4.2.18)$$

as can be calculated from the time dependence of the donor emission given by Powell et al. [133]. Here R_A is the effective trapping radius of the acceptor sites, D is the exciton diffusion constant and $4\pi D R_A N_A$ is the diffusion limited rate of donor excitations reaching a distance R_A of the acceptor. Figure 4.6 shows the application of these two models to the energy transfer observed in **BG** and **BR**. Using an acceptor density of $N_A = 5 \times 10^{23} \text{ m}^{-3}$ and $\eta_{B \rightarrow G} = 0.704$, the Förster radius for blue-green transfer is $R_0 = 8 \text{ nm}$. This value is significantly higher than those typically found for efficient donor-acceptor transfer. [129, 134] This deviation is attributed to diffusion of the excitons along the polymer backbone which leads to enhanced transfer rates as pointed out by Becker et al. [135]. For blue-red energy transfer, R_0 -values are expected to be much smaller due to the reduced spectral overlap. Figure 4.6 (right) shows the application of equation (4.2.18), assuming that blue excitons have to diffuse to red chromophores before efficient transfer occurs. Using $\eta_{B \rightarrow R} = 0.27$ as determined above for **BR** and a typical chromophore size $R_A = 1 \text{ nm}$, the exciton diffusion length is calculated as $\lambda = 8 \text{ nm}$ using the diffusion coefficient $D = k_D \lambda^2$. The energy transfer rates are not studied in greater detail here, since in what follows the main focus will be on the ratio r_{RET} of red and blue/green emission due to resonant energy transfer,

$$r_{RET} := \left(\frac{R}{B + G} \right)_{RET} = \frac{\eta_{B \rightarrow R, total}^{BGR}}{1 - \eta_{B \rightarrow R, total}^{BGR}}, \quad (4.2.19)$$

which is uniquely defined by the total transfer efficiency $\eta_{B \rightarrow R, total}^{BGR} = \eta_{B \rightarrow R}^{BGR} + \eta_{B \rightarrow G}^{BGR} \eta_{G \rightarrow R}^{BGR}$ from blue and green to red chromophores. Using the formalism discussed above, $r_{RET} \approx 0.20$ is readily determined by fitting with a linear combination of the chromophore spectra.

Both models for energy transfer discussed above feature a roughly linear concentration dependence of the transfer efficiency when evaluated to lowest order in acceptor concentration. For the polymer studied, concentration of the red chromophore was varied by blending

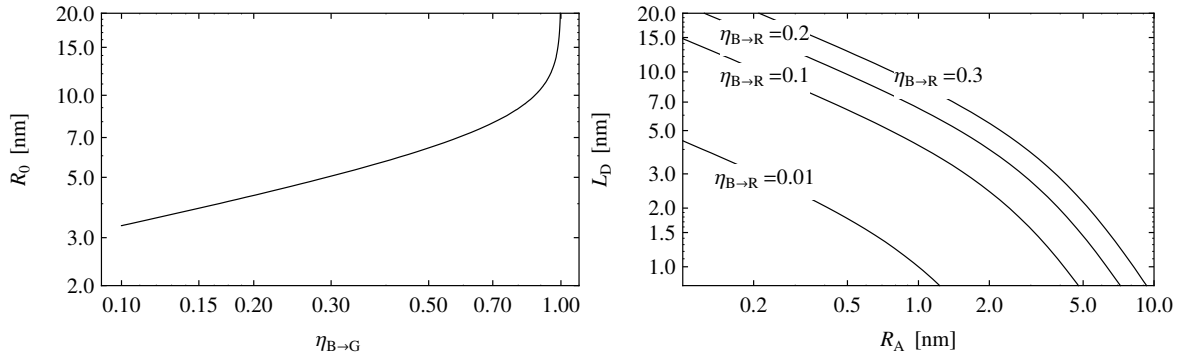


Figure 4.6: Left: Förster radius R_0 plotted against the transfer efficiency $\eta_{B \rightarrow G}$ according to equation (4.2.17), using $N_A = 5 \times 10^{23} \text{ m}^{-3}$. Right: Diffusion length $L_D = \sqrt{\tau D}$ for blue excitons plotted against the transfer radius R_A for diffusion-controlled B \rightarrow R energy transfer according to equation (4.2.18), assuming $\tau = 1 \text{ ns}$.

PW and **BG**, see figure 4.7. $R/(B+G)$ decreases as the concentration $c_{\text{red,rel.}}$ of red chromophores relative to its value in **PW** is lowered. When plotted on a double-logarithmic scale, r_{RET} is approximately linear in $c_{\text{red,rel.}}$, as expected from equation (4.2.19) for small values of $\eta_{B \rightarrow R, \text{total}}^{\text{BGR}} \propto c_{\text{red,rel.}}$. Deviations from this occur at $c_{\text{red,rel.}} = 0.1$: Fitting of the red emission becomes increasingly difficult due to the spectral overlap with the green chromophore's emission.

Due to film thicknesses of less than 100 nm, OLEDs are usually operated under conditions of significant electric field strengths. Excitonic molecular states are known to destabilize and dissociate into charge transfer or bipolaronic states under these conditions. This ultimately leads to modifications of the fluorescence quantum efficiency and since multiple type of chromophores are present in **PW**, this may impact the emission spectrum and alter $R/(B+G)$. Photoluminescence excited at 385 nm was collected in reflection geometry from encapsulated OLED devices of structure glass/ITO/PEDOT:PSS/**BR**(80 nm)/CsF/Al under applied reverse bias voltages of up to 20 V, see figure 4.8. Optical excitation and the collection of photoluminescence from the polymer film was done through the glass substrate. Under reverse bias, the PEDOT:PSS anode (the CsF/Al cathode) was biased negative (positive) and current densities remained low compared to forward bias conditions. At an external bias of 10 V, the internal field across the polymer layer was approximately $1.5 \times 10^8 \text{ V/m}$ taking into account the typical built-in potential of $\sim 2.1 \text{ V}$ due to the electrode work functions as estimated from the turn-on voltage of the device. The photoluminescence was reduced by 45% at this field strength. Following the model proposed by Arkhipov et al. [136], this is attributed to a dissociation of excitons into geminate charge pairs which are stabilized by the applied electric field. The suggested field dependence of the quenching parameter $Q(E) = L(0) - L(E)/L(0)$ should in this case be roughly proportional to E^2 at low fields and saturate at high fields, which is also observed for the devices studied here, see figure 4.8. Due to non-vanishing charge injection at the electrodes, this could also be partly caused by charge-induced exciton quenching, although this would be somewhat surprising at the expected low charge densities. No changes whatsoever could be observed for the R/B emission

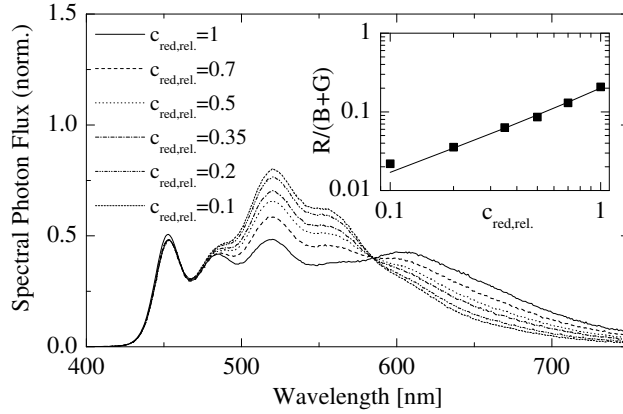


Figure 4.7: Emission spectra for varying red chromophore concentrations $c_{\text{red,rel.}}$, relative to c_{red} of PW after excitation at 385 nm. Spectra are normalized to the integrated emission and were collected at a spectral bandwidth of 1 nm. The inset shows that the emission ratio $R/(B+G)$ is approximately linear in the red concentration as expected for energy transfer in disordered systems. The solid line was calculated according to equation (4.2.19) assuming $\eta_{\text{B} \rightarrow \text{R}, \text{total}}^{\text{BGR}} \propto c_{\text{red,rel.}}$.

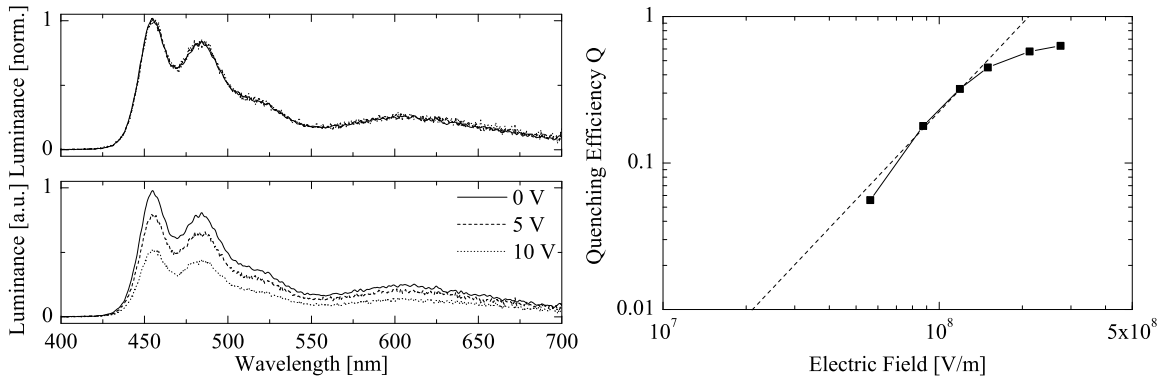


Figure 4.8: Left: Photoluminescence spectra (not corrected for the spectral response of the detector) measured on a BR OLED structure under 385 nm excitation wavelength. The polymer layer thickness was 80 nm and luminance was reduced by $\sim 45\%$ when reverse-biased with 10 V electrical potential (bottom left). No alteration of the normalized spectra could be observed, though (top left). Right: Field dependence of the quenching efficiency Q in double-logarithmic representation. The dashed line has a slope of 2, i.e. it corresponds to $Q \propto E^2$.

ratio, and similar was found for the G/B ratio measured for **BG** OLEDs (not shown).

The results described so far show that under conditions of sufficiently low charge densities, the $R/(B+G)$ emission color ratio is uniquely determined by the resonant energy transfer properties of the chromophores. Balanced white emission from **PW** is observed under photoexcitation of only the blue chromophores although very low concentrations of green and red chromophores are employed. Any deviation from the emission spectra observed under photoexcitation for the electrically driven devices is thus attributed to direct trapping of positive and negative charge carriers by the chromophores. This is discussed in the next section.

4.3 Charge Transport and Deep Trapping

Time-of-flight photocurrent experiments* were conducted for **PB**, **BG**, **BR** and **PW** polymer films of varying thicknesses between 1.2 μm and 22 μm . Details of the experimental procedure were given in chapter 2.2, also see appendix D. In terms of charge transport properties, **PB** represents the most simple polymer, featuring fast electron transport and slow but non-dispersive hole transport. Charge transport in **PB** has already been discussed in chapter 2.2. The specific role of the chromophores in determining the charge transport properties is assessed by comparing TOF results for **PB** with those for **BG** and **PW** over a range of temperatures between 300 K and 380 K, see figure 4.9. Table 4.1 summarizes the results of an analysis of these mobilities in terms of the Gaussian disorder model discussed in chapter 1.1. As a simple approach to understand the effects of potentially charge trapping chromophores, consider the transport to be well characterized by a single transport level with density of states (DOS) N_0 . The introduction of trap states of depth ε_T and density N_T reduces the effective mobility to

$$\mu_{\text{eff}} = \frac{n_e \mu}{n_e + n_T} = \frac{\mu_e}{1 + \frac{N_T}{N_0} \exp\left(\frac{\varepsilon_T}{k_B T}\right)} \quad (4.3.1)$$

if trapping and detrapping times are much smaller than t_{tr} (*shallow traps*). In what follows, only trapping of electrons is considered, where n_e and n_T are the densities of free and trapped carriers, respectively. If the detrapping times are on the order of t_{tr} (*deep traps*), no equilibrium is achieved during the transit time. This will usually lead to a continuously degrading current transient by which the arrival time t_{tr} of charges at the counterelectrode is difficult to define.

The role of the green chromophore is discussed first. Figure 4.9 shows the approximate energy levels for the highest occupied and lowest unoccupied molecular orbitals of the constituent moieties of **PW** and its model copolymers determined by cyclic voltammetry by Gather et al. [48]. From these results it is obvious that the green chromophore should not constitute a trapping site for hole transport and only a weak trap for electrons, which are supposed to move via the backbone and the blue chromophores. The blue chromophore LUMO level was not determined from CV directly but should be above that of the backbone

*The author is indebted to Andriy Kuksov and Dennis Plüschke (then both with the University of Potsdam) for carrying out most of the time-of-flight experiments reported in this section.

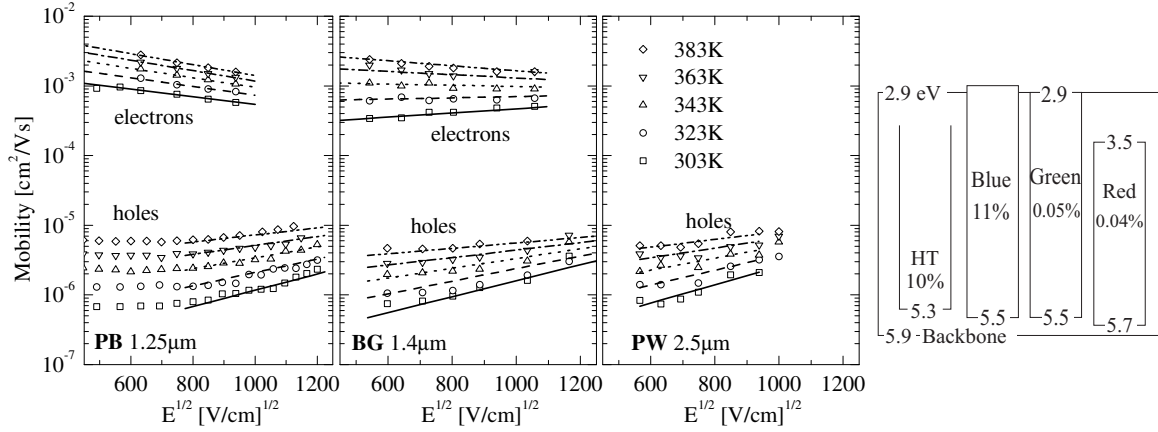


Figure 4.9: Left: Field dependence of electron and hole mobilities for the polymers **PB**, **BG** and **PW**. The straight lines result from the Gaussian disorder model with parameters as given in table 4.1. Right: Energy levels for the highest occupied and lowest unoccupied molecular orbitals of **PW** as published in [48]. The LUMO level for the blue chromophore was estimated from the HOMO level assuming an optical band gap of 2.8 eV.

	μ_0 [cm ² /Vs]	C_0 [10 ⁻⁴ (cm/V) ^{1/2}]	σ [meV]	Σ	$\mu(E=0)$ [cm ² /Vs]
electrons					
PB	0.10	1.6	78	4.1	1.7×10^{-3}
BG	0.38	2.4	106	3.7	2.1×10^{-4}
BR	<i>transit time not resolved</i>				
PW	<i>transit time not resolved</i>				
holes					
PB	5.8×10^{-4}	2.0	117	2.6	6.4×10^{-8}
BG	3.4×10^{-4}	2.6	111	2.8	9.7×10^{-8}
PW	3.1×10^{-4}	2.7	110	2.5	9.9×10^{-8}

Table 4.1: Gaussian disorder model parameters for electron and hole transport in the polymers **PB**, **BG** and **PW**. Current transients for electron transport in **BR** and **PW** were highly dispersive ($\alpha \approx 0$) and no transit time could be determined.

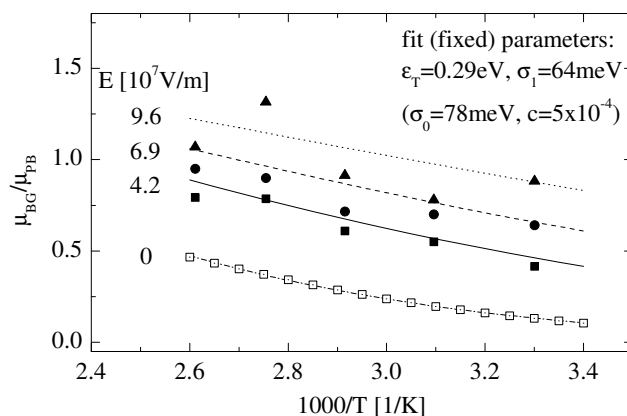


Figure 4.10: Influence of the green chromophores on the electron mobility determined by TOF experiments. The measured mobility ratio for **BG** and **PB** between between 300 K and 380 K is shown at electric fields of 4.2×10^7 V/m (solid squares), 6.9×10^7 V/m (circles) and 9.6×10^7 V/m (triangles). Solid, dashed and dotted lines show the mobility ratio calculated from the Gaussian disorder parameters of table 4.1. The dot-dashed line gives the extrapolation to zero applied field as calculated from the disorder model. The results of fitting equation (4.3.2) to this data is shown as open squares.

as estimated from the HOMO level and the optical bandgap. Only few analytic theories of charge transport in disordered media have been developed for the situation of Gaussian distributed hopping site energies, among these the effective medium approximation (*EMA*) theory has been most successful.[137] Fishchuk et al. [138] developed a formalism that allows to calculate the relaxed charge mobility for a situation in which both the transport states and the trap states of depth ε_T are distributed in energy according to Gaussian distributions of widths $\sigma_0 \gg k_B T$ and $\sigma_1 \gg k_B T$, respectively. The full result is too lengthy to be included here, but within the approximation of low electric fields and $\varepsilon_T > \sigma_0$, the normalized electron mobility can be expressed as

$$\frac{\mu_e(c_{\text{rel.}})}{\mu_e(0)} = \frac{1 + c_{\text{rel.}}^2 \exp\left(\frac{\varepsilon_T}{k_B T}\right)}{1 + c_{\text{rel.}} \exp\left[\frac{\varepsilon_T}{k_B T} + \frac{1}{2} \left(\frac{\sigma_0}{k_B T}\right)^2 \left(\frac{\sigma_1^2}{\sigma_0^2} - 1\right)\right]}, \quad (4.3.2)$$

assuming a concentration $c_{\text{rel.}} = N_T/N_0$ of the traps (green chromophores) relative to the density of transport sites which is taken to be approximately equal to the monomer density. From the disorder analysis of charge transport in **PB**, $\sigma_0 = 78$ meV is known while the relative monomer concentration of the green chromophores is $c_{\text{rel.}} = 5 \times 10^{-4}$. The Gaussian disorder model is then used to calculate the ratio of electron mobilities $\mu_{\text{BG}}/\mu_{\text{PB}}$ extrapolated to zero electric field, see figure 4.10. A nonlinear fit of equation (4.3.2) to this data was used to determine $E_T = 0.29$ eV and $\sigma_1 = 64$ meV. The trap depth thus determined is at first sight inconsistent with the notion of electron transport by the backbone since no trapping of electrons would be expected from the backbone to the green LUMO, both having very similar energies. This reasoning is solely based on the CV data, where in-house quantum chemical calculations on model trimers provided by Merck KGaA indicate that the backbone LUMO level is 0.25 eV *above* that of the blue chromophore and 0.32 eV above that of the green chro-

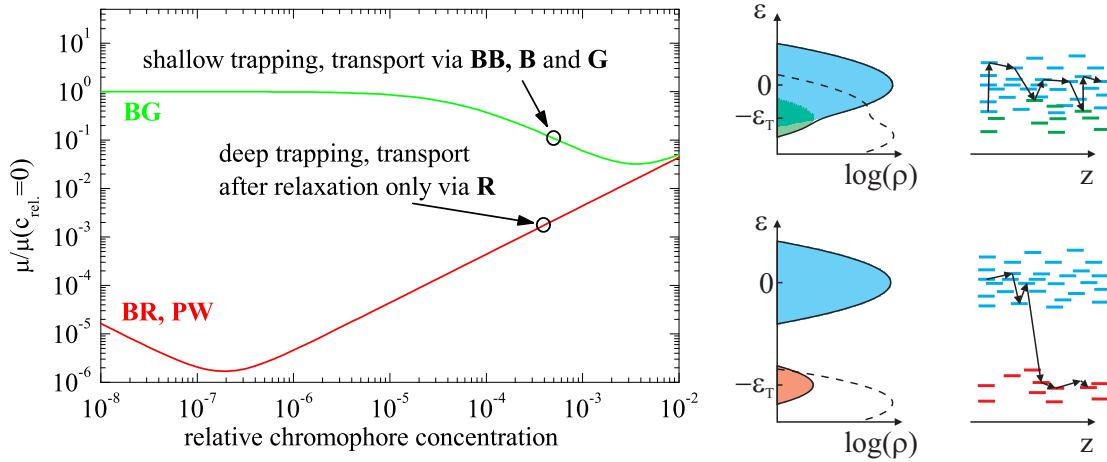


Figure 4.11: Left: Concentration dependence of relaxed charge mobility in presence of green (BG) and red (BR and PW) chromophores as calculated from the EMA theory. Right: Sketch of the energetic distribution of the density of states ρ for transport and trapping levels as well as the normalized density of occupied states (dashed) in thermal equilibrium. Electron transport in BG proceeds via intermediate hopping visits on green chromophores. In contrast to this, the red chromophore is a strong trap and electrons cannot reach the transport manifold after their energetic relaxation.

mophore. There is thus considerable ambiguity concerning the LUMO level of the backbone, but the results presented here indicate that the actual position is higher than estimated from the CV results. The energetic disorder of the trap level is comparable to that of the transport states, which is not surprising since the disorder arises from fluctuations of the local chemical environment, which should be similar for backbone and chromophore monomers. Figure 4.11 shows the concentration dependence of electron mobility calculated from equation (4.3.2) using the determined parameters. Electron mobility is predicted to decrease monotonously with the concentration of the green chromophore up to a critical concentration of $c_{\text{crit.}} = \exp(-\varepsilon_T/k_B T) \approx 3.7 \times 10^{-3}$. At $c_{\text{rel.}} < c_{\text{crit.}}$, electrons are mainly transported by hopping between the backbone and blue chromophores since only small amounts of activation energy are needed after visiting a green chromophore. At $c_{\text{rel.}} = 5 \times 10^{-4}$, the green chromophore is thus considered a shallow trap in terms of the EMA theory. The expansion of equation (4.3.2) to non-vanishing electric fields can be found in [138]. For $E < 1 \times 10^8$ V/m no significant change in $\mu_{\text{BG}}/\mu_{\text{PB}}$ is predicted, which is in contrast to the measurement results shown in figure 4.10. This is attributed to the moderately dispersive electron transport found in TOF measurements: At finite electric fields, the charge carriers do not completely relax towards their equilibrium mobility before reaching the counterelectrode. Extrapolation to zero field yields an approximation of the relaxed mobility and is thus much better suited for an analysis in terms of the EMA theory applied here.

While charge transport in presence of the green chromophore can thus be well understood from the EMA theory and only slightly alters the electron transport, the situation is much more complex for the deep trap presented by the red chromophores. CV results of figure 4.9 predict ε_T in the range of 0.8 eV to 1.0 eV for electron transport, while hole transport should not be affected seriously. This is consistent with the results of TOF measurements conducted

on **BR** and **PW** polymers: While the hole transport properties are very similar to those of **PB** and **BG**, the electron transit time could not be resolved from photocurrent transients even on a double logarithmic representation. The observed transients decayed as $t^{-1+\alpha}$ with $\alpha = 0 \dots 0.3$, indicating a highly dispersive transport in the context of the Scher/Montroll analysis. Figure 4.11 shows the prediction of the concentration dependence in the context of the EMA theory, using $\sigma_1 = 64$ meV as determined for the green chromophores and $\varepsilon_T = 0.8$ eV. The relative concentration $c_{\text{rel.}} = 4 \times 10^{-4}$ of red chromophores is well beyond $c_{\text{crit.}} = 2 \times 10^{-7}$ indicating that after energetic relaxation, electrons can only move by hopping between isolated red chromophores. The absolute magnitude of the predicted mobility in this regime is not central to the EMA theory and is thus not considered any further. The EMA theory deals with the non-dispersive, relaxed equilibrium situation only and thus cannot cover the processes occurring during electron transit in TOF experiments in the presence of deep traps. Although the electron transport thus cannot be assessed directly, it is conceivable that electron transit times in polymer films of less than 100 nm thickness as used for OLEDs are very similar to those determined for **PB** and **BG**, since at the low concentration of traps most electrons will be able to cross the film without visiting a red chromophore. During continuous device operation, a significant amount of charges would still be trapped and accumulated in the traps and is thus lost for charge transport, contributing mainly to the space charge field. The red chromophores will ultimately determine the spectral emission properties of **BR** and **PW** under electrical excitation, since electrons cannot thermally detrapp from these states and will eventually recombine with holes leading to a strong red emission contribution.

In order to account for these electron trapping effects and obtain insight into their role in determining the device emission spectrum, an effective rate equation approach is used in the following section. The trap depth $\varepsilon_T \gg \sigma_0, \sigma_1$ is much larger than the typical width of the energetic disorder σ_0 and σ_1 of host and trap states. This motivates an approximate treatment of trapping by replacing the trapping and detrapping time distributions with effective first-order trapping and detrapping rate constants and treating the transport solely in terms of free electrons (with charge mobility as determined for **BG**) and trapped electrons. The continuum model described in appendix A is extended here to calculate the time dynamics of trap occupation, setting all spatial derivatives to zero. This effectively collapses the model into a description of the effective emission zone only, which contributes most strongly to the device emission. The density n_T of occupied electron traps thus has the time dynamics

$$\frac{\partial}{\partial t} n_T = n_e \gamma_T (N_T - n_T) - \gamma_D n_T (N_0 - n_e) - \frac{e\mu_h}{\varepsilon\varepsilon_0} n_h n_T, \quad (4.3.3)$$

where N_T is the total density of traps and γ_T (γ_D) is the trapping (detrapping) coefficient. The right-hand side of the continuity equation (A.2) is complemented by charge trapping and becomes

$$\frac{\partial n_e}{\partial t} = -\frac{e\mu_{\text{eff}}}{\varepsilon\varepsilon_0} n_e n_h - n_e \gamma_T (N_T - n_T) + \gamma_D n_T (N_0 - n_e) \quad (4.3.4)$$

$$\frac{\partial n_h}{\partial t} = -\frac{e\mu_{\text{eff}}}{\varepsilon\varepsilon_0} n_e n_h - \frac{e\mu_h}{\varepsilon\varepsilon_0} n_T n_h, \quad (4.3.5)$$

accounting for a Langevin-type bimolecular recombination of mobile holes with the trapped electrons. As discussed in chapter 1.1, time-of-flight photocurrent transients usually display a large amount of dispersion or ‘apparent diffusivity’. As pointed out by Albrecht et

al. [139], Langevin-type recombination of charge carriers consistent with $D/\mu = k_B T/e$ is to be expected independent of disorder, i.e. although the apparent diffusivity might exceed this value by three orders of magnitude. The steady state occupation of traps follows from $\partial n_T/\partial t = 0$:

$$n_T = N_T \left(1 + \frac{\gamma_D}{\gamma_T} \left(\frac{N_0}{n_e} - 1 \right) + \frac{e\mu_h n_h}{\epsilon\epsilon_0 \gamma_T n_e} \right)^{-1}. \quad (4.3.6)$$

With the usual definition of the quasi Fermi levels $\epsilon_{F,e}$ and $\epsilon_{F,T}$ by

$$n_e = \frac{N_0}{1 + \exp\left(\frac{\epsilon_{LUMO} - \epsilon_{F,e}}{k_B T}\right)} \quad (4.3.7)$$

$$n_T = \frac{N_T}{1 + \exp\left(\frac{\epsilon_{LUMO} - \epsilon_T - \epsilon_{F,T}}{k_B T}\right)}, \quad (4.3.8)$$

detailed balancing between trapping and detrapping requires

$$\frac{\gamma_D}{\gamma_T} = \frac{n_e(N_T - n_T)}{n_T(N_0 - n_e)} = \exp\left(\frac{-\epsilon_T}{k_B T}\right) \quad (4.3.9)$$

if thermodynamic equilibrium $\epsilon_{F,e} = \epsilon_{F,T}$ prevails and detrapping by recombination of holes is neglected. [20, 140] For deep traps $\epsilon_T \sim 1$ eV, thermal detrapping can thus be neglected. It is assumed that this is not strongly violated under conditions of current flow, moderate electric fields and detrapping by recombination with holes. Similar assumption have been made by Staudigel et al. [141] and Lee et al. [142] for numerical simulations of light-emitting diodes.

Finally, two models for the trapping coefficient γ_T are discussed. For band-type transport and mean free paths $\lambda \gg a$ much larger than the intersite distance a , it is usually expressed as $\gamma_T = \sigma_T v$, where σ_T is the trapping cross section and $v = \mu E + v_{\text{thermal}}$ is the sum of charge drift speed and thermal velocity $v_{\text{thermal}} = \sqrt{k_B T/m_e^*}$. This is obviously incorrect for hopping-type charge transport. Diffusion-limited reactions have been treated in detail by Waite [43, 143, 144], with the result $\gamma_T = 4\pi r_0 D_e$ where $r_0 = (\sigma_T/\pi)^{1/2}$ is the trapping radius and $D_e = \delta\mu_e k_B T/e$ the electron diffusion coefficient ($\delta \sim 1$). Here, it is assumed that additional charge trapping by drift occurs and that this contribution follows $\gamma_T = \sigma_T \mu_e E$, where not necessarily $\sigma_T = \pi r_0^2$ since diffusion and drift might occur along different pathways. Thus,

$$\gamma_T = \sigma_T \mu_e (E + E_{\text{diff}}) \quad (4.3.10)$$

where $E_{\text{diff}} = 4\pi r_0 k_B T \delta / (e\sigma_T)$ (model I). An alternative is to replace the disordered hopping system by an effective ordered medium and consider the random walk of electrons hopping at a frequency ν_0 in a regular lattice of transport sites of intersite distance a where not necessarily $a = N_0^{-1/3}$, since hopping might effectively occur on some subset of the sites determined from the monomer density or it might involve delocalized states spanning multiple monomers. This replacement is similar to the approach used for EMA theories. [145] Traps are assumed to occupy a single lattice site, thus to have an electron wavefunction localization comparable to the host sites. For a random walk on this lattice, the positional variance $\sigma = a\sqrt{\nu_0 t}$ after time t relates to the diffusion coefficient D_e of the corresponding Brownian motion by $\sigma = \sqrt{Z D_e t}$. The corresponding diffusion coefficient is $D_e = \nu_0 a^2 / Z$ where $Z = 6$

in case of a three-dimensional lattice. According to Montrol et al. [146], the number of distinct lattice sites S_m visited within m carrier hops is $S_m \approx b^{-1}m$ ($S_m = (8m/\pi)^{1/2}$) for 3D cubic lattices (1D lattices), where $b \approx 1.52$. The average number m_T of hops needed to trap a carrier follows from $S_{m_T} = N_0(N_T - n_T)^{-1}$, while the trapping rate per electron is $v_0 m_T^{-1}$. The resulting trapping coefficient is $\gamma_T = ZD_e/(a^2 b N_0)$ ($\gamma_T = 8ZD_e(N_T - n_T)/(\pi a^2 N_0^2)$) for 3D (1D) diffusion. Note that γ_T is independent of N_T and n_T only for three-dimensional diffusion. Electrons drifting at a speed $\mu_e E$ in the electric field E visit new lattice sites at a rate of $\mu_e E/a'$, corresponding to the trapping coefficient $\gamma_T = \mu_e E/(a' N_0)$. As before, $a \sim a'$ may differ if the charges probe different subsets of the lattice during diffusion and drift. The total trapping coefficient is thus expected to be

$$\gamma_T = \frac{\mu_e}{a' N_0} (E + E_{\text{diff}}) \quad (4.3.11)$$

where $E_{\text{diff}} = \frac{Zk_B T \delta a'}{a^2 b e}$ ($E_{\text{diff}} = \frac{8Zk_B T \delta (N_T - n_T) a'}{\pi a^2 e N_0}$) for 3D (1D) lattices (model II). Random walks on a 3D lattice as treated here are thus very similar to the Waite results for diffusion-limited reactions, with small differences arising from the treatment of trap size and trapping cross sections.

4.4 Color Balance in Electroluminescence

It is a well established concept that the emitting species generated by the recombination of uncorrelated charges in homopolymers are the same as those generated by photoexcitation. This does not necessarily imply that emission spectra recorded under conditions of photoexcitation and electrical excitation are always identical. As shown above, green and red chromophores are available at low concentrations only and their efficient photoexcitation occurs indirectly by energy transfer from blue chromophores. Mobile charges, on the other hand, are able to probe a large amount of transport sites prior to recombination or extraction at the electrodes. Sites of sufficiently low energy are thus able to trap large amounts of charges despite their low concentrations. This can have significant impact on the electroluminescence spectra of white-emitting copolymers as compared to their photoluminescence spectra and opens up the possibility of obtaining insight into the charge trapping dynamics directly from spectral measurements.

The role of charge trapping in determining the electroluminescence emission spectrum was assessed by measurements on encapsulated OLED devices with the structure glass / ITO / PEDOT:PSS / **PW** / CsF / Al under varying driving and environmental conditions. Figure 4.12 shows the electroluminescence spectra under either constant temperature, electric field or current density, where the remaining parameters were varied. While the green/blue emission ratio is stable under varying driving conditions, the red/blue ratio could be tuned over a wide range by either changing the temperature at constant current densities or by variation of the driving voltage at constant temperature. Table 4.2 summarizes the observations and suggests that the red/blue emission ratio is either directly or indirectly determined by the electric field applied to the OLED or that two concurring processes compensate for each other, resulting in a constant red/blue ratio under constant electric field conditions. This was already investigated by Gather et al. [48] for the same polymer as studied here.

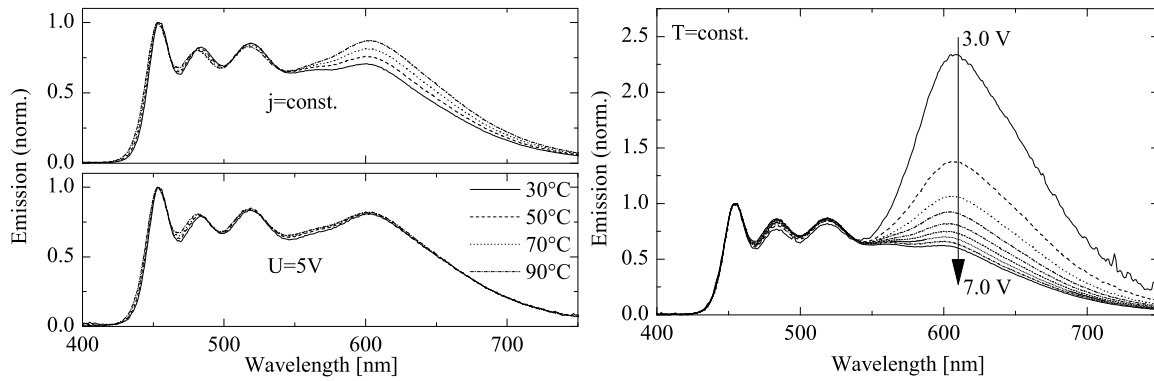


Figure 4.12: Electroluminescence spectra of **PW** OLEDs under varying conditions of temperature (left) and applied voltage (right). Each figure shows results under conditions of the indicated parameter held constant and corresponds to one row of table 4.2. Significant impact of the driving voltage on the red / blue emission ratio is observed, the spectrum being dominated by red emission near the onset voltage. For the voltage dependence, applied voltages of 3.0 V to 7.0 V are shown in steps of 0.5 V.

temperature	electric field	current density	red/blue ratio
const.	↑	↑	↓
↑	const.	↑	const.
↑	↓	const.	↑

Table 4.2: General observations of the red/blue ratio of **PW** OLEDs and its dependence on the external parameters temperature, electric field and current density. Increasing values are marked ↑, decreasing values by ↓.

	d/l_T	$Dd^2/l_T^2\mu_e$ [V]	U_{bi} [V]	D/μ_e [V]
Gather et al.	0.30 ± 0.03	1.19 ± 0.03	2.329 ± 0.002	13 ± 3
this work	0.11 ± 0.01	0.46 ± 0.03	2.51 ± 0.03	38 ± 7

Table 4.3: Results of fitting equation (4.4.2) to the data shown in figure 4.13. Due to the nonlinear fitting procedure, the stated uncertainties only represent lower limits to the errors.

They proposed an explanation for the voltage-dependent color shifts based on what will herein be referred to as *kinetic* arguments. Electrons were either to be trapped (leading to red emission) during drift through the polymer layer or, upon reaching the opposite electrode, would account for blue/green emission. The ratio of red (*trap*) emission S_T to blue and green (*host*) emission rates $S_T/S \propto R/(B+G)$ was thus determined by the ratio between a trapping rate constant k_T and a transit rate constant k_{transit} via

$$\frac{S_T}{S} = \frac{k_T}{k_{\text{transit}}} = \frac{k_{\text{drift}} + k_{\text{diff}}}{k_{\text{transit}}}. \quad (4.4.1)$$

Electrons that could not be trapped during their time of flight $1/k_{\text{transit}} = \mu_e E/d$ through the polymer layer of thickness d at an electric field E thus always lead to blue and green emission. The trapping rate $k_T = k_{\text{drift}} + k_{\text{diff}}$ was decomposed into drift and diffusion terms. For the electrons, the mean free path l_T before being trapped by a red chromophore was calculated by $l_T = (\sigma_T N_T)^{-1}$ from the trapping cross-section σ_T and the trap density N_T . Electrons drifting in the electric field would encounter a trap after an average time of $k_{\text{drift}}^{-1} = \tau_T = l_T/\mu_e E$. To estimate the diffusion-driven trapping, it is observed that a diffusing charge of diffusivity D will propagate a mean distance of $l = \sqrt{Dt}$ during time t . Equating this with the mean free path l_T , the diffusion-controlled trapping rate is $k_{\text{diff}} = D/l_T^2$ and the red/blue ratio is given by

$$\frac{S_T}{S} = \frac{d}{l_T} \left(1 + \frac{D}{l_T \mu_e E} \right) \approx \frac{d}{l_T} \left(1 + \frac{Dd}{l_T \mu_e (U - U_{bi})} \right). \quad (4.4.2)$$

The authors showed that the red/blue ratio determined experimentally features a reciprocal dependence on the driving voltage and concluded that the proposed model is well suited to describe the red/blue emission ratio of **PW**. Figure 4.13 shows the application of this model to the $R/(B+G)$ emission ratio determined from the voltage dependent spectra shown in figure 4.12. The data was fitted with equation (4.4.2), where the free parameters have been d/l_T , $Dd^2/l_T^2\mu_e$ and U_{bi} . Table 4.3 summarizes the results of the nonlinear fitting procedure. Approximate fitting results for the data published in [48] are given in the table for comparison. Assuming $N_T \sim 4 \times 10^{23} \text{ m}^{-3}$ and $\sigma_T \sim 0.1 \dots 10 \text{ nm}^2$, the mean free path of electrons should be on the order of $l_T = 25 \text{ }\mu\text{m} \dots 250 \text{ nm}$, such that the ratios $d/l_T \sim 10^{-1}$ resulting from the fitting procedure are reasonable for polymer layers of $d \sim 10^2 \text{ nm}$ thickness. The resulting values for D/μ_e are much larger than predicted by the Einstein relation $D/\mu = k_B T/e \sim 25 \text{ mV}$. As discussed by Roichman et al. [147], violation of the Einstein relation is expected to some extent due to the Gaussian distribution of transport state energies present in disordered organic semiconductors. Nonetheless, this depends on the charge density and thus cannot be independent of the driving voltage. Also, D/μ calculated by

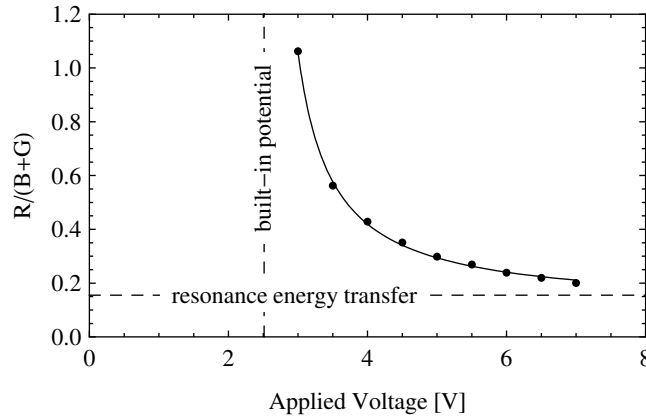


Figure 4.13: The ratio of emission $R/(B+G)$ calculated from the spectra shown in figure 4.12. The solid line is a nonlinear fit according to equation (4.4.2) using the parameters given in table 4.3. The color ratio due to resonance energy transfer as observed under photoexcitation is indicated by a dashed line. The built-in potential obtained from the fitting procedure is larger than what would be expected on basis of the turn-on voltage of the device of approximately 2.3 V.

Roichman et al. for typical charge densities found in OLED devices are much smaller than the values found here.

The explanation of voltage dependent color shifts as discussed above suffers some fundamental shortcomings:

Method of trap/host emission ratio determination: Gather et al. analyzed the red/blue emission ratio as determined from the red and blue peak emission. This introduces an unknown error into the model parameters since the determined red/blue ratios do not represent the ratio of excitations funneled to each chromophore. The emission ratios determined in the present work are extracted from the emission spectra by linear combination of the emitter spectra as discussed in section 4.2. This gives a direct estimate of the ratio of recombinations on each of the chromophores.

Resonant energy transfer: Equation (4.4.2) neglects the blue-red and green-red resonant energy transfer, overestimating the role of charge trapping for the red emission. More correctly, equation (4.4.2) should be modified by

$$\frac{S_T}{S} = \left(\frac{S_T}{S}\right)_{\text{RET}} + \left(\frac{S_T}{S}\right)_{\text{trap}} = r_{\text{RET}} + \frac{d}{l_T} \left(1 + \frac{D}{l_T \mu_e E}\right), \quad (4.4.3)$$

where $r_{\text{RET}} \approx 0.20$ as discussed in section 4.2. The results presented in table 4.3 thus neither allow to determine d/l_T nor D/μ_e .

The influence of temperature: Equation (4.4.2) is based on the assumption that S_T/S is independent of temperature at constant drive voltages. Gather et al. support this by measurements at $U = 5$ V in the temperature range 120 K to 295 K, observing only minor variations. This is not sufficient to support their claim since at this operating voltage the red/blue ratio is close to $(S_T/S)_{\text{RET}}$ and thus dominated by resonant energy

transfer which does not depend on the temperature. Nonetheless, this indicates that temperature-induced mobility changes do not strongly influence the red/blue emission ratio. Although not discussed, their model suggests an indirect temperature dependence since the diffusion constant should be proportional to the temperature. This temperature dependence of the diffusion constant remains true also for the generalized form of the Einstein equation proposed by Roichman et al. [147].

Saturation of the red emitter: Equation (4.4.2) assumes that the red chromophores are only weakly occupied, since their number density is expected to be much higher than that of mobile electrons. In equilibrium, deep charge traps are well known to accumulate significant amounts of immobilized charges which may even outnumber the mobile charge carriers.[142] It should be carefully checked that the occupation of the red emitters stays low during typical bipolar LED operation.

Concentration of charge carriers: The proposed model neglects the role of charge carrier densities. The amount of red emission is directly controlled by the occupation of deep traps, which should depend sensitively on the density of free electrons and holes via trapping and recombination events. Therefore, the red/blue emission ratio cannot be independent of the density of charge carriers, both electrons and holes.

To solve these issues, an alternative approach based on the rate equation model for the effective recombination zone is discussed in the remainder of this section. This will show under which conditions the kinetic results still hold and when deviations have to be expected. The rate equation model for the effective recombination zone has been introduced in section 4.3. In order to couple the two-component charge transport model (host and traps) to the three-component energy transfer calculations of chapter 4.2, the integrated blue and green emission is taken as that of virtual “host” chromophores. It is assumed that direct charge recombination on the green chromophores can be neglected, thus they are only populated via energy transfer from blue. While $\eta_T^T = \eta_R^R$ is the quantum efficiency of trap (red) emission, it can be shown that

$$\eta_H^H = \frac{\eta_B^B(1 - \eta_{B \rightarrow G}^{BG}) + \eta_G^G \eta_{B \rightarrow G}^{BG}(1 - \eta_{B \rightarrow R}^{BGR})}{1 - \eta_{B \rightarrow G}^{BG} \eta_{G \rightarrow R}^{BGR}} \quad (4.4.4)$$

is the corresponding quantum efficiency of the host (blue+green) emission. The total energy transfer efficiency from host to trap becomes $\eta_{H \rightarrow T}^{HT} = \eta_{B \rightarrow R}^{BGR, total}$ as defined by equation (4.2.19). The photon emission rate S from the host (due to recombination of free electrons with free holes) and the photon emission rate S_T from the trapping chromophores (due to recombination of trapped electrons with free holes) thus are calculated from

$$S = (1 - \eta_{H \rightarrow T}^{HT}) \eta_H^H \frac{e(\mu_e + \mu_h)}{\epsilon \epsilon_0} n_e n_h \quad (4.4.5)$$

$$S_T = \frac{\eta_{H \rightarrow T}^{HT}}{1 - \eta_{H \rightarrow T}^{HT}} \frac{\eta_T^T}{\eta_H^H} S + \eta_T^T \frac{e \mu_h}{\epsilon \epsilon_0} n_T n_h, \quad (4.4.6)$$

where the bimolecular recombination of free holes and trapped electrons as described by equation (4.3.5) generates excitons on the charge trapping red chromophores at the rate

$\frac{e\mu_h}{\varepsilon\varepsilon_0}n_hn_T$. The corresponding emission ratio finally becomes

$$\frac{S_T}{S} = \left(\frac{S_T}{S}\right)_{\text{RET}} + \frac{\eta_T^T}{(1 - \eta_{H \rightarrow T}^{\text{HT}})\eta_H^H} \frac{\mu_h}{\mu_e + \mu_h} \frac{N_T}{n_e + (N_0 - n_e) \exp(-\frac{\varepsilon_T}{k_B T}) + \frac{e\mu_h}{\gamma_T \varepsilon \varepsilon_0} n_h}. \quad (4.4.7)$$

In this notation, the ratio of trap and host emission due to energy transfer reads

$$\left(\frac{S_T}{S}\right)_{\text{RET}} = \frac{\eta_{H \rightarrow T}^{\text{HT}} \eta_T^T}{(1 - \eta_{H \rightarrow T}^{\text{HT}})\eta_H^H}. \quad (4.4.8)$$

Note that when experimental emission spectra are fitted by the emitter spectra $f_X \eta_X^X$ as discussed in section 4.2, the determined fitting coefficients B , G , R are proportional to the rate of excitations funneled to each chromophore and

$$r := \frac{R}{B + G} = \frac{S_T}{S} \frac{\eta_H^H}{\eta_T^T}. \quad (4.4.9)$$

This is an important conclusion since it allows to directly compare the analytical model to measurements of the device emission spectra without detailed knowledge of the emitter quantum efficiencies. For **PW**, it is assumed that $n_e \ll N_0$ due to high electron mobilities and low injection efficiency, while $n_e \gg N_0 \exp(-\frac{\varepsilon_T}{k_B T})$ since $\varepsilon_T \sim 1$ eV. The red/blue emission ratio thus reads

$$\frac{R}{B + G} = r_{\text{RET}} + (1 + r_{\text{RET}}) \frac{\mu_h}{\mu_e + \mu_h} \frac{\gamma_T N_T}{\gamma_T n_e + \frac{e\mu_h}{\varepsilon \varepsilon_0} n_h}, \quad (4.4.10)$$

where $r_{\text{RET}} = \eta_{H \rightarrow T}^{\text{HT}} / (1 - \eta_{H \rightarrow T}^{\text{HT}})$. The reduction this ratio due to an increase of the electron density n_e is associated with the saturation rate $\gamma_T n_e$ of the trap's LUMO level. Its reduction due to an increase of the hole density is associated with the recombination rate $e\mu_h n_h / \varepsilon \varepsilon_0$ of trapped electrons with free holes. Both processes lower n_T / n_e and thus the trap/host emission ratio. Equation (4.4.10) cannot be further simplified without sacrificing its generality. Qu et al. [148] used a similar rate equation approach to explain the guest emission of poly(vinylcarbazole) doped with polyphenylene dendrimers. As compared to equation (4.4.10), they did not include electron density nor charge trapping by diffusion. Also, in the approach described here, charge-trapping parameters can potentially be calculated absolutely due to the trap/host emission ratio being linked to the chromophore spectra fitting coefficients B , G , R . Two useful approximations of equation (4.4.10) are discussed.

Assuming $n_T \ll N_T$, equation (4.3.3) is simplified by $N_T - n_T \approx N_T$. It turns out that this is equivalent to $\gamma_T \varepsilon \varepsilon_0 n_e \ll e\mu_h n_h$ in the denominator of equation (4.4.10) such that the electron density can be neglected. As discussed in section 4.3, it is still reasonable to assume $\mu_e \gg \mu_h$, although deep trapping by the red chromophore leads to dispersive charge transport. The trapping coefficient is $\gamma_T = \mu_e (E + E_{\text{diff}}) / (a' N_0)$ from equation (4.3.11) in the random walk approximation. Equation (4.4.10) then becomes

$$\frac{R}{B + G} = r_{\text{RET}} + (1 + r_{\text{RET}}) \frac{\varepsilon \varepsilon_0 N_T}{ea' n_h N_0} (E + E_{\text{diff}}), \quad (4.4.11)$$

which shows that at low trap filling levels, the ratio of trap to host emission is indeed determined by the ratio of thermal to drift motion of the electrons. If the electron density remains

low and hole injection is barrierless (Ohmic injection conditions), the average hole density is $n_h = \frac{3}{2} \frac{\epsilon \epsilon_0 E}{ed}$. Thus, equation (4.4.11) further simplifies to

$$\frac{R}{B+G} = r_{\text{RET}} + (1 + r_{\text{RET}}) \frac{2}{3} c_T \frac{d}{a'} \left(1 + \frac{Za'D_e}{ab} \right), \quad (4.4.12)$$

where $c_T = N_T/N_0$. This result is very similar to equation (4.4.3) and can be compared directly by setting $a = a' = c_T l_T$, resulting in

$$\frac{R}{B+G} = r_{\text{RET}} + (1 + r_{\text{RET}}) \frac{2}{3} \frac{d}{l_T} \left(1 + \frac{ZD_e}{bc_T} \right). \quad (4.4.13)$$

The main difference thus arises from the treatment of diffusion: for equation (4.4.3), diffusion is trap-controlled via $l_T \sim \sqrt{D_e \tau_T}$, where τ_T is some average trapping time. For equation (4.4.13), this is replaced by $a \sim \sqrt{D_e \tau_{\text{hop}}}$ with the trap-free diffusion coefficient $D_e = k_B T \mu_e / e$, intersite (scattering) distance a and average hopping time τ_{hop} . D_e as used in (4.4.3) inevitably drops at rising trap density and is not a well-defined parameter since trapping-detrapping equilibrium is not achieved.

Equations (4.4.10) and (4.4.11) represent a more general model of changes in the emission spectrum related to charge trapping. They account for the effects of charge density and simplify to purely kinetic considerations under adequate assumptions for the charge density. As to which extent the charge density determines the emission color in the white-light emitting devices considered here is discussed in the next section.

4.5 Charge Density Effects on the Emission Color

Light-emitting devices of structure ITO/PEDOT:PSS/polymer/CsF/Al were fabricated comprising various concentrations of the red emitter in the active polymer layer. This was achieved by spincoating from blends of **PW** and **BG** which are, apart from their red chromophore content, chemically nearly identical and thus easily mixed in arbitrary ratios. Details of the preparation procedure were given in section 4.2. The effective concentrations of the red chromophore thus achieved was $c_{\text{red,rel.}} = 1, 0.5, 0.2, 0.1$ relative to the monomer concentration $c_{\text{red}} = 4 \times 10^{-4}$ of **PW**. The film thickness was not optimized separately for each device and varied between 55 nm and 80 nm. Electroluminescence spectra were measured over the whole range of typical operating voltages. The emission spectra were recorded using a Fluorolog spectrometer with photon-counting detector operated at dark count rates of less than 10 photons/s. The spectrally integrated photon rate spanned eight orders of magnitude and spectra were recorded well down to operating voltages near to the built-in potential. The spectra were fitted by a linear combination of the emitter spectra of figure 4.4 where the fitting coefficients were B, G, R for the blue, green and red component, respectively. Figure 4.14 shows the voltage dependence of the red/blue color ratio $R/(B+G)$ calculated from these. At an electric field of 3.5×10^7 V/m (region II), the concentration dependence of $R/(B+G)$ is linear. Apart from increasingly large fitting errors for the lowest concentration of red emitters, the color ratio reproduces the results obtained by the photoluminescence measurements discussed in section 4.2. Contrary to this, the red/blue ratio rises by almost

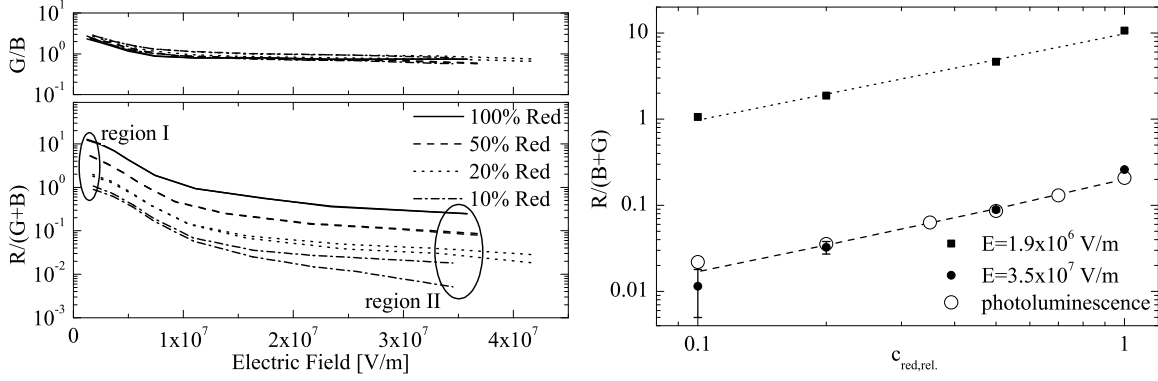


Figure 4.14: Left: Field-dependence of $R/(B+G)$ and G/B for varying red chromophore concentrations $c_{red,rel.}$ relative to that of PW. Two samples were measured for each concentration. Right: Mean concentration dependence of $R/(B+G)$ at fixed electric fields. The dashed line is calculated according to equation (4.2.19) while the dotted line is a guide to the eye of unit slope. Variations observed between like devices are indicated by error bars. Data from figure 4.7 for photoluminescence energy transfer are reproduced as open circles.

two orders of magnitude when lowering the electric field down to $\sim 1.3 \times 10^6$ V/m (region I). This increased red/blue ratio is only observed in electroluminescence and is thus ascribed to the direct trapping of charges by red chromophores. As predicted by equation (4.4.7), the variation of $R/(B+G)$ is linear in the red chromophore concentration. This also indicates that the transport properties (and thus density) of electrons are not altered significantly by the red emitter in the thin active layer as suggested in section 4.3. Equation (4.4.7) is also readily applied to assess the green/blue emission ratio G/B since it is open as to the choice of *host* and *trap* states. Since the green chromophore is a shallow trap only, the G/B ratio is limited by the detrapping of electrons. From equation (4.4.7) using $n_h > 0$ and $n_e > 0$,

$$\frac{\varepsilon_T}{k_B T} > \log \left[\frac{G N_0}{B N_T} (1 - \eta_{B \rightarrow G}^{BGR}) \frac{\mu_e + \mu_h}{\mu_h} \right]. \quad (4.5.1)$$

Using $N_T/N_0 = 5 \times 10^{-4}$, a measured $G/B - (G/B)_{PL} > 1.8$ at the lowest electric field, $\mu_e/\mu_h \approx 10^2$ and an estimated $\eta_{B \rightarrow G}^{BGR} \sim 0.5$ (see figure 4.5), the trap depth for the green chromophore amounts to $\varepsilon_t > 0.3$ eV. This is consistent with the energy levels shown in figure 4.9 and those calculated in section 4.3 from electron mobility measurements. At $E > 1 \times 10^7$ V/m, charge densities have increased enough such that G/B is determined by energy transfer alone. Such reasoning is not easily applied to the $R/(B+G)$ values to predict the corresponding trap depth, since the detrapping term $(N_0 - n_e) \exp(-\varepsilon_T/k_B T)$ in equation (4.4.7) is small and the color ratio thus determined by the charge density. Assuming that trap filling of the red chromophore is much less than unity and controlled by the hole density, it follows from equation (4.4.11) that

$$n_h = \frac{1 + r_{RET}}{r - r_{RET}} \frac{Z \varepsilon \varepsilon_0 k_B T}{b e^2} a^{-2} \frac{N_T}{N_0}. \quad (4.5.2)$$

Now, using $N_T/N_0 = 4 \times 10^{-4}$, the experimental values $r = R/(B+G) > 12.5$, $r_{RET} = \eta_{B \rightarrow R, total}^{BGR} / (1 - \eta_{B \rightarrow R, total}^{BGR})$, $\eta_{B \rightarrow R, total}^{BGR} = 0.17$ and assuming $a = 1$ nm, the hole density in the low-field opera-

	μ_0 [cm ² /Vs]	C_0 [10 ⁻⁴ (cm/V) ^{1/2}]	σ [meV]	Σ	$\mu(E=0)$ [cm ² /Vs]
electrons					
PB2a	0.42	2.9	103	3.5	3.6×10^{-4}
PB2b	0.17	1.6	101	2.4	1.8×10^{-4}
BG2	0.16	2.8	100	3.4	2.0×10^{-4}
BR2	<i>transit time not resolved</i>				
PW2	<i>transit time not resolved</i>				
holes					
PB2a	5.4×10^{-3}	2.3	118	2.9	3.1×10^{-7}
PB2b	3.3×10^{-3}	2.0	115	2.9	8.1×10^{-7}
PW2	6.3×10^{-3}	1.5	114	2.4	1.0×10^{-6}

Table 4.4: Results of time-of-flight photocurrent measurements on **PW2** and related copolymers analyzed in terms of the Gaussian disorder model.

tion regime I is $n_h < 6 \times 10^{20} \text{ m}^{-3}$. This is much lower than $n_h = \frac{3}{2} \frac{\epsilon \epsilon_0 E}{ed} \approx 4 \times 10^{21} \text{ m}^{-3}$ expected for Ohmic hole injection using $d = 80 \text{ nm}$, $E = 1.3 \times 10^6 \text{ V/m}$ and $\epsilon = 3$. The reciprocal field dependence of equation (4.4.12) thus cannot properly describe the results presented here and it is clearly demonstrated that the strong hole injection barriers reported for **PB** devices in chapter 3 with injection efficiencies around 0.1 also prevail for **PW**.

Since material supply of **PW** was limited, additional experiments assessing the role of electron injection were conducted on the closely related copolymer **PW2**, the structure of which cannot be disclosed due to intellectual property reasons. This copolymer features the same blue (11%), green (0.05%) and red emitting (0.03%) chromophores as used for **PW**. The hole transporter has been slightly modified and its concentration raised to 24%. The backbone monomer is also modified and an additional 7% of a second blue chromophore emitting at longer wavelengths has been included, strongly improving the operational lifetime and stability. The blue emission is dominated by this new species. Charge mobilities were found to be similar to those of **PW**, with improved hole transport capabilities. Table 4.4 shows the results of an analysis of TOF charge mobility measurements on **PW2** and related model copolymers in terms of the Gaussian disorder model. The available model copolymers were **PB2a** (only the original blue emitter), **PB2b** (both blue emitters), **BG2** (as **PW2** but without red chromophores) and **BR2** (as **PW2** but without green chromophores). The results for these are included here for completeness only. Figure 4.15 shows representative photocurrent transients from time-of-flight experiments on $1.7 \mu\text{m}$ thick **PW2** samples at an electric field of $E = 1.8 \times 10^7 \text{ V/m}$. Hole transport is found to be nondispersive as in **PW**, with a flat plateau current under low-energy laser pulse illumination. At higher pulse energies, the current transient develops a new maximum (*cusp*). Here, this behavior is attributed to the onset of space charge limitations whenever the amount of photogenerated charges is $Q > CU/20$ (cmp. chapter 2.2), although similar effects have been observed for other polymers in absence of space-charge effects and were attributed to energetic carrier relaxation.[54, 149] Contrary to the transients observed for hole transport, no transit time of electrons could be resolved from the measured photocurrent transients. Their photocur-

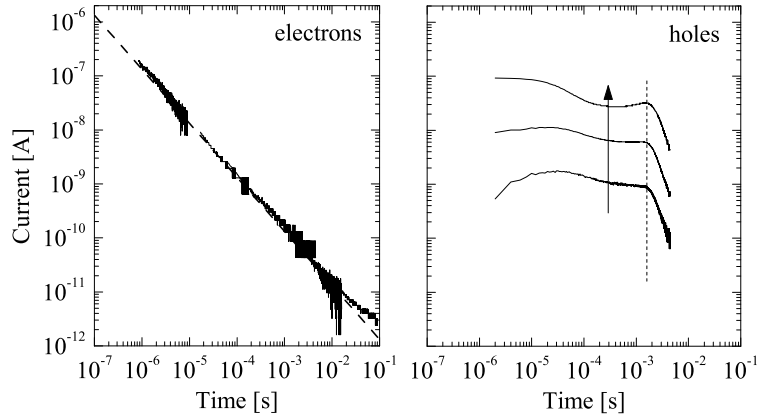


Figure 4.15: Representative TOF transients measured for 1.7 μm thick **PW2** layers for electron (left) and hole (right) transport at an electric field $E = 1.8 \times 10^7$ V/m. Hole photocurrent transients are shown for three different laser pulse energies (rising in direction of arrow) with comparable transit time results (dotted line). The electron transient is shown for the highest laser pulse energy, stitched together from several measurements using different settings of the current amplifier to maximize the dynamic range of the measurement. The dashed line is a guide to the eye of slope -1.

rent decayed approximately proportional to t^{-1} over at least 5 orders of magnitude, which is attributed to strong trapping on the red-emitting chromophore in the 1.7 μm thick layers used for these experiments. As such, the observed transport properties of **PW2** were found to be very similar to those of **PW** discussed in chapter 4.3.

The effects of varying driving conditions on the emission color of **PW2** light-emitting diodes were found to follow the same rules as **PW** devices. Using a new preparation scheme described in more detail in appendix C on page 137, electron-only devices of structure Al/**PW2** (80 nm)/cathode were fabricated. The electron injection efficiency was varied by employing vacuum evaporated metal cathodes consisting of 0.5 nm CsF, 5 nm Ba or 20 nm Ca, each capped by a 200 nm thick layer of Al. Alternatively, a 200 nm thick Al layer was deposited without additional low work-function metals underneath. The corresponding current-voltage curves are shown in figure 4.16. Electron injection currents were reduced by up to six orders of magnitude compared to CsF electrodes when only Al was used as cathode. Bipolar devices were fabricated by substituting the bottom Al anode by a PEDOT:PSS hole injection layer, keeping all other parameters the same. As shown in figure 4.16, the observed current densities were independent of the choice of CsF, Ba or Ca cathodes, minor differences being on the same order as typical sample-to-sample variations. The current in bipolar **PW2** devices is thus primarily attributed to hole transport, such that the observed differences in terms of electron injection do not impact the total device current. Figure 4.17 shows that although the total current barely changes for these devices, the external quantum efficiency is reduced, consistent with the reduced electron injection. When Al was used as cathode instead, the bipolar device current was surprisingly reduced by up to one order of magnitude. This cannot be understood from a reduction of electron injection only. The analysis provided in chapter 3 has shown that hole injection can be improved by an accumulation of electrons near the anode interface. It is thus proposed that **PW2** devices with Al cathodes

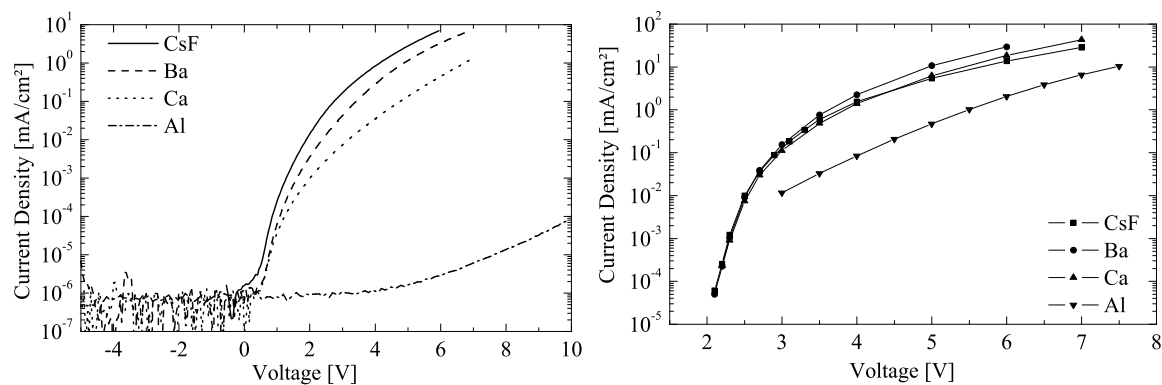


Figure 4.16: Current-voltage characteristics of PW2 devices with CsF, Ba, Ca and Al electrodes. Left: Electron-only devices with Al anodes, right: bipolar devices with PEDOT:PSS anodes. Current densities of electron-only devices measured under reverse bias are limited by the measurement range of the experimental setup at the lowest values shown.

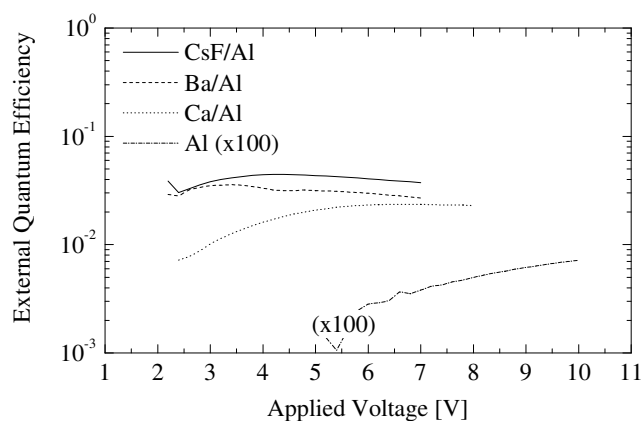


Figure 4.17: Calculated external quantum efficiencies for PW2 bipolar devices employing four different cathode structures. Quantum efficiencies were calculated according to the procedure described in appendix D.

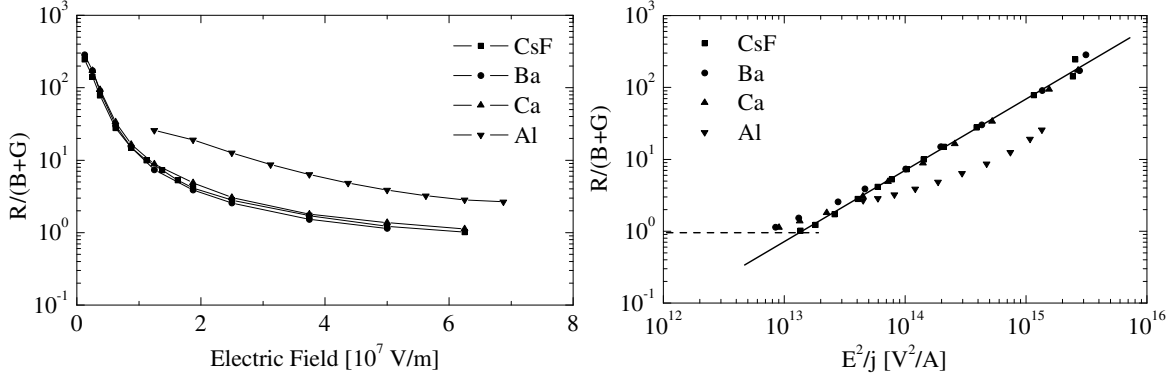


Figure 4.18: Left: Color ratio $R/(B+G)$ of **PW2** bipolar devices with several types of metallic cathodes as function of electric field. Right: The same data plotted against E^2/j . The dashed line indicates the color ratio obtained in PL experiments, the solid line is a linear fit to the data.

lack the amount of electron accumulation needed to promote hole injection, resulting in strongly reduced hole injection currents. The emission spectra of the bipolar devices were analyzed in terms of the corresponding chromophore spectra as discussed in section 4.2. These deviate to some extent from those of **PW** due to the different chemical environment. Figure 4.18 shows that the calculated $R/(B+G)$ ratios are independent of the choice of electrode metals CsF, Ba or Ca. The electron density term in equation (4.4.10) thus does not contribute significantly to $R/(B+G)$ for **PW2** devices and equation (4.4.11) can be used instead. Contrary to these findings, the red emission contribution increased up to fourfold when pure Al was used as cathode. Electron injection is strongly hindered for this electrode type, and thus one should expect a shift of the emission zone towards the cathode. It is well known that the position of the emission zone within the thin-film structure influences the external emission spectrum. Shifting a thin emission zone completely towards the metallic cathode, a roughly tenfold *reduction* of the red spectral contribution is to be expected.[48] Thus, emission zone shifts cannot account for the observed spectra when the red/blue ratio is considered a function of electric field only, as suggested by equation (4.4.3). Using equation (4.4.11) instead and approximating the injection limited hole density by $n_h = j/e\mu_h E$, the $R/(B+G)$ ratio should be linear in E^2/j whenever $E \gg E_{\text{diff}}$. Figure 4.18 shows that this indeed correlates well with the experimental data for CsF, Ba and Ca electrodes. In this plot, the color ratio for the device with Al cathode is reduced by one order of magnitude and thus coherent with the notion of an emission zone shifted heavily towards the cathode. Since the color ratio approaches that of devices with better electron injection at higher operating voltages (lower E^2/j), it is suspected that the emission zone moves away from the cathode when sufficiently large electric fields are applied to the device. Since free electron densities remain low throughout the operation regime of **PW2** devices in bipolar operation, the simplified equation (4.4.11) provides a reasonable description of the emission color. This opens up the possibility to directly gain quantitative insight into the constituent charge trapping dynamics. In order to facilitate a quantitative treatment, equation (4.4.11) is rewritten as

$$A := \frac{r - r_{\text{RET}}}{1 + r_{\text{RET}}} \frac{1}{N_T} \frac{j}{\epsilon \epsilon_0 \mu_h E} = (a' N_0)^{-1} (E + E_{\text{diff}}), \quad (4.5.3)$$

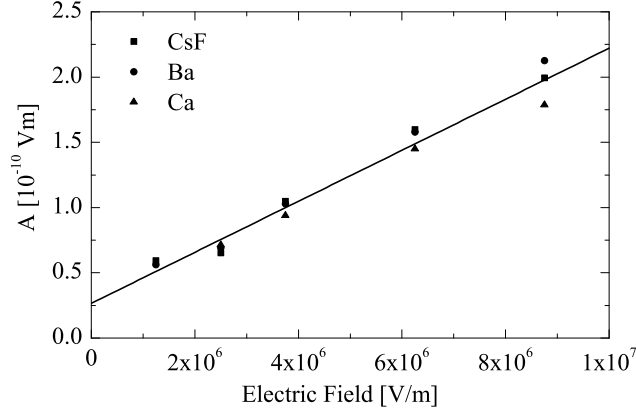


Figure 4.19: Plot of parameter A as defined by equation (4.5.3) for devices with CsF, Ba and Ca cathodes. The solid line is the result of a linear regression analysis.

using $\eta_{B \rightarrow R, \text{total}}^{\text{BGR}} = 0.49$, $r_{\text{RET}} = 0.96$, $N_{\text{T}}/N_0 = 3 \times 10^{-4}$ and $N_0 \approx 8.5 \times 10^{26} \text{ m}^{-3}$. The field-dependence of the hole mobility μ_{h} was determined from time-of-flight photocurrent measurements as $\mu_{\text{h}}(E) = \mu_0 \exp(\beta \sqrt{E})$, where $\mu_0 = 1.0 \times 10^{-6} \text{ cm}^2/\text{Vs}$ and $\beta = 2.0 \times 10^{-4} \text{ m/V}$ at room temperature. Figure 4.19 shows A for the range of electric fields where $r \gg r_{\text{RET}}$. A linear regression yields $(a'N_0)^{-1} = (2.0 \pm 0.1)10^{-17} \text{ m}^2$ and $E_{\text{diff}} = (1.4 \pm 0.4)10^6 \text{ V/m}$, by which $a' = (5.0 \pm 0.3) \times 10^{-11} \text{ m}$ and $a = (2.1 \pm 0.3) \times 10^{-9} \text{ m}$ can be calculated from E_{diff} defined by equation (4.3.11) using $Z = 6$, $b = 1.52$ and $\delta = 1$. When using the extended Waite formalism of equation (4.3.10) instead, $\sigma_{\text{T}} = (a'N_0^{-1})$ and $r_0 = \frac{e\sigma_{\text{T}}E_{\text{diff}}}{4\pi k_{\text{B}}T\delta}$, thus $r_0 = (8.4 \pm 0.3) \times 10^{-11} \text{ m}$. With both approaches, the amount of diffusion-driven trapping is weaker and that of drift-induced trapping two orders of magnitude stronger than what would be expected from the geometrical size of the corresponding monomer unit of $\sim 1.2 \text{ nm}$ diameter. This situation can obviously be resolved by choosing an *effective* hopping site density $N'_0 \ll N_0$ such that $(a'N_0)^{-1} = (1.2 \text{ nm} \cdot N'_0)^{-1}$, thus $N'_0 = (5.0 \pm 0.3) \times 10^{-2}N_0$. Trapping by diffusion and drift are still inconsistent since under this assumption $a = (9.4 \pm 1.4) \text{ nm} \neq a'$. As discussed in section 4.3, diffusion in a hopping system of reduced dimensionality results in reduced E_{diff} due to differing statistics of the random walk. When using $E_{\text{diff}} = \frac{8Zk_{\text{B}}T\delta(N_{\text{T}} - n_{\text{T}})a'}{\pi a^2 e N'_0}$ valid for 1D diffusion, $a = (0.82 \pm 0.12) \text{ nm} \approx a'$.

Two reasons are conceivable to explain the reduced site density. First, from studies of electron transport in **PB** and the pure backbone polymer it is known that introduction of the blue emitter at a concentration of 11% reduces the electron mobility by a factor of seven, the blue chromophores thus might be the preferred transport channel. This is consistent with the observed charge trapping on the green chromophore analyzed above in terms of the EMA theory. It would reduce the density of sites available for carrier hopping by one order of magnitude. It remains an open question whether this picture is consistent with an unchanged hopping distance of $\sim 1 \text{ nm}$. One explanation might be that transport of electrons is constrained to filaments or percolation pathways. It is difficult to argue that all of the trap states are included in these paths as required by the analysis to achieve higher effective trapping cross sections.

Alternatively, matching of the lattice spacing a' and the site density N'_0 is enforced by

requiring $a' = N_0'^{-1/3}$. This results in $N_0'/N_0 = (1.4 \pm 0.2) \times 10^{-3}$, $a' = (4.4 \pm 0.4)$ nm and $a = (18 \pm 3)$ nm ($a = (3 \pm 0.5)$ nm) for 3D (1D) diffusion. As before, the effective density of transport states is strongly reduced, but with a' matching the lattice dimensions of N_0' the conjecture of filamental conduction can be dropped. Again, the diffusional charge trapping rate is consistently described by an average hopping length approximately equal to that of drift motion only when a reduction of the dimensionality of diffusion is assumed. It is a general property of random walks in constrained dimensions to require more hopping steps for a charge to find a trap site than in 3D random walks at the same trap concentration. The one-dimensional random walk model correctly accounts for the observed weak diffusion-driven charge trapping. Such reduced dimensionality may be appointed to intrachain diffusion being preferred against interchain diffusion and/or electron transport occurring via quasi-1D percolation pathways.

4.6 Temperature Effects on the Emission Color

The emission color observed from **PW** and **PW2** light-emitting devices has been shown to follow equation (4.4.11). Devices with **PW2** polymer layers presented an opportunity for a detailed investigation since the electron currents remain low throughout the whole range of driving conditions, significantly simplifying an assessment of the dominant charge density. At variance with the purely kinetic trapping considerations, the *density* of occupied trap states determines the red/blue ratio of these devices. This density is a function of the densities of holes and mobile electrons that together establish a certain trap filling level. The devices followed the proposed model over nearly six orders of magnitude in device currents, compare figures 4.16 and 4.18. The operating temperature of these devices presents another opportunity to directly test the predictions of the proposed model. Experiments were carried out on **PW2** devices with CsF, Ba and Ca cathodes, using the same device configurations as in the last section. For these, the analysis of temperature effects is significantly simplified since only the temperature-dependent injection current of holes needs to be considered. Assuming that the external device current is mainly due to hole injection and that the hole density in the emission zone follows $j = en\mu E$, equation (4.4.11) predicts the color ratio

$$r = r_{\text{RET}} + (1 + r_{\text{RET}}) \frac{N_{\text{T}} \epsilon \epsilon_0 \mu_{\text{h}} E}{a' N_0 j} (E + E_{\text{diff}}). \quad (4.6.1)$$

Temperature variation of the color ratio r is mediated by the hole injection current $j = j(E, T)$, the hole mobility $\mu_{\text{h}} = \mu_{\text{h}}(E, T)$ and the amount of diffusive trapping described by $E_{\text{diff}} = Zk_{\text{B}}T\delta a'/(a^2be)$. The Gaussian disorder model for charge transport predicts a temperature-activated mobility

$$\mu_{\text{h}}(T) \propto \exp\left(-\frac{4}{9}\hat{\sigma}^2\right) \exp[C_0(\hat{\sigma}^2 - \Sigma^2)\sqrt{E}] \quad (4.6.2)$$

where $\hat{\sigma} = \sigma/k_{\text{B}}T$. The diagonal and off-diagonal disorder parameters were determined from time-of-flight experiments on the model copolymer **PB2b** without green and red dye as $\sigma = 115$ meV and $\Sigma = 2.9$, respectively, see table 4.4. The scaling parameter is $C_0 = 2.0 \times 10^{-5} \text{ V}^{-1/2} \text{ m}^{1/2}$. As for **PW** and its corresponding model polymers, introduction of the

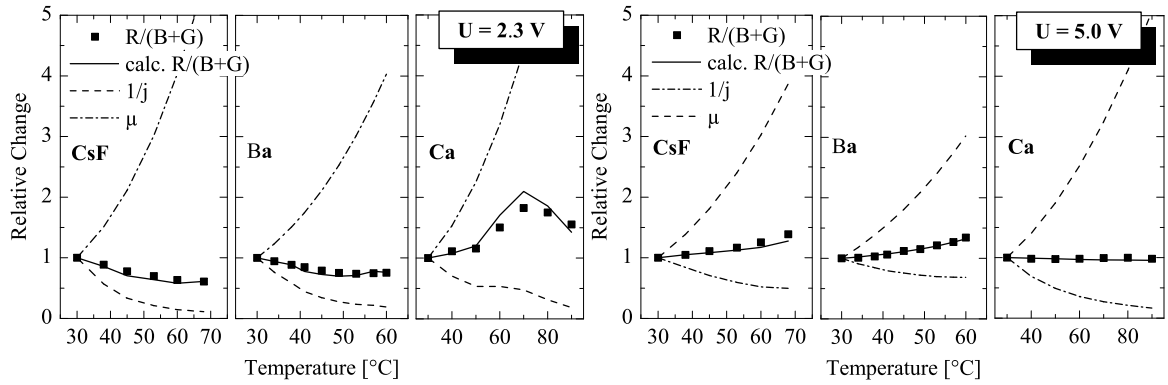


Figure 4.20: Prediction of the change of $R/(B+G)$ relative to its value at 30°C for PW2 light-emitting diodes, based on the changes in device current ($1/j$ denoted by dashed lines) and charge mobility (denoted by dot-dashed lines) when the temperature is varied. The temperature dependence of charge mobility was calculated assuming a diagonal disorder parameter of $\sigma \approx 110$ meV. Measured data points for $R/(B+G)$ are shown as squares.

green and red chromophores into the hole transport path was found to have only small effects on the hole mobility. The variations of the red/blue ratio $R/(B+G)$ with the device's operating temperature was determined both at low operating voltage ($U = 2.3$ V), where charge trapping effects are strong, as well as at high operating voltage ($U = 5$ V), where red emission is mostly due to energy transfer. Temperature was varied between 30°C and 90°C , where the highest temperatures were only used when a sufficient stability of the current density could be achieved. The results are summarized in figure 4.20, which shows the change of hole mobility according to equation (4.6.2), of the measured device current and the $R/(B+G)$ ratio relative to the corresponding values at 30°C . A consistent fit of the measured temperature dependence of $R/(B+G)$ is achieved for $\sigma \approx 110$ meV, only slightly smaller than the value determined from time-of-flight measurements. At $U = 2.3$ V, $r \gg r_{\text{RET}}$ and the energy transfer contribution can be neglected. At $U = 5.0$ V, the measured $r \approx r_{\text{RET}}$ and thus energy transfer has to be taken into account in equation (4.6.1) to get correct results. Here, $r_{\text{RET}}/r = 0.7$ at 30°C . Using the same disorder parameters as used for the low-voltage data, the measured r is reproduced faithfully by equation (4.6.2). The color ratio is thus a very sensitive probe of the temperature dependence of charge injection and mobility. The actual tendency of rising or falling red contribution with increasing temperature depends on the details of the charge injection mechanisms. Since charge injection is governed by a multitude of effects, it is out of the scope of this work to give a detailed analysis of observed variations in injection currents. It is merely noted that in the two investigated voltage regimes, the injection current is not any simple function of temperature. Indeed, while most of the measurements are consistent with a rising hole density upon heating, devices with CsF or Ba electrodes showed the opposite behavior at low operating voltages.

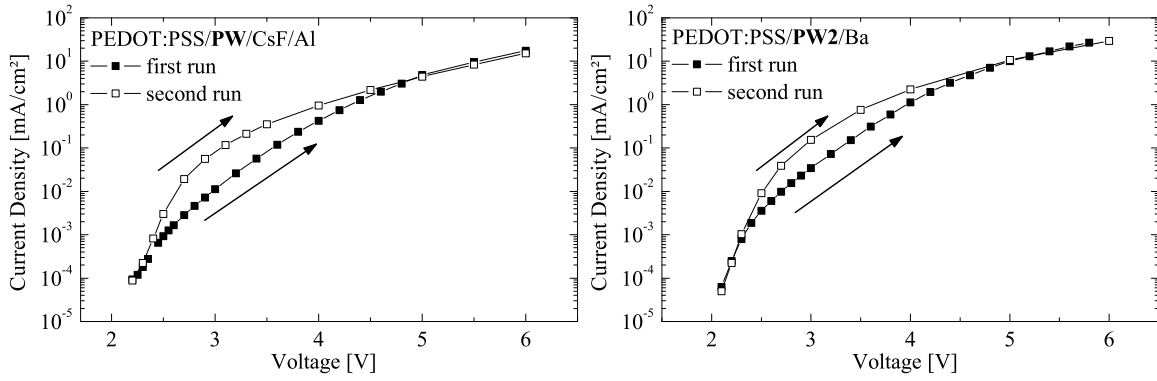


Figure 4.21: Electrical conditioning effects for **PW** and **PW2** light-emitting devices upon prolonged driving at a voltage of 6 V. The current-voltage characteristics are steeper after conditioning, while the behavior at high and low operating voltages is not affected.

4.7 Anode Interface Conditioning Effects

The measurement of current-voltage characteristics of electron-only devices presented in section 4.5 indicated that hole injection from PEDOT:PSS into **PW2** is improved in presence of electrons within the polymer layer. Variations of the charge injection efficiency during operation were reported for a broad class of polymeric materials and cover a wide range of time dynamics. These were explained by an accumulation of electrons due to an extraction barrier at the polymer/anode interface [150, 151] and trapping of electrons in defect states near the electrode [94, 152]. The time scale of these effects is supposed to range from μs for electron accumulation to several seconds for deep charge trapping. Interface conditioning in **PB** reported in chapter 3 was found to occur on an intermediate timescale of $\sim 10^{-3}$ s. Being a model polymer for **PW**, some kind of interface conditioning effects thus should also be expected for the corresponding white emitting polymer. In this chapter, interface conditioning is studied for encapsulated OLED devices of structures PEDOT:PSS/**PW** (80 nm)/CsF/Al as well as PEDOT:PSS/**PW2** (80 nm)/Ba by measuring current-voltage characteristics, see figure 4.21. It was generally observed that the current-voltage characteristics improve upon operating the devices for some minutes at elevated voltages. These effects were not found to be of permanent nature, but lasted at least for some hours. After driving the devices for some minutes at $U = 6$ V (hereafter: *conditioning*), subsequent current-voltage measurement sweeps features an increased slope up to $U = 3$ V while being hardly affected above $U = 5$ V and below $U = 2.3$ V. Fluorescence spectra were simultaneously recorded both in the unconditioned and the conditioned states. The spectrum acquisition time at each voltage step was approximately 1 min, with ample time allowed for the device to reach constant current readings prior to measurement. The $R/(B+G)$ color ratios calculated from these spectra are shown in figure 4.22 as a function of voltage and current density for both unconditioned and conditioned states. After conditioning, the red spectral contribution is reduced up to four-fold at a voltage of $U = 3$ V. No spectral changes were observed at the lowest and highest operation voltages for either **PW** or **PW2** devices. At a fixed electric field and constant temperature, equation (4.6.1) predicts $R/(B+G) \propto j^{-1}$. This equation was shown to faithfully

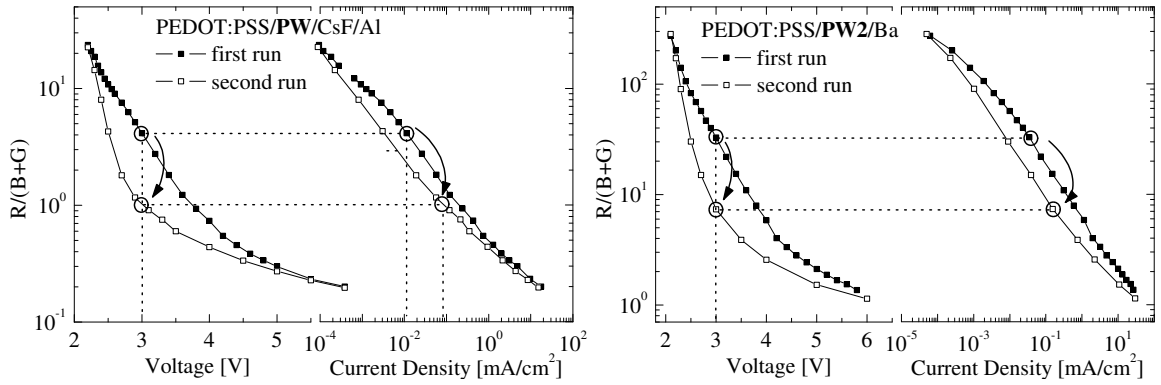


Figure 4.22: Color shift due to electrical conditioning of **PW** and **PW2** light-emitting devices upon prolonged driving at a voltage of 6 V. For both device configurations, the $R/(B+G)$ emission ratio is reduced up to fourfold at a driving voltage of 3 V.

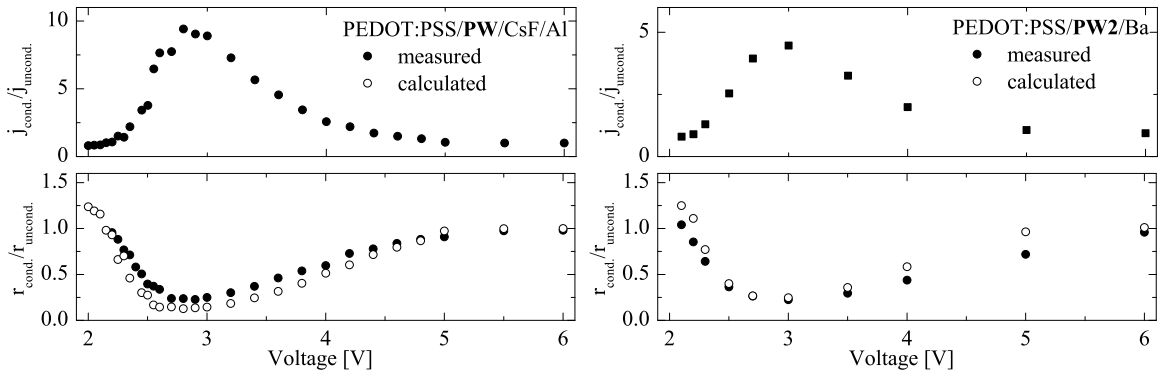


Figure 4.23: The effect of electrical conditioning on current density and $r = R/(B+G)$ color ratio for **PW** and **PW2** devices. The observed increased current densities after conditioning are consistent with the reduction of the color ratio.

reproduce the temperature dependence of emission color for **PW2** devices since electron currents were found to be negligible in these devices. For devices comprising a **PW** polymer layer, the situation is more complicated since the influence of electron currents for these devices cannot *a priori* be neglected. Figure 4.23 shows the ratio $j_{\text{cond.}}/j_{\text{uncond.}}$ of device currents after/before conditioning. Equation (4.6.1) was applied to calculate the corresponding ratio of $r_{\text{cond.}}/r_{\text{uncond.}}$ after/before conditioning, where $r = R/(B+G)$. For **PW** the parameters $\eta_{\text{B} \rightarrow \text{R}, \text{total}}^{\text{BGR}} = 0.17$, $r_{\text{RET}} = 0.20$ were used, while for **PW2** they were $\eta_{\text{B} \rightarrow \text{R}, \text{total}}^{\text{BGR}} = 0.49$, $r_{\text{RET}} = 0.96$. The resulting values for $r_{\text{cond.}}/r_{\text{uncond.}}$ closely reproduce the measured values, although the color ratio itself spans a range of up two orders of magnitude for **PW2** devices. For **PW** devices, the calculated $r_{\text{cond.}}/r_{\text{uncond.}}$ slightly overestimates the effect of conditioning. This is consistent with the notion of electron currents being unaffected by electrical conditioning, since this would reduce the effect of hole current changes on the $R/(B+G)$ emission ratio.

4.8 Conclusion

In this chapter, the spectral properties of white polymeric light-emitting diodes were studied. In particular, the work was focused on copolymers comprising multiple types of singlet-emitting chromophores. It was shown that the emission color of such devices is determined by resonance energy transfer between the chromophores as well as by direct charge trapping. Detailed analysis of a three-component rate-equation modelling the photoluminescence response allowed to quantify the energy transfer efficiencies without resolving to fluorescence lifetime measurements and detailed knowledge of the chromophore fluorescence quantum efficiencies. Based on the knowledge of these effects, a quantification of charge trapping from measurements of the emission spectrum was possible. A multitude of external parameters was shown to influence the ratio of red to blue emission observed from these devices, among them the driving voltage, temperature and the choice of electrodes. So far, models discussed in literature fail to account for most of these effects, being based on a kinetic approach to charge trapping. An alternative model was introduced which relies on a rate-equation description of charge trapping to a discrete trapping level. It is able to account for trap saturation, detrapping of charge carriers and correctly models the role of charge mobilities both for the charge carriers being trapped as well as those that remain unaffected by the traps. The parameter which determines the emission color is basically given by the filling level of trap states. The model was shown to correctly reproduce the influence of the total trap density, the role of the charge-injecting electrodes and the temperature dependence both under conditions of high operating voltages as well as near the turn-on voltage. A detailed analysis was given concerning the field-dependence of the emission ratio for light-emitting devices made from **PW2** polymer layers. Since the electrical properties of these devices were dominated by hole injection currents, the description could be further simplified up to a point where direct access to some fundamental parameters became possible.

From an analysis of the voltage-dependent emission spectra, the trapping cross section for drifting electrons and the amount of electron trapping caused by charge diffusion were determined. The trapping cross section was found to be much larger than what was expected from the geometrical size of the corresponding monomers. At the same time, diffusive capture of electrons into trap states was quite small, having a significant effect on the emission color only at electric fields of less than 2×10^6 V/m. In the context of an effective random walk description of charge trapping, these effects were attributed to a reduced density of hopping sites for the electron motion and electron diffusion in reduced dimensionality, probably preferably along polymer chains or quasi-1D percolation pathways. Although the hole injection currents into **PW2** turned out not to be any simple function of temperature, the model correctly predicted the impact of temperature on the emission color. Finally, an analysis of the electrical conditioning effects observed during operation of these light-emitting devices was given. It was shown that for both types of polymers studied here, anode (hole) injection currents improve upon driving the devices at elevated voltages. This improvement of charge injection efficiency was shown to directly affect the emission color, where the corresponding color shifts could be consistently explained by the rate equation trapping model. Being able to predict most of the spectral variations observed under varying driving conditions of such OLEDs underlines that color variations due to shifts of the emission zone were not dominant for the devices and operation regimes studied.

Chapter 5

Analysis of Electroluminescence Decay Transients: the Role of Charge Traps

5.1 Introduction

The preceding chapters have shown that by combining experimental evidence of charge transport characteristics, transient and equilibrium device behavior and spectral emission properties it is possible to gain detailed insight into the role of charge trapping chromophores for the white-light emitting devices based on **PW** and **PW2** copolymers. It was shown in which way the observed transient luminescence of such devices correlates with charge transport and injection phenomena and that the luminance onset observed for the most simple devices lacking green and red chromophores could even be simulated numerically. As a matter of fact, such simulations get much more complex upon introducing the red-emitting charge traps, since the gradual filling of trap levels then determines the onset properties of device emission. As discussed in chapter 4.5 it as yet remains an open question as to the exact mechanisms of charge trapping in these devices. The amount of trap filling impacts the simulated current densities of both hole and electron mobile carriers due to the involved buildup of space charge fields. Experimentally the trap filling dynamics depends on a multitude of parameters such as inadvertent sample contamination and variations of the performance of evaporated metal cathodes and thus of the injected currents. It is difficult to assess the amount of electrons that remain trapped in between two pulses of the necessarily repetitive transient EL measurements although this would be of major importance for the measured average onset transient. It was found that experimentally the transient device behavior of red-emitting devices lacked the amount of reproducibility that would be needed to further improve the numerical simulations of the transient luminance onset.

Despite the difficulties encountered when analyzing transient EL experiments, they remain attractive for gaining insight into functional device properties since they provide a straightforward access to the charge recombination physics. Having already analyzed the transient EL emission onset as well as the equilibrium device behavior, it appears natural to also model the transient EL decay behavior observed upon termination of the driving voltage. In principle the analysis of such decay transients should be significantly simpler since the starting conditions are equal to the equilibrium device characteristics. In this respect they are not influenced by pulse length and duty cycle issues as found for transient EL onset behavior, facilitating both experiment and analysis. In this chapter the transient EL decay of light-emitting devices with **PW** copolymer layers is analyzed. Figure 5.1 shows an example of transient luminance of a device with an active polymer layer of the **BR** model

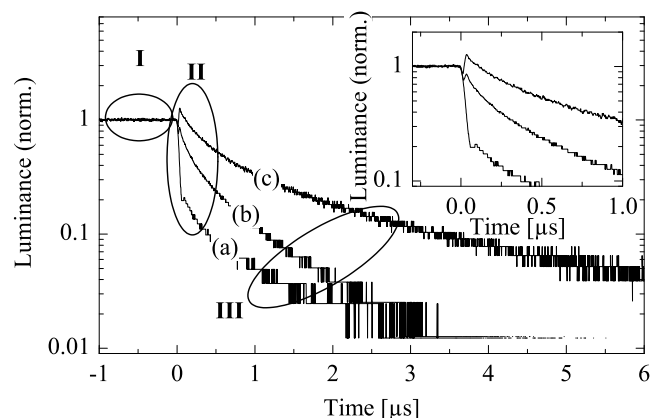


Figure 5.1: Transient luminance of a **BR** light emitting diode after switching the applied voltage from 3.74 V to 0 V. Three measurements are shown: emission at 30°C operating temperature at wavelengths 453 nm (a) and 605 nm (c) and at 90°C, 605 nm (b). Luminance levels are shown normalized to the equilibrium emission. The inset shows details of the transients up to 1 μ s after termination of the driving voltage.

copolymer. The device was driven at a voltage of 3.74 V prior to switching off the externally applied voltage. Generally, the decay of electroluminescence of the devices studied here can be subdivided into three sections along the time axis. In section I before switch-off, the device is still in (dynamic) equilibrium and emits at a steady luminance level at constant applied voltage. When the external voltage is switched off, a fast modulation of luminance level is observed in the blue spectral region, typically limited by the experimental resistance-capacitance time (section II). After this fast modulation, a delayed luminescence of much slower decay behavior is observed (section III). This emission typically lasts from a few μ s up to several 100 μ s.

5.2 Experimental

Sample design and preparation is described in detail in appendix C. Copolymers **PB**, **BG**, **BR** and **PW** (see chapter 4) were dissolved in toluene at varying concentrations and spin-coated onto indium-tin oxide covered glass substrates pretreated by applying a thin film of PEDOT:PSS. Metallic cathodes comprising 0.5–1.0 nm of CsF and 250 nm aluminum were evaporated onto the polymer layers of thicknesses between 50 nm and 100 nm. All measurements discussed here were done on encapsulated samples outside of the protective glovebox nitrogen atmosphere, where it was ensured that the encapsulation itself did not alter device behavior in any way.

As evident from figure 5.1, transient emission features occur on a range of timescales reaching down to a few nanoseconds. Obtaining time and spectrally resolved emission data from light-emitting diodes is a non-trivial task if time resolutions on the order of 10 ns are required. Since thin-film devices intrinsically act as capacitors of significant capacitance, precautions have to be taken to ensure that the total resistance-capacitance (RC) time of the setup is not degraded. The sample design was optimized for transient experiments by

reducing the active emitting area to a size of 1 mm² while keeping the trace resistance as low as possible, for details see appendix C. This is especially critical for the ITO traces since they have much larger sheet resistance than the cathodic metal electrodes. The devices were driven by an arbitrary function generator (10 ns rise and fall time) via a purpose-built linear amplifier stage, details of which are given in appendix D. Total RC time (10%-90%) on the driving side was $\tau_{10-90} \leq 23$ ns as determined from voltage transients measured directly across the emitting area's electrodes in Kelvin (four probe contacts) configuration. Here, we are mainly interested in the observation of transient emission attributed to different chromophores, i.e. to separate the emission of charge trapping species by spectrometric equipment. Intensified charge-coupled devices (ICCD) in principal allow to take full spectra at time-resolutions down to less than 5 ns, but it becomes inherently tedious to collect transients by accumulating time slices. Photomultiplier tubes (PMT) are common and readily provide sufficient time resolution, but lack the option to gather full spectra. Here, a standard uncooled Hamamatsu side-window R928 PMT (rise time < 5 ns) coupled to a grating monochromator (Amko MultiMode) was used. The photocurrent was amplified by fast transimpedance amplifiers and the complete detection system had time constants smaller than those of the driving side, see appendix D. Alternatively, additional measurements were obtained by detecting the device emission with an ICCD camera system (iStar DH734 by Andor Technologies coupled to a LOT MS257 spectrometer) employing various gating times of the image intensifier down to 5 ns.

From the analysis of emission spectra provided by chapter 4 it is understood that a measurement of luminescence at only a few wavelengths does not necessarily provide enough information to directly characterize the emission attributed to specific chromophores since the emission spectra overlap each other. Suppose that the emission is measured at two distinct wavelengths $\lambda_B = 453$ nm in the blue and $\lambda_R = 605$ nm in the red spectral region with measurement results M_B and M_R , respectively. They are related to the spectral photon flux $L_{B,R}$ at these wavelengths by $M_{B,R} = \eta_{B,R} L_{B,R}$ where $\eta_{B,R}$ is the spectral sensitivity of the detection equipment at $\lambda_{B,R}$. The spectral photon flux can be decomposed by $L_B = B\alpha_{BB}$ and $L_R = B\alpha_{BR} + G\alpha_{GR} + R\alpha_{RR}$ where B, G, R were defined in section 4.2. Figure 4.14 shows that $B/G = (B/G)_{RET}$ is near to the level defined by B→R resonant energy transfer whenever $E > 1 \times 10^7$ V/m. Further assuming $\alpha_{BR} \ll \alpha_{GR}$, the measured red/blue emission ratio is

$$\frac{M_R}{M_B} \approx \frac{\eta_R}{\eta_B} \left(\frac{\alpha_{GR}}{\alpha_{BB}(B/G)_{RET}} + \frac{\alpha_{RR}}{\alpha_{BB}} (1 + (B/G)_{RET}^{-1}) \frac{R}{B+G} \right). \quad (5.2.1)$$

Thus, $M_R/M_B \propto R/(B+G)$ whenever

$$\frac{R}{B+G} \gg \frac{\alpha_{GR}}{\alpha_{RR}} (1 + (B/G)_{RET}^{-1}). \quad (5.2.2)$$

Now, using $(B/G)_{RET} \approx 1$, $\alpha_{GR} = 0.207$ and $\alpha_{RR} = 1.26$, this is equivalent to requiring $R/(B+G) \gg 0.082$. Since $R/(B+G) \geq r_{RET} = 0.20$, the determined emission ratio is $M_R/M_B \approx R/(B+G)$ and thus can be used to directly assess the red/blue emission ratio defined in chapter 4. In principle, $(B/G) \approx (B/G)_{RET}$ could be violated during the decay transients observed here since figure 4.14 only assesses the situation during equilibrium operation. Figure 5.2 compares full spectra of PW light emitting diode emission within the first 200 ns

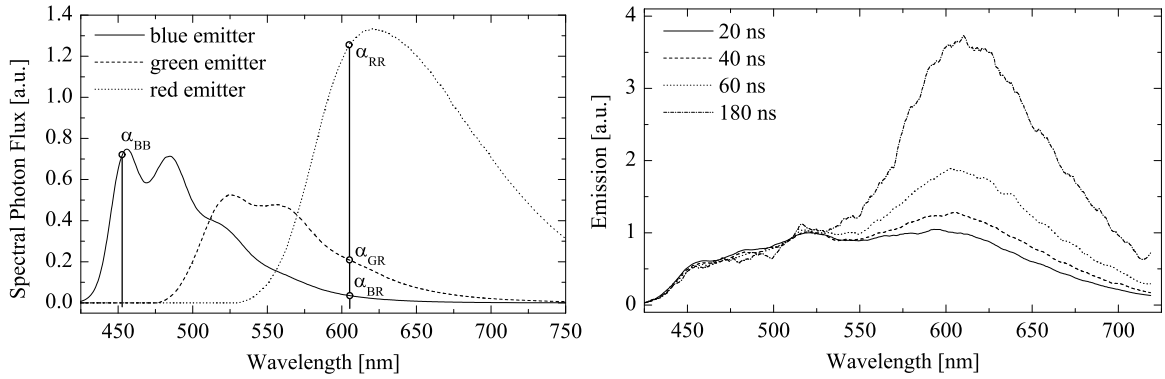


Figure 5.2: Left: Selection of detection wavelengths for transient EL experiments using single-wavelength photomultiplier detection. Right: Emission spectra of a PW light emitting diode at several times after switching off an applied external voltage of 6.4 V. The data is not corrected for the detection equipments spectral sensitivity and is shown here normalized to the blue wavelength range.

after termination of a 6.4 V external driving voltage. The spectra were acquired by gating an intensified charge coupled device equipped spectrometer. Gating times were ~ 5 ns. While strong changes in the R/B ratio are obvious, no alteration of the B/G ratio was observed.

Time-resolved luminance decay data was acquired by applying a square-pulse waveform to the light-emitting diode with various high (low) voltage levels U_{\max} (U_{\min}) at a repetition frequency of usually 200 Hz and duty cycles of 98%, i.e. U_{\min} being applied for 100 μ s. The remaining 4.9 ms of each cycle allowed ample time for the device to again reach steady state emission conditions at U_{\max} . Raw luminance data was processed by setting the time origin equal to the time of switching to U_{\min} , taking into account the additional propagation delays of the photomultiplier and electronic equipment and normalizing to the steady-state luminance value. Data was smoothed by a moving average procedure with exponentially increasing window size, effectively compressing data to 10 points per decade of time. This strongly reduces the data set size and facilitates data analysis while retaining all relevant transient features. The averaging procedure also improves luminance data resolution at long times, where the luminance levels are near the 8 bit resolution limit of the digital oscilloscope, see figure 5.3.

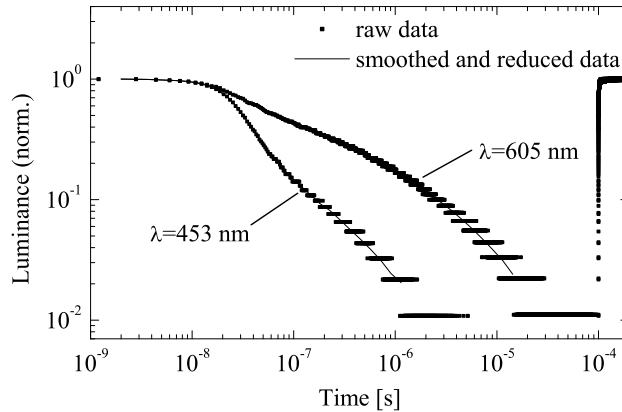


Figure 5.3: Data reduction and smoothing for transient luminance decay data. Raw data was obtained from PW devices at a temperature of 30°C and driving voltage levels $U_{\max} = 5.0$ V and $U_{\min} = 2.0$ V. The raw data was reduced and smoothed to 10 points per decade while still faithfully reproducing the transient features.

5.3 Review of Delayed EL Mechanisms

The transient luminescence phenomena observed upon switching off an organic light emitting diode are due to a multitude of physical effects and before delving deeper into an analysis of the effects observed for the devices studied here, a short review of the relevant physics will be given. It has become widely accepted that the equilibrium emission (section I in figure 5.1) is determined by recombination of electrons and holes to excited molecular states through bimolecular reactions, owned to the relatively low number density of these charges. Langevin treated such reactions in one of his 1903 papers where he showed that the mutual coulomb attraction of two charges results in the total reaction rate $e(\mu_e + \mu_h)/(\epsilon\epsilon_0)n_e n_h$ where $n_{e,h}$ are the densities of electrons and holes, respectively.[41] This is the same result as predicted from the Smoluchovski result $4\pi r_C D n_e n_h$ for capture by diffusion to neutral traps of radius $r_C = e^2/(4\pi\epsilon\epsilon_0 k_B T)$ using the Einstein relation $D = (\mu_e + \mu_h)k_B T/e$. This is not surprising since r_C is the critical distance below which the mutual binding energy exceeds the thermal energy $k_B T$. The Langevin treatment strictly holds only for charges of infinitely small wavefunction extent and for finite-sized charge carrying species one should in general suspect drift-induced charge recombination. Such reactions were studied in chapter 4.4 for electron trapping on red-emitting chromophores in the neutral charge state, where they dominated over diffusion-driven charge trapping. For recombination of electron-hole pairs the situation is different since the Coulomb radius $r_C \sim 10 - 20$ nm is much larger than the localization radius of the charge carriers, which is expected to be on the order of one monomer site of 0.5 nm. Direct trapping by charge drift was analyzed by Isoda et al. [153]. Their general result was that if the spatial extent of the charged species is not larger than $\sim 0.2 r_C$, direct field-induced recombination can be neglected under practical electric field strengths achieved in OLED operation.

During device operation, charge carriers recombine, continuously being replenished by injection through the anode/polymer and cathode/polymer interfaces. When the externally

applied voltage is lowered, no further charge injection can occur and the time evolution of emission is fully determined by the intrinsic dynamics of charges and excited molecular states. Three main mechanisms are held responsible for the observed fast transient luminescence response. The most fundamental of these is the fluorescence decay dynamics of the excited molecular states which for singlet emitting states in disordered polymers leads to exponential or stretched-exponential transients with lifetimes of typically less than 1 ns. Triplet excited states exhibit much longer lifetimes but are only weakly emitting in organic semiconductors free of heavy-metal compounds as used in this work. As discussed in chapter 2, disordered semiconductors typically exhibit field-dependent charge mobilities. This results in a Langevin recombination coefficient which indirectly depends on the electric field within the polymer layer. When the external electric field is turned off, the remaining internal field is determined by space charges and the electrode work functions. This modulates the recombination speed of charges, where the observed time scale is that of the rate of external field modulation, itself being determined by resistance-capacitance effects. As shown in figure 5.1, some samples exhibit a transient luminance overshoot directly after switching of the external field. It may exceed the equilibrium level of emission and thus cannot be explained easily by the effects discussed so far. Observations of such EL spikes were reported for small-molecule multilayer organic light-emitting diodes comprising an emitting layer embedded between charge transport layers [154–156], for polymeric bilayer devices comprising a diffuse organic/organic interface [78] and for polymeric single-layer devices [74, 157]. Having passed through the emission zone, unrecombined charge carriers of both polarities tend to accumulate at organic/organic heterojunctions due to an imbalance in charge mobility and/or energetic barriers. Upon termination of the driving voltage, the internal field reverses and drives these space charges into mutual recombination. For single layer devices, the overshoot has been associated with charge transport barriers due to metal oxidation at the polymer/metal electrode interface. The transient recombination behavior of the space charges has been analyzed in terms of dispersive charge drift [78] and the Onsager [34] recombination model by Lupton et al. [157] using the approximate time domain solution provided by Mozumder [158], although the involved geometry is planar rather than spherical. The difficulty lies in the assumptions needed to simplify the dynamics of space charge recombination sufficiently for an analytic description. The analytic models used in the treatment of charge recombination in organic light-emitting diodes fall into one of two general classes. *Geminate* recombination is usually used to describe the fate of electron-hole pairs created by photoionization. The theories of Onsager [34, 35], Noolandi and Hong [159, 160] and Braun [161] have been used to calculate the yield of free charges and the time-dependence of recombination. Contrary to such charges of *correlated* origin, the bimolecular recombination of *uncorrelated* charges follows Langevin dynamics if the recombination rate is limited by the rate of charge encounters. As also pointed out by Arkhipov and Nikitenko [162], both processes are based on the Smoluchowski diffusion equation describing diffusion under the mutual Coulomb attraction and merely differ in the choice of initial and boundary conditions. Correlated charge pair recombination has been used at least by some authors [154, 155] as a distinct physical mechanism held responsible for transient EL spikes exceeding the equilibrium luminance level. From a fit to the data, Cheon et al. calculate correlated charge-pair distances equal to the average interchromophoric distance within the emission zone. They fail to provide evidence that such a recombina-

tion mechanism should remain inactive during the equilibrium emission as is achieved by the charge accumulation models discussed above and the case discussed by Arkhipov and Nikitenko [162]. As discussed in chapter 4.2, excitons are quenched by the electric field since the geminate pair states formed after dissociation are energetically favored if their binding energy exceeds that of the excited state. Schweitzer et al. [163] analyzed such states generated upon photoexcitation in a ladder-type poly-(paraphenylene) and found that when the stabilizing electric field is removed, they recombine on timescales of less than 160 ns limited by their setup's RC time. From the efficient field quenching of luminescence and the inefficient photogeneration of free charges, one should generally expect a significant amount of such geminate pair states. Fast luminance spikes may thus result also for electrically driven devices although Onsager-type of recombination dynamics is not to be expected since the geminate pairs are mainly situated on neighboring sites.

Finally, the slow decay observed on longer timescales (section III in figure 5.1) is discussed. Due to the low remaining electric field strength after termination of the driving voltage, charge extraction through the electrodes is low and space charge carriers may survive for several hundred microseconds before being neutralized by bimolecular recombination. In this case the observed EL reflects the slow decay of space charges and can potentially be used to gain insight into their dynamics. [81, 164] The situation is complicated further by the dispersive transport characteristics of disordered hopping systems. Over time, carriers tend to become more immobile since each transport hop will preferentially occur to lower sites of lower energy. Additionally, mobile carriers preferentially recombine or leave the device while carriers at the lower end of the density of states remain. For systems with strongly dispersive transport characteristics, the Langevin recombination constant will thus be a time-dependent quantity, rendering the recombination dynamics difficult to analyze. For devices with strong luminance overshoots, the luminance dynamics on long timescales may well be dominated by the corresponding interfacial space charge layers discussed above instead of a more homogeneous charge distribution. Nikitenko and Arkhipov [78] presented an analytic theory of the corresponding decay dynamics but employed assumptions concerning the dispersive charge transport not easily generalized to other devices. A reverse argument holds if charges are deeply trapped during device operation, since the delayed EL may become controlled by the release time from these traps. Such effects were reported by Sinha et al. [165]. For multilayer systems comprising a defined emission layer, outdiffusion of accumulated charges was discussed as another mechanism for the slow decay of EL. Cheon and Shinar [154] showed that if the doped emission layer is thin and the recombination coefficient sufficiently small, the luminance will follow a power-law decay $\propto t^{-1}$. Devices which employ electrophosphorescent emitters usually also feature a slow decay of EL after turn-off, but this is normally related to the emitting states lifetime as discussed above for the fast transient response observed for singlet-emitting devices. Sinha et al. [166] report the observation of slow EL dynamics in normally singlet-emitting polyfluorene based devices which they attribute to intrinsic phosphorescence and delayed EL from triplet-triplet annihilation processes. Due to the low oscillator strength and long lifetime of the excited triplet states in organic semiconductors which are free of heavy-metal compounds, delayed emission of such origin is easily quenched by charge carriers and is not expected to contribute to room-temperature emission.

5.4 Results and Discussion

The polymer used in this work is more complex concerning its functional moieties compared to those used for the published studies discussed so far. It was shown in chapter 4 that the red-emitting chromophore present in **PW** at a monomer concentration of only 0.04% represents a strong trap for mobile electrons and thus dominates the device emission at low driving voltages. Owned to the different recombination speeds of free and trapped electrons, one should suspect significant differences in the delayed EL transients measured in the blue and red spectral regions.

Figure 5.4 shows the amount of delayed EL measured at 470 nm and 620 nm at fixed times t after switching the driving voltage from 2.8 V or 5.0 V to a range of bias voltages between $U_{\text{bias}} = 0$ V and $U_{\text{bias}} = 2.2$ V, the highest value being just below the turn-on voltage. Since the turn-on voltage is mainly determined by the built-in potential U_{bi} , the average internal electric field during the off-phase can be calculated from $E_{\text{bias}} = (U_{\text{bias}} - U_{\text{bi}})/d$, neglecting space charge effects inside the device. Since no charge injection occurs for the bias voltages chosen, the observed luminance dynamics is solely determined by the remaining charges inside the device. The effect of the remaining electric field is different for the emission of the blue and red chromophores: While the red luminance decays almost exponentially with rising electric field, the blue emission experiences a saturation upon which it becomes field-independent. Since red emission is due to the recombination of mobile holes with electrons trapped on the red chromophore, the decay of red luminance with the electric field is interpreted as the extraction of holes from the device by the field-induced charge drift. The observed luminance decrease of around 30% within 1 μs at $E_{\text{bias}} = -3 \times 10^7$ V/m is consistent with the extraction of holes of mobility $\mu_{\text{h}} \approx 1 \times 10^6$ cm²/Vs from a relatively thin emission layer of less than 20 nm near the anode. In this interpretation the emission layer widens at higher operating voltages, since the luminance decrease is smaller for the devices operated at $U_{\text{drive}} = 5.0$ V. Extraction of mobile electrons is expected to occur on much shorter timescales due to the high electron mobilities. The observed blue emission should then be attributed to electrons at least partly immobilized in the lowest part of the density of states, upon which decay dynamics similar to that observed for the red emission is expected (compare eq. (5.4.6) below). The fact that the field dependence becomes flat above a critical time-dependent field value is indicative of the remaining emission being due to overall neutral states. This is attributed to tightly bound electron-hole pairs (geminate pair states) formed during device operation, which are only weakly influenced by the electric field and decay over time according to an Onsager-type mechanism. This decay is obvious from the dropping level of field-independent emission upon shifting the time of observation to larger values. By comparison of the remaining luminance values at 1 μs and 7 μs after termination of the driving voltage, an approximate lifetime of 7 μs is obtained for these geminate electron-hole pairs.

According to equation (5.2.1), the measured luminance ratio of red to blue emission can be renormalized to the $R/(B+G)$ color ratio discussed in chapter 4, upon which it also faithfully represents the ratio of the chromophore excitation rates. According to equation (4.4.6), both energy transfer from blue and green chromophores as well as sequential charge trapping contribute to the red emission. Using the already known efficiency $\eta_{\text{FT}} = 0.17$ of resonant energy transfer, it is possible to calculate the red emission attributed to sequential

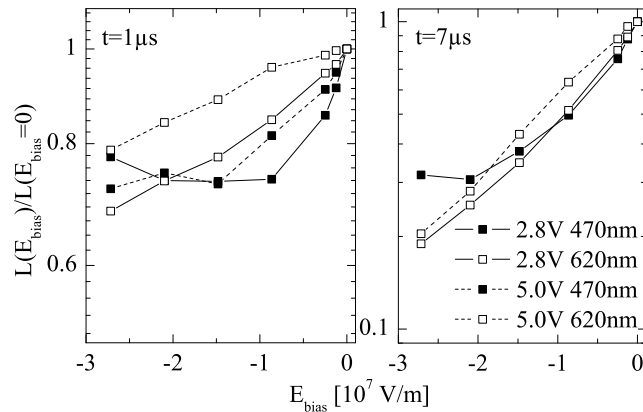


Figure 5.4: Delayed luminescence 1 μs (left) and 7 μs (right) after termination of the external driving voltage of 2.8 V (solid lines) and 5.0 V (dashed lines), measured at wavelengths of 470 nm (closed symbols) and 620 nm (open symbols). The bias electric field E_{bias} was varied between -2.7×10^7 V/m and approximately zero by applying bias voltages between 0 V and 2.2 V.

charge trapping. Figure 5.5 shows the result of such calculations applied to the delayed luminescence output under conditions of both low and high operating voltages as well as low and high bias electric fields. It is not surprising that the delayed red emission observed after driving the device at low operating voltages is mainly due to sequential charge trapping as significant amounts of electrons are expected to be trapped on the red chromophores during low-voltage equilibrium device operation. In this situation the blue and red emission rates follow the same decay behavior as long as the bias electric field is low. In accordance with the interpretation of the bias field dependence given above, this is attributed to the recombination of electrons that are immobilized on the blue-emitting manifold with mobile holes still present in the device due to their lower mobility. The recombination of these holes with the large quantity of electrons trapped on the red chromophores determines the decay behavior of the red emission. Since the recombination of the much lower density of immobilized electrons is proportional to the hole density, it actually follows the same decay behavior as the red emission. This is not as clearly seen for the experimental data collected at higher bias fields, since here both geminate pair recombination and recombination of immobilized electrons contribute to the blue emission. At the high driving voltage of $U_{\text{drive}} = 5.0$ V the situation is different as already known from chapter 4.5: A significant contribution to the excitation of red chromophores is attributed to resonant energy transfer from blue and green excitons, only a fraction being contributed by direct sequential charge trapping. During the first 500 ns after termination of the driving voltage, this situation changes drastically: While the contribution of energy transfer to red emission decays rapidly with the blue emission, the trapping contribution rises on the same time scale as the fast decay of blue emission, then levels off and slowly decays on longer timescales. Figure 5.6 shows the dependence of this fast blue luminance decay on the concentration of red chromophores. It is observed to be mainly independent of their concentration. The fast decay of blue emission is thus again attributed to extraction of the highly mobile electrons by the external bias and inadvertent space charge fields present in the device, before leveling off at some value determined by the

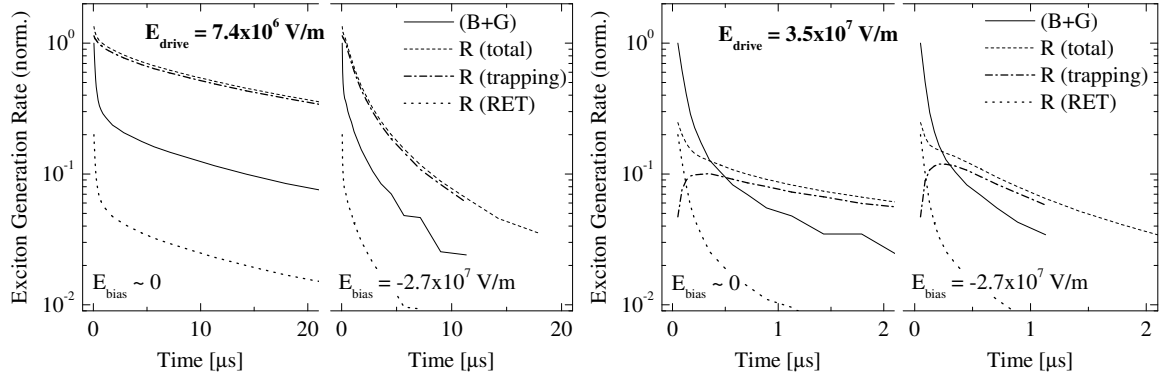


Figure 5.5: Measured excitation rates of blue+green ($B+G$) and red (R) chromophores after terminating the driving electric field of $E_{\text{drive}} = 7.4 \times 10^6$ V/m (left, operating voltage 2.8 V) and $E_{\text{drive}} = 3.5 \times 10^7$ V/m (right, operating voltage 5.0 V), normalized to that of the blue chromophores during equilibrium emission ($t = 0$). The bias electric field $E_{\text{bias}} = 0$ ($E_{\text{bias}} = 2.7 \times 10^7$ V/m) corresponds to a bias voltage of 2.2 V (0 V). The generation rate of red excitons (dashed) is shown splitted into the contribution of sequential charge trapping (dash-dotted) and resonant energy transfer from green and blue chromophores (dotted), which is proportional to the generation rate of blue and green excitons (solid line).

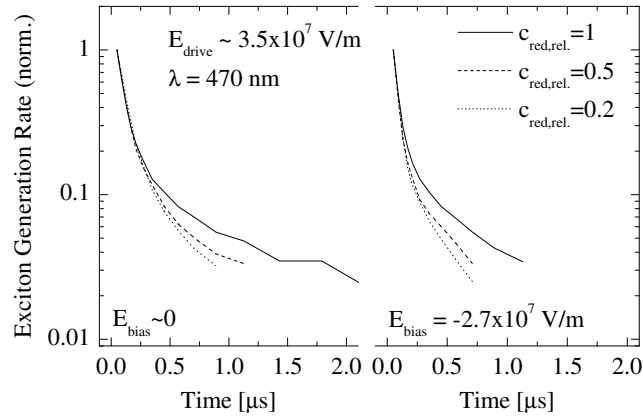


Figure 5.6: Concentration dependence of the blue chromophores luminance decay at two different electric bias fields. The concentration of the red chromophores is stated relative to that of PW. The active layer thickness varied, resulting in different driving voltages used to achieve a driving field of $E_{\text{drive}} \sim 3.5 \times 10^7$ V/m.

amount of immobilized electrons and geminate electron-hole pairs. During this extraction time, mobile electrons are trapped by red chromophores such that after only 1 μs the generation rate of red excitons from recombination of these trapped electrons with free holes dominates over that of blue excitons.

The slow decay of red emission has been shown to be due to recombination of trapped electrons and free holes whenever the bias electric field is low enough. A quantitative analysis of the time-domain decay behavior should thus provide insight into the density of recombining charges. Consider that according to equations (4.4.5) and (4.4.6)

$$L_B \propto \frac{e\mu_h}{\varepsilon\varepsilon_0} n_e n_h \quad (5.4.1)$$

$$L_R \propto \frac{e\mu_h}{\varepsilon\varepsilon_0} n_T n_h, \quad (5.4.2)$$

assuming that all remaining non-trapped electrons of density n_e are immobilized in deep states of the DOS and thus recombine with free holes at a rate $\gamma = e\mu_h/\varepsilon\varepsilon_0$ determined by the hole mobility. Further assume that the red emission attributed to energy transfer has been subtracted from L_R or is negligible. The charge densities evolve in time according to

$$\frac{\partial n_e}{\partial t} = +\frac{1}{e} \frac{\partial j_e}{\partial z} - \gamma n_e n_h, \quad (5.4.3)$$

$$\frac{\partial n_h}{\partial t} = -\frac{1}{e} \frac{\partial j_h}{\partial z} - \gamma(n_e + n_T)n_h, \quad (5.4.4)$$

$$\frac{\partial n_T}{\partial t} = -\gamma n_T n_h. \quad (5.4.5)$$

After termination of the driving voltage, the current densities $j_{e,h}$ of electrons and holes are solely determined by the evolution of space charges inside the device. Since the interest here lies in modeling the slow luminance decay, it is understood that the currents associated to redistribution of charges have decayed to a level where they might be neglected. Note that the model by design will not be able to deal with the occurrence of luminance spikes and similar events. It is further assumed, as in chapter 4.5, that the integrated luminance can be approximated by the recombination of charges inside an effective recombination zone characterized by a single charge density value for each species. Under the condition that the density of free electrons $n_e \ll n_T$ is much less than that of trapped electrons n_T , the time evolution is

$$n_e(t) = \frac{n_e(0)n_T(t)}{n_T(0)}, \quad (5.4.6)$$

$$n_h(t) = \frac{\Delta n_h(0)}{n_h(0) - n_T(0) \exp(-t\gamma\Delta)}, \quad (5.4.7)$$

$$n_T(t) = \frac{\Delta n_T(0)}{n_h(0) \exp(t\gamma\Delta) - n_T(0)} = n_h(t) - \Delta, \quad (5.4.8)$$

where $\Delta = n_h(0) - n_T(0)$. Two limiting cases are discussed: for $-\Delta \gg n_h(0)$,

$$n_h(t) \approx n_h(0) \exp(-t\gamma n_T(0)) \quad (5.4.9)$$

$$n_T(t) \approx n_T(0) \quad (5.4.10)$$

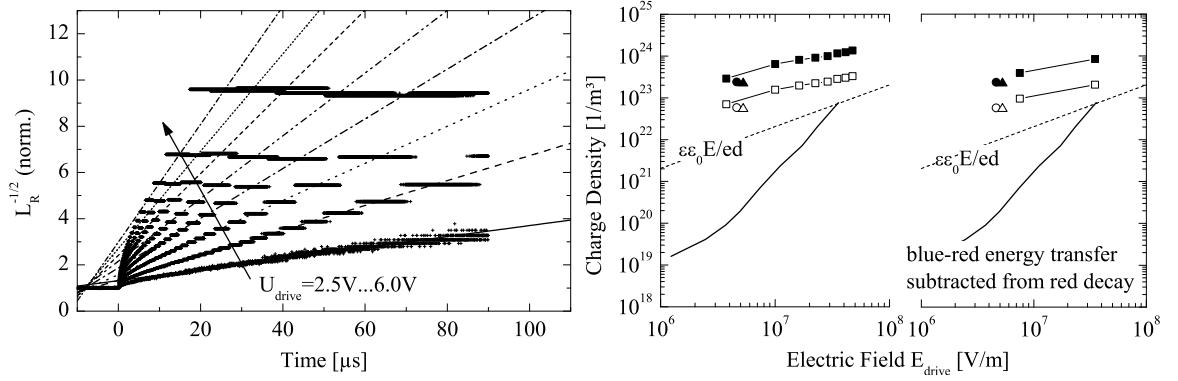


Figure 5.7: Left: Results of fitting the red emission decay observed for **PW** devices by equation (5.4.13). Drive voltages were varied between 2.5 V and 6.0 V in steps of 0.5 V, the bias voltage was 2.2 V, the raw data (not smoothed as described above) is shown. Right: Calculated charge densities plotted against the driving electric field strength, using hole mobilities according to the parameters of table 4.1 for an assumed electric field of $E = 0$ (solid symbols) and $E = 2 \times 10^7$ V/m (open symbols). Results are shown for devices with full (squares), 50% (circles) and 20% (triangles) concentration of the red chromophore relative to **PW**. The solid line indicates the approximate hole density calculated from the experimental $R/(B+G)$ color ratio.

and the density of filled traps decreases exponentially in time with a characteristic decay time of $\tau = (\gamma n_T(0))^{-1}$. The luminance accordingly decays as $L_B(t)/L_B(0) = L_R(t)/L_R(0) = \exp(-t\gamma n_T(0))$. A similar result holds for $\Delta \gg n_T(0)$. On the contrary, it is generally reasonable to assume $\Delta \ll n_h(0), n_T(0)$ since overall charge neutrality is generally considered to be one of the driving forces in bipolar devices. The solution of equations (5.4.6) to (5.4.8) is then simplified to

$$n_h(t) \approx n_T(t) \quad (5.4.11)$$

$$n_T(t) \approx \frac{n_T(0)}{1 + t\gamma n_T(0)}, \quad (5.4.12)$$

upon which the luminance decay is

$$L_B(t)/L_B(0) = L_R(t)/L_R(0) = \frac{1}{(1 + t\gamma n_T(0))^2}. \quad (5.4.13)$$

As evidenced by figure 5.5, the luminance decay is clearly not a single exponential function of time and thus an analysis in terms of equation (5.4.13) might be more appropriate. Figure 5.7 shows the raw data of a delayed EL measurement at a wavelength of 620 nm parametric in the drive voltage U_{drive} . The luminance values were rescaled to the equilibrium emission and are shown as inverse square root. According to equation (5.4.13)

$$L_R^{-1/2}(t) = L_R(0)(1 + \gamma n_T(0)t), \quad (5.4.14)$$

which is a linear function of time. The experimental data does indeed follow an approximately linear slope when the first 10 μ s are excluded from the analysis. The hole mobility μ_h

was already determined and is described in the framework of the Gaussian disorder formalism using the parameters from table 4.1. The initial density of filled traps $n_T(0)$ can thus be calculated from the slope to intercept ratio determined from a linear regression of the data. Figure 5.7 shows the result of such calculations for the luminance decay measured for a **PW** device as well as for devices where the concentration of red chromophores was reduced to 50% and 20% relative to that of **PW**. In order to calculate the charge mobility some knowledge of the prevailing electric field is needed. Note that the relevant value is not directly connected to the driving electric field since this only prevails during equilibrium operation. After termination of the driving voltage, the remaining electric field is determined by space charges. The approximate spread of possible results is indicated by calculating the charge densities using hole mobilities at two different field strengths. Estimated hole densities are also shown for comparison, being derived from the experimental $R/(B+G)$ color ratio using equation (4.4.11) and using the values of E_{diff} and $a'N_0$ as determined for the similar polymer **PW2** in section 4.5. The charge densities obtained from the decay analysis are nearly proportional to the driving electric field, in contrast to the calculated hole densities which are roughly proportional to E_{drive}^3 . Note that the calculated $n_T(0)$ values are comparable both in field dependence as well as absolute values to the capacitance space charge limitation $n = \epsilon\epsilon_0 E/ed$ where d is the thickness of the active polymer layer. One could thus speculate that the amount of filled trap states is mainly determined by space charge limitations: when the trapped charge density rises to much higher values, charge transport is inhibited since the space charge field dominates over the externally applied driving field. The question arises as to why strong variation of the red emission contribution is observed even though the trap filling level is rather constant. According to equation (4.3.6) the trap occupation is proportional to n_e/n_h if not limited by space charges or the total amount of available traps, while the amount of red emission is determined by the product $n_T n_h$ which varies more strongly with the electric field due to the field dependence of n_h . It is somewhat surprising that equation (5.4.14) should yield reasonable results since $\Delta \ll n_h(0), n_T(0)$ is not met under the conditions of figure 5.7. Additionally, the determined charge densities are near the actual density of red chromophores of roughly $3.4 \times 10^{23} \text{ m}^{-3}$. Since it is inherently difficult to analyze the space-charge determined recombination dynamics much further in an analytic way, numerical device simulations are employed to explore the recombination dynamics during delayed EL.

The device simulations used here are based on a numerical solution of drift-diffusion equations and include appropriate rate equations for charge trapping on the red chromophores. The simulation algorithm is described in more detail in appendix A. The **PW** light-emitting devices are modeled as 80 nm thick emission layer consisting of 160 equidistant simulation cells, the simulated device area (sample capacity) and series resistance are chosen to match the experimental conditions. Charge transport is modeled using the charge mobilities for electron and hole drift as determined in chapters 2 and 4 for **PB** and **PW** devices. Electron injection currents are modeled by a fixed field-dependent injection current as determined in chapter 3 for blue light-emitting devices comprising a **PB** layer. This approach was already successfully employed to model the transient luminescence observed for **PB** light-emitting devices, see chapter 3. It was shown that hole injection into devices comprising a **PB** emission layer is inefficient and enhanced by electron accumulation or trapping near the anode/polymer interface. Hole injection into **PW** is thus also expected to display a compli-

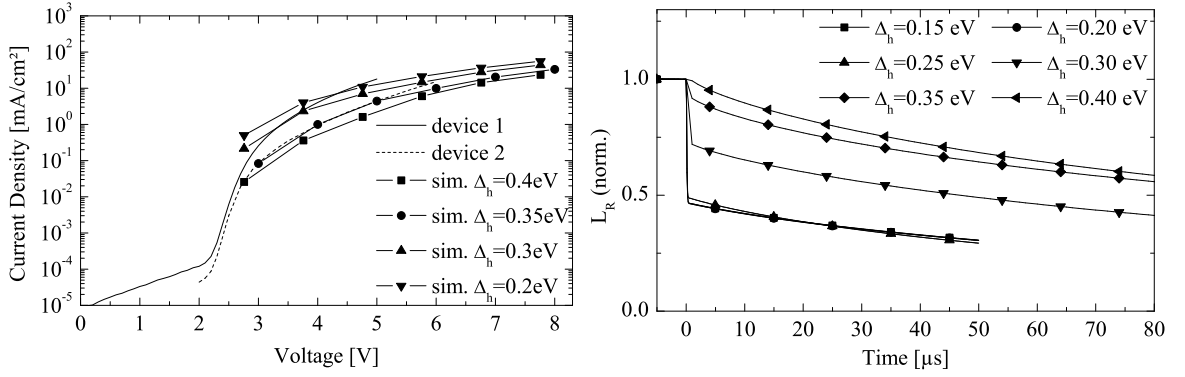


Figure 5.8: Left: Comparison of simulated (symbols) and measured (solid and dashed lines) current-voltage characteristics for different choices of the hole injection barrier used in the simulation. Right: Simulated delayed EL from recombination of trapped electrons after termination of a 3 V driving voltage ($U_{\text{bias}} = U_{\text{bi}}$ V), parametric in the hole injection barrier.

cated field dependence, not easily modeled without detailed studies of the device behavior. Since this chapter mainly deals with the delayed EL processes, it is not of central interest to achieve a numerical simulation of switch-on or equilibrium device behavior. The hole injection is therefore modeled by the field-dependent charge injection model by Scott and Malliaras [28] which is described in more detail in appendix A. The hole injection barrier energy is considered as a model parameter and its impact will be discussed in the context of the analysis of simulation results where appropriate. The density of states was assumed as $N_0 = 10^{27} \text{ m}^{-3}$, the trap density was $N_T = 4 \times 10^{23}$. Blue-red energy transfer as quantified in chapter 4.2 is included in the simulation by rate equations relating the corresponding exciton densities. It is not expected that the simulated decay transients faithfully reproduce the measurement results over the whole time range. The simulation model in terms of free and trapped charges is strongly simplified and does not reproduce the device behavior at short timescales, where geminate charge recombination has been shown to be significant.

Figure 5.8 compares simulated current-voltage characteristics for different choices of the hole injection barrier with experimental results from two independently prepared devices. The experimental spread of current densities is rather large, partially owned to interface conditioning effects, inadvertent sample contaminations and imperfections. The simulated current-voltage characteristics deviates from the measured values at voltages lower than 4 V, mainly due to the details of the injection model used. At higher voltages, the correspondence is sufficiently good since the interest here lies in the analysis of the decay dynamics. A general tendency exists towards a stronger contribution of red emission in equilibrium and stronger red emission in delayed EL at higher hole injection barriers, which is attributed to the reduced hole densities as predicted by equation (4.4.11). Figure 5.9 shows the calculated electric field distribution for equilibrium device operation at an average electric field of $3.2 \times 10^7 \text{ V/m}$. At termination of the external driving voltage, the average internal field drops to zero, but the space charges and strong field gradients remain. Thus, electric fields on the order of $2 \times 10^7 \text{ V/m}$ should be expected and will inevitably impact the recombination rate of free holes with trapped electrons. The right side of figure 5.9 shows the simulated

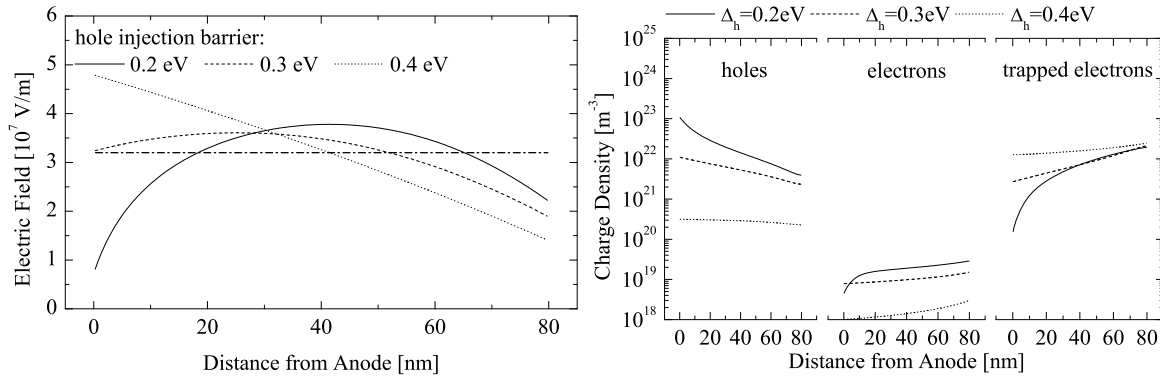


Figure 5.9: Left: Simulated distribution of the internal electric field at an average value of 3.2×10^7 V/m (dash-dotted line), parametric in the hole injection barrier. Right: Simulated charge density distributions of free holes, free electrons and trapped electrons, parametric in the hole injection barrier Δ_h .

steady-state charge distributions of free holes and electrons as well as of trapped electrons. While the free electron density is rather low, free hole and trapped electron densities are on the same order of magnitude and thus mutually determine device operation both before and after termination of the driving voltage. The hole density is strongly influenced by the hole injection barrier, so absolute values should be considered with caution. To gain additional insight into the driving field dependence of the charge densities, their values at $z = 40$ nm in the center of the polymer layer are plotted as function of field in figure 5.10. Strongly field-dependent hole densities as suggested by figure 5.7 are only found for large hole injection barriers on the order of 0.4 eV, consistent with the notion of strongly injection limited hole currents found in these devices. At lower injection barriers, the density of holes and trapped electrons is similar since charge neutrality prevails under that condition. It is important to note that strong negative space charges are accumulated by electron trapping although the density of free electrons remains low throughout device operation. The simulated delayed EL dynamics was analyzed according to equation (5.4.14). Figure 5.10 shows that this analysis indeed provides reasonable insight into the actual simulated density of trapped electrons. Again, this is rather surprising since the results are nearly independent of the hole injection barrier although equation (5.4.14) is not applicable in the case of the reduced hole densities. In order to clarify this, an additional evaluation of the simulated decays is carried out according to the assumptions of equation (5.4.9) which predicts

$$\log(L_R(t)) = \log(L_R(0)) - \gamma n_T(0)t. \quad (5.4.15)$$

The results of fitting the luminance decay in the time range of 40 μ s to 50 μ s after termination of the driving voltage by equation (5.4.15) are shown in figure 5.11 in direct comparison to those obtained via equation (5.4.14). Surprisingly, the Langevin and exponential decay analysis yield very similar results, proving that each of these analysis methods is sufficient to at least approximately calculate trapped charge densities from the decay of trap emission. Approximate equivalence of both analysis methods was also found for the experimentally determined delayed EL (not shown). The equivalence of these results is not evident from

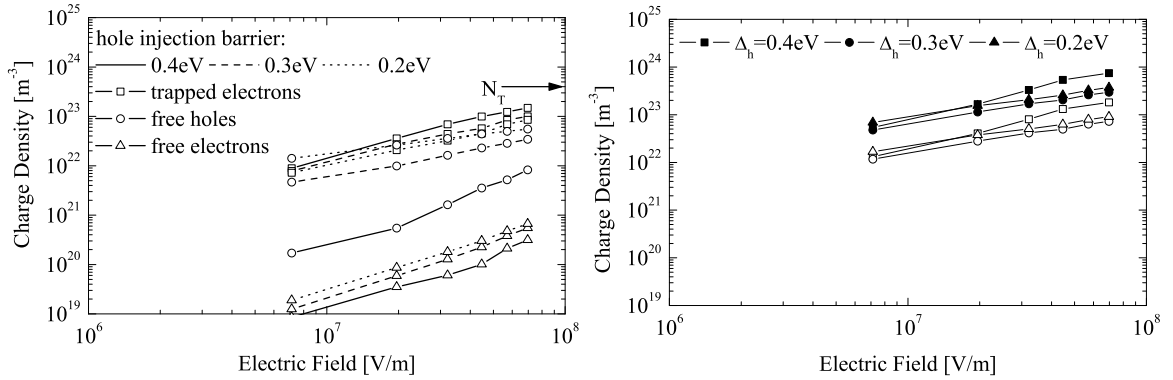


Figure 5.10: Left: Simulated charge densities for free holes, free electrons and trapped electrons at $z = 40$ nm. Right: Charge densities calculated from an analysis of the simulated transient EL decay according to equation (5.4.14), the corresponding transients are shown in figure 5.11. The hole mobilities used were that of zero electric field (solid symbols) and that at 2×10^7 V/m.

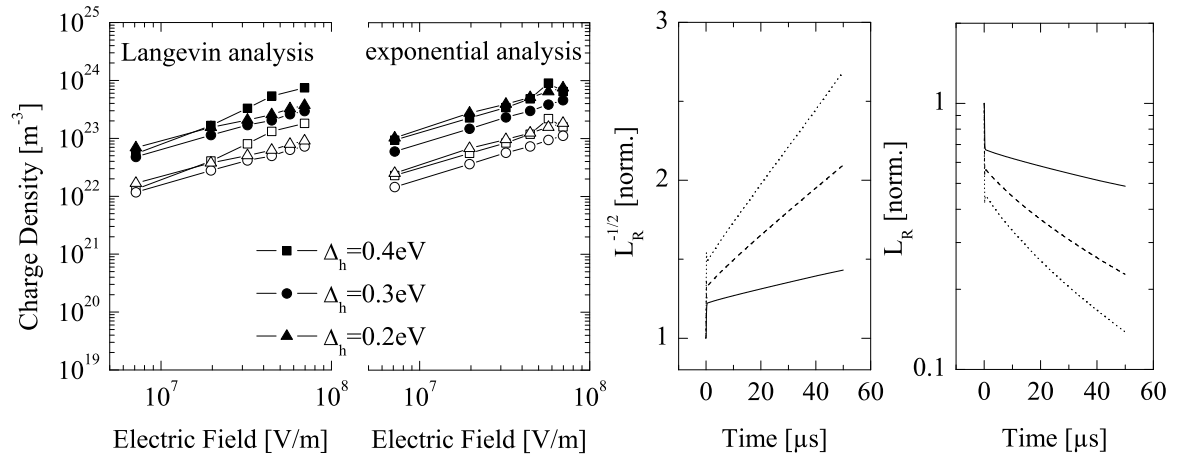


Figure 5.11: Left: Comparison of charge densities calculated from simulated decay transients via equation (5.4.14) (left side, compare fig. 5.10) and equation (5.4.15) (right side). Hole mobilities were calculated at either $E = 0$ (closed symbols) or at $E = 2 \times 10^7$ V/m (open symbols) to estimate the effect of space charge fields on the results. Right: Simulated decay transients for $\Delta_h = 0.3$ eV at $E_{\text{drive}} = 7 \times 10^6$ V/m (solid lines), 3.2×10^7 V/m (dashed lines) and 5.7×10^7 V/m (dotted lines), normalized to the equilibrium emission. The bias voltage is $U_{\text{bias}} = U_{\text{bi}}$ such that the internal field after termination of the driving voltage is only determined by the space charges. As discussed, the simulation model does not (and is not expected to) faithfully reproduce the experimental transients on timescales of less than $5 \mu\text{s}$, compare figure 5.7.

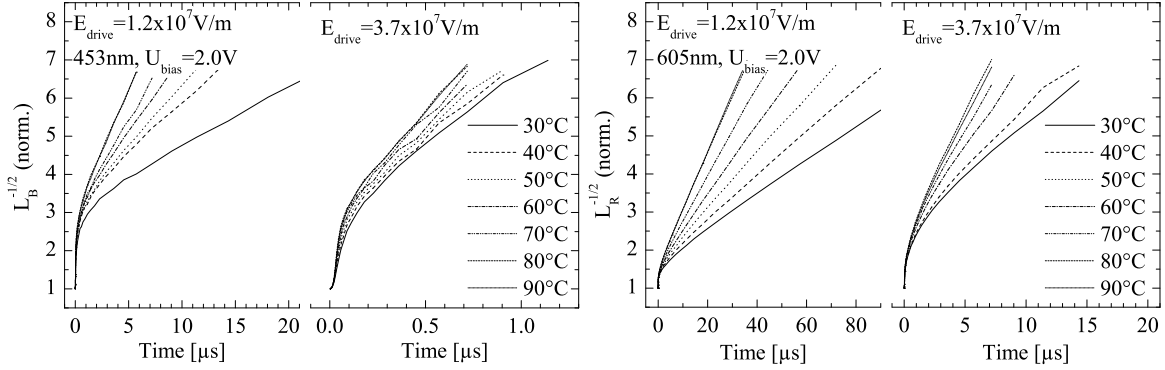


Figure 5.12: Temperature dependence of the delayed emission measured for PW light emitting devices at 453 nm (left) and 605 nm (right) for low (left side of each plot) and high (right side of each plot) driving fields.

equations (5.4.14) and (5.4.15) and is attributed to non-vanishing space-charge induced currents, leading to some averaging effect not covered by the simple approximations used for these equations.

Finally, the temperature dependence of the luminance decay was measured between 30°C and 90°C and is displayed in figure 5.12 in terms of the inverse square root representation suggested by equation (5.4.14). The observed time scale of emission decay strongly depends on the ambient temperature, where the faster decays are found at higher temperature. The decay of delayed blue emission measured after driving the device at $E_{\text{drive}} = 3.7 \times 10^7$ V/m is rather different from the other measured dynamics in not being accelerated significantly by rising temperatures. Further above, this emission was already attributed to the recombination of geminate electron-hole pairs formed during device operation instead of the recombination of free holes with trapped electrons. The bias field dependence discussed for figure 5.4 indicated that in excess of 70% of the emission up to 1 μs after termination of the driving voltage is due to geminate charge pairs, which are not easily separated by raising the electric field or temperature. For those cases where the delayed EL was attributed to space charges, the effect of temperature cannot be neglected. Again, the case of low driving voltage and emission in the red spectral region is the easiest to analyze, the blue emission as before showing similar decay dynamics being coupled to the same hole density. A pronounced dependence of the density of trapped electrons on the ambient temperature is not expected, the trap depth being too large for thermal detrapping to occur. The trap filling level is more or less determined by space charge effects with only slight variations upon changing the hole density due to recombination. Figure 5.13 shows an analysis of the temperature dependent delayed EL according to equation (5.4.14), explicitly pointing out the influence of the temperature dependence of hole mobility. Assuming that significant space charge induced electric fields remain after termination of the driving voltage, the analysis indeed reproduces the approximate independence of the trap filling level on temperature. This has to be considered only as indicative of the role of charge mobility since the actual value of electric field needed to yield temperature-independent charge densities is somewhat higher than what would be expected at low driving fields.

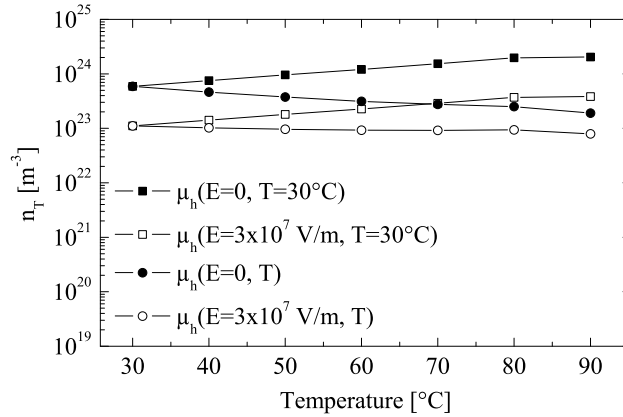


Figure 5.13: Analysis of the temperature dependence of the red luminance decay at $E_{\text{drive}} = 1.2 \times 10^7 \text{ V/m}$ and $E_{\text{bias}} \approx 0$. Square symbols denote trapped electron densities calculated using equation (5.4.14) by neglecting the temperature dependence of charge mobility. Results obtained by including it into the calculation are shown as circles. Results were obtained for an assumed space charge field of $E = 0$ (closed symbols) as well as of $E = 3 \times 10^7 \text{ V/m}$ (open symbols).

5.5 Conclusion

This chapter analyzed the physical effects governing delayed electroluminescence observed from polymer light-emitting devices after termination of the driving electric field. It was shown that the delayed EL of devices with an emission layer comprising the **PW** polymer can be separated into the dynamics of free electrons/free holes and trapped electrons/free holes. Free electrons, having a rather high mobility, leave the device rapidly and are partly responsible for the observed fast luminance modulation. A significant part of electrons is found to be bound by a geminate hole forming a neutral species which cannot be extracted by an electric field. These states are supposed to be formed during device operation and exhibit lifetimes on the order of $7 \mu\text{s}$. During extraction, electrons are additionally found to be trapped on the red chromophore, which enhances the contribution of trapping-induced red emission compared to red emission attributed to blue-red resonant energy transfer. The trapping-induced red emission was analyzed in more detail by employing a simple analytical model for the recombination of free holes with trapped electrons. The method was shown to provide reasonable insight into the prevailing density of trapped electrons, which is found to be rather high and closely following the space charge limitation imposed by the sample capacitance. Numerical simulations of the delayed EL emission were employed to assess the applicability of this method despite the obviously strong approximations used in its derivation. Finally, the influence of temperature on the decay of red emission was analyzed. The fraction of blue emission that was attributed to geminate pair recombination showed only negligible thermal activation, contrary to the trapping-induced red emission. The thermal activation behavior of this emission could at least partly be explained by the thermal activation of hole mobility in the **PW** polymer layer assuming the presence of sufficiently strong space-charge fields.

Chapter 6

Applications and Limits of the CELIV Technique

6.1 Introduction

The measurement of charge carrier mobilities by the time-of-flight (*TOF*) technique as discussed in chapter 2 has been in use already for several decades to study organic semiconductors. It allows to assess the charge mobilities for both electrons and holes individually and the interpretation of results is straightforward. Current research in the field of small molecule and polymeric semiconductor devices focuses on the properties of single and multilayer thin film structures with a typical total thickness of less than 100 nm. Such structures are of considerable interest for research both in the field of organic light-emitting diodes as well as for organic solar cells. While for polymeric light-emitting diodes, efforts are often concentrated on materials that yield amorphous structures, polymer/small molecular as well as polymer/polymer solar cells with mixed donor/acceptor materials usually require phase separation to provide sufficient interface area for an efficient splitting of excitons into free charge carriers. Fabrication of these material blends requires to strictly follow recipes concerning the solution parameters, spincoating and thermal annealing steps to yield certain morphologies. This prohibits the manufacturing of TOF samples since the desired layer morphology can only be achieved for specific film thicknesses. Although the absorption coefficient of typical solar cell organic materials is rather high, the functional structures are thin and radiation is absorbed over nearly the whole layer and thus TOF experiments are not feasible. It has been demonstrated that such experiments can be performed by injecting charges from a selectively excited charge generation layer, but this requires sufficient matching of energy levels to prevent the creation of injection barriers for the charges. Another drawback of the TOF technique is its limitation to low charge carrier densities. TOF measurements do not provide reasonable results when the dielectric relaxation time $\tau_{\sigma} = \epsilon\epsilon_0/en\mu$ is much shorter than the transit time of charges $t_{tr} = d/\mu E$ in the applied field E across the film thickness d . Thus, TOF measurements are usually limited to $n \ll 5 \times 10^{22} \text{ m}^{-3}$, assuming $E = 3 \times 10^7 \text{ V/m}$, $d = 100 \text{ nm}$ and $\epsilon = 3$.

As an alternative to time-of-flight photocurrent measurements, Juška et al. [167, 168] introduced the ‘current extraction under linearly increasing voltage’ (*CELIV*) technique for the measurement of charge carrier mobility even under conditions of $\tau_{\sigma} \ll t_{tr}$. The basic CELIV principle assumes the presence of a homogeneous density of (intrinsic) charge carriers, where the total charge density is zero, i.e. electrons and holes compensate for each other. The technique is only applicable to analyze the charge mobility of the majority charge carrier, i.e. in case of organic semiconductors the carrier type with higher mobility. The mobile charges are extracted by an applied voltage that increases linearly in time, thereby charging

the capacitance provided by the sample electrodes with a constant current. The resulting current deviation from the purely capacitive response is due to moving charges and can be used to calculate charge mobility as well as charge density. Since organic semiconductors usually have negligible intrinsic carrier density due to the large bandgap, the method was later expanded by creating the charge density needed for the measurement by the absorption of pulsed laser radiation.[169–171] Contrary to TOF, these charges should be created homogeneously across the layer which explicitly allows the measurement to be performed on thin films.

6.2 Analytic Description of CELIV Transients

Assume that at $t = 0$ the density of holes and electrons is equal ($n_h = n_e = n$) and independent of position within the semiconductor. Assume that only one type of charge carrier is mobile (here, hole mobility $\mu = \mu_h \gg \mu_e$ is much larger than electron mobility without loss of generality) and that bimolecular recombination of electrons and holes can be neglected. Consider a semiconductor sheet between two noninjecting electrodes as in the one-dimensional model shown in figure 6.1 and the application of an external voltage $U_{\text{ext}} = U'_{\text{ext}} \cdot t$ with constant time derivative U'_{ext} . At sufficiently low densities of free charge carriers, space charge effects can be ignored and a mobile charge will take the transit time $t_{\text{tr}} = d \sqrt{\frac{2}{\mu U'_{\text{ext}}}}$ to travel across the layer from the anode side ($z = 0$) to the cathode ($z = d$). The situation is somewhat more complex in case of arbitrary densities of free charges. In this case, the electric field will drop across the region which has been depleted of free charges but else stays constant. Thus, the mobile charges move homogeneously at the same speed and the total charge density $\rho(z, t)$ is given by

$$\rho(z, t) = \begin{cases} -en & 0 \leq z \leq l(t) \\ 0 & \text{else,} \end{cases} \quad (6.2.1)$$

see figure 6.1. Here, $l(t)$ is the time-dependent extraction depth up to which holes are depleted from the layer due to drift in the electric field. The electric field $E(z, t)$ due to the

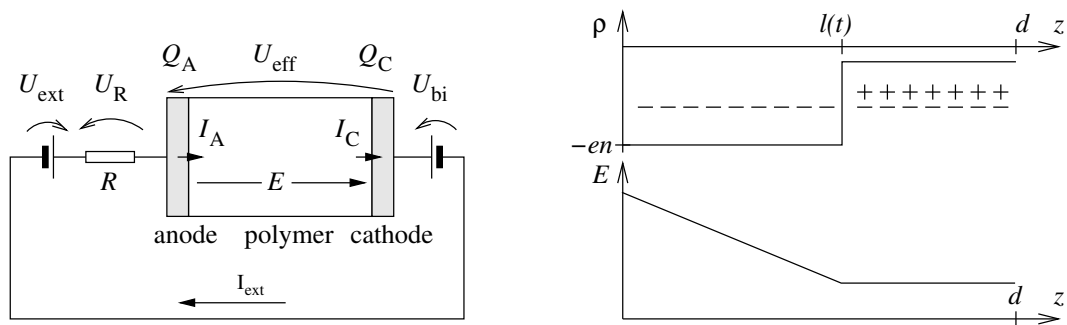


Figure 6.1: Left: Schematic circuit model used for the discussion of the CELIV measurement technique. Right: Schematic charge distribution and resulting electric field for the case of mobile holes and immobile electrons.

time dependent charge density is calculated from the Poisson equation $\partial_z E = \rho/\epsilon\epsilon_0$ as

$$E(z) = \frac{Q_A - Q_C}{2\epsilon\epsilon_0 A} + \frac{enl(t)}{2\epsilon\epsilon_0} - \begin{cases} \frac{enz}{\epsilon\epsilon_0} & 0 \leq z \leq l(t) \\ \frac{enl(t)}{\epsilon\epsilon_0} & \text{else,} \end{cases} \quad (6.2.2)$$

where A is the electrode surface area and $Q_{A,C}$ are the anodic and cathodic surface charges with time dependence $\partial_t Q_A = I_{\text{ext}} = (U_{\text{ext}} - U_{\text{eff}})/R$ and $\partial_t Q_C = -I_{\text{ext}} + I_C = -(U_{\text{ext}} - U_{\text{eff}})/R + Aen\partial_t l(t)$, assuming a vanishing contact potential $U_{\text{bi}} = 0$ without loss of generality. The effective potential drop across the sample is

$$U_{\text{eff}} = \int_0^d E(z)dz = \frac{Q_A - Q_C}{2C} - \frac{enld}{2\epsilon\epsilon_0} \left(1 - \frac{l}{d}\right), \quad (6.2.3)$$

where $C = \epsilon\epsilon_0 A/d$ is the sample capacitance. The electric field is constant for $l < z < d$ and thus the extraction depth $l(t)$ has the time dependence

$$\frac{dl(t)}{dt} = \mu E(l(t), t) \quad (6.2.4)$$

and using equations (6.2.2) and (6.2.3) can be rewritten as

$$\frac{dl(t)}{dt} + \frac{en\mu l^2(t)}{2d\epsilon\epsilon_0} = \frac{\mu U'_{\text{eff}} t}{d}, \quad (6.2.5)$$

This is a first order nonlinear differential equation of Ricatti type for $l(t)$. Before discussing an appropriate solution in more detail, the resulting current density is calculated. This can be done in a consistent way by calculating the explicit time dependence of $U_{\text{eff}}(t)$. From equation (6.2.3),

$$U'_{\text{eff}}(t) = \frac{U_{\text{ext}} - U_{\text{eff}}}{RC} + \frac{enl'(t)}{\epsilon\epsilon_0} (l - d), \quad (6.2.6)$$

which has the solution

$$U_{\text{eff}}(t) = U'_{\text{ext}} \cdot t + RC \left(\frac{enl'(t)}{\epsilon\epsilon_0} (l(t) - d) - U'_{\text{ext}} \right) (1 - e^{-t/RC}) + U_{\text{eff}}(0) e^{-t/RC} \quad (6.2.7)$$

In the limit of $t \gg RC$, the current flowing in the external circuit is

$$I_{\text{ext}} = \frac{U_{\text{ext}} - U_{\text{eff}}}{R} \xrightarrow{t \gg RC} CU'_{\text{ext}} + Aenl'(t) \left(1 - \frac{l(t)}{d}\right), \quad (6.2.8)$$

and using equation (6.2.5) the current density with respect to the electrode area is

$$j_{\text{ext}} = \frac{\epsilon\epsilon_0}{d} U'_{\text{ext}} + \begin{cases} \frac{en}{d} \left(1 - \frac{l(t)}{d}\right) \left(\mu U'_{\text{eff}} t - \frac{en\mu l^2(t)}{2\epsilon\epsilon_0}\right) & l(t) \leq d \\ 0 & l(t) > d. \end{cases} \quad (6.2.9)$$

The initial conditions at $t \rightarrow 0$ ($t \gg RC$) are

$$l(0) = 0 \quad (6.2.10)$$

$$\left. \frac{dl}{dt} \right|_{t=0} = 0 \quad (6.2.11)$$

$$j_{\text{cap}} := j_{\text{ext}}(0) = \frac{\epsilon\epsilon_0 U'_{\text{ext}}}{d} \quad (6.2.12)$$

$$\left. \frac{d}{dt} \left(\frac{j_{\text{ext}}(t)}{j_{\text{ext}}(0)} \right) \right|_{t=0} = \frac{en\mu}{\epsilon\epsilon_0}, \quad (6.2.13)$$

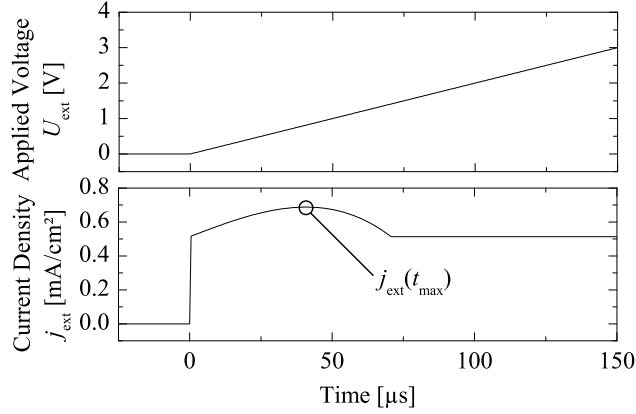


Figure 6.2: Approximate CELIV current transient in the low conductivity approximation $\tau_\sigma \gg t_{tr}$ according to equation (6.2.15), using the parameters $R = 30 \Omega$, $\varepsilon = 2.9$, $A = 1 \text{ mm}^2$, $d = 100 \text{ nm}$, $\mu = 2 \times 10^6 \text{ cm}^2/\text{Vs}$, $n = 10^{22} \text{ m}^{-3}$, $U'_{ext} = 2 \times 10^4 \text{ V/s}$.

where $j_{ext}(0) = j_{cap}$ is the capacitive charging current.

The Riccati equation (6.2.5) admits an analytic solution in case of sufficiently small charge mobility $\mu \ll \left(\frac{\varepsilon\varepsilon_0}{end}\right)^2 \frac{U'_{ext}}{2}$, i.e. when the dielectric relaxation time $\tau_\sigma = \frac{\varepsilon\varepsilon_0}{en\mu} \gg t_{tr}$ is much larger than the transit time t_{tr} at sufficiently low charge densities:

$$l(t) = \frac{\mu U' t^2}{2d}. \quad (6.2.14)$$

Since in this case

$$\frac{en\mu l^2}{2\varepsilon\varepsilon_0} \sim \frac{en\mu d^2}{2\varepsilon\varepsilon_0} \ll \mu U'_{ext} t \sim \mu U'_{ext} t_{tr},$$

the current transient simplifies to

$$j_{ext}(t) = \frac{\varepsilon\varepsilon_0}{d} U'_{ext} \left(1 - e^{-t/RC}\right) \left(1 - \begin{cases} \frac{t}{\tau_\sigma} \left(\frac{t^2}{t_{tr}^2} - 1\right) & t \leq t_{tr} \\ 0 & t > t_{tr} \end{cases}\right), \quad (6.2.15)$$

which is of parabolic shape and assuming $t \gg RC$ has a maximum at $t_{max} = d\sqrt{\frac{2}{3\mu U'_{ext}}} = t_{tr}/\sqrt{3}$ of height

$$j_{ext}(t_{max}) = \frac{\varepsilon\varepsilon_0 U'_{ext}}{d} + en \left(\frac{2}{3}\right)^{3/2} \sqrt{\mu U'_{ext}},$$

compare to figure 6.2. The relative height of this maximum is

$$\frac{\Delta j_{ext}}{j_{cap}} = \frac{j_{ext}(t_{max}) - j_{cap}}{j_{cap}} \quad (6.2.16)$$

$$= \frac{end}{\varepsilon\varepsilon_0} \left(\frac{2}{3}\right)^{3/2} \sqrt{\frac{\mu}{U'_{ext}}} = \frac{2}{3\sqrt{3}} \frac{t_{tr}}{\tau_\sigma} \quad (6.2.17)$$

which means that this approximation is only useful when $\Delta j_{\text{ext}} \ll j_{\text{cap}}$. While equation (6.2.13) in principle allows to calculate the mobility for a known carrier density n , equation (6.2.17) results in

$$en\mu = \frac{3 \Delta j_{\text{ext}} \varepsilon \varepsilon_0}{2 j_{\text{cap}} t_{\text{max}}} \quad (6.2.18)$$

$$\mu = \frac{2d^2}{3U'_{\text{ext}} t_{\text{max}}^2}, \quad (6.2.19)$$

from which the conductivity $\sigma = en\mu$, the charge mobility μ and the charge density n can be calculated using only experimentally accessible parameters. Since $\Delta j/j(0) \ll 1$ implies a low signal to noise ratio, this approximation does not provide adequate analysis for an experimental determination of charge mobility.

6.3 Numerical Analysis of CELIV Transients

Dimensionless variables are introduced by choosing

$$\underline{l} = d^{-1}l \quad (6.3.1)$$

$$\underline{t} = \tau_{\sigma}^{-1}t \quad (6.3.2)$$

$$\underline{U}' = \frac{\varepsilon^2 \varepsilon_0^2}{2e^2 n^2 \mu d^2} U'_{\text{ext}} \quad (6.3.3)$$

$$\underline{j} = \frac{\varepsilon \varepsilon_0}{2e^2 n^2 \mu d} j_{\text{ext}}, \quad (6.3.4)$$

upon which equation (6.2.5) is transformed into the form

$$\frac{d\underline{l}(\underline{t})}{d\underline{t}} + \frac{1}{2}\underline{l}^2(\underline{t}) = 2\underline{U}'\underline{t}. \quad (6.3.5)$$

The time evolution of the dimensionless current density \underline{j} is

$$\underline{j}(\underline{t}) = \underline{U}' + \begin{cases} [1 - \underline{l}(\underline{t})] (\underline{U}'\underline{t} - \frac{1}{4}\underline{l}^2) & \underline{l}(\underline{t}) \leq 1 \\ 0 & \underline{l}(\underline{t}) > 1. \end{cases} \quad (6.3.6)$$

Thus, the extraction depth \underline{l} only depends on the derivative \underline{U}' . As shown below, the experimentally accessible range of this parameter is $-3 < \log(\underline{U}') < 3$. Figure 6.3 shows the numerical solutions of equation (6.3.5) as obtained by the `NDSolve[]` function provided by *Mathematica 6.0* (Wolfram Research) for the boundary condition $\underline{l}(0) = 0$ in the range $0 \leq \underline{t} \leq 10$. Based on this solution set, the current density is easily calculated, see figure 6.3. Figure 6.4 shows characteristic parameters and their dependence on the dimensionless voltage derivative \underline{U}' , which compare well with those published by Juška et al. [167]. The resulting values for $\Delta j/j(0) = \Delta j_{\text{ext}}/j_{\text{cap}}$ are in the range of 10^{-2} to 10 and thus correspond well to the parameter regime accessible by experimental methods, being bounded below by the resolution of oscilloscopes used for recording the current transient and above by the amount

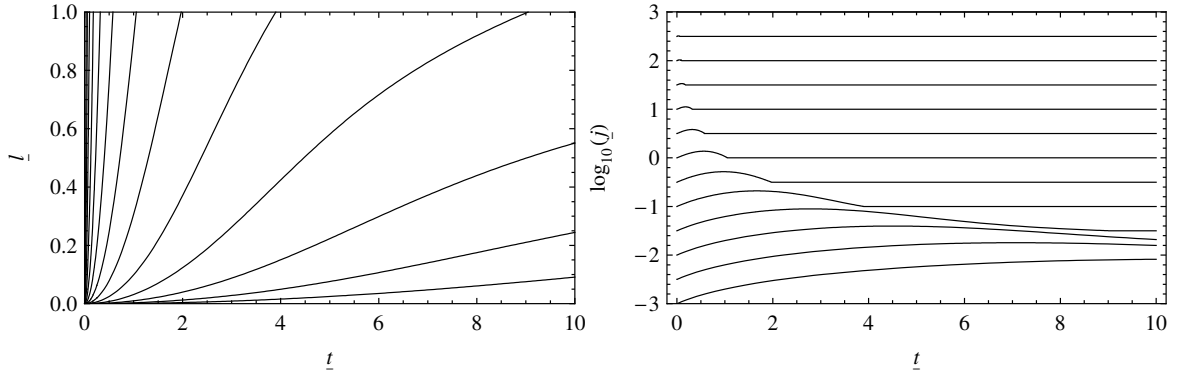


Figure 6.3: Left: Numerical solutions of the Riccati differential equation (6.3.5) for the charge carrier extraction depth L , parametric in the voltage derivative $\log(\underline{U}')$ which varies from -3 to 3 in steps of 0.5 (top to bottom curves). Right: Time evolution of the dimensionless current density \underline{j} calculated by equation (6.3.6), parametric in \underline{U}' . The range of \underline{U}' shown is the same, top to bottom.

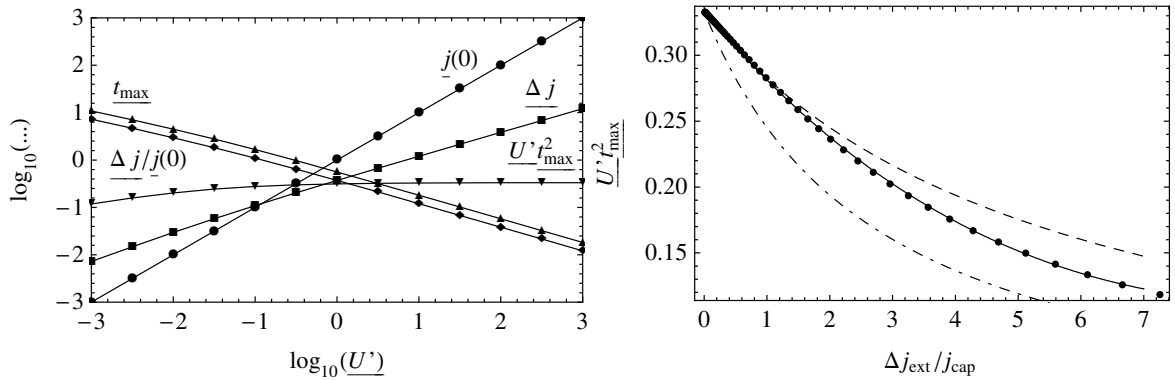


Figure 6.4: Left: Characteristic parameters of the numerical solution of equation (6.3.5) as function of the dimensionless voltage derivative \underline{U}' , plotted in double-logarithmic representation. Compare to figure 3 in [167]. Right: Nonlinear fits of $\underline{U}' t_{\max}^2$ as function of $\Delta j / j(0)$. Nonlinear fits correspond to equation (6.3.10) (solid line), equation (6.3.9) (dashed line) as well as equation (6.3.13) (dot-dashed line).

of charges created, their mobility and typical time regimes of the experiment. This validates the restriction of \underline{U}' made above. In order to apply the numerical analysis to the determination of charge mobility from measured CELIV transients, note that by using equations (6.3.2) and (6.3.3)

$$\underline{U}' = \frac{U'_{\text{ext}} \mu \epsilon^2 \epsilon_0^2}{2d^2 e^2 n^2 \mu^2} = \frac{U'_{\text{ext}} \mu t_{\text{max}}^2}{2d^2 t_{\text{max}}^2} \quad (6.3.7)$$

$$\Leftrightarrow \mu = \frac{2d^2}{U'_{\text{ext}} t_{\text{max}}^2} \underline{U}' t_{\text{max}}^2. \quad (6.3.8)$$

Here, $\underline{U}' t_{\text{max}}^2$ can be expressed as a function of $\Delta j_{\text{ext}}/j_{\text{cap}}$ by using the numerical results, compare figure 6.4. This function is only available in numerical form, so analytical approximations will be provided to facilitate its application to data analysis. Two function were found to provide reasonable accuracies within the specified bounds of $\Delta j_{\text{ext}}/j_{\text{cap}}$:

$$\underline{U}' t_{\text{max}}^2 = \frac{1}{3(1 + 0.18 \frac{\Delta j_{\text{ext}}}{j_{\text{cap}}})} \quad (\Delta j_{\text{ext}}/j_{\text{cap}} < 1) \quad (6.3.9)$$

$$\underline{U}' t_{\text{max}}^2 = 0.329e^{-0.180\Delta j_{\text{ext}}/j_{\text{cap}}} + 0.005e^{0.253\Delta j_{\text{ext}}/j_{\text{cap}}} \quad (\Delta j_{\text{ext}}/j_{\text{cap}} < 7). \quad (6.3.10)$$

Thus, the charge mobility can be determined via

$$\mu = \frac{2d^2}{3U'_{\text{ext}} t_{\text{max}}^2 (1 + 0.18 \frac{\Delta j_{\text{ext}}}{j_{\text{cap}}})} \quad (\Delta j_{\text{ext}}/j_{\text{cap}} < 1) \quad (6.3.11)$$

$$\mu = \frac{2d^2}{U'_{\text{ext}} t_{\text{max}}^2} \cdot \left(0.329e^{-0.180\Delta j_{\text{ext}}/j_{\text{cap}}} + 0.005e^{0.253\Delta j_{\text{ext}}/j_{\text{cap}}} \right) \quad (\Delta j_{\text{ext}}/j_{\text{cap}} < 7), \quad (6.3.12)$$

where equation (6.3.11) is in variance with the result

$$\mu = \frac{2d^2}{3U'_{\text{ext}} t_{\text{max}}^2 (1 + 0.36 \frac{\Delta j_{\text{ext}}}{j_{\text{cap}}})} \quad (\Delta j_{\text{ext}}/j_{\text{cap}} < 1) \quad (6.3.13)$$

published by Juška et al. [168] and used in several articles [61, 169, 170, 172]. In order to provide an independent test for these equations, numerical charge transport simulations of CELIV current transients were conducted employing the drift/diffusion simulation model discussed in appendix A. Figure 6.5 compares these to the numerical solution discussed here. The main parameters used for the simulation were the charge mobility of $\mu = 2 \times 10^6 \text{ cm}^2/\text{Vs}$, a layer thickness of $d = 65 \text{ nm}$, a voltage slope of $U'_{\text{ext}} = 2 \times 10^4 \text{ V/s}$ and an initial free charge carrier density of $n = 4 \times 10^{22} \text{ m}^{-3}$. For these simulations, mutual charge carrier recombination was neglected, while the effect of charge diffusion is indicated in the figure. The numerical simulation faithfully reproduces the simulated transient for the case of vanishing charge diffusion. The characteristic parameters of the simulation results are $\Delta j_{\text{ext}}/j_{\text{cap}} = 0.781$ and $t_{\text{max}} = 25.125 \text{ }\mu\text{s}$, from which the following charge mobilities can be calculated:

$$\text{from (6.3.9):} \quad \mu = 1.96 \times 10^{-6} \text{ m}^2/(\text{Vs}) \quad (6.3.14)$$

$$\text{from (6.3.12):} \quad \mu = 1.95 \times 10^{-6} \text{ m}^2/(\text{Vs}) \quad (6.3.15)$$

$$\text{from (6.3.13):} \quad \mu = 1.74 \times 10^{-6} \text{ m}^2/(\text{Vs}). \quad (6.3.16)$$

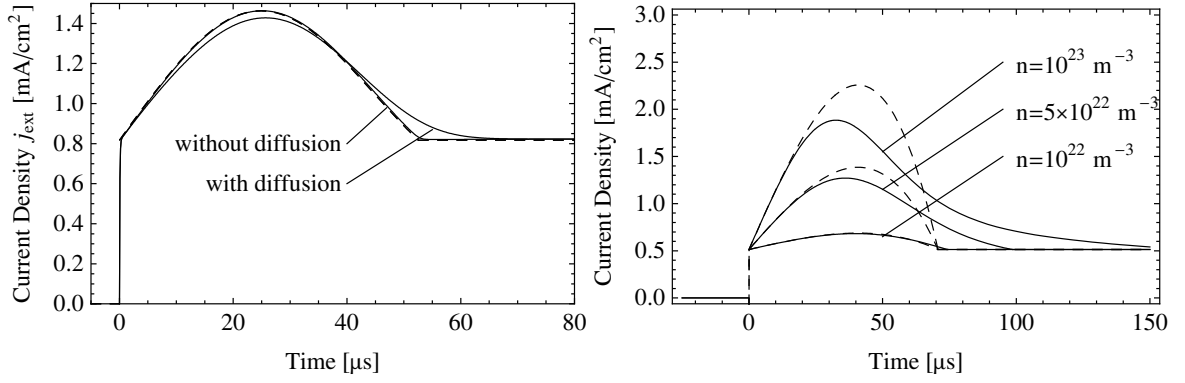


Figure 6.5: Left: Numerically simulated CELIV transients (solid lines), for simulation parameters see text. Simulation results are shown both excluding and including charge diffusion according to the Einstein relation. The dashed line corresponds to the numerical solution of equation (6.3.5) and closely follows the simulation results excluding charge diffusion. Right: Comparison of the low-conductivity approximate solution (6.2.15) (dashed lines) with the numerical solution (solid lines), parametric in charge density. Parameters are the same as for figure 6.2, except for the varying charge densities which are indicated in the plot.

Indeed, equation (6.3.13) underestimates the charge mobility when applied to CELIV current transients, although the relative error is low. Stronger errors are expected for much larger $\Delta j_{\text{ext}}/j_{\text{cap}}$, which are seldomly realized in the experiments. In this work, CELIV results are analyzed according to equation (6.3.12) since it provides the widest range of approximation. Figure 6.5 also compares the approximate current transient (6.2.15) with the full numeric solution using parameters similar to figure 6.2. It is obvious that at charge densities already within the experimental range the approximate solution does not provide adequate accuracy. At high densities, the current transient deviates from the approximately parabolic shape due to the buildup of significant space charge and a corresponding reduction in the effective electric field $E(l(t))$ driving the mobile charge carriers.

The CELIV transient current method has the advantage of not only providing a value for the charge mobility, but also for the charge density. Consider equation (6.2.17), which using (6.3.3) yields

$$\underline{U}' = \frac{4}{27} \left(\frac{\Delta j_{\text{ext}}}{j_{\text{cap}}} \right)^{-2} \quad (\Delta j_{\text{ext}}/j_{\text{cap}} \ll 1). \quad (6.3.17)$$

The numerical solution discussed in this section provides a reliable way to determine the quality of this approximation for arbitrary values of $\Delta j_{\text{ext}}/j_{\text{cap}}$ by using the parameter dependence already shown in figure 6.4. Figure 6.6 compares both approaches and shows that equation (6.3.17) provides a reasonably good fit up to $\Delta j_{\text{ext}}/j_{\text{cap}} \approx 1$. The relative error of this approximation reaches 10% (50%) at $\Delta j_{\text{ext}}/j_{\text{cap}} = 0.955$ ($j_{\text{ext}}/j_{\text{cap}} = 1.101$). Thus, the charge density is calculated as

$$n = \frac{9}{4} \frac{\varepsilon \varepsilon_0 U'_{\text{ext}} t_{\text{max}}}{ed^2} \frac{\Delta j_{\text{ext}}}{j_{\text{cap}}} \sqrt{1 + 0.18 \frac{\Delta j_{\text{ext}}}{j_{\text{cap}}}} \quad (\Delta j_{\text{ext}}/j_{\text{cap}} < 1) \quad (6.3.18)$$

using approximation (6.3.11).

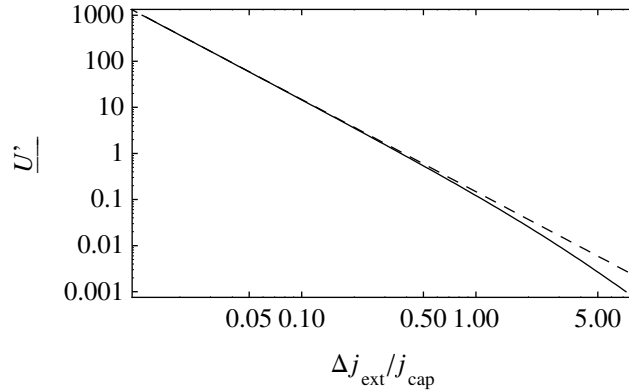


Figure 6.6: Dependence of U' on $\Delta j_{\text{ext}}/j_{\text{cap}}$ as calculated from the numerical solution (solid line), compared to the result (6.3.17) of the low conductivity approximation (dashed lined).

6.4 CELIV Transients under Non-Ideal Conditions

While the CELIV technique as it stands is attractive for its facile experimental realization and for allowing the calculation of both charge mobility and density, it is based on a strongly simplified analysis. This section discusses generalizations to ‘real-life’ experimental conditions and the extent to which reliable results are still obtained by application of equations (6.3.12) and (6.3.18).

One of the main processes neglected up to now is charge recombination. This is sufficiently justified for the analysis of equilibrium charge carrier properties in inorganic semiconductors, e.g. in the context of amorphous silicon for which the method was originally developed.[168] In the field of organic semiconductors, the equilibrium charge carrier densities are much too low for CELIV measurements. It was demonstrated that deliberate doping by oxygen exposure can introduce enough free charges (holes),[61] but usually the main interest lies in the intrinsic properties of these materials. Photogeneration of non-equilibrium charge carriers by the absorption of laser pulses (photo-CELIV) is more popular in this case and can be applied directly to standard solar cell structures, strongly facilitating the study of the morphology-mobility relationship. Photogenerated non-equilibrium charges of density $n(0)$ will decay according to the Langevin mechanism as discussed in chapter 5.4 and thus

$$n(t) = \frac{n(0)}{1 + t\gamma n(0)} = \frac{n(0)}{1 + t/\tau_\sigma} \quad (6.4.1)$$

is time-dependent with decay constant $\gamma = e\mu/\epsilon\epsilon_0$. As in the analysis above, in what follows it is assumed that only one charge carrier is mobile. The time dependence of n , coupled with the time-dependence of the extraction depth $l(t)$ leads to an inhomogeneous charge density $\rho(z, t)$ and renders the applied numerical analysis useless. Indeed, experimental conditions should be chosen to keep the charge transit time (and thus the length of the extraction voltage pulse) much smaller than the average lifetime of charges $(\gamma n(0))^{-1} = \tau_\sigma$, identical to the dielectric relaxation time. Otherwise, significant errors in the calculated mobility values should be expected. Figure 6.7 compares numerically simulated CELIV current transients

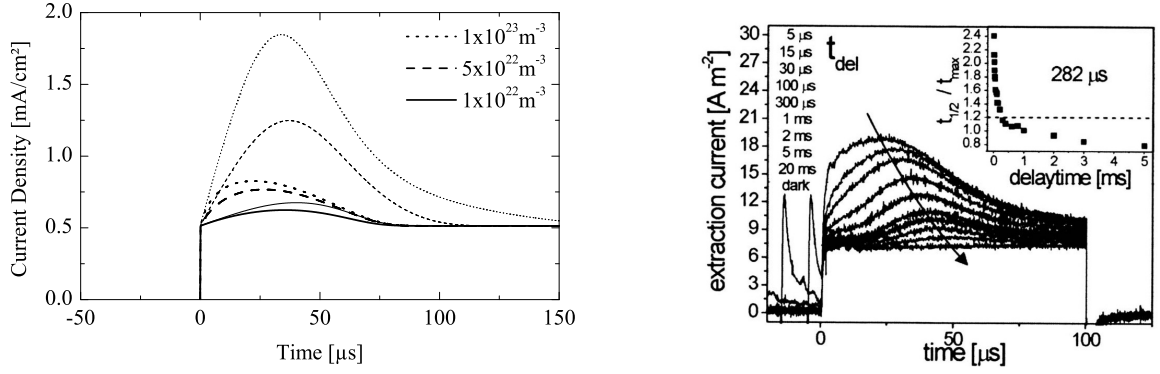


Figure 6.7: Left: Comparison of numerically simulated CELIV transients without (thin lines) and with (thick lines) charge recombination according to the Langevin mechanism, parametric in charge density n as indicated. The parameters were $U'_{\text{ext}} = 2 \times 10^4$ V/s, $\mu = 2 \times 10^6$ V/m and $d = 100$ nm. Right: Figure 5 reproduced from reference [171]. Photo-CELIV transients measured for a MDMO-PPV/PCBM blend at 150 K, parametric in delay time t_{del} after photoexcitation.

for the case of homogeneous initial charge distributions without and with Langevin-type charge recombination using the same parameters as for figure 6.5 (right hand side). Under experimental conditions chosen to maximize the $\Delta j_{\text{ext}}/j_{\text{cap}}$ level and thus at long extraction times and charge densities, serious errors are introduced into the determined mobility values. Note that

$$\tau_{\sigma} \gg t_{\text{tr}} \Leftrightarrow n \ll \frac{\epsilon \epsilon_0}{ed} \sqrt{\frac{U'_{\text{ext}}}{2\mu}} \quad (6.4.2)$$

gives an upper bound of the allowable charge density. Assuming that the applied voltage is bound by $U_{\text{ext,max}} < d \cdot E_{\text{max}}$ where $E_{\text{max}} \sim 10^8$ V/m to prevent electrical breakthrough and the extraction pulse length should be at least as long as the transit time $\Delta t > t_{\text{tr}}$, the charge density is bounded by

$$n \ll \frac{\epsilon \epsilon_0 E_{\text{max}}}{2ed}. \quad (6.4.3)$$

At $d = 100$ nm and $\epsilon = 3$, this corresponds to $n \ll 8.3 \times 10^{22}$ m⁻³. Since $\tau_{\sigma} \gg t_{\text{tr}}$ also implies $\Delta j_{\text{ext}}/j_{\text{cap}} \ll 1$, a violation of condition (6.4.3) should be expected for most of the measurement data published so far, where $\Delta_{\text{ext}}/j_{\text{cap}} \sim 1$ has typically been chosen [61, 167]. Figure 6.7 shows photo-CELIV transients measured by Mozer et al. [171] for a poly[2-methoxy-5-(3,7-dimethyloctyloxy)-phenylene vinylene] (MDMO-PPV) blended with 1-(3-methoxycarbonyl)propyl-1-phenyl-(6,6)-C₆₁ (PCBM), parametric in the delay time t_{del} between photoexcitation and the start of the extraction voltage pulse. The data was interpreted in terms of a relaxation of charge carriers towards the low-energy end of the density of states distribution. Note that the shape of the measured transients is significantly distorted at the shortest delay times and reminiscent of the asymmetric shape obtained in the numerical simulation. Several articles have been published reporting a time dependence of charge mobilities determined in CELIV measurements [170, 172–174]. While in reference [172] the intensity and thus charge density dependence of the apparent mobility was explicitly studied, condition (6.4.3) has not been considered explicitly in any publica-

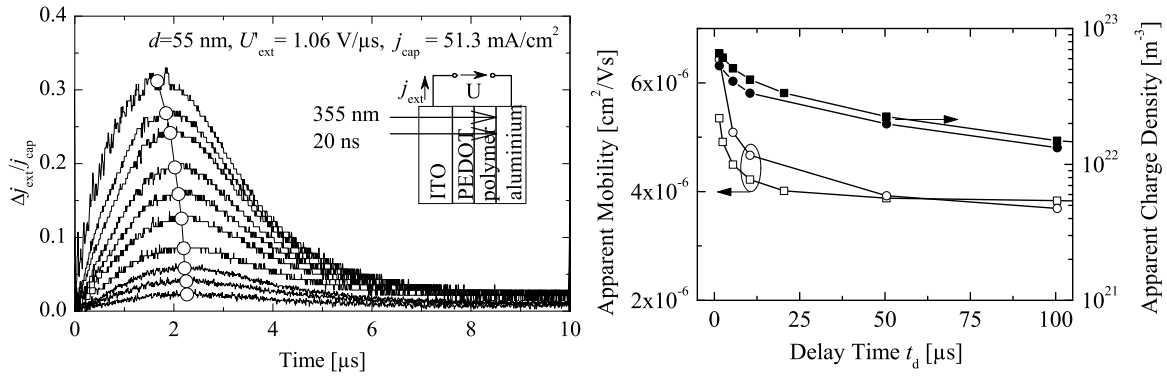


Figure 6.8: Left: CELIV transients obtained for 55 nm thick samples with a M3EH-PPV:CN-ether-PPV blend layer (spincoated from chlorobenzene, non-annealed layer) at $U'_{\text{ext}} = 1.06 \text{ V}/\mu\text{s}$. Connected circles indicate the determined t_{max} points. The inset shows a schematic sample structure. Right: Charge mobilities (open symbols) calculated from this data according to equation (6.3.11) for annealed (circles) and non-annealed (squares) blend layers. The apparent charge density (filled symbols) was calculated according to equation (6.3.18).

tion so far. Figure 6.8 shows the results of photo-CELIV measurements on polymer blends of **M3EH-PPV** with **CN-ether-PPV** spincoated from chlorobenzene solution. For details on these polymers see appendix B. The impact of annealing on the layer morphology and photovoltaic device performance of this donor-acceptor blend was investigated in detail in reference [173] for blends spincoated from either chloroform solutions or from mixtures of 1,2,4-trichlorobenzene with chloroform. Similar to the results shown here, no significant impact of annealing on the charge mobility of these layers has been observed. The apparent mobility calculated from the measured current transients via equation (6.3.11) exhibits relaxation behavior within the first 25 μs after photoexcitation. In order to analyze if this is caused by deviations from condition (6.4.3), numerical simulations of these CELIV experiments were conducted using a layer thickness of $d = 55 \text{ nm}$, $\epsilon = 3$, extraction voltage pulse lengths of 10 μs , a voltage slope parameter of $U'_{\text{ext}} = 1.06 \text{ V}/\mu\text{s}$ and a charge mobility of $\mu = 3.8 \times 10^{-6} \text{ cm}^2/\text{Vs}$. The simulated transients were evaluated according to the same protocol used for the experimental results and the apparent charge mobility calculated from t_{max} and $\Delta j_{\text{ext}}(t_{\text{max}})/j_{\text{cap}}$. Figure 6.9 shows the impact of the initial charge density at the beginning of the extraction pulse on the calculated mobility values. The results remain accurate up to charge densities of $\sim 5 \times 10^{23} \text{ m}^{-3}$ after which a strong increase in apparent mobility is observed due to the distortion of the current transient as shown in figure 6.7. This corresponds to $\Delta j_{\text{ext}}/j_{\text{cap}} \sim 0.14$ which shows that for the measured CELIV transients the charge recombination effects cannot be neglected. A direct comparison of the measured apparent mobility values and those obtained from an evaluation of the simulation data is shown on the right side of figure 6.9. Assuming an initial charge density on the order of $n(0) = 2 \times 10^{23} \text{ m}^{-3}$ reproduces the apparent mobility ‘relaxation’ although this parameter is fixed in the simulations. While the initial charge density is above 10^{23} m^{-3} , those calculated via equation (6.3.18) tend to settle at lower values due to the strong recombination rates at higher density levels that reduce the charge density during the extraction voltage

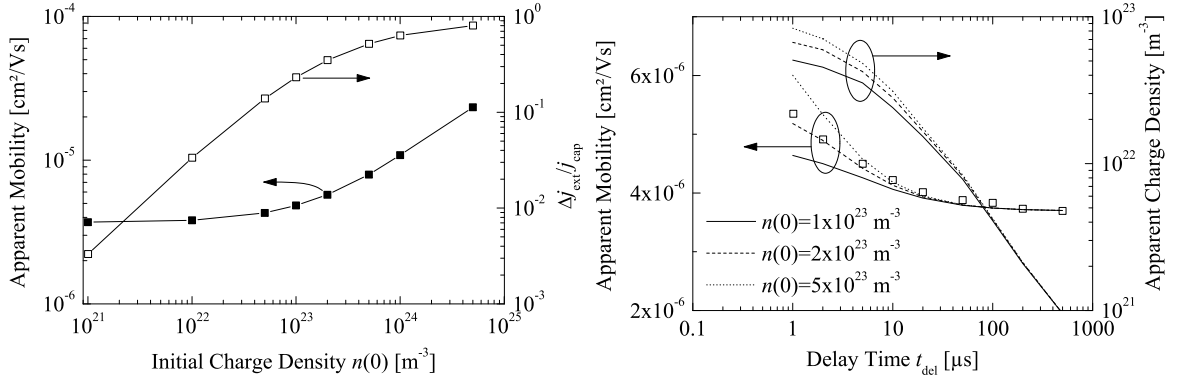


Figure 6.9: Analysis results of numerically simulated CELIV transients with parameters chosen to model the experimental situation of figure 6.8. Left: Apparent mobility according to equation (6.3.11) and $\Delta j_{\text{ext}}/j_{\text{cap}}$ at $t = t_{\text{max}}$ as a function of the initial charge density, for extraction voltage pulses of 10 μs length and voltage slopes of 1.06 V/ μs . Right: The apparent mobility and charge density as function of the delay time before the extraction pulse, parametric in the initially photogenerated charge density. The squares show the experimental data for non-annealed M3EH-PPV/CN-ether-PPV blends taken from figure 6.8.

pulse. This result suggests that studies of charge mobility relaxation employing the CELIV technique should be carefully revisited to check for the role of charge recombination during the extraction pulse. Indeed, choosing low charge densities as required by equation (6.4.3) and thus $\Delta j_{\text{ext}}/j_{\text{cap}} \ll 1$ will make the experimental realization of this technique more complicated.

As another deviation from non-ideal CELIV conditions, the role of charge mobility is investigated in more detail. In the simplified theory discussed in the previous section, charge mobility for the mobile carrier was assumed to be constant under all experimental conditions. As discussed in chapter 2, at fixed temperature the charge mobility is instead usually assumed to follow a Poole-Frenkel type field dependence $\mu = \mu_0 \exp(\beta\sqrt{E})$ due to the interplay between energetic and spatial disorder present in organic semiconductors. The effect of field-dependent mobility on CELIV transients is analyzed within the $\tau_\sigma \gg t_{\text{tr}}$ approximation, where $E(l(t)) = U'_{\text{ext}}t/d$ is still valid. The time dependence of the extraction depth is

$$\frac{dl(t)}{dt} = \mu(E(l(t))) \frac{U'_{\text{ext}}t}{d}, \quad (6.4.4)$$

with the solution

$$l(t) = \frac{2\mu_0}{U'_{\text{ext}}\beta^4} \left[6d + 6de^{\beta\sqrt{\frac{U'_{\text{ext}}t}{d}}} \left(\beta\sqrt{\frac{U'_{\text{ext}}t}{d}} - 1 \right) + U'_{\text{ext}}\beta^2 t e^{\beta\sqrt{\frac{U'_{\text{ext}}t}{d}}} \left(\beta\sqrt{\frac{U'_{\text{ext}}t}{d}} - 3 \right) \right]. \quad (6.4.5)$$

Based on this, the current is calculated as

$$j_{\text{ext}}(t) = \frac{\epsilon\epsilon_0}{d} U'_{\text{ext}} + \frac{en}{d} \left(1 - \frac{l(t)}{d} \right) U'_{\text{ext}} t \mu_0 \exp(\beta\sqrt{\frac{U'_{\text{ext}}t}{d}}), \quad (6.4.6)$$

which unfortunately doesn't provide any closed analytic expression for the determination of t_{max} from $dj_{\text{ext}}(t)/dt = 0$, but can be evaluated numerically. Juška et al. [168] suggested that

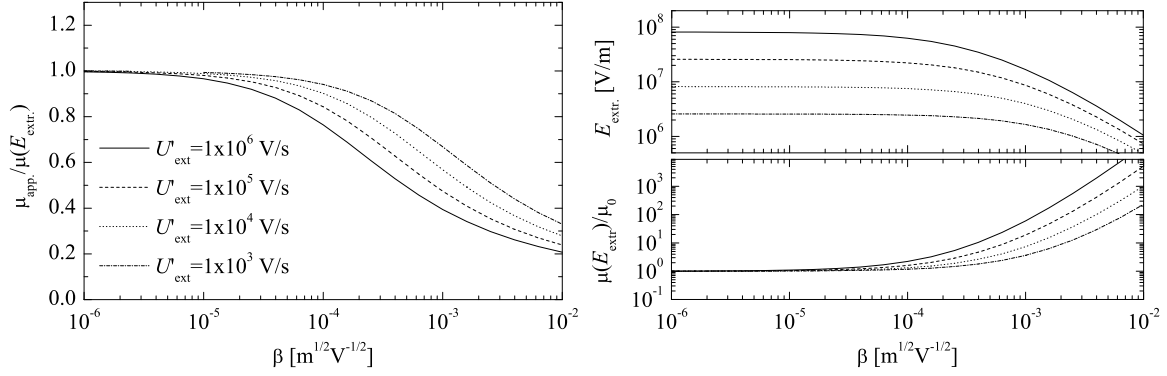


Figure 6.10: Left: Ratio of the apparent mobility μ_{app} calculated via equation (6.3.11) and the actual charge mobility calculated from equation (6.4.6) at an electric field of $E_{\text{extr.}} = U'_{\text{ext}} t_{\text{max}}/d$. The data shown was calculated assuming $\mu_0 = 1 \times 10^{-6} \text{ cm}^2/\text{Vs}$. The voltage slope parameter U'_{ext} used for the curves is indicated in the figure. Right: $E_{\text{extr.}}$ and the relative mobility $\mu(E_{\text{extr.}})/\mu_0$ for the same parameters.

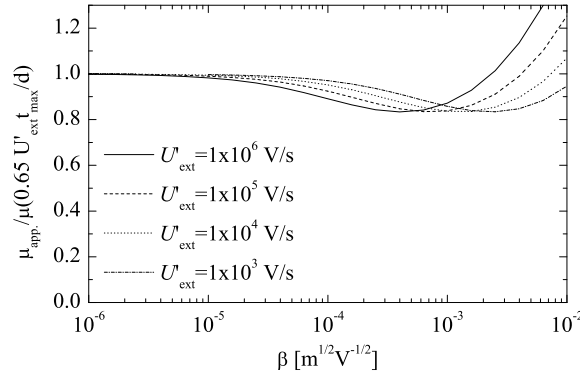


Figure 6.11: Ratio of the apparent mobility and the actual charge mobility at an extraction field defined by $E_{\text{extr.}} = 0.65 \cdot U'_{\text{ext}} t_{\text{max}}/d$. The parameters are the same as for figure 6.10.

in case of a field-dependent mobility, the apparent mobility determined by equation (6.3.11) from t_{max} and $\Delta j_{\text{ext}}(t_{\text{max}})/j_{\text{cap}}$ should correspond to the charge mobility at an effective *extraction field* of $E_{\text{extr.}} = \frac{U'_{\text{ext}} t_{\text{max}}}{d}$. By varying the parameters of the extraction pulse and thus t_{max} and $E_{\text{extr.}}$, the field dependence of mobility should be recovered. Figure 6.10 compares the ratio of the apparent mobility and the actual mobility at t_{max} as calculated numerically from equation (6.4.6). The zero-field mobility used for the calculations was $\mu_0 = 10^{-6} \text{ cm}^2/\text{Vs}$, the charge density was fixed at a low value of $n = 10^{17} \text{ m}^{-3}$ to stay within the limits $\Delta j_{\text{ext}}/j_{\text{cap}} < 1$ of equation (6.3.11). The results are considered to be fairly general since they are independent of d and invariant under the transformation $\mu_0 \rightarrow \alpha \mu_0$, $U'_{\text{ext}} \rightarrow \alpha U'_{\text{ext}}$ for arbitrary α . The apparent mobility is found to deviate from $\mu(E_{\text{extr.}})$ as soon as $\exp(\beta \sqrt{E_{\text{extr.}}}) \gg 1$, introducing a systematic error in the determined field dependence of mobility. Figure 6.11 shows the same data using an extraction field defined by $E_{\text{extr.}} = 0.65 \cdot U'_{\text{ext}} t_{\text{max}}/d$. This minimizes the systematic errors as long as $\beta < 10^{-2} \text{ m}^{1/2} \text{V}^{-1/2}$, which is typically not vi-

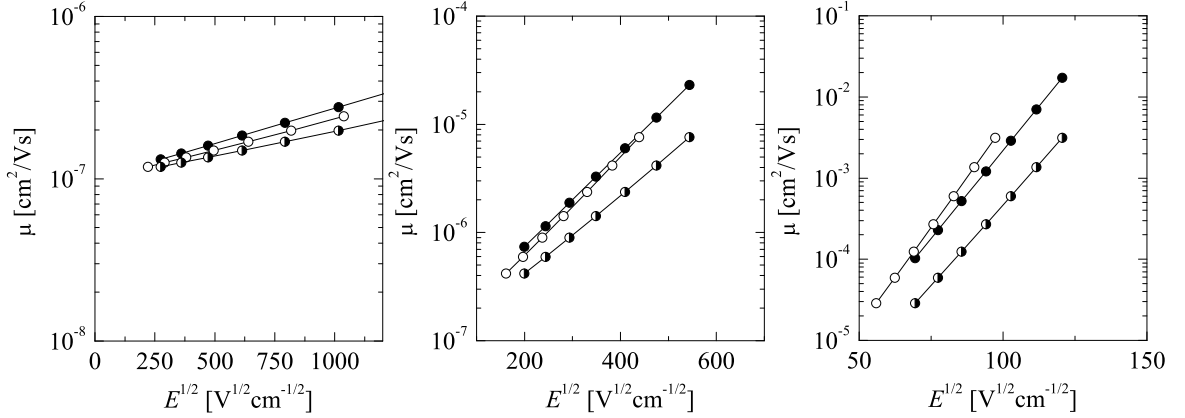


Figure 6.12: Calculated field dependence of the apparent charge mobility using $E_{\text{extr.}} := 0.65 \cdot U'_{\text{ext}} t_{\text{max}} / d$ (open symbols) and $E_{\text{extr.}} := U'_{\text{ext}} t_{\text{max}} / d$ (half filled symbols) with the true mobility. The results were calculated from the exact solution (6.4.6) for Poole-Frenkel type field dependence. Zero field mobility is $\mu_0 = 1 \times 10^{-7} \text{ cm}^2/\text{Vs}$ for all plots while the Poole-Frenkel parameter varies as $\beta = 1 \times 10^{-4} \text{ m}^{1/2} \text{V}^{-1/2}$ (left plot), $\beta = 1 \times 10^{-3} \text{ m}^{1/2} \text{V}^{-1/2}$ (middle plot) and $\beta = 1 \times 10^{-2} \text{ m}^{1/2} \text{V}^{-1/2}$ (right plot). The film thickness was assumed as $d = 100 \text{ nm}$, the charge density was $n_0 = 1 \times 10^{17} \text{ m}^{-3}$ and the voltage slope parameter varied in the range $U'_{\text{ext}} = 10^3 \dots 10^6 \text{ V/s}$.

olated for organic semiconductors. An improved protocol for the determination of field dependent mobilities is thus suggested: mobilities should be determined according to equation (6.3.11) at reasonably $\Delta j_{\text{ext}}(t_{\text{max}}) / j_{\text{cap}}$ values with the corresponding electric field being calculated as $E_{\text{extr.}} := 0.65 \cdot U'_{\text{ext}} t_{\text{max}} / d$. Figure 6.12 compares field-dependent mobilities calculated using the new approach with those calculated using the extraction field defined as $E_{\text{extr.}} := U'_{\text{ext}} t_{\text{max}} / d$. The corresponding current transients were calculated using the exact solution (6.4.6) by numerical evaluation and analyzed in terms of t_{max} and $\Delta j_{\text{ext}}(t_{\text{max}}) / j_{\text{cap}}$. The field dependence of mobility was assumed as $\mu = \mu_0 \exp(\beta \sqrt{E})$ with $\mu_0 = 1 \times 10^{-7} \text{ cm}^2/\text{Vs}$ and β varying from $10^{-4} \text{ m}^{1/2} \text{V}^{-1/2}$ to $10^{-2} \text{ m}^{1/2} \text{V}^{-1/2}$. The voltage slope U'_{ext} was varied from 10^3 V/s to 10^6 V/s , thereby covering the whole range of values typically used in CELIV experiments. As already suggested by figure 6.11, the deviation of the calculated apparent mobilities from the true charge mobilities is much smaller using the new definition of extraction field.

Summary

This work contains a detailed study of the charge carrier dynamics and emission properties of two commercially available blue and white electrofluorescent polymeric semiconductors. The focus was on improving the detailed understanding of the physical mechanisms underlying the bipolar operation of such polymers as light-emitting devices. It has thus been organized into chapters detailing the various functional aspects of device behavior, among them the charge injection properties, the charge transport in relatively trap-free blue-emitting copolymers and the role of charge trapping and energy transfer between chromophores for the operational color stability of white light-emitting polymer diodes. Apart from the approach centered on device physics, several concepts were introduced that allowed the determination of transport or injection properties, among them all-polymeric solution processed sensitized EL structures, *quasi* electron-only devices, electron-only devices with ultra-low leakage currents and improvements of the ‘current extraction under linearly increasing voltage’ (CELIV) method concerning its application to measurements of charge recombination and field-dependent mobilities.

Chapter 2 summarized the results on the charge transport properties of a blue-emitting copolymer based on a spiro-linked polyfluorene derivative, the general class of which is of considerable interest for commercial applications as blue-emitting layer or as wide-bandgap host for singlet or triplet emitting chromophores. The polymer was shown to exhibit a remarkably high electron mobility with only weak dispersion, both in time-of-flight photocurrent studies on films of more than 1 μm thickness as well as in transient electroluminescence investigations on thin films of 100 nm thickness. An all-polymeric bilayer design was introduced in order to reliably measure electron transit times below 50 ns in transient electroluminescence experiments.

The same polymeric semiconductor was studied in chapter 3 in terms of the electron and hole injection properties from common polymeric and metallic electrodes. The injection of holes from the polymeric anode PEDOT:PSS was studied by the characterization of unipolar devices and by ultraviolet photoelectron spectroscopy. It could be concluded that a significant energetic barrier hinders hole injection in unipolar hole-only devices. The properties of the polymer/cathode interface are usually more difficult to assess due to the buried interface hindering photoelectron spectroscopy and also by experimental difficulties in realizing unipolar electron-only devices. Here, the concept of quasi electron-only devices was introduced, utilizing an electron-hole recombination layer in form of a thin insoluble layer on top of PEDOT:PSS. This interlayer sufficiently suppressed hole injection into the bulk, allowing for a quantification of electron injection which is found to be significantly lower than the space charge limitations. The determined charge injection and transport properties were then used to set up a numerical device simulation of both steady state and transient emission properties that was essentially free of unknown parameters. The comparison of simulated to experimental data supported the conclusion that an extraction barrier of ap-

proximately 50 meV hinders electrons from leaving the polymer layer into the anode. This process mainly contributes to the first μs of transient electroluminescence observed after application of a voltage pulse and is attributed to an insulating phase-segregated PEDOT:PSS surface layer enriched in PSS content. However, the steady-state emission properties of the light-emitting devices were faithfully reproduced by the simulation model only by assuming an Ohmic, i.e. barrierless injection of holes from PEDOT:PSS into the semiconductor. This improved charge injection was only observed in bipolar devices and attributed to electron trapping at the interface, but it occurred in a time regime typically not observed in either transient or steady-state investigations.

Chapter 4 presented a conclusive picture of the interplay between charge injection, transport and emission in a class of single layer white-light emitting polymeric diodes based on polyspirofluorene-type copolymers. It was shown that the interplay of charge trapping with interchromophoric energy transfer determines the emission spectrum of these devices. Control of the emission spectrum over a wide range of operating conditions is of paramount importance for industrial applications but up to now seldomly achieved. The two polymers studied here were ideal systems for such investigations due to their well-defined charge transport and charge trapping properties. Using an analytic rate equation approach, it was shown that the shift of emission color observed under varying electrical drive conditions is due to the varying density of free holes. The analysis provided separate insight into the role of diffusion and drift-induced trapping of free electrons by the red chromophore, which was discussed in terms of both continuum diffusion models as well as random walk models of charge hopping in an effective lattice. The measurement results were explained by a reduced rate of diffusion-driven charge trapping that could be attributed to the diffusion of charges occurring along energetically preferred quasi-1D percolation pathways or to a preference of intrachain against interchain hopping. The model discussed for the explanation of the emission color correctly predicted the observed spectral shifts under temperature variation both near the onset voltage of the devices as well as under strong driving conditions. It was further shown that conditioning effects are observed upon first electrical driving of the light-emitting devices, contributing both to altered current-voltage characteristics as well as to a blue-shift of the emission color. This effect was also correctly predicted by the proposed model and is attributed to a significant reduction of the hole injection barrier upon bipolar device operation, similar to the effects observed for blue-emitting devices.

Chapter 5 analyzed the transient response of such white light emitting diodes upon termination of the driving voltage. The decay dynamics was shown to be separable into the recombination dynamics of free electrons and free holes as well as trapped electrons and free holes, where electrons were trapped on the red chromophores. A significant part of the electrons was shown to be geminately bound to holes during equilibrium device operation, forming neutral species with only low thermal activation and lifetimes on the order of 7 μs . Free electrons are extracted during the voltage transition, with a significant amount remaining trapped on the red chromophore. The total amount of trapped charges was shown to closely follow space charge limitations set by the sample capacitance, a situation that was analyzed by a Langevin-type recombination model. Numerical simulation were additionally performed to ensure the reliability of the simplified analytic approach.

Chapter 6 studied the CELIV method introduced recently into the field of organic semiconductors. Rederiving the original equations, it was shown that the published analytic result

contains numerical errors, a conclusion that was additionally supported by numerical simulations. Correcting for this, the chapter further studied the effects of deviations from the simplified assumptions used for the original results by a combination of analytic derivations and numerical simulations. An improved method for calculating the field-dependence of charge mobility was suggested, resulting in smaller errors compared to the established approach. Although CELIV was originally introduced especially for measurements under conditions of high charge density, it was possible to show that the popular photo-excited CELIV measurements are error prone due to the neglect of non-equilibrium charge recombination in the original derivation. Reintroducing this effect, results that have formerly been purely attributed to a time-dependent relaxation of mobility were shown to be artifacts caused by the simplified analytic approach. Suitable boundaries of photogenerated initial charge densities were derived, suggesting that at least some published results interpreting data solely in terms of mobility relaxation should be revisited.

Appendix A

Numerical Simulation of Drift-Diffusion Equations

This chapter presents an overview of the techniques used to implement a numerical drift-diffusion simulation to study charge transport processes. As was already discussed in the introduction, the equations for drift and diffusion of charges are usually insufficient to completely cover the physics of charge transport in disordered organic semiconductors. Being largely of an incoherent, hopping-type of motion, charge transport in disordered media displays a multitude of effects not covered by drift and diffusion, among these time-dependent mobilities due to relaxation (dispersive transport) and a complex dependence of macroscopic mobility parameters on charge density, electric field and temperature. The main drawbacks of microscopic approaches to charge transport such as Monte-Carlo techniques is that they are parametrized in terms of properties which are not accessible directly, such as hopping frequencies and the extent of electronic wavefunctions. In contrast to continuum models, the treatment of electron-electron interaction and space charges is more complicated. On the other hand, it is often possible to define effective averaged transport properties such as the charge mobility for a limited range of operating conditions. Time-evolution of charge densities based on drift and diffusion equations then allows to cover the macroscopic physics involved such as the build-up of space charges, charge trapping by deep states and the recombination zones for electrons and holes. Using a set of parameters that has to be adapted to the simulated system, drift-diffusion numerical simulations have shown that they are useful in predicting current-voltage and luminance-voltage characteristics, luminance efficiencies of organic LED and the design of multilayer structures to tune the recombination zones for charge carriers. Care has to be exerted whenever a detailed knowledge of the microscopic physical processes is needed, such as for the description of charge transport across semiconductor heterojunctions and across semiconductor-metal electrode interfaces.

Equations for Charge Carrier Drift and Diffusion The one-dimensional continuum model of charge transport is defined by the Poisson equation

$$\frac{\partial}{\partial z} E(z,t) = \frac{e}{\epsilon\epsilon_0} [n_h(z,t) - n_e(z,t)] \quad (\text{A.1})$$

describing the field generated by charge distributions and by the continuity equation

$$\frac{\partial}{\partial t} n_{e,h}(z,t) = \pm \frac{1}{e} \frac{\partial}{\partial z} j_{e,h}(z,t) - \frac{e}{\epsilon \epsilon_0} \mu_{\text{eff}}(z,t) (n_e(z,t)n_h(z,t) - n_i^2) \quad (\text{A.2})$$

$$j_{e,h}(z,t) = \pm e D_{e,h}(z,t) \frac{\partial}{\partial z} n_{e,h}(z,t) + \mu_{e,h}(z,t) n_{e,h}(z,t) \left(eE(z,t) + \frac{\partial}{\partial z} \epsilon_{\text{LUMO,HOMO}} \right) \quad (\text{A.3})$$

for the charge densities $n_{e,h}$ of electrons and holes, which cover the diffusion (first term in the definition of the current density j) and drift in the electrical field E (second term). Signs are arranged such that those valid for electron transport are on top, those for hole transport below. The current density due to the gradient of the energy levels $\epsilon_{\text{LUMO,HOMO}}$ of transport states results from the inclusion of the chemical potential into the total energy of charge carriers.[175] This allows to include the effect of gradients in the energetic positions of transport states such as those occurring at heterojunctions. Charge carrier recombination is treated in terms of the Langevin mechanism, since the charges are expected to have short scattering lengths and to be initially uncorrelated. The motion is thus of diffusive type and the mutual coulombic attraction occurs with the effective mobility $\mu_{\text{eff}}(z,t) = \mu_e(z,t) + \mu_h(z,t)$. In equilibrium, the recombination rate balances the generation rate due to thermal excitation. Due to the large bandgap energies of organic semiconductors, this rate is small and the density of intrinsic carriers $n_i^2 = N_0^2 \exp(\epsilon_{\text{HOMO}} - \epsilon_{\text{LUMO}})/k_B T$, where N_0 is the total density of states, remains orders of magnitude lower than charge densities due to extrinsic (injection and doping) processes.

The diffusion of charges is treated by assuming the validity of the Einstein relation

$$D_{e,h}(z,t) = \mu_{e,h}(z,t) \frac{k_B T}{e}, \quad (\text{A.4})$$

which is not strictly correct. It was shown [147] that D/μ is modified by a coefficient depending both on the charge density n as well as on the energetic disorder of the transport states. The field dependence of the mobility at constant temperature is assumed to follow a Poole-Frenkel type behavior described by

$$\mu_{e,h}(z,t) = \mu_{e0,h0} \exp\left(\beta_{e,h} \sqrt{E(z,t)}\right), \quad (\text{A.5})$$

where $\beta_{e,h}$ represents the effective Poole-Frenkel constant. This treatment, as described above, is expected to be valid only in a limited range of electric fields, sample temperature and total charge density. The equations for charge densities are supplemented by the continuity equation

$$\frac{\partial}{\partial t} n_s(z,t) = \eta_{\text{ST}} \frac{e \mu_{\text{eff}}(z,t)}{\epsilon \epsilon_0} n_e(z,t)n_h(z,t) + \frac{\partial}{\partial z} \left[D_s \frac{\partial}{\partial z} n_s(z,t) \right] - \frac{n_s(z,t)}{\tau} \quad (\text{A.6})$$

for excitons of density n_s , which are created by the recombination of free electrons and holes. The fraction of radiatively recombining singlet excitons is $\eta_{\text{ST}} = 1/4$ assuming an equal splitting between one singlet state and three possible triplet states of the two recombining electrons. Exciton diffusion by energy transfer processes is included using the diffusion coefficient $D_s = L_D^2/\tau$ resulting from the diffusion length L_D and the exciton lifetime τ . The last term in (A.6) describes the (radiative or nonradiative) decay of the singlet exciton density.

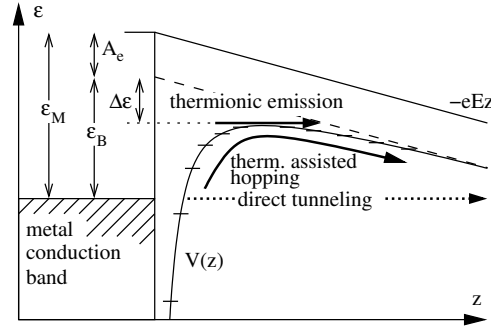


Figure A.1: Classical injection mechanisms at the metal-semiconductor interface. The electric field E and the image charge potential reduce the energetic barrier $\varepsilon_B = \varepsilon_M - A_e$ for charge injection by $\Delta\varepsilon = \sqrt{e^3 E / 4\pi\varepsilon\varepsilon_0 E}$. Here, ε_M is the metal work function and A_e is the electron affinity of the semiconductor.

Boundary Conditions The internal electric field distribution $E(z, t)$ has to follow the effective electric potential

$$U_{\text{eff}}(t) = \int_0^d E(z, t) dz, \quad (\text{A.7})$$

where the integration extends from the anode side ($z = 0$) to the cathode side ($z = d$) of the semiconductor layer. The boundary conditions for the current densities at $z = 0, L$ represent an important part of the model, since they determine the total amount of charge injected into the transport layer and its dependence on the local electric field at the metal-semiconductor interface. Figure A.1 schematically shows the energetical situation at the interface for injection of electrons into the lowest unoccupied states of the organic semiconductor. The theoretical concepts of thermionic emission, direct tunneling and thermally assisted hopping through disordered localized states have been discussed in chapter 1. In classical Schottky theory, the effective potential resulting from the incorporation of the image charge potential is $V(z) = \varepsilon_B - eEz - e^2 / 16\pi\varepsilon\varepsilon_0 z$, such that the effective injection barrier is $\varepsilon_B - \Delta\varepsilon$, where $\Delta\varepsilon = \sqrt{e^3 E / 4\pi\varepsilon\varepsilon_0 E}$ is the barrier lowering due to the applied electric field. For the present work, the injection model discussed by Scott and Malliaras[27, 28] is used. The injection current at the electrode is given by

$$j = AT^2 \exp\left(-\frac{\Phi_B - \Delta\phi}{k_B T}\right) - enR_s, \quad (\text{A.8})$$

where A is the modified Richardson constant

$$A = 16\pi\varepsilon\varepsilon_0 k_B^2 \frac{N_0 \mu}{e^2}, \quad (\text{A.9})$$

R_s is the surface recombination velocity

$$R_s = \frac{A^* T^2}{4eN_0} \left[\frac{1}{\psi^2} - f \right] \quad (\text{A.10})$$

and ψ is defined by

$$\psi = f^{-1} + f^{-1/2} - f^{-1} \left(1 + 2f^{1/2} \right)^{1/2} \quad (\text{A.11})$$

using $f = \frac{\Delta\Phi}{k_B T}$. In this approach, the interface recombination current is treated in terms of a diffusion of electrons in the electric potential of their image charge within the Langevin theory of charge recombination. Disorder and space-charge effects at the interface are neglected. The application of such simplified injection models is attractive, since they allow to spare the detailed numerical simulation of the processes at the interface by giving an effective resulting interface current. The simulation will thus differ from more microscopic ones in the nearest vicinity to the electrode interfaces, typically on the order of 5 nm. Charge injection at metal/organic interfaces has been studied by several other authors, and it was shown that the above equation fail to completely cover the involved physics since charge transport is better described by incoherent hopping motion in a distribution of states. An approach to explicitly include the contact region into the numerical simulation has been published by Preezant et al. [176]. They included the image-charge potential into the numerical simulation and were able to show that charge densities in the contact region are much higher when treated explicitly. This implies that in this region the D/μ ratio might deviate more strongly from the Einstein equation due to the high charge densities. It was also shown that replacing the direct treatment by an effective injection current may overestimate the injection barrier lowering expected from the Schottky effect.

Heterogeneous organic-organic interfaces represent discontinuities of the chemical potential. Under conditions of electrochemical equilibrium, the quasi Fermi levels $\epsilon_F = \epsilon_{\text{LUMO,HOMO}} \pm k_B T \log(\frac{n}{N})$ for electrons and holes are continuous and equal on both sides of the interface. The discretization of equation A.3 has to be done carefully in case of discontinuities of $\epsilon_{\text{LUMO,HOMO}}$.

The boundary conditions for the exciton density are normally assumed to be $n_s(0) = n_s(d) = 0$, since fast quenching of excitons due to a large amount of accessible states is expected near metallic contacts. The simulations additionally assume that no exciton diffusion across organic-organic heterojunctions occurs. This model could be extended by including formation of exciplex states and free charges at such heterojunctions, which would be of particular interest for the simulation of transport processes in organic solar cells.

A.1 Summary of the Simulation Algorithm

The model for the external circuit is shown in figure A.2. The external resistor R models the series resistance present in the device (mainly due to the low conductance of the ITO anode traces) and in the external circuit. The potential drop $U_R = U_{\text{ext}} - U_{\text{bi}} - U_{\text{eff}}$ at this resistor is calculated from the external applied voltage U_{ext} , the built-in potential U_{bi} due to the work function difference of the electrodes and from the effective potential U_{eff} across the semiconductor due to the internal electric field distribution. The electrical current flowing in the external circuit is thus $I = U_R/R$, charging and discharging the electrodes accordingly. The injection and extraction currents at the electrodes are summed over both electron and hole currents according to $I(0) = I_e(0) + I_h(0)$ and $I(d) = I_e(d) + I_h(d)$. Using the electrode area A , they can be calculated from the current densities j_0, j_{N+1} of the first and last simulation cells. The semiconductor layer is split into a one-dimensional grid of N cells with fixed lengths Δz , see figure A.2. The cell size is chosen to be comparable with typical intersite distances ~ 0.5 nm. The electric field E , the current densities $j_{e,h}$, the charge mobilities $\mu_{e,h}$

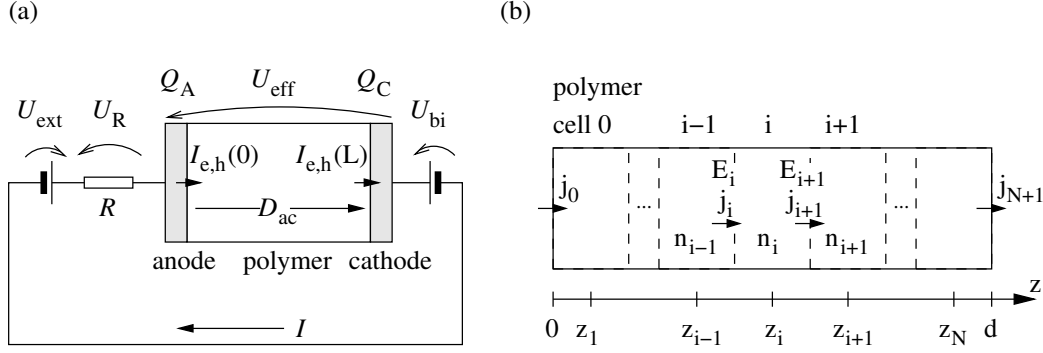


Figure A.2: (a) The model for the external electrical circuit used in the numerical charge transport simulations. The external resistance R determines the current I that charges the anode and cathode electrodes. (b) The one-dimensional discretization scheme used for the drift-diffusion equations. While charge densities n_i are defined in the center of each cell, the electric fields E_i and currents j_i are associated with the cell boundaries.

and the diffusion constants $D_{e,h}$ are defined at the cell borders $1/2(z_i + z_{i+1})$ ($i = 1 \dots N - 1$), while the charge densities $n_{e,h}$ and the density of excitons n_s are defined in the center of the cells at z_i ($i = 1 \dots N$).

The time evolution of the simulation parameters is done following the idea of *operator splitting* as described in [177]. Thus, the time-evolution is split into multiple steps:

1. Recalculation of the displacement field \mathcal{D} due to the total charge density $\rho = e(n_h - n_e)$ and the charge on the electrodes according to

$$\mathcal{D}(z) = \frac{Q_a - Q_c}{2A} - \frac{1}{2} \int_0^d \rho(z') dz' + \int_0^z \rho(z') dz' \quad (\text{A.1})$$

2. Calculation of the charge carrier mobilities from the local electric field according to equation (A.5)
3. Calculation of the current density due to diffusion (see below) and the corresponding changes in the charge carrier density $n_{e,h}$
4. Calculation of the amount of charge and exciton generation and recombination
5. Calculation of the exciton diffusion
6. Application of the externally defined source voltage U_{ext}
7. Calculation of the electric potential U_{eff} across the semiconductor according to equation (A.7)
8. Calculation of the current $I = U_R/R$ in the external circuit and the charging of anode and cathode according to $dQ_{a,c}/dt = I - I_{a,c}$

A.2 Methods and Algorithms

Charge Carrier Drift The central part of the simulation has to calculate the time evolution of the charge carrier densities according to the parabolic partial differential equation (PDE) (A.2) describing charge drift and diffusion. A popular approach for such problems is the *method of lines*[178], which discretizes the spatial coordinates to convert the PDE into a system of ordinary differential equations (ODE). This can be implemented as follows[179, 180]: Using a discretization according to Scharfetter and Gummel[181], the spatial coordinates are treated symmetrically by using

$$\frac{\partial n_i}{\partial t} = \pm \frac{1}{e} \frac{j_{i+1} - j_i}{\Delta z}. \quad (\text{A.1})$$

Here, $n_i := n(z_i)$ and $j_i = j(z_i - \Delta z/2)$ on a uniform grid z_i with intersite distances $\Delta z = z_i - z_{i-1}$, where the current densities are defined at the cell interfaces $z_i - \Delta z/2$. As before, upper signs are for electrons, lower signs for holes. The current densities are then approximated by

$$j_{i+1} = v_i \frac{n_i \exp(\frac{v_i \Delta z}{2D}) - n_{i+1} \exp(\frac{-v_i \Delta z}{2D})}{\exp(\frac{v_i \Delta z}{2D}) - \exp(\frac{-v_i \Delta z}{2D})} \quad (\text{A.2})$$

where $v_i = \mp \mu_i (E_i + (\epsilon_{\text{LUMO,HOMO},i+1} - \epsilon_{\text{LUMO,HOMO},i})/\Delta z)$. Combining this expression with equations (A.2) and (A.1) yields a three-point discretization scheme for n , where the coefficients depend on the local ratio $\mu E \Delta z / 2D$ of drift and diffusion. The resulting ODE for the n_i can then be solved by a fourth order numerical method due to Rosenbrock to account[177] for the stiffness of the equations and to gain access to the numerical errors and provide an adaptive control of the time step.

The discretization scheme used here is somewhat simpler in that the time evolution of the density is considered in an explicit Euler scheme, which rewrites equation (A.1) as

$$n_i(t + \Delta t) = n_i(t) \pm \frac{\Delta t}{e} \frac{j_{i+1} - j_i}{\Delta z}. \quad (\text{A.3})$$

The error due to discretization is of first order in Δt . This method is much simpler than the Rosenbrock ansatz and proved stable and fast enough for the intended application. Following the idea of operator splitting, the current density $j_i = j_i^T + j_i^D$ is split into transport and diffusion-related parts. For each of these, a separate discretization scheme is used to account for the stability issues involved with drift and diffusion-type equations. The drift current

$$j_i^T = \mp e W \begin{cases} v_i n_{i-1} & (v_i > 0) \\ v_i n_i & (v_i < 0) \end{cases} \mp e(1 - W) v_i \left[\frac{1}{2} (n_i + n_{i-1}) - \frac{v_i \Delta t}{\Delta z} (n_i - n_{i-1}) \right] \quad (\text{A.4})$$

is calculated according to a stabilised WILSON scheme.[182] A weighting factor

$$W = \frac{|n_i - n_{i-1}|}{|n_i + n_{i-1}|} \quad (\text{A.5})$$

is introduced to mix an upwind differencing scheme (in case of strong gradients in density) with the WILSON differencing scheme (in case of weak gradients). Upwind differencing is

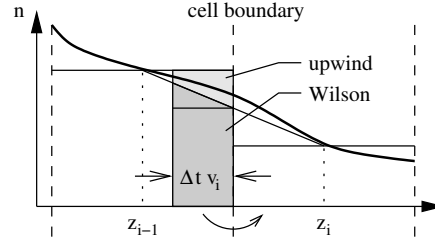


Figure A.3: WILSON-scheme for the discretization of the transport equations: the amount of charges transported into cell i within a time interval Δt equals the area beneath the linear interpolation in between $n(x_i)$ and $n(x_{i-1})$.

usually not the best choice for the treatment of weak density gradients, since numerical diffusion effects due to the discretization of spatial coordinates cannot be neglected. The WILSON scheme reduces these effects by introducing a linear interpolation as sketched in figure A.3. In situations of strong density gradients, the *Wilson* scheme may result in moving more charges than available out of a cell. The weighting parameter effectively removes this limitation by pronouncing the upwind differencing scheme in this situation.

Charge Carrier and Exciton Diffusion The time evolution of the diffusion current defined by equation (A.3) could simply be discretized according to

$$j_i^D = \pm e D_i \frac{n_i - n_{i-1}}{\Delta z}, \quad (\text{A.6})$$

where the diffusion constant $D_i = D(z_i - \Delta z/2)$ and the currents j_i^D are defined at the cell boundaries. This corresponds to choosing a forward time centered space (FTCS) scheme for the discretization of the diffusion equation according to

$$\frac{n_i(t + \Delta t) - n_i(t)}{\Delta t} = \frac{D_{i+1}(n_{i+1} - n_i) - D_i(n_i - n_{i-1})}{(\Delta z)^2}, \quad (\text{A.7})$$

which is numerically stable only[177] for

$$\Delta t \leq \min_i \left[\frac{(\Delta z)^2}{2D_i} \right]. \quad (\text{A.8})$$

This implies that the largest timestep allowed in the simulation must stay below the mean time for the diffusion of a charge across a cell of width Δz . This cannot be guaranteed in the simulations: At a charge mobility of $\mu = 10^{-3} \text{ cm}^2/\text{Vs}$, the diffusion constant at room temperature is already $2.5 \times 10^{-5} \text{ cm}^2/\text{s}$ according to equation (A.4), implying $\Delta t < 4.8 \times 10^{-11} \text{ s}$. For the calculation of exciton diffusion this scheme is even worse: using an exciton diffusion length of $L = 10 \text{ nm}$ and a mean lifetime of $\tau = 1 \text{ ns}$, $D = L^2/\tau$, the allowed time step is $\Delta t < 1.3 \times 10^{-12} \text{ s}$. This time step is too small and does not allow to efficiently calculate time evolutions up to 10^{-3} s of simulation time.

In order to achieve numerical stability also for much larger time steps, a fully implicit discretization is used: the calculation of spatial derivatives uses the (yet undetermined)

densities $n_i(t + \Delta t)$. The discretization is then done by writing

$$\frac{n_i(t + \Delta t) - n_i(t)}{\Delta t} = \pm \frac{1}{e} \frac{j_{i+1}(t + \Delta t) - j_i(t + \Delta t)}{\Delta z} \quad (\text{A.9})$$

$$j_i(t + \Delta t) = \pm e D_i \frac{n_i(t + \Delta t) - n_{i-1}(t + \Delta t)}{\Delta z} \quad (\text{A.10})$$

such that

$$\frac{n_i(t + \Delta t) - n_i(t)}{\Delta t} = \frac{D_{i+1}[n_{i+1}(t + \Delta t) - n_i(t + \Delta t)] - D_i[n_i(t + \Delta t) - n_{i-1}(t + \Delta t)]}{(\Delta z)^2}. \quad (\text{A.11})$$

Using $a_i = -D_i \Delta t / (\Delta z)^2$, $b_i = 1 + \Delta t(D_i + D_{i+1}) / (\Delta z)^2$ and $c_i = -D_{i+1} \Delta t / (\Delta z)^2$, this can be rewritten as

$$c_i n_{i+1}(t + \Delta t) + b_i n_i(t + \Delta t) + a_i n_{i-1}(t + \Delta t) = n_i(t). \quad (\text{A.12})$$

The choice of $n_{-1} = n_{N+1} = 0$ implies that all charge carriers reaching the electrode interface are effectively removed from the system. Thus, equations (A.12) constitute a tridiagonal system

$$\begin{pmatrix} b_0 & c_0 & 0 & \dots & & & & & \\ a_1 & b_1 & c_1 & 0 & \dots & & & & \\ 0 & a_2 & b_2 & c_2 & 0 & \dots & & & \\ & & & \ddots & & & & & \\ & & & & \dots & 0 & a_N & b_N & \end{pmatrix} \cdot \begin{pmatrix} n_0(t + \Delta t) \\ n_1(t + \Delta t) \\ n_2(t + \Delta t) \\ \vdots \\ n_N(t + \Delta t) \end{pmatrix} = \begin{pmatrix} n_0(t) \\ n_1(t) \\ n_2(t) \\ \vdots \\ n_N(t) \end{pmatrix}. \quad (\text{A.13})$$

Numerically efficient algorithms exist[177] which solve this system of equations within $\mathcal{O}(2N)$ steps and provide the unknown $n_i(t + \Delta t)$ as function of $n_i(t)$. The diffusion-current density $j_i(t + \Delta t)$ responsible for the corresponding changes in density $n_i(t + \Delta t) - n_i(t)$ are not directly provided by this method. Since they are necessary for the simulation to correctly calculate the total charge current, they can be calculated from equation (A.10) afterwards.

The treatment of exciton diffusion is analogous to that of charge diffusion. The diffusion coefficient D_i is defined in the center of each cell i and the matrix coefficients are used in the form $a_i = c_i = -D_i \Delta t / (\Delta z)^2$, $b_i = 1 + 2D_i \Delta t / (\Delta z)^2$. As discussed above, excitons are not allowed to cross organic/organic interfaces. Assuming the interface is positioned between cells i and $i + 1$, this is accounted for by choosing $b_i = 1 + D_i \Delta t / (\Delta z)^2$, $b_{i+1} = 1 + D_{i+1} \Delta t / (\Delta z)^2$ and $c_i = a_{i+1} = 0$. This eliminates cross-boundary diffusion and ensures conservation of the total number of excitons on each side of the interface. Similar to this, quenching of excitons at the electrode boundaries can be suppressed by adapting the coefficients b_0 and b_N if this is needed.

Appendix B

Organic Materials

PW A copolymer that is capable of emitting white electrofluorescence, provided by Merck KGaA, Germany. It comprises 78.91% (monomer feed ratio) **BB** polyspirofluorene backbone monomers, 11% **B** blue emitter, 10% **HT** hole transporter, 0.05% **G** green emitter, 0.04% **R** red emitter moieties, for structure see figure B.1 on page 135. For energy levels as measured by cyclic voltammetry, see figure 4.9 on page 65. Copolymers with similar structural elements have been studied by Laquai et al.[15, 53, 55] and by Parshin et al.[183] in terms of charge (mainly hole) transport properties. The main difference between these studies and the polymer used here lies in the backbone side chains. While the published work studied charge transport properties on polymers with backbone monomers featuring alkoxy sidechains, **PW** backbone monomers have alkyl side chains. Alkoxy side chains generally have a strong electron-donating character[5] and contribute to an increase in the HOMO energy and a reduction of the bandgap. Correspondingly, while space charge limited hole injection was observed by Parshin et al., chapter 3 shows that hole transport in the alkyl-type polymers is strongly injection limited.

PB Similar to **PW** but without green and red chromophores.

BG Similar to **PW** but without red chromophores.

BR Similar to **PW** but without green chromophores.

PW2 A copolymer based on a polyspirofluorene backbone capable of emitting white electrofluorescence, with structure similar to **PW** (the exact structure cannot be given for intellectual property reasons), provided by Merck KGaA, Germany. Compared to **PW**, the **B** (11%), **G** (0.05%) and **R** (0.03%) chromophores are identical, but the backbone structure differs and a second blue emitter (7%) is introduced which emits at slightly longer wavelengths.

PB2a Similar to **PW2** but only containing the backbone, HT and the shorter wavelength type blue emitter.

PB2b Similar to **PW2** but without green and red chromophores.

BG2 Similar to **PW2** but without red chromophores.

BR2 Similar to **PW2** but without green chromophores.

M3EH-PPV Poly[2,5-dimethoxy-1,4-phenylene-1,2-ethynylene-2-methoxy-5-(2-ethylhexyloxy)-(1,4-phenylene-vinylene-1,2-ethynylene)], provided by H. H. Hörhold, University of Jena. Molecular weights $M_n = 1.2 \times 10^4$ g/mol, $M_w = 4.4 \times 10^4$ g/mol, glass transition temperature $T_g = 113^\circ\text{C}$. [184, 185] According to [184], the energy levels are $\epsilon_{\text{HOMO}} = -5.2$ eV, $\epsilon_{\text{LUMO}} = -2.7$ eV.

MEH-M3EH-PPV Poly[2-methoxy-5-(2-ethylhexyloxy)-1,4-phenylenevinylene]-*block*-poly[2,5-dimethoxy-1,4-phenylenevinylene-2-methoxy-5-(2-ethylhexyloxy)-1,4-phenylenevinylene], a copolymer of **MEH-PPV** and **M3EH-PPV** provided by H. H. Hörhold, University of Jena. Molecular weights $M_n = 1.14 \times 10^4$ g/mol, $M_w = 3.23 \times 10^4$ g/mol, glass transition temperature $T_g = 81^\circ\text{C}$. [185] The energy levels are expected to be similar to those of **M3EH-PPV**. [184]

CN-ether-PPV Poly[oxa-1,4-phenylene-1,2-(1-cyano)-ethylene-2,5-dioctyloxy-1,4-phenylene-1,2-(2-cyano)-ethylene-1,4-phenylene] provided by H. H. Hörhold, University of Jena. Molecular weights $M_n = 1.2 \times 10^4$ g/mol, $M_w = 2.06 \times 10^4$ g/mol, glass transition temperature $T_g = 62^\circ\text{C}$, energy levels are according to [184] $\epsilon_{\text{HOMO}} = -5.7$ eV, $\epsilon_{\text{LUMO}} = -3.2$ eV (-5.9 eV/-3.5 eV according to [185, 186]).

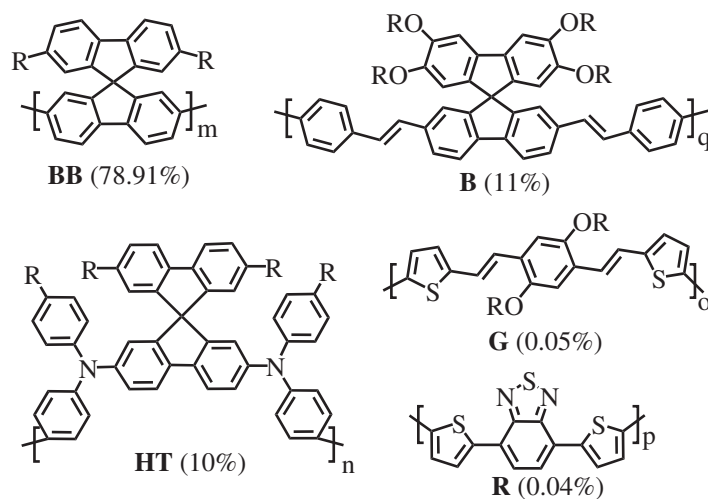


Figure B.1: Structure of the copolymer PW.

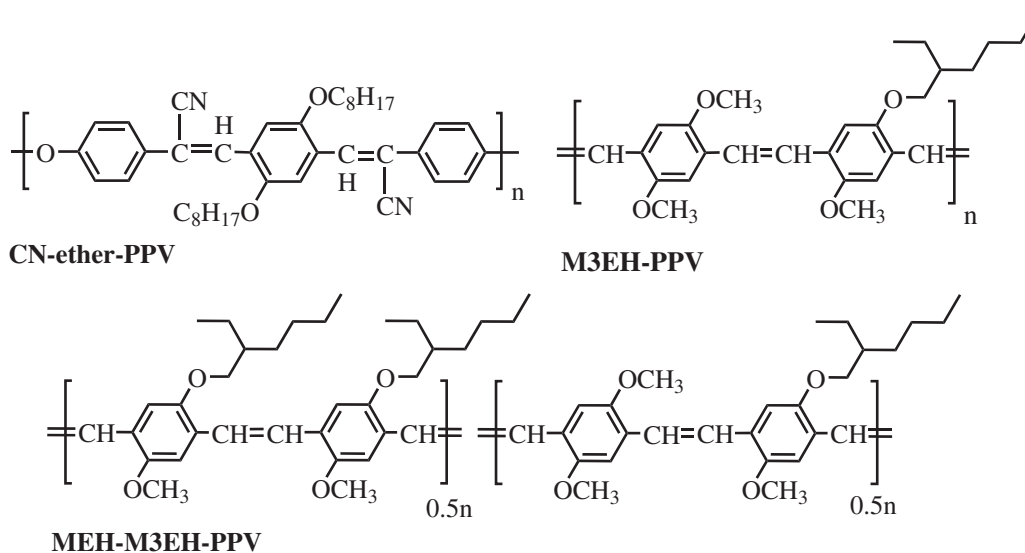


Figure B.2: Structure of the PPV-type polymers used in this thesis.

Appendix C

Sample Preparation

Thin film samples for absorption spectroscopy were fabricated in nitrogen atmosphere on top of standard microscope glass slides after thorough ultrasonic cleaning in Hellmanex II (Hellma International) alkaline detergent solution, ultrapure water and 2-propanol. The polymers were spincoated from organic solvent solution and annealed following the same recipe as used for light emitting devices. These samples were either measured as is or encapsulated using a ring spacer and a second glass slide and Araldite 2011 (Huntsman International) two-component epoxy resin dried at 65°C for 45 min before taking the samples out of the nitrogen-filled glovebox.

Light-emitting devices were fabricated on top of indium-tin oxide (*ITO*) covered glass substrates of $25 \times 25 \text{ mm}^2$ size provided by Merck KGaA (Germany) and Präzisionsglas & Optik GmbH (Germany) with sheet resistance of less than 20Ω . The ITO was structured by masking with adhesive tape and etching in $\text{HCl}:\text{FeCl}_2$ solution at 60°C. Alternatively, for devices used in transient EL experiments, pre-etched ITO covered glass substrates (sheet resistance $< 30 \Omega$) were obtained from Optrex Europe GmbH (Germany). The substrates were cleaned by ultrasonication in acetone, Hellmanex II, ultrapure water and 2-propanol. To improve the surface wettability, the precleaned substrates were treated with oxygen plasma (Tepla 200-G plasma asher, 2.45 GHz excitation frequency, 200 W power setting) for a few minutes. Directly afterwards, PEDOT:PSS obtained under the trade name Clevios AI4083 from H.C.Starck GmbH (Germany) was spincoated onto these substrates at 1500 rpm under dust-free environmental conditions through a $0.2 \mu\text{m}$ nylon syringe filter, transferred to the inert nitrogen atmosphere glove-box system and dried at 180°C for 10 min. Subsequently the active polymer layer(s) were deposited by spincoating from organic solvent solutions after which the samples were transferred to a high-vacuum chamber metal evaporator without braking of the nitrogen atmosphere. Metal cathodes were deposited through shadow masks at base pressures better than 2×10^{-6} mbar. The geometric sample design as used for transient EL samples is shown in figure C.1. It provides two independent ITO anode traces and six independent cathodes, forming two emission zones of 4 mm^2 each and four emission zones of 1 mm^2 each. After completion of the devices, the ITO was accessed by carefully scratching the polymer and PEDOT:PSS coverage of the ITO contact pads and applying conductive silver paint for improvement of the contact resistance. Metal cathodes were protected against scratches by also applying conductive silver paint in case multiple measurements on the same sample were intended. Electrical contact was established by spring loaded test probes (INGUN Prüfmittelbau GmbH, Germany) with serrated tips. For current-voltage measurements of such devices, the lower limit of leakage currents is defined

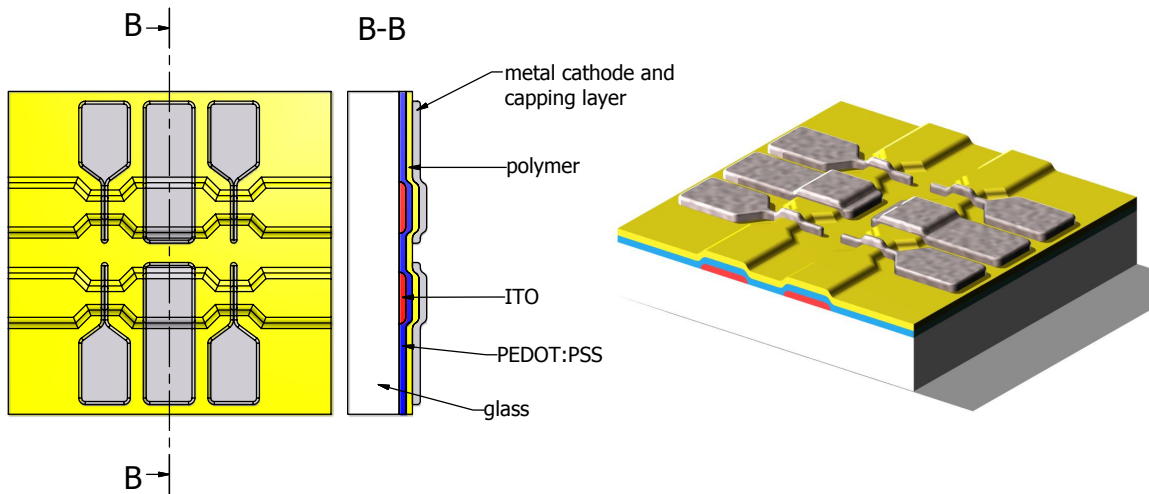


Figure C.1: Schematic design of light-emitting devices for transient EL experiments (not to scale). White: glass substrate, red: transparent conductive ITO traces, blue: transparent PEDOT:PSS layer, yellow: active polymer layer, gray: evaporated metal cathodes.

by in-plane conduction of the PEDOT:PSS film since the test probe normally punches through the thin metal cathode and polymer layer, contacting the low-conductivity PEDOT:PSS layer. This leakage resistance was reproducibly found to be on the order of 80 M Ω and thus does not interfere with measurements on bipolar light-emitting diodes. For measurements under ambient conditions outside of the glovebox nitrogen atmosphere, samples were encapsulated by a standard microscope cover glass using two-component epoxy resin (Araldite 2011) cured at 65°C for 45 min, see figure C.2. The glue is applied to the full surface of the cover glass prior to its positioning on the sample. The electrically active volume of the light-emitting polymer layer is protected from the resin by the evaporated metal cathodes and no difference in device performance was observed when as-prepared and encapsulated devices were compared in terms of luminance-voltage and current-voltage characteristics. Extensive studies of the shelf lifetime of the encapsulated devices were not conducted but the general tendency was that samples with sufficiently thick aluminum barrier capping layer on the actual cathode (itself consisting e.g. of a layer of barium, calcium or CsF/Al) survive several months being stored in the glovebox without apparent degradation effects, see figure C.3. The main degradation pathway of encapsulated devices stored for several weeks *outside* the glovebox was found to be oxidation along the cathode traces. This might be related to increased surface roughness of oxidized metal areas and consequently enhanced oxygen permeability along the polymer/metal or metal/epoxy resin interfaces.

Electron-only devices with low leakage currents were made based on glass / ITO / PEDOT:PSS substrates prepared as described above, but using unstructured ITO covering the

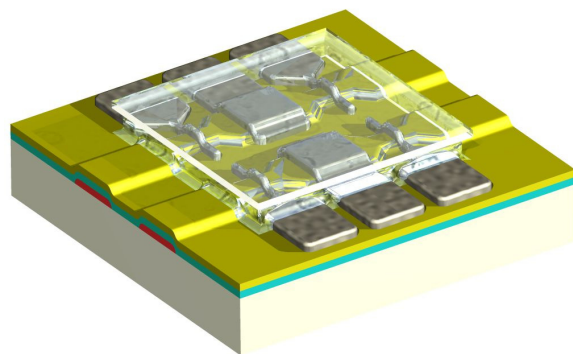


Figure C.2: Schematic design of encapsulated light-emitting devices (not to scale). The functional parts of the light-emitting polymer and the reactive metal cathodes are protected from environmental oxygen and water molecules by a cover glass slide and two-component epoxy resin.

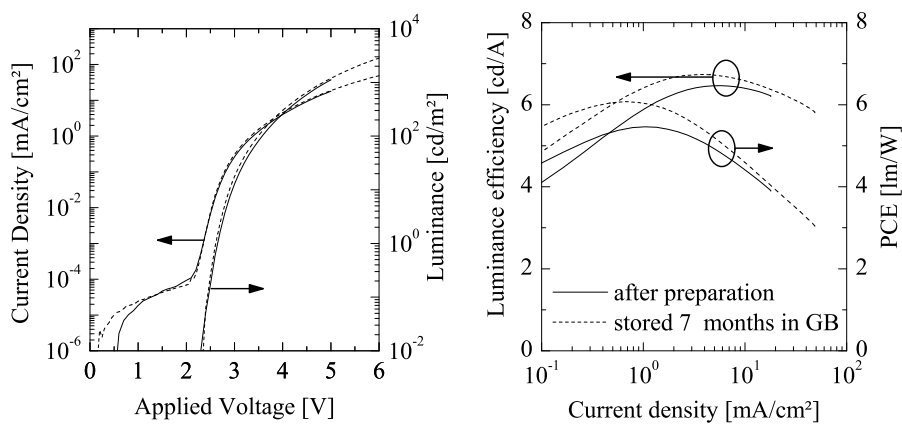


Figure C.3: Comparison of optoelectric device characteristics of a PW light-emitting diode with 80 nm thick polymer layer and CsF/Al cathode capped by 250 nm aluminum and encapsulated with two-component epoxy resin and a glass slide. The sample was stored for 7 months inside the glovebox nitrogen atmosphere without apparent degradation of performance.

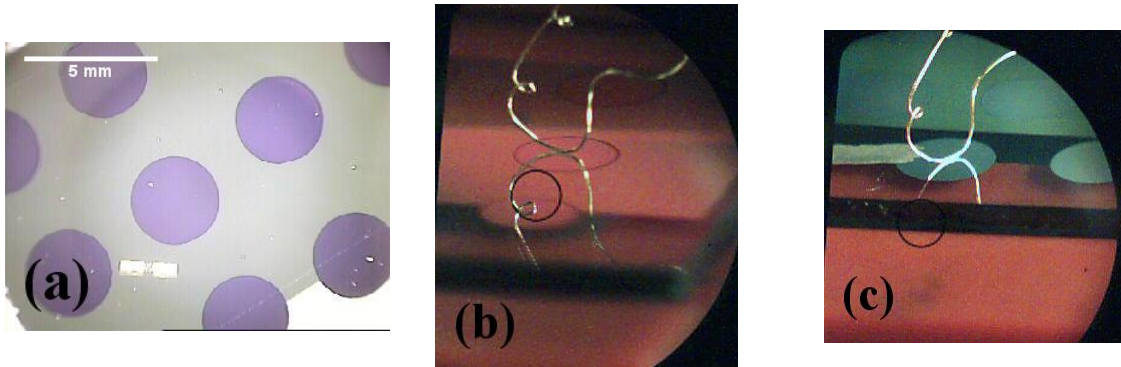


Figure C.4: (a) Electron-only devices cathode layout as viewed perpendicular to the substrate. The contrast is due to thin-film interference. (b) Electron-only devices during measurement viewed under oblique angle (substrate edge visible in the foreground). A gold wire of 100 μm diameter is in contact with a circular (aluminum top layer) cathode on top of a thin polymer film, the wire's mirror image due to reflection from the substrate surface is seen below. (c) The gold wire contacting an aluminum cathode spot directly contacted by silver paint. This setup was used to assess the contact resistance. The black circles are due to taking the pictures through the luminance meter's optics and can be ignored here.

full sample surface. An aluminum layer of 50 nm thickness was thermally evaporated over the whole surface of PEDOT:PSS in high vacuum of base pressures below 2×10^{-6} mbar at a nominal evaporation rate of 0.5 nm/s. The thin aluminum layer was found to completely suppress hole injection into the polymers studied here, while retaining the surface quality of the underlying PEDOT:PSS layer. Following preparation of these substrates, polymers were spincoated as for light-emitting devices. The electron-injecting cathode layer (0.5 nm CsF, 5 nm Ba or 20 nm Ca) was then thermally deposited, again under high vacuum conditions, followed by a thick capping layer of more than 200 nm aluminum. Cathode deposition was done through a shadow mask with circular apertures, see figure C.4 (a). The devices were handled in nitrogen atmosphere at all times, all measurement steps were performed on non-encapsulated samples within the nitrogen glovebox systems. Electrical contact to the active sample area was provided by the ITO/PEDOT:PSS/aluminum bottom anode and via the circular aluminum cathode. This was contacted by gently approaching a bend gold wire of 100 μm diameter to the cathode surface, see figure C.4 (b). The gold wire was sufficiently elongated to provide a low elastic force upon contact and it was handled by a three-axis stepper motor setup for reproducibility. Usually, the gold wire was lowered onto the cathode while monitoring the current flowing through the circuit at an applied voltage of 1 V. The current was found to settle at low, stable values when some bending of the gold wire and small amounts of bending-induced slipping of the contact point across the cathode indicated sufficient contact force. The 200 nm aluminum capping layer was strong enough to sustain repeated contacts to the same point without changes in leakage current or measured current-voltage curves. The total contact resistance provided by this method was assessed by directly contacting a cathode patch via a thin conductive trace of silver paint before approaching the gold wire as before, see figure C.4 (c). The total resistance measured for this type of contacting was below 5 Ω .

Appendix D

Measurement Techniques

Current-Voltage Characteristics The current voltage characteristics of light-emitting diodes and unipolar devices were measured using a model 2400 source / measure unit (Keithley Instruments) and a computer-controlled measurement procedure. Except for electron-only samples, devices were contacted by spring-loaded test probes with serrated tips (INGUN Prüfmittelbau, Germany) in custom sample holders while the typically 200 nm thick cathode layers were additionally protected from scratches by coating them with silver paint.

External Quantum Efficiency Here: the ratio of emitted photon flux to the input flux of charges.

Fluorescence Spectra Thin film fluorescence spectra were obtained with a LS 55 fluorescence spectrometer (PerkinElmer) in direct-beam front surface geometry or via a fiber bundle coupled remote input, alternatively the spectra were obtained with a FluoroLog-3 fluorescence spectrometer (Horiba Jobin Yvon). Emission spectra were spectrally corrected by measuring an incandescent lamp of known standard spectrum, excitation spectra were corrected by measuring the emission of a quantum counter solution (concentrated rhodamine) in front surface geometry.

Layer Thickness The layer thickness was usually determined by scratching of the film and determination of the scratch depth by a Dektak 3ST (Veeco) stylus profilometer under ambient conditions in air. Alternatively, an atomic force microscope (Solver, NT-MDT) was used to measure the scratches.

Luminance The luminance L_V is measured by a CS-100a (Konica Minolta) luminance meter with a 1° acceptance angle perpendicular to the sample substrate. The measurement range is 10^{-2} cd/m² to 3×10^5 cd/m².

Luminous Power The luminous power Φ_V is calculated from the measured luminance L_V and size A of the light-emitting area by assuming a Lambertian radiation distribution, $\Phi_V = \pi A L_V$. This introduces an error in the result since the radiation distribution pattern is normally modified by thin film interference effects and Fresnel-type reflections.

Photon Flux The external photon flux of devices is calculated from the determined luminous power as

$$\Phi_v = \frac{\Phi_v}{683 \text{ lm/W} \cdot hc} \frac{\int \frac{s(\lambda)\lambda}{V(\lambda)} d\lambda}{\int s(\lambda) d\lambda}$$

for the case that the emission spectrum $s(\lambda)$ is specified in terms of radiative (in contrast to quantal) units, i.e. for $s(\lambda) \propto \Phi_E(\lambda)$.

Transient Luminescence Samples were electrically excited using an Agilent 33220A 20 MHz arbitrary function generator producing rectangular voltage pulses of variable length and repetition rate with 10 ns rise time, amplified by a custom-build linear amplifier stage based on the LT1210 operational amplifier integrated circuit by Linear Technologies. It has a voltage slope speed of 900 V/ μ s, 66 MHz bandwidth and is able to drives currents up to 1 A. Since thin-film organic light-emitting diodes have a significant capacitance, such high-performance driving stages are necessary to keep the capacitance charging times shorter than the physical effects of interest. Light emission from the devices was collected by a multimode fiber bundle, spectrally dispersed by a 1200 lines/mm f/4.0 grating monochromator (AMKO MuLTImode4) and detected by a standard side-window photomultiplier tube (Hamamatsu R928) at an effective bandwidth of ~ 32 nm. The photocurrent was amplified by a fast transimpedance amplifier (FEMTO HCA-20M-100K-C with a rise time of $\tau_{10-90} \sim 18$ ns or FEMTO DHCPA-100 with rise times down to 1.8 ns) and digitized/averaged by a digital storage oscilloscope (Yokogawa DL9040) with 400 MHz bandwidth.

Appendix E

List of Abbreviations

Abbreviation	Description
BB	backbone
BE	binding energy of electrons in electronic states of the semiconductor as determined by UPS
CELIV	current extraction under linear increasing voltage, method for measuring charge carrier mobilities
CIE	Comission Internationale de l'Éclairage
DOS	density of states, usually the site density available for charge carriers
EL	electroluminescence, the phenomena of luminescence observed in bipolar devices due to the injection, transport and mutual recombination of charge carriers
EMA	effective medium approximation
FTCS	forward-time centered-space, a discretization scheme for PDE
GDM	gaussian disorder model of charge transport
HOMO	highest occupied molecular orbital
HT	hole transporter
ICCD	charge-coupled device with multichannel plate image intensifier
ITO	indium tin oxide
LED	light-emitting device
LUMO	lowest unoccupied molecular orbital
photo-CELIV	CELIV measurements following photoexcitation of charge carriers, usually by short laser pulses
MIM	metal/insulator/metal
MSM	metal/semiconductor/metal
ODE	ordinary differential equation
OLED	organic light-emitting device
PDE	partial differential equation
PEDOT:PSS	poly(3,4-ethylenedioxythiophene):poly(styrenesulphonate), a transparent, conductive polymer
PMT	photomultiplier tube
PPI	polymer/polymer interface

continued on next page

Appendix E List of Abbreviations

continued from previous page

Abbreviation	Description
RC	resistance capacitance, characteristic time for charging a capacitance
RET	resonant energy transfer
SCL	space charge limited
SCLC	space charge limited current, the maximum current that can be injected by an Ohmic contact
TEL	transient electroluminescence, the time-resolved luminescence observed after pulsed electrical excitation of bipolar devices due to injection and recombination of charges
TOF	time-of-flight photocurrent method for measurements of charge carrier mobility
UPS	ultraviolet photoelectron spectroscopy
XPS	x-ray photoelectron spectroscopy

Appendix F

List of Symbols

In this work, the logarithm to base e is written as $\log(\dots)$ while the logarithm to base 10 is written as $\log_{10}(\dots)$. The following table lists the most important parameters used within this work together with their physical units and definitions or notes where appropriate. Greek symbols were sorted according to their english pronunciation.

Symbol	Units	Name	Notes
a	m	intersite distance	
A	m^2	area	
β	$(\text{m}/\text{V})^{1/2}$	Poole-Frenkel slope parameter	
b	1	numerical parameter	used in the treatment of random walk, $b = m/S_m$ where S_m is the number of distinct sites visited within m hops
χ	1	injection efficiency	defined via $\chi = j/j_{\text{SCLC}}$
c	1	concentration	
d	m	layer thickness	
D	m^2/s	diffusion constant	
ϵ	1	relative permittivity or energy	depending on the context, this symbol either denotes relative permittivity or energy (differences in energy)
ϵ_0	C/Vm	electric constant	$\epsilon_0 \approx 8.854 \times 10^{-12} \text{ C/Vm}$
e	C	elementary charge	$e \approx 1.602 \times 10^{-19} \text{ C}$
E	V/m	electric field	
η_{E}	1	radiant efficiency	ratio of emitted radiant flux and input electrical power, $\eta_{\text{E}} = \Phi_{\text{E}}/P$
η_{ext}	1	external quantum efficiency	here: ratio of emitted photon flux Φ_{V} and charge injection rate calculated from the measured current I , $\eta_{\text{ext}} = \Phi_{\text{V}}e/I$
η_{ST}	1	singlet-triplet branching ratio	
η_{V}	lm/W	luminous efficacy	the luminous efficacy of a light source, $\eta_{\text{V}} = \eta_{\text{E}}K$
γ	m^3/s	bimolecular rate constant	

continued on next page

Appendix F List of Symbols

continued from previous page

Symbol	Units	Name	Notes
h	Js	Planck constant	$h \approx 6.626 \times 10^{-34}$ Js
j	A/m ²	current density	
j_{cap}	A/m ²	capacitive current density	current density used for charging the sample capacitance $j_{\text{cap}} = \epsilon\epsilon_0 U'_{\text{ext}}/d$
j_{ext}	A/m ²	external current density	current density flowing in an external (w.r.t. the semiconductor device) electric circuit
k_{B}	J/K	Boltzmann constant	$k_{\text{B}} \approx 1.381 \times 10^{-23}$ J/K
k	1/s	first-order rate constant	used for rate equations
K	lm/W	luminous efficacy of radiation	this characterizes the spectrum emitted by light sources in terms of luminous power divided by radiant flux, $K = 683 \text{ lm/W} \int \Phi_{\text{E}}(\lambda)V(\lambda)d\lambda / \int \Phi_{\text{E}}(\lambda)d\lambda$
l_{T}	m	mean free path	
L_{D}	m	exciton diffusion length	
L_{E}	W/m ² sr	radiance	radiant power emitted per solid angle and source area projected into emission direction, $L_{\text{E}} = d^2\Phi_{\text{E}}/(d\Omega dA \cos \vartheta)$
L_{V}	cd/m ²	luminance	integrated spectral radiance L_{E} of a light source weighted by the photopic luminous efficiency $V(\lambda)$, $L_{\text{V}} = 683 \frac{\text{lm}}{\text{W}} \int L_{\text{E}}(\lambda)V(\lambda)d\lambda$
μ	m ² /Vs	charge mobility	defined by $\mu = v/E$, where v is the average drift speed of charges and E is the electric field
m_{e}	kg	electron mass	
M_{n}	kg/mol	number-average molecular weight	$M_{\text{n}} = \sum_i n_i M_i / \sum_i n_i$, where n_i is the number of molecules having molar mass M_i
M_{w}	kg/mol	weight-average molecular weight	$M_{\text{w}} = \sum_i w_i M_i / \sum_i w_i$, where w_i is the fraction by weight of molecules having molar mass M_i
n	m ⁻³	charge density or index of refraction	depending on the context, n is used for both the charge carrier density as well as for the index of refraction
N	1 or 1/m ³	total number or total density	depending on context, used for both the total number as well as the total number density (e.g. of states, acceptors, charge-trapping molecules)
Φ_{E}	W	radiant power	radiant energy emitted per time
Φ_{v}	1/s	photon flux	the rate of emitted photons
Φ_{V}	lm	luminous power	the luminous power is the integrated spectral radiant power weighted by the photopic luminous efficiency, $\Phi_{\text{V}} = 683 \frac{\text{lm}}{\text{W}} \int \Phi_{\text{E}}(\lambda)V(\lambda)d\lambda$

continued on next page

continued from previous page

Symbol	Units	Name	Notes
$Q_{A,C}$	C	charge	charge stored on the anodic and cathodic electrodes
r	1	color ratio	$r = R/(B + G)$
R	Ω	resistance	
σ	eV	diagonal disorder	energetic disorder parameter for the GDM
σ_T	m ²	trapping cross section	
Σ	1	off-diagonal disorder	spatial disorder parameter for the GDM
τ	s	lifetime or characteristic time	
τ_σ	s	dielectric relaxation time	$\tau_\sigma = \epsilon\epsilon_0/en\mu$
t	s	time coordinate	
T	K	temperature	
U	V	electric voltage	
$V(\lambda)$	1	photopic luminous efficiency	this is the standard photopic luminosity function and equal to the Commission Internationale de l'Eclairage (CIE) 1931 color space color matching function $\bar{y}(\lambda)$
z	m	spatial coordinate	
Z	1	dimensionality factor	used in the treatment of diffusion

Bibliography

- [1] H. Shirakawa, *The discovery of polyacetylene film: the dawning of an era of conducting polymers in Nobel Lectures, Chemistry 1996-2000* edited by I. Grenthe, World Scientific Publishing Co. Singapore, 2003.
- [2] A. G. MacDiarmid, 'Synthetic metals': a novel role for organic polymers in *Nobel Lectures, Chemistry 1996-2000* edited by I. Grenthe, World Scientific Publishing Co. Singapore, 2003.
- [3] J. H. Burroughes, D. D. C. Bradley, A. R. Brown, R. N. Marks, K. Mackay, R. H. Friend, P. L. Burns, and A. B. Holmes, *Light-emitting-diodes based on conjugated polymers*, *Nature* **347** (6293), 539–541, 1990.
- [4] C. W. Tang and S. A. VanSlyke, *Organic electroluminescent diodes*, *Applied Physics Letters* **51** (12), 913–915, 1987.
- [5] J. Roncali, *Molecular engineering of the band gap of pi-conjugated systems: Facing technological applications*, *Macromolecular Rapid Communications* **28** (17), 1761–1775, 2007.
- [6] T. Blythe and D. Bloor, *Electrical properties of polymers*, Cambridge University Press, Cambridge, 2. edition 2005.
- [7] M. Pope and C. E. Swenberg, *Electronic processes in organic crystals and polymers*, Oxford University Press, New York/Oxford, 2. edition 1999.
- [8] S. Baranovski, *Charge transport in disordered solids with applications in electronics*, Wiley, 2006.
- [9] H. Bässler, *Charge transport in disordered organic photoconductors - a monte-carlo simulation study*, *Physica Status Solidi B* **175** (1), 15–56, 1993.
- [10] T. Holstein, *Studies of polaron motion 2: The small polaron*, *Annals of Physics* **8** (3), 343–389, 1959.
- [11] P. M. Borsenberger, L. Pautmeier, and H. Bässler, *Charge transport in disordered molecular solids*, *Journal of Chemical Physics* **94** (8), 5447–5454, 1991.
- [12] J. Frenkel, *On pre-breakdown phenomena in insulators and electronic semi-conductors*, *Physical Review* **54** (8), 647–648, 1938.
- [13] J. G. Simmons, *Conduction in thin dielectric films*, *Journal of Physics D* **4** (5), 613, 1971.

- [14] Y. N. Gartstein and E. M. Conwell, *High-field hopping mobility in molecular-systems with spatially correlated energetic disorder*, *Chemical Physics Letters* **245** (4-5), 351–358, 1995.
- [15] F. Laquai, G. Wegner, and H. Bässler, *What determines the mobility of charge carriers in conjugated polymers?*, *Philosophical Transactions of the Royal Society A* **365** (1855), 1473–1487, 2007.
- [16] G. Horowitz, *Organic thin film transistors in Semiconducting Polymers: Chemistry, Physics and Engineering* vol. 2 edited by G. Hadziioannou and G. G. Malliaras, Wiley-VCH Weinheim, 2. edition 2007.
- [17] R. Coehoorn, W. F. Pasveer, P. A. Bobbert, and M. A. J. Michels, *Charge-carrier concentration dependence of the hopping mobility in organic materials with gaussian disorder*, *Physical Review B* **72** (15), 155206, 2005.
- [18] W. Graupner, S. Tasch, and G. Leising, *Solid state aspects of conjugated semiconductors in Semiconducting Polymers: Chemistry, Physics and Engineering* edited by G. Hadziioannou and P. F. v. Hutten, Wiley-VCH Weinheim, 1. edition 2000.
- [19] R. H. Fowler and L. Nordheim, *Electron emission in intense electric fields*, *Proceedings of the Royal Society of London Series A* **119** (781), 173–181, 1928.
- [20] S. M. Sze, *Physics of semiconductor devices*, John Wiley & Sons, 2. edition 1981.
- [21] I. D. Parker, *Carrier tunneling and device characteristics in polymer light-emitting diodes*, *Journal of Applied Physics* **75** (3), 1656–1666, 1994.
- [22] D. V. Khramtchenkov, H. Bässler, and V. I. Arkhipov, *A model of electroluminescence in organic double-layer light-emitting diodes*, *Journal of Applied Physics* **79** (12), 9283–9290, 1996.
- [23] D. Braun, *Electronic injection and conduction processes for polymer devices*, *Journal of Polymer Science Part B: Polymer Physics* **41** (21), 2622–2629, 2003.
- [24] O. W. Richardson, *Thermionic phenomena and the laws which govern them in Nobel Lectures, Physics 1922-1941*, Elsevier Publishing Co. Amsterdam, 1965.
- [25] J. G. Simmons, *Richardson-Schottky effect in solids*, *Physical Review Letters* **15** (25), 967–968, 1965.
- [26] P. S. Davids, I. H. Campbell, and D. L. Smith, *Device model for single carrier organic diodes*, *Journal of Applied Physics* **82** (12), 6319–6325, 1997.
- [27] J. C. Scott, G. G. Malliaras, J. R. Salem, P. J. Brock, L. Bozano, and S. A. Carter, *Injection, transport and recombination in organic light-emitting diodes*, in *Conference on Organic Light-Emitting Materials and Devices II* edited by Z. H. Kafafi, pages 111–122, SPIE, San Diego 1998.

- [28] J. C. Scott and G. G. Malliaras, *Charge injection and recombination at the metal-organic interface*, Chemical Physics Letters **299** (2), 119, 1999.
- [29] M. A. Abkowitz and H. A. Mizes, *Emission limited injection by thermally assisted tunneling into a trap-free transport polymer*, Applied Physics Letters **66** (10), 1288–1290, 1995.
- [30] Y. N. Gartstein and E. M. Conwell, *Field-dependent thermal injection into a disordered molecular insulator*, Chemical Physics Letters **255** (1-3), 93–98, 1996.
- [31] T. van Woudenberg, *Charge injection into organic semiconductors*, PhD thesis, Rijksuniversiteit Groningen, Groningen, Netherlands 2005.
- [32] V. I. Arkhipov, E. V. Emelianova, Y. H. Tak, and H. Bässler, *Charge injection into light-emitting diodes: Theory and experiment*, Journal of Applied Physics **84** (2), 848–856, 1998.
- [33] U. Wolf, V. I. Arkhipov, and H. Bässler, *Current injection from a metal to a disordered hopping system. I. Monte-Carlo simulation*, Physical Review B **59** (11), 7507–7513, 1999.
- [34] L. Onsager, *Initial recombination of ions*, Physical Review **54** (8), 554, 1938.
- [35] L. Onsager, *Deviations from Ohm's law in weak electrolytes*, The Journal of Chemical Physics **2** (9), 599–615, 1934.
- [36] S. Barth, U. Wolf, H. Bässler, P. Müller, H. Riel, H. Vestweber, P. F. Seidler, and W. Riess, *Current injection from a metal to a disordered hopping system. III. Comparison between experiment and Monte-Carlo simulation*, Physical Review B **60** (12), 8791–8797, 1999.
- [37] H. H. Fong, A. Papadimitratos, J. Hwang, A. Kahn, and G. G. Malliaras, *Hole injection in a model fluorene-triarylamine copolymer*, Advanced Functional Materials **19** (2), 304–310, 2009.
- [38] M. Pope, P. Magnante, and H. P. Kallmann, *Electroluminescence in organic crystals*, Journal of Chemical Physics **38** (8), 2042, 1963.
- [39] M. Sano, M. Pope, and H. Kallmann, *Electroluminescence and band gap in anthracene*, Journal of Chemical Physics **43** (8), 2920, 1965.
- [40] P. M. Borsenberger and D. S. Weiss, *Organic photoreceptors for xerography*, Marcel Dekker Inc., New York, 1998.
- [41] P. Langevin, *The recombination and mobilities of ions in gases*, Annales De Chimie Et De Physique **28**, 433–530, 1903.
- [42] B. Ries and H. Bässler, *Monte carlo study of bimolecular charge-carrier recombination in anisotropic lattices*, Chemical Physics Letters **108** (1), 71–75, 1984.

- [43] T. R. Waite, *Theoretical treatment of the kinetics of diffusion-limited reactions*, Physical Review **1** (2), 463–470, 1957.
- [44] R. H. Friend and N. C. Greenham, *Electroluminescence in conjugated polymers* in *Handbook of conducting polymers* edited by T. A. Skotheim, R. L. Elsenbaumer, and J. R. Reynolds, Marcel Dekker Inc. New York, 2. edition 1998.
- [45] J. S. Wilson, A. S. Dhoot, A. J. A. B. Seeley, M. S. Khan, A. Kohler, and R. H. Friend, *Spin-dependent exciton formation in pi-conjugated compounds*, Nature **413** (6858), 828–831, 2001.
- [46] M. Wohlgenannt, X. M. Jiang, Z. V. Vardeny, and R. A. J. Janssen, *Conjugation-length dependence of spin-dependent exciton formation rates in pi-conjugated oligomers and polymers*, Physical Review Letters **88** (19), 4, 2002.
- [47] S. Difley, D. Beljonne, and T. Van Voorhis, *On the singlet-triplet splitting of geminate electron-hole pairs in organic semiconductors*, Journal of the American Chemical Society **130** (11), 3420–3427, 2008.
- [48] M. C. Gather, R. Alle, H. Becker, and K. Meerholz, *On the origin of the color shift in white-emitting oleds*, Advanced Materials **19** (24), 4460, 2007.
- [49] A. Parham, S. Heun, A. Falcou, A. Büsing, J. Pan, and H. Becker, World patent no. PCT WO/2005/104263 2005.
- [50] H. Becker, K. Treacher, H. Spreitzer, A. Falcou, A. Büsing, and A. Parham, World patent no. PCT WO/2003/020790 2003.
- [51] T. P. I. Saragi, T. Spehr, A. Siebert, T. Fuhrmann-Lieker, and J. Salbeck, *Spiro compounds for organic optoelectronics*, Chemical Reviews **107** (4), 1011–1065, 2007.
- [52] J. U. Wallace and S. H. Chen, *Fluorene-based conjugated oligomers for organic photonics and electronics*, Polyfluorenes **212**, 145–186, 2008.
- [53] F. Laquai, G. Wegner, C. Im, H. Bässler, and S. Heun, *Comparative study of hole transport in polyspirobifluorene polymers measured by the charge-generation layer time-of-flight technique*, Journal of Applied Physics **99** (2), 023712, 2006.
- [54] F. Laquai, G. Wegner, C. Im, H. Bässler, and S. Heun, *Nondispersive hole transport in carbazole- and anthracene-containing polyspirobifluorene copolymers studied by the charge-generation layer time-of-flight technique*, Journal of Applied Physics **99** (3), 033710–7, 2006.
- [55] F. Laquai and D. Hertel, *Influence of hole transport units on the efficiency of polymer light emitting diodes*, Applied Physics Letters **90**, 142109, 2007.
- [56] W. E. Spear, *Drift mobility techniques for the study of electrical transport properties in insulating solids*, Journal of Non-Crystalline Solids **1** (3), 197–214, 1969.

- [57] H. Scher and E. W. Montroll, *Anomalous transit-time dispersion in amorphous solids*, Physical Review B **12** (6), 2455, 1975.
- [58] A. I. Rudenko and V. I. Arkhipov, *Drift and diffusion in materials with traps - I. Quasi-equilibrium transport regime*, Philosophical Magazine Part B **45** (2), 177 – 187, 1982.
- [59] V. I. Arkhipov and A. I. Rudenko, *Drift and diffusion in materials with traps - II. Non-equilibrium transport regime*, Philosophical Magazine Part B **45** (2), 189 – 207, 1982.
- [60] A. I. Rudenko and V. I. Arkhipov, *Drift and diffusion in materials with traps - III. Analysis of transient current and transit time characteristics*, Philosophical Magazine Part B **45** (2), 209 – 226, 1982.
- [61] A. J. Mozer, N. S. Sariciftci, A. Pivrikas, R. Österbacka, G. Juska, L. Brassat, and H. Bässler, *Charge carrier mobility in regioregular poly(3-hexylthiophene) probed by transient conductivity techniques: A comparative study*, Physical Review B **71** (3), 035214, 2005.
- [62] H.-E. Tseng, T.-H. Jen, K.-Y. Peng, and S.-A. Chen, *Measurements of charge mobility and diffusion coefficient of conjugated electroluminescent polymers by time-of-flight method*, Applied Physics Letters **84** (9), 1456–1458, 2004.
- [63] A. Hirao, H. Nishizawa, and M. Sugiuchi, *Diffusion and drift of charge carriers in molecularly doped polymers*, Physical Review Letters **75** (9), 1787, 1995.
- [64] V. R. Nikitenko, H. v. Seggern, and H. Bässler, *Non-equilibrium transport of charge carriers in disordered organic materials*, Journal of Physics: Condensed Matter **19** (13), 136210, 2007.
- [65] L. Pautmeier, R. Richert, and H. Bässler, *Anomalous time-independent diffusion of charge-carriers in a random potential under a bias field*, Philosophical Magazine B **63** (3), 587–601, 1991.
- [66] I. I. Fishchuk, A. Kadashchuk, H. Bässler, and M. Abkowitz, *Low-field charge-carrier hopping transport in energetically and positionally disordered organic materials*, Physical Review B **70** (24), 2004.
- [67] P. M. Borsenberger, L. T. Pautmeier, and H. Bässler, *Nondispersive-to-dispersive charge-transport transition in disordered molecular solids*, Physical Review B **46** (19), 12145, 1992.
- [68] J. S. Facci and M. Stolka, *Redox migration mechanism of charge transport in molecularly doped polymers*, Philosophical Magazine B **54** (1), 1–18, 1986.
- [69] S. R. Mohan, M. P. Joshi, and A. K. Srivastava, *On the field and temperature dependence of hole mobility in molecularly doped polymer*, Synthetic Metals **155** (2), 372–375, 2005.
- [70] S. Heun and P. M. Borsenberger, *Hole transport in doubly-doped polystyrene*, Journal of Imaging Science and Technology **43** (3), 206–212, 1999.

- [71] L. Y. Chen, T. H. Ke, C. C. Wu, T. C. Chao, K. T. Wong, and C. C. Chang, *Anisotropic ambipolar carrier transport and high bipolar mobilities up to $0.1 \text{ cm}^2\text{V}^{-1}\text{s}^{-1}$ in aligned liquid-crystal glass films of oligofluorene*, *Applied Physics Letters* **91** (16), 2007.
- [72] C. C. Wu, T. L. Liu, Y. T. Lin, W. Y. Hung, T. H. Ke, K. T. Wong, and T. C. Chao, *Influences of oligomer length on carrier-transport properties of oligofluorenes*, *Applied Physics Letters* **85** (7), 1172–1174, 2004.
- [73] C. Hosokawa, H. Tokailin, H. Higashi, and T. Kusumoto, *Transient-behavior of organic thin-film electroluminescence*, *Applied Physics Letters* **60** (10), 1220–1222, 1992.
- [74] J. Pommerehne, D. V. Nikolaenkov, V. R. Nikitenko, and H. Bässler, *Overshoot effect in transient electroluminescence from single layer organic light-emitting diodes*, *Journal of Applied Physics* **90** (11), 5554–5560, 2001.
- [75] V. Savvateev, A. Yakimov, and D. Davidov, *Transient electroluminescence from poly(phenylenevinylene)-based devices*, *Advanced Materials* **11** (7), 519, 1999.
- [76] S. Barth, P. Müller, H. Riel, P. F. Seidler, W. Riess, H. Vestweber, and H. Bässler, *Electron mobility in tris(8-hydroxy-quinoline)aluminum thin films determined via transient electroluminescence from single- and multilayer organic light-emitting diodes*, *Journal of Applied Physics* **89** (7), 3711–3719, 2001.
- [77] S. C. Tse, H. H. Fong, and S. K. So, *Electron transit time and reliable mobility measurements from thick film hydroxyquinoline-based organic light-emitting diode*, *Journal of Applied Physics* **94** (3), 2033–2037, 2003.
- [78] V. R. Nikitenko, V. I. Arkhipov, Y. H. Tak, J. Pommerehne, H. Bässler, and H. H. Hörhold, *The overshoot effect in transient electroluminescence from organic bilayer light emitting diodes: Experiment and theory*, *Journal of Applied Physics* **81** (11), 7514–7525, 1997.
- [79] V. Savvate'ev, J. H. Friedl, L. Zou, K. Christensen, W. Oldham, L. J. Rothberg, Z. Chen-Esterlit, R. Kopelman, and J. Shinar, *Nanosecond electroluminescence (EL) spikes at the voltage turn-off from a small molecular organic light-emitting device (OLED)*, *Synthetic Metals* **121** (1-3), 1713–1714, 2001.
- [80] D. J. Pinner, R. H. Friend, and N. Tessler, *Transient electroluminescence of polymer light emitting diodes using electrical pulses*, *Journal of Applied Physics* **86** (9), 5116–5130, 1999.
- [81] D. J. Pinner, R. H. Friend, and N. Tessler, *Analysis of the turn-off dynamics in polymer light-emitting diodes*, *Applied Physics Letters* **76** (9), 1137–1139, 2000.
- [82] D. J. Pinner, R. H. Friend, and N. Tessler, *Use of multiple electrical pulses to study charge transport in polymer light-emitting diodes*, *Applied Physics Letters* **77** (10), 1493–1495, 2000.

- [83] D. J. Pinner, R. H. Friend, and N. Tessler, *The use of electrical pulses to study the physics of bilayer organic light-emitting diodes*, *Journal of Applied Physics* **97** (1), 014504, 2005.
- [84] J. Wang, R. G. Sun, G. Yu, and A. J. Heeger, *Fast pulsed electroluminescence from polymer light-emitting diodes*, *Journal of Applied Physics* **91** (4), 2417–2422, 2002.
- [85] R. A. Klenkler, G. Xu, H. Aziz, and Z. D. Popovic, *Charge-carrier mobility in an organic semiconductor thin film measured by photoinduced electroluminescence*, *Applied Physics Letters* **88** (24), 242101, 2006.
- [86] J. S. Kim, R. H. Friend, I. Grizzi, and J. H. Burroughes, *Spin-cast thin semiconducting polymer interlayer for improving device efficiency of polymer light-emitting diodes*, *Applied Physics Letters* **87** (2), 023506, 2005.
- [87] X. H. Yang, F. Jaiser, B. Stiller, D. Neher, F. Galbrecht, and U. Scherf, *Efficient polymer electrophosphorescent devices with interfacial layers*, *Advanced Functional Materials* **16** (16), 2156–2162, 2006.
- [88] C. Yin, B. Pieper, B. Stiller, T. Kietzke, and D. Neher, *Charge carrier generation and electron blocking at interlayers in polymer solar cells*, *Applied Physics Letters* **90** (13), 133502, 2007.
- [89] W. Brütting, H. Riel, T. Beierlein, and W. Riess, *Influence of trapped and interfacial charges in organic multilayer light-emitting devices*, *Journal of Applied Physics* **89** (3), 1704–1712, 2001.
- [90] N. Koch, A. Vollmer, and A. Elschner, *Influence of water on the work function of conducting poly(3,4-ethylenedioxythiophene)/poly(styrenesulfonate)*, *Applied Physics Letters* **90** (4), 043512, 2007.
- [91] A. M. Nardes, M. Kemerink, R. A. J. Janssen, J. A. M. Bastiaansen, N. M. M. Kiggen, B. M. W. Langeveld, A. van Breemen, and M. M. de Kok, *Microscopic understanding of the anisotropic conductivity of PEDOT:PSS thin films*, *Advanced Materials* **19** (9), 1196, 2007.
- [92] N. Koch, *Organic electronic devices and their functional interfaces*, *ChemPhysChem* **8** (10), 1438–1455, 2007.
- [93] N. Koch and A. Vollmer, *Electrode-molecular semiconductor contacts: Work-function-dependent hole injection barriers versus fermi-level pinning*, *Applied Physics Letters* **89** (16), 162107, 2006.
- [94] D. Poplavskyy, J. Nelson, and D. D. C. Bradley, *Ohmic hole injection in poly(9,9-dioctylfluorene) polymer light-emitting diodes*, *Applied Physics Letters* **83** (4), 707–709, 2003.
- [95] C.-K. Yang, C.-M. Yang, H.-H. Liao, S.-F. Horng, and H.-F. Meng, *Current injection and transport in polyfluorene*, *Applied Physics Letters* **91** (9), 093504, 2007.

- [96] P. A. Lane, J. C. deMello, R. B. Fletcher, and M. Bernius, *Electric field screening in polymer light-emitting diodes*, Applied Physics Letters **83** (17), 3611–3613, 2003.
- [97] P. J. Brewer, P. A. Lane, J. S. Huang, A. J. DeMello, D. D. C. Bradley, and J. C. DeMello, *Role of electron injection in polyfluorene-based light emitting diodes containing PEDOT:PSS*, Physical Review B **71** (20), 205209, 2005.
- [98] P. A. Anderson, *Work function of gold*, Physical Review **115** (3), 553, 1959.
- [99] S. Trasatti, *Operative (electrochemical) work function of gold*, Journal of Electroanalytical Chemistry **54** (1), 19–24, 1974.
- [100] J. M. Heras, G. Estiu, and L. Viscido, *The interaction of water with clean palladium films: A thermal desorption and work function study*, Applied Surface Science **108** (4), 455–464, 1997.
- [101] G. G. Malliaras and J. C. Scott, *Numerical simulations of the electrical characteristics and the efficiencies of single-layer organic light emitting diodes*, Journal of Applied Physics **85** (10), 7426–7432, 1999.
- [102] M. Abkowitz, J. S. Facci, and J. Rehm, *Direct evaluation of contact injection efficiency into small molecule based transport layers: Influence of extrinsic factors*, Journal of Applied Physics **83** (5), 2670–2676, 1998.
- [103] A. J. Campbell, D. D. C. Bradley, and H. Antoniadis, *Quantifying the efficiency of electrodes for positive carrier injection into poly(9,9-dioctylfluorene) and representative copolymers*, Journal of Applied Physics **89** (6), 3343–3351, 2001.
- [104] G. Greczynski, M. Fahlman, and W. R. Salaneck, *An experimental study of poly(9,9-dioctyl-fluorene) and its interfaces with Li, Al, and LiF*, Journal of Chemical Physics **113** (6), 2407–2412, 2000.
- [105] N. Koch, A. Elschner, J. R. Rabe, and R. L. Johnson, *Work function independent hole-injection barriers between pentacene and conducting polymers*, Advanced Materials **17** (3), 330, 2005.
- [106] C. Tengstedt, W. Osikowicz, W. R. Salaneck, I. D. Parker, C. H. Hsu, and M. Fahlman, *Fermi-level pinning at conjugated polymer interfaces*, Applied Physics Letters **88** (5), 2006.
- [107] J. Hwang, E. G. Kim, J. Liu, J. L. Bredas, A. Duggal, and A. Kahn, *Photoelectron spectroscopic study of the electronic band structure of polyfluorene and fluorene-arylamine copolymers at interfaces*, Journal of Physical Chemistry C **111** (3), 1378–1384, 2007.
- [108] R. Steyrlleuthner, S. Bange, and D. Neher, *Reliable electron-only devices and electron transport in n-type polymers*, Journal of Applied Physics **105** (6), 064509, 2009.
- [109] R. Steyrlleuthner, *Bestimmung der Elektronenmobilität in Schichten konjugierter Polymere*, diploma thesis, University of Potsdam, Potsdam 2009.

- [110] S. A. Choulis, V.-E. Choong, M. K. Mathai, and F. So, *The effect of interfacial layer on the performance of organic light-emitting diodes*, Applied Physics Letters **87** (11), 113503, 2005.
- [111] S. A. Choulis, V.-E. Choong, A. Patwardhan, M. K. Mathai, and F. So, *Interface modification to improve hole-injection properties in organic electronic devices*, Advanced Functional Materials **16** (8), 1075–1080, 2006.
- [112] P. J. Brown, D. S. Thomas, A. Kohler, J. S. Wilson, J. S. Kim, C. M. Ramsdale, H. Sirringhaus, and R. H. Friend, *Effect of interchain interactions on the absorption and emission of poly(3-hexylthiophene)*, Physical Review B **67** (6), 2003.
- [113] A. Zen, *Charge transport in poly(3-hexylthiophene) and in highly soluble oligothiophene*, PhD thesis, University of Potsdam, Potsdam 2006.
- [114] M. P. Keane, S. Svensson, A. N. Debrito, N. Correia, S. Lunell, B. Sjogren, O. Inganas, and W. R. Salaneck, *Gas-phase x-ray photoelectron-spectroscopy of model molecules relating to the thermochromism in poly(3-alkylthiophene)*, Journal of Chemical Physics **93** (9), 6357–6362, 1990.
- [115] N. C. Greenham, I. D. W. Samuel, G. R. Hayes, R. T. Phillips, Y. Kessener, S. C. Moratti, A. B. Holmes, and R. H. Friend, *Measurement of absolute photoluminescence quantum efficiencies in conjugated polymers*, Chemical Physics Letters **241** (1-2), 89–96, 1995.
- [116] N. I. Craciun, J. J. Brondijk, and P. W. M. Blom, *Diffusion-enhanced hole transport in thin polymer light-emitting diodes*, Physical Review B **77** (3), 2008.
- [117] N. C. Greenham, R. H. Friend, and D. D. C. Bradley, *Angular-dependence of the emission from a conjugated polymer light-emitting diode - implications for efficiency calculations*, Advanced Materials **6** (6), 491–494, 1994.
- [118] B. Ruhstaller, S. A. Carter, S. Barth, H. Riel, W. Riess, and J. C. Scott, *Transient and steady-state behavior of space charges in multilayer organic light-emitting diodes*, Journal of Applied Physics **89** (8), 4575–4586, 2001.
- [119] A. B. Walker, A. Kambili, and S. J. Martin, *Electrical transport modelling in organic electroluminescent devices*, Journal of Physics: Condensed Matter **14** (42), 9825, 2002.
- [120] H. Becker, S. E. Burns, and R. H. Friend, *Effect of metal films on the photoluminescence and electroluminescence of conjugated polymers*, Physical Review B **56** (4), 1893–1905, 1997.
- [121] K. H. Yim, R. Friend, and J. S. Kim, *Anisotropic optical properties in electroluminescent conjugated polymers based on grazing angle photoluminescence measurements*, Journal of Chemical Physics **124** (18), 8, 2006.
- [122] J. H. Kim, P. Herguth, M. S. Kang, A. K. Y. Jen, Y. H. Tseng, and C. F. Shu, *Bright white light electroluminescent devices based on a dye-dispersed polyfluorene derivative*, Applied Physics Letters **85** (7), 1116–1118, 2004.

- [123] L. S. C. Pingree, B. A. MacLeod, and D. S. Ginger, *The changing face of PEDOT:PSS films: Substrate, bias, and processing effects on vertical charge transport*, *Journal of Physical Chemistry C* **112** (21), 7922–7927, 2008.
- [124] G. N. Taylor and T. M. Wolf, *Oxygen plasma removal of thin polymer-films*, *Polymer Engineering and Science* **20** (16), 1087–1092, 1980.
- [125] F. D. Egitto, *Plasma-etching and modification of organic polymers*, *Pure and Applied Chemistry* **62** (9), 1699–1708, 1990.
- [126] A. Colsmann, F. Stenzel, G. Balthasar, H. Do, and U. Lemmer, *Plasma patterning of poly(3,4-ethylenedioxythiophene):poly(styrenesulfonate) anodes for efficient polymer solar cells*, *Thin Solid Films* **517** (5), 1750–1752, 2009.
- [127] Y. F. Zhou, Y. B. Yuan, L. F. Cao, J. Zhang, H. Q. Pang, J. R. Lian, and X. Zhou, *Improved stability of OLEDs with mild oxygen plasma treated PEDOT:TSS*, *Journal of Luminescence* **122**, 602–604, 2006.
- [128] T. Förster, *Zwischenmolekulare Energiewanderung und Fluoreszenz*, *Annalen der Physik* **437** (1-2), 55–75, 1948.
- [129] M. Anni, S. Lattante, M. M. De Kok, R. Cingolani, and G. Gigli, *Intermolecular sequential energy transfer in thin films of a white emitting copolymer*, *Applied Physics Letters* **89** (22), 221903, 2006.
- [130] T. Förster, *10th Spiers memorial lecture. Transfer mechanisms of electronic excitation*, *Discussions of the Faraday Society* **27**, 7–17, 1959.
- [131] K. B. Eisenthal and S. Siegel, *Influence of resonance transfer on luminescence decay*, *Journal of Chemical Physics* **41** (3), 652–655, 1964.
- [132] R. C. Powell and R. G. Kepler, *Evidence for long-range exciton-impurity interaction in tetracene-doped anthracene crystals*, *Physical Review Letters* **22** (13), 636, 1969.
- [133] R. C. Powell and Z. G. Soos, *Singlet exciton energy-transfer in organic solids*, *Journal of Luminescence* **11** (1-2), 1–45, 1975.
- [134] K. O. Cheon and J. Shinar, *Förster energy transfer in combinatorial arrays of selective doped organic light-emitting devices*, *Applied Physics Letters* **84** (7), 1201–1203, 2004.
- [135] K. Becker, J. M. Lupton, J. Feldmann, S. Setayesh, A. C. Grimsdale, and K. Müllen, *Efficient intramolecular energy transfer in single endcapped conjugated polymer molecules in the absence of appreciable spectral overlap*, *Journal of the American Chemical Society* **128** (3), 680–681, 2006.
- [136] V. I. Arkhipov and H. Bässler, *Exciton energy relaxation and dissociation in pristine and doped conjugated polymers* in *Physics of Organic Semiconductors* edited by W. Brütting, Wiley-VCH Weinheim, 2005.

- [137] V. I. Arkhipov, I. I. Fishchuk, A. Kadashchuk, and H. Bässler, *Charge transport in neat and doped random organic semiconductors* in *Semiconducting Polymers: Chemistry, Physics and Engineering* vol. 1 edited by G. Hadziioannou and G. G. Malliaras, Wiley-VCH Weinheim, 2. edition 2007.
- [138] I. I. Fishchuk, A. K. Kadashchuk, H. Bässler, and D. S. Weiss, *Nondispersive charge-carrier transport in disordered organic materials containing traps*, *Physical Review B* **66** (20), 205208, 2002.
- [139] U. Albrecht and H. Bässler, *Langevin-type charge-carrier recombination in a disordered hopping system*, *Physica Status Solidi B* **191** (2), 455–459, 1995.
- [140] W. Shockley and W. T. Read, *Statistics of the recombinations of holes and electrons*, *Physical Review* **87** (5), 835, 1952.
- [141] J. Staudigel, M. Stössel, F. Steuber, and J. Simmerer, *A quantitative numerical model of multilayer vapor-deposited organic light emitting diodes*, *Journal of Applied Physics* **86** (7), 3895–3910, 1999.
- [142] C.-C. Lee, M.-Y. Chang, P.-T. Huang, Y. C. Chen, Y. Chang, and S.-W. Liu, *Electrical and optical simulation of organic light-emitting devices with fluorescent dopant in the emitting layer*, *Journal of Applied Physics* **101** (11), 114501, 2007.
- [143] T. R. Waite, *Bimolecular reaction rates in solids and liquids*, *The Journal of Chemical Physics* **32** (1), 21–23, 1960.
- [144] J. Yguerabide, M. A. Dillon, and M. Burton, *Kinetics of diffusion-controlled processes in liquids. theoretical consideration of luminescent systems: Quenching and excitation transfer in collision*, *The Journal of Chemical Physics* **40** (10), 3040–3052, 1964.
- [145] I. I. Fishchuk, A. K. Kadashchuk, and H. Bässler, *Charge carrier transport in disordered organic materials in the presence of traps*, *Molecular Crystals and Liquid Crystals* **426**, 71–80, 2005.
- [146] E. W. Montroll and G. H. Weiss, *Random walks on lattices II*, *Journal of Mathematical Physics* **6** (2), 167, 1965.
- [147] Y. Roichman and N. Tessler, *Generalized Einstein relation for disordered semiconductors – implications for device performance*, *Applied Physics Letters* **80** (11), 1948–1950, 2002.
- [148] J. Qu, J. Zhang, A. C. Grimsdale, K. Müllen, F. Jaiser, X. Yang, and D. Neher, *Den-dronized perylene diimide emitters: Synthesis, luminescence, and electron and energy transfer studies*, *Macromolecules* **37** (22), 8297–8306, 2004.
- [149] M. Novo, M. v. d. Auweraer, F. C. d. Schryver, P. Borsenberger, and H. Bässler, *Anomalous field dependence of the hole mobility in a molecular doped polymer*, *physica status solidi (b)* **177** (1), 223–241, 1993.

- [150] K. Murata, S. Cina, and N. C. Greenham, *Barriers to electron extraction in polymer light-emitting diodes*, Applied Physics Letters **79** (8), 1193–1195, 2001.
- [151] N. Koch, A. Elschner, and R. L. Johnson, *Green polyfluorene-conducting polymer interfaces: Energy level alignment and device performance*, Journal of Applied Physics **100** (2), 5, 2006.
- [152] A. J. A. B. Seeley, R. H. Friend, J.-S. Kim, and J. H. Burroughes, *Trap-assisted hole injection and quantum efficiency enhancement in poly(9,9' dioctylfluorene-alt-benzothiadiazole) polymer light-emitting diodes*, Journal of Applied Physics **96** (12), 7643–7649, 2004.
- [153] K. Isoda, N. Kouchi, Y. Hatano, and M. Tachiya, *The effect of an external electric-field on diffusion-controlled bulk ion recombination*, Journal of Chemical Physics **100** (8), 5874–5881, 1994.
- [154] K. O. Cheon and J. Shinar, *Electroluminescence spikes, turn-off dynamics, and charge traps in organic light-emitting devices*, Physical Review B **69** (20), 201306, 2004.
- [155] B. Choudhury, *Organic light emitting devices (OLEDs) and structurally integrated photoluminescence based chemical and biological sensors excited by OLEDs*, Phd thesis, Iowa State University, Ames 2005.
- [156] V. Savvate'ev, J. H. Friedl, L. Zou, J. Shinar, K. Christensen, W. Oldham, L. J. Rothberg, Z. Chen-Esterlit, and R. Kopelman, *Nanosecond transients in the electroluminescence from multilayer blue organic light-emitting devices based on 4,4'-bis(2,2'-diphenyl vinyl)-1,1'-biphenyl*, Applied Physics Letters **76** (12), 1501–1503, 2000.
- [157] J. M. Lupton, V. R. Nikitenko, I. D. W. Samuel, and H. Bässler, *Time delayed electroluminescence overshoot in single layer polymer light-emitting diodes due to electrode luminescence quenching*, Journal of Applied Physics **89** (1), 311–317, 2001.
- [158] A. Mozumder, *Theory of neutralization of an isolated ion pair: Application of the method of prescribed diffusion to random walk in a coulomb field*, The Journal of Chemical Physics **48** (4), 1659–1665, 1968.
- [159] K. M. Hong and J. Noolandi, *Solution of the Smoluchowski equation with a coulomb potential. I. General results*, The Journal of Chemical Physics **68** (11), 5163–5171, 1978.
- [160] J. Noolandi and K. M. Hong, *Theory of photogeneration and fluorescence quenching*, Journal of Chemical Physics **70** (7), 3230–3236, 1979.
- [161] C. L. Braun, *Electric field assisted dissociation of charge transfer states as a mechanism of photocarrier production*, The Journal of Chemical Physics **80** (9), 4157–4161, 1984.
- [162] V. I. Arkhipov and V. R. Nikitenko, *Langevin-recombination-controlled explosive kinetics of electroluminescence in organic semiconductors*, Semiconductors **33** (8), 862–864, 1999.

- [163] B. Schweitzer, V. I. Arkhipov, and H. Bässler, *Field-induced delayed photoluminescence in a conjugated polymer*, Chemical Physics Letters **304** (5-6), 365–370, 1999.
- [164] N. Tessler, D. J. Pinner, V. Cleave, D. S. Thomas, G. Yahioglu, P. Le Barny, and R. H. Friend, *Pulsed excitation of low-mobility light-emitting diodes: Implication for organic lasers*, Applied Physics Letters **74** (19), 2764–2766, 1999.
- [165] S. Sinha and A. P. Monkman, *Delayed recombination of detrapped space-charge carriers in poly[2-methoxy-5-(2'-ethyl-hexyloxy)-1,4-phenylene vinylene]-based light-emitting diode*, Journal of Applied Physics **97** (11), 7, 2005.
- [166] S. Sinha, C. Rothe, R. Guntner, U. Scherf, and A. P. Monkman, *Electrophosphorescence and delayed electroluminescence from pristine polyfluorene thin-film devices at low temperature*, Physical Review Letters **90** (12), 2003.
- [167] G. Juska, K. Arlauskas, M. Viliunas, and J. Kocka, *Extraction current transients: New method of study of charge transport in microcrystalline silicon*, Physical Review Letters **84** (21), 4946–4949, 2000.
- [168] G. Juska, K. Arlauskas, M. Viliunas, K. Genevicius, R. Österbacka, and H. Stubb, *Charge transport in pi-conjugated polymers from extraction current transients*, Physical Review B **62** (24), 16235–16238, 2000.
- [169] A. J. Mozer, N. S. Sariciftci, L. Lutsen, D. Vanderzande, R. Österbacka, M. Westerling, and G. Juska, *Charge transport and recombination in bulk heterojunction solar cells studied by the photoinduced charge extraction in linearly increasing voltage technique*, Applied Physics Letters **86** (11), 112104, 2005.
- [170] G. Juska, N. Nekrasas, K. Genevicius, J. Stuchlik, and J. Kocka, *Relaxation of photoexcited charge carrier concentration and mobility in $\mu\text{-Si:H}$* , Thin Solid Films **451-452**, 290–293, 2004.
- [171] A. J. Mozer, G. Dennler, N. S. Sariciftci, M. Westerling, A. Pivrikas, R. Österbacka, and G. Juska, *Time-dependent mobility and recombination of the photoinduced charge carriers in conjugated polymer/fullerene bulk heterojunction solar cells*, Physical Review B **72** (3), 035217, 2005.
- [172] R. Österbacka, A. Pivrikas, G. Juska, K. Genevicius, K. Arlauskas, and H. Stubb, *Mobility and density relaxation of photogenerated charge carriers in organic materials*, Current Applied Physics **4** (5), 534–538, 2004.
- [173] C. Yin, M. Schubert, S. Bange, B. Stiller, M. Castellani, D. Neher, M. Kumke, and H. H. Hörhold, *Tuning of the excited-state properties and photovoltaic performance in PPV-based polymer blends*, Journal of Physical Chemistry C **112** (37), 14607–14617, 2008.
- [174] M. Schubert, C. Yin, M. Castellani, S. Bange, T. L. Tam, A. Sellinger, H.-H. Hörhold, T. Kietzke, and D. Neher, *Heterojunction topology versus fill factor correlations in novel hybrid small-molecular/polymeric solar cells*, Journal of Chemical Physics **130** (9), 094703, 2009.

- [175] P. Würfel, *Physics of solar cells*, Wiley-VCH, Weinheim, 2005.
- [176] Y. Preezant and N. Tessler, *Self-consistent analysis of the contact phenomena in low-mobility semiconductors*, *Journal of Applied Physics* **93** (4), 2059–2064, 2003.
- [177] W. H. Press, *Numerical recipes in C: The art of scientific computing*, Cambridge University Press, 2. edition 2002.
- [178] W. E. Schiesser, *Computational mathematics in engineering and applied science. ODEs, DAEs, and PDEs*, CRC Press, Boca Raton, 1994.
- [179] B. K. Crone, P. S. Davids, I. H. Campbell, and D. L. Smith, *Device model investigation of bilayer organic light emitting diodes*, *Journal of Applied Physics* **87** (4), 1974–1982, 2000.
- [180] C. Pflumm and M. Neiger, *Modellierung der homogenen transienten Barrierenentladung*, Abschlussbericht zum BMBF Forschungsvorhaben FKZ 13N7352/1 Lichttechnisches Institut der Universität Karlsruhe 2003.
- [181] D. L. Scharfetter and H. K. Gummel, *Large-signal analysis of a silicon read diode oscillator*, *IEEE Transactions on Electron Devices* **ED16** (1), 64, 1969.
- [182] J. F. Hawley, L. L. Smarr, and J. R. Wilson, *A numerical study of nonspherical black-hole accretion. 2. Finite differencing and code calibration*, *Astrophysical Journal Supplement Series* **55** (2), 211–246, 1984.
- [183] M. A. Parshin, J. Ollevier, M. V. d. Auweraer, M. M. d. Kok, H. T. Nicolai, A. J. Hof, and P. W. M. Blom, *Hole transport in blue and white emitting polymers*, *Journal of Applied Physics* **103** (11), 113711, 2008.
- [184] C. Yin, *The interplay of nanostructure and efficiency of polymer solar cells*, PhD thesis, University of Potsdam, Potsdam 2009.
- [185] A. Bahtiar, *Optical waveguides of conjugated polymers for all-optical switching devices*, PhD thesis, Johannes Gutenberg-Universität, Mainz 2004.
- [186] S. V. Chasteen, S. A. Carter, and G. Rumbles, *The effect of broken conjugation on the excited state: Ether linkage in the cyano-substituted poly(p-phenylene vinylene) conjugated polymer poly(2,5,2',5'-tetrahexyloxy-8,7'-dicyano-di-p-phenylene vinylene)*, *The Journal of Chemical Physics* **124** (21), 214704, 2006.

Publications and Conference Attendance

Publications

1. Robert Steyrlleuthner, Sebastian Bange and Dieter Neher: *Reliable electron-only devices and electron transport in n-type polymers*, Journal of Applied Physics **105**, 064509 (2009).
2. Marcel Schubert, Chunhong Yin, Mauro Castellani, Sebastian Bange, Teck Lip Tam, Alan Sellinger, Hans-Heinrich Hörhold, Thomas Kietzke and Dieter Neher: *Heterojunction topology versus fill factor correlations in novel small-molecular / polymeric solar cells*, Journal of Chemical Physics **130**, 094703 (2009).
3. Sebastian Bange, Andriy Kuksov, Dieter Neher, Antje Vollmer, Norbert Koch, Aurelie Ludemann and Susanne Heun: *The role of poly(3,4-ethylenedioxythiophene): poly(styrenesulphonate) as a hole injection layer in a blue-emitting polymer light-emitting diode*, Journal of Applied Physics **104**, 104506 (2008).
4. Chunhong Yin, Marcel Schubert, Sebastian Bange, Burkhard Stiller, Mauro Castellani, Dieter Neher, Michael Kumke and Hans-Heinrich Hörhold: *Tuning of the excited-state properties and photovoltaic performance in PPV-based polymer blends*, Journal of Physical Chemistry C **112**, 14607 (2008).
5. Sebastian Bange, Andriy Kuksov and Dieter Neher: *Sensing electron transport in a blue-emitting copolymer by transient electroluminescence*, Applied Physics Letters **91**(14), 143516 (2007).

Conference Attendance

1. Sebastian Bange and Dieter Neher: *Charge trapping and color shifts in 'single polymer' white light-emitting diodes*, talk, OP2009 meeting, Beijing, China 2009.
2. Sebastian Bange and Dieter Neher: *Charge trapping and color stability in a white-emitting copolymer*, poster, DPG spring meeting, Dresden 2009.
3. Robert Steyrlleuthner, Sebastian Bange and Dieter Neher: *Reliable electron-only devices and electron transport in n-type polymers*, poster, DPG spring meeting, Dresden 2009.
4. Sebastian Bange and Dieter Neher: *The role of the interface between PEDOT:PSS and a wide-bandgap blue-emitting polymer for efficient OLED operation*, talk, ICCEL-7 conference, Dresden 2008.

5. Robert Steyrlleuthner, Sebastian Bange, Dieter Neher: *Reliable electron-only devices and electron transport in n-type polymers*, poster, ICEL-7 conference, Dresden 2008.
6. Sebastian Bange, Andriy Kuksov and Dieter Neher: *Revealing the dynamics in polymer-based optoelectronic devices*, poster, DPG spring meeting, Regensburg 2007.
7. Sebastian Bange, Andriy Kuksov, Dieter Neher: *Measurement of electron transport in a blue-emitting wide-bandgap copolymer by transient electroluminescence*, poster, ECME conference, Strasbourg 2007.

Acknowledgement/Danksagung

Zunächst möchte ich mich bei Prof. Dr. Dieter Neher dafür bedanken, mir die Möglichkeit zu dieser Dissertation in seiner Arbeitsgruppe gegeben zu haben. Seine kontinuierliche Anleitung und Motivation, seine vielen Vorschläge für Messungen und deren Interpretation und seine präzise Kenntnis aller experimentellen Befunde trugen ungemein zum wissenschaftlichen Fortgang der Arbeit bei.

Die in dieser Arbeit maßgeblich untersuchten Materialien wurden von Merck KGaA, Frankfurt zur Verfügung gestellt. Hier sei insbesondere Dr. Susanne Heun und Dr. Aurélie Ludemann für die Synthese und Optimierung der Polymere gedankt sowie Dr. Frank Voges, Dr. Anna Hayer und Dr. Christof Pflümm für den intensiven Erfahrungsaustausch zu den Funktionsprinzipien von polymeren Leuchtdioden. Die Gespräche und Kooperation mit Dr. Andreas Elschner (H.C. Starck, Mainz) und Dr. Norbert Koch (Humboldt-Universität Berlin) trugen wesentlich zu den Erkenntnissen über Funktion und Verhalten des polymeren Anodenmaterials PEDOT:PSS bei.

Zum Thema der Emissionszone von Leuchtdioden möchte ich mich für die anregende Zusammenarbeit mit Dipl.-Phys. Michael Flämmich, Dr. Dirk Michaelis und Dr. Norbert Danz bedanken. Im Bereich der zeitaufgelösten Photostrommessungen gilt mein Dank der exzellenten experimentellen Kooperation mit Dipl.-Phys. Andriy Kuksov, dessen Kreativität und Improvisationsgabe sehr hilfreich waren. Viele der Ladungstransportmessungen an den weiß-emittierenden Kopolymeren wurden von Dipl.-Phys. Dennis Plüschke und von Viktor Kuxhaus durchgeführt, für deren unermüdliche Arbeit ich mich hier auch noch einmal bedanken möchte. Für die Möglichkeit zur Nutzung des ICCD-Kamerasystems zur Vermessung von OLED-Transienten danke ich ganz herzlich Prof. Dr. Anna Köhler und Dr. Carsten Dosche.

Die Präparation und Vermessungen von organischen Halbleiterbauteilen erfordert Zeit, Geduld, Präzision und viel Fleiß. Trotz der vielen eigenen Stunden im Labor ist der Arbeitsaufwand alleine nicht immer zu bewältigen. Hier gilt mein ganz besonderer Dank Thomas Manicke und Dipl.-Phys. Robert Steyrleuthner, die mir im Laufe der letzten drei Jahre immer wieder unermüdlich Arbeit abnahmen und damit den kontinuierlichen Zufluss an Messdaten aufrechterhielten. Viele der hier versammelten Messergebnisse, gerade im Bereich der schnellen transienten EL, wurden erst durch die fortwährende Unterstützung durch Dipl.-Ing. Andreas Pucher ermöglicht, der mit Fleiß und Erfahrung immer wieder Problemlösungen in Form elektronischer Schaltungen hervorzauberte. Prof. Dr. Matias Bargheer und Dipl.-Phys. Mareike Kiel danke ich für die interessanten Diskussionen und die Möglichkeit, Messungen zur feldinduzierten Frequenzverdopplung in Polymerschichten an ihrem Femtosekundenlaser durchzuführen, die jedoch leider keinen Eingang mehr in diese Arbeit fanden.

Ein ganz besonderer Dank gilt meinem Bürokollegen Dr. Frank Jaiser, der mich immer wieder mit seinem Detailwissen unterstützt hat und von dem ich fast alle experimentellen Feinheiten lernen konnte, die im Bereich organischer Halbleiter nötig sind. Die Arbeitsgrup-

pe „Physik weicher Materie“ ist über die Zeit kontinuierlich gewachsen, hat dabei jedoch nicht ihre freundschaftliche und entspannte Arbeitsatmosphäre verloren. Für viele interessante wissenschaftliche und nichtwissenschaftliche Gespräche, Ausflüge und Kaffeerunden danke ich den gegenwärtigen und ehemaligen Mitgliedern der Arbeitsgruppe (in alphabetischer Reihenfolge): Steve Albrecht, Dr. Mauro Castellani, Elke Derlig, Christoph Fahrenson, Andreas Horka, Dr. Jaroslav Ilnytskyi, Sahika Inal, Dr. Frank Jaiser, Dipl.-Phys. Andriy Kuksov, Dr. Lazar Kulikovsky, Viktor Kuxhaus, Ilja Lange, Thomas Manicke, Dr. Knut Morawetz, Patrick Parnow, Dipl.-Ing. Sylvia Paul, Dipl.-Phys. Patrick Pingel, Dipl.-Phys. Dennis Plüschke, Dipl.-Ing. Andreas Pucher, Dipl.-Phys. Beate Reinhold, Dipl.-Phys. Marcel Schubert, Dipl.-Phys. Robert Steyrleuthner, Dipl.-Ing. Burkhard Stiller, Dr. Harry Weigt, Dr. Xiaohui Yang, Dr. Chunhong ‘Debby’ Yin und Dr. Achmad Zen.

Diese Arbeit wurde maßgeblich finanziell ermöglicht durch das vom BMBF geförderte Forschungsvorhaben „Hochwertige organische Leuchtdioden für Beleuchtungsanwendungen auf der Basis innovativer Technologien“ (HOBBIT).

Zu guter Letzt danke ich meiner Familie für die über die vielen Jahre meines Studiums hinweg vermittelte Unterstützung. Den größten Anteil am Gelingen dieses Unternehmens jedoch hatte meine Frau Dörte, die mir mit viel Verständnis, kritischem Blick und Aufmunterung stets zur Seite stand und die sich über die vielen außerplanmäßigen Stunden, die ich im Labor und am Computer verbrachte, nie beklagt hat.

Curriculum Vitae

Sebastian Bange
Zeppelinstrasse 7, 14471 Potsdam
+49 331 9676436, +49 176 64023038 (cell)
electronic mail: sbange@uni-potsdam.de, sbange05@googlemail.com

Date of birth June 18, 1980 in Berlin

Nationality German

Marital status married

Education

since 2006/03 Graduate studies at the **University of Potsdam**, Advisor: Prof. Dr. Dieter Neher

2006/02 Dipl.-Phys., **University of Potsdam**, “with distinction” (1.0), Thesis: “Erzeugung verschränkter Photonen durch optische Ultrakurzpuls-Anregung von parametrischer Fluoreszenz für Anwendungen in der Quantenkommunikation” (“Generation of entangled photons by optical ultrashort pulse excitation of parametric fluorescence”), Advisor: Prof. Dr. Martin Ostermeyer

Awards

2007/06 “Physik-Studienpreis” of the Wilhelm and Else Heraeus Foundation
Awarded for excellence to the top ten graduated diploma physicists at Berlin and Potsdam.

Professional Experience

2006/03 – 2008/09 Research and Teaching Assistant with Prof. Dr. Dieter Neher, **University of Potsdam, Germany**

2004/03 – 2004/06 Research Assistant with Prof. Dr. Ralf Menzel and Dr. Martin Ostermeyer, **University of Potsdam, Germany**, frequency stabilization of a MOPA pump laser for LIDAR systems.

2003/09 – 2003/10 Student employee (contract work), **IBL Industrial Broad-Spectrum Laser AG, Berlin, Germany**, mode-matching of a seed laser for a LIDAR system’s MOPA pump laser with excellent beam parameters and pulse energy

2001/05 – 2003/09 Student Assistant to Prof. Dr. Reimund Gerhard

2000/02 – 2000/03 Student Assistant to Prof. Dr. Reimund Gerhard, **University of Potsdam, Germany**, development and implementation of scientific experiments in polymer science (thermally and photo-stimulated discharge, Kramers-Kronig analysis)

Declaration

I hereby certify that the work presented in this thesis has not been submitted to any other university or higher education institute and that this work is my own and that all sources and aids used are listed within. Any results not of my own creation are clearly indicated as such.

Potsdam, May 28, 2009

Signed,

A handwritten signature in blue ink that reads "Sebastian Bange". The signature is written in a cursive style with a long, sweeping underline.

Sebastian Bange